TESIS DE LA UNIVERSIDAD DE ZARAGOZA

2024 304

Marcos Rubin Osanz

Pump-probe experiments on superconducting resonators coupled to molecular spins
TESIS CORREGIDA

Director/es
Luis Vitalla, Fernando
Zueco Láinez, David

ISSN 2254-7606

Prensas de la Universidad
Universidad Zaragoza

Universidad de Zaragoza
Servicio de Publicaciones

ISSN 2254-7606

Universidad Zaragoza
1542

Tesis Doctoral

PUMP-PROBE EXPERIMENTS ON SUPERCONDUCTING RESONATORS COUPLED TO MOLECULAR SPINS
TESIS CORREGIDA

Autor

Marcos Rubin Osanz

Director/es

Luis Vitalla, Fernando
Zueco Láinez, David

UNIVERSIDAD DE ZARAGOZA
Escuela de Doctorado

Programa de Doctorado en Física

2024

Universidad Zaragoza
1542

Tesis Doctoral

PUMP-PROBE EXPERIMENTS ON SUPERCONDUCTING RESONATORS COUPLED TO MOLECULAR SPINS

Autor

Marcos Rubín Osanz

Directores

Fernando Luis Vitalla
David Zueco Láinez

Universidad de Zaragoza
Escuela de Doctorado

Programa de Doctorado en Física

2023

Arrakis teaches the attitude of the knife – chopping off what's incomplete and saying: "Now, it's complete because it's ended here."

Frank Herbert, "Dune"

A mis padres.

Contents

1 Introduction **5**

2 Experimental setup and techniques **13**

2.1 Superconducting chip 13

2.1.1 Design and fabrication 15

2.1.2 Interface with microwave coaxial lines: PCBs and wire bonding 17

2.2 Cryogen-free dilution refrigerator 18

2.2.1 Operating principle of a ^{3}He-^{4}He dilution refrigerator . . 19

2.2.2 Superconducting magnet 21

2.2.3 Microwave coaxial lines and cryogenic amplifier 21

2.3 Microwave setup for pump-probe experiments 22

2.3.1 Characterization with continuous wave experiments . . . 22

2.3.2 Pulse generation 24

2.3.3 Readout 25

2.4 Complementary experimental techniques 25

2.4.1 SQUID magnetometry 26

2.4.2 Micro-Hall magnetometry 27

2.4.3 Heat capacity experiments 28

2.4.4 Electron Paramagnetic Resonance 30

3 Background on spin systems coupled to superconducting resonators **35**

3.1 Molecular spin systems 35

3.1.1 The ground spin multiplet 36

3.1.2 Effective spin Hamiltonian 37

3.1.3 Decoherence and relaxation processes 40

3.1.4 The molecular spin qubit 42

3.1.5 The molecular spin qudit 43

3.2 Lumped-element resonators 44

3.2.1 The classical LC resonator 44

3.2.2 Quantization of the LC resonator 45

3.3 Coupling molecular spin qubits to lumped-element resonators . 46
3.3.1 Molecular spin qubit-resonator coupling 47
3.3.2 Spin 1/2 ensembles 50
3.3.3 Generalization to a higher spin ensemble 54
3.4 Dispersive regime 55
3.4.1 Qubit coupled to a resonator 56
3.4.2 Spin 1/2 ensembles 58
3.4.3 Generalization to higher spin systems 60

4 Measurement of the quantum processor 65
4.1 Transmission line 65
4.1.1 The classical transmission line 67
4.1.2 Quantization of the transmission line 68
4.2 Input-output theory 70
4.2.1 Input-output relations 71
4.2.2 Coherent drive 72
4.3 Dissipation of the quantum system through the transmission line 73
4.3.1 Time-dependent perturbation theory in the interaction picture 74
4.3.2 Tracing the line 75
4.3.3 Secular and rotating wave approximations 77
4.3.4 Markovian regime 77
4.3.5 Back to the Schrödinger picture 78
4.4 Measurement of a lumped-element resonator 79
4.4.1 Dynamics of a resonator without driving 79
4.4.2 Driving the resonator 80
4.5 Measurement of a spin 1/2 ensemble 81
4.5.1 Dynamics of a single spin without driving 81
4.5.2 Driving a single spin 83
4.5.3 Driving a spin 1/2 ensemble 84
4.6 Measurement of a spin 1/2 ensemble-resonator system 86
4.6.1 Spin-resonator system 86
4.6.2 Ensemble-resonator system 86
4.6.3 Driving the ensemble-resonator system 87
4.6.4 Weak and strong coupling 89
4.7 Generalization to high spin systems 91
4.7.1 Single spin $S > 1/2$ coupled to a transmission line . . . 91
4.7.2 Driving a single spin $S > 1/2$ through the transmission line 93
4.7.3 Driving a spin $S > 1/2$ ensemble through the transmission line 95
4.7.4 Driving a spin $S > 1/2$ ensemble-resonator system . . . 95

5 Strong coupling of organic free-radical molecules to lumped-element resonators 99
5.1 Chip design and characterization . . . 100
5.1.1 Chip design . . . 100
5.1.2 Characterization of *Test 1* . . . 103
5.1.3 Characterization of *Test 2* . . . 105
5.2 DPPH samples . . . 108
5.2.1 The DPPH radical . . . 108
5.2.2 Sample characterization . . . 109
5.3 Coupling of DPPH to LERs in *Test 1* . . . 114
5.3.1 Effect of the resonator geometry and orientation on its visibility . . . 114
5.3.2 Strong coupling of a DPPH ensemble to a LER . . . 116
5.3.3 Effect of the magnetic field orientation . . . 120
5.4 Coupling of DPPH to LERs in *Test 2* . . . 126
5.4.1 Testing the bare resonator response with magnetic field 126
5.4.2 Frequency shift by sample deposition . . . 127
5.4.3 Spin-photon coupling in chip *Test 2*: coupling to remote resonators and dependence on ω_r . . . 128
5.4.4 Effect of the magnetic field inhomogeneity: coupling to small spin ensembles . . . 132
5.5 Conclusions . . . 136

6 Dispersive qubit readout: pump-probe experiments on PTM organic free radicals 141
6.1 Experimental setup for pulse experiments . . . 142
6.1.1 Chip design . . . 142
6.1.2 Molecular spin samples . . . 143
6.1.3 Microwave setup for pulse experiments . . . 145
6.2 Characterization of the collective spin-resonator coupling . . . 147
6.3 Testing pulse generation and the resonator dynamics . . . 151
6.4 First pump-probe experiments on PTM radicals: measurement of the spin ensemble absorption spectrum and relaxation time T_1 155
6.4.1 Basics of dispersive readout with pump-probe experiments 155
6.4.2 Microwave generation and detection setups . . . 157
6.4.3 Spin ensemble absorption spectrum and T_1 measurements 159
6.4.4 Modulating T_1 with the magnetic field . . . 164
6.5 Towards a coherent manipulation of molecular spin qubits . . . 168
6.5.1 Testing the setup for shorter pump pulses . . . 168
6.5.2 Parallel pathways to generate the dispersive shift . . . 171
6.5.3 Detection of damped oscillations . . . 175
6.6 Conclusions . . . 176

7 Circuit QED with electro-nuclear spin qudits 179
7.1 Experimental setup . . . 180
7.1.1 [Yb(trensal)] samples . . . 180
7.1.2 Chip design . . . 183
7.2 High cooperativity coupling to nuclear spin transitions . . . 184
7.2.1 Electronic spin transitions . . . 185
7.2.2 Nuclear spin transitions . . . 187
7.3 Pulse experiments on [Yb(trensal)] molecular spin qudits . . . 191
7.3.1 Electronic spin transitions . . . 191
7.3.2 Nuclear spin transitions . . . 193
7.4 Pump-probe experiments with isotopically purified samples . . 198
7.4.1 Characterization of electronic spin transitions . . . 198
7.4.2 Dispersive readout in an electro-nuclear qudit . . . 203
7.4.3 First pump-probe experiments . . . 206
7.5 Conclusions . . . 207

8 Circuit QED beyond non-interacting magnetic molecules 211
8.1 Competition between spin-photon and spin-spin interactions in DPPH organic free radicals coupled to a superconducting transmission line . . . 212
8.1.1 Paramagnetic phase: spin-photon coupling enhancement 213
8.1.2 Breakdown of superradiance by magnetic correlations . . 216
8.2 On-chip magnetic spectroscopy across a magnetic phase transition 219
8.2.1 Qubits based on spin clock states . . . 219
8.2.2 Molecular design of the simplest system with spin-clock states: the case of [Ni(2-Imdipa)] . . . 221
8.2.3 Determination the molecular axes of [Ni(2-imdipa)] with transmission experiments . . . 225
8.2.4 Coupling spin-clock states to superconducting transmission lines . . . 227
8.2.5 Coupling spin-clock states to lumped-element resonators 232
8.3 Conclusions . . . 236

9 Conclusions 239

Resumen

La evolución de la computación clásica en las últimas décadas ha estado marcada por el desarrollo de componentes cada vez más pequeños y rápidos. Sin embargo, este proceso de miniaturización tiene un límite en las escalas en las que los efectos cuánticos empiezan a ser relevantes. Este problema es una oportunidad para desarrollar un nuevo tipo de computación, la *computación cuántica*, que toma precisamente como elemento básico un sistema con propiedades cuánticas. Este elemento básico es el bit cuántico o *qubit*, el análogo cuántico del bit clásico. Mientras un bit clásico solo puede estar en uno de dos estados, 0 o 1, un qubit puede estar en cualquier superposición $|\psi\rangle := \alpha\,|0\rangle + \beta\,|1\rangle$ de dos estados base $|0\rangle$ y $|1\rangle$, donde α y β son dos números complejos. Esta propiedad de superposición permite hacer operaciones paralelas de manera natural. Además, también son posibles los estados de superposición de más de un qubit, conocidos como estados entrelazados. De esta manera, un conjunto de qubits tiene acceso a un número de estados exponencialmente mayor que el mismo número de bits clásicos. Las posibilidades de procesamiento de información que introducen los estados de superposición permitirían a un futuro ordenador cuántico resolver ciertos problemas complejos como la factorización de números primos muy grandes, la búsqueda en grandes bases de datos o la simulación de sistemas cuánticos. Algunos de estos problemas están lejos de las capacidades de los ordenadores clásicos en tiempo y recursos finitos.

Desde finales del siglo pasado se han propuesto diversos sistemas cuánticos como realizaciones físicas del concepto de qubit. A día de hoy, el abanico de sistemas es amplio: circuitos superconductores, defectos de espín en semiconductores, fotones, átomos ultrafríos, y más, cada uno con sus ventajas y sus inconvenientes. Uno de los retos más importantes a los que se enfrenta cualquiera de estos dispositivos es el fenómeno de *decoherencia*, en el que la interacción del qubit con su entorno destruye la información que éste almacena, generando errores de computación. Incluso los ordenadores cuánticos más avanzados y sofisticados están limitados por errores al manipular un número considerable de qubits. Una solución para mitigar estos errores es la implementación de códigos de corrección de errores basados en un almacenamiento redundante de

la información. Para cada qubit lógico protegido frente a errores se necesitan qubits físicos adicionales, lo que genera un nuevo problema asociado a tener que controlar un número mucho mayor de qubits. Una alternativa prometedora es pasar de la lógica binaria de los qubits, con dos estados base, a sistemas cuánticos más complejos con $d > 2$ estados base, conocidos como *qudits*. Los estados adicionales de los que dispone un qudit se han propuesto como una plataforma para codificar una unidad de corrección de errores.

Los espines presentes en las moléculas magnéticas pueden codificar tanto qubits como qudits. Como unidades básicas de un ordenador cuántico, las moléculas magnéticas destacan por su pureza y reproducibilidad, ya que las características de todas quedan definidas por las mismas propiedades químicas. La principal fuente de decoherencia en estos sistemas es la interacción dipolar magnética, ya que los espines son relativamente inmunes a las fluctuaciones del campo eléctrico. Esto hace que los tiempos de coherencia de los qubits de espín puedan ser mucho más largos que en otros tipos de qubits, con valores récord de más de 30 segundos. El reto de desarrollar un procesador cuántico basado en qubits de espín molecular es diseñar una plataforma escalable en la que el estado de espín de cada molécula magnética puede ser inicializado, controlado y medido con pulsos de microondas. Una propuesta prometedora, basada en la electrodinámica cuántica de circuitos (*Circuit Quantum Electrodynamics* o *circuit-QED*), integra los qubits de espín molecular en circuitos superconductores, donde el espín interacciona con el campo magnético de microondas generado por fotones individuales confinados en resonadores.

Un elemento crucial en la manipulación del estado del espín es la frecuencia de Rabi, Ω_{R}, que establece la velocidad a la que se produce el cambio de estado. Esta frecuencia, que depende de la potencia de los pulsos de microondas, debe ser lo suficientemente alta como para controlar el estado del espín antes de que su coherencia decaiga con un tiempo característico T_2. Esta condición viene dada por $\Omega_{\mathrm{R}} T_2 \gg 1$. De la misma forma, el acoplo espín-resonador G_1 también debe cumplir $G_1 T_2 \gg 1$. Por desgracia, conseguir detectar moléculas individuales acopladas a resonadores es todavía una tarea desafiante, tanto por la deposición como por la detección de éstas (G_1 es demasiado pequeño). Los avances más recientes en este aspecto exploran la fabricación de una nanoconstricción en el inductor del resonador superconductor, la cual concentra y amplifica el campo magnético de microondas en un pequeño volumen en el que se depositan moléculas con nanolitografía 'dip pen' (DPN).

Los hitos experimentales en el camino hacia un procesador cuántico basado en qubits o qudits de espín molecular pueden resumirse en:

- Acoplar moléculas individuales a resonadores individuales. Este requisito, como ya se ha comentado, es bastante complicado actualmente, pero

los experimentos de prueba de concepto pueden realizarse con muestras con volúmenes cada vez más pequeños.

- Controlar coherentemente el estado de los qubits/qudits de espín molecular con pulsos de microondas. Caracterizar el efecto del acoplo de los qubits/qudits a resonadores en sus tiempos de relajación y coherencia.

- Leer el estado de los qubits/qudits tras modificar su estado. Esto puede hacerse a través de su acoplo a resonadores superconductores, trabajando en el régimen dispersivo en el que las frecuencias asociadas a qubit y resonador son suficientemente distintas. En concreto, su diferencia de frecuencias debe ser mucho mayor que el acoplo espín-fotón.

- Explorar moléculas magnéticas capaces de codificar qudits y con un buen acoplo a campos de microondas generados por resonadores.

- Caracterizar el efecto de las interacciones entre espines en el acoplo de éstos a los fotones de microondas en los circuitos superconductores. Mientras no se llegue al límite de trabajar con moléculas individuales, estas interacciones estarán presentes, y pueden ser muy relevantes en algunos sistemas al disminuir la temperatura para inicializar los qubits/qudits en el estado fundamental ($T \ll 1$ K).

- Diseñar y fabricar distintos tipos de resonadores superconductores. En concreto, los resonadores de elementos concentrados (Lumped-element resonators o LERs) son interesantes por sus propiedades de multiplexación en frecuencia y su libertad de diseño. Integrar un SQUID en el inductor de estos resonadores para tener una inductancia modulable.

A continuación, se resumen los experimentos presentados en esta tesis, los cuales constituyen los primeros pasos hacia la realización de algunos de los hitos descritos arriba.

Acoplo fuerte de conjuntos de qubits de espín molecular basados en radicales orgánicos a LERs

El radical libre DPPH, con espín electrónico 1/2, es un marcador común en experimentos de resonancia paramágnética. El régimen de acoplo fuerte de muestras en polvo de DPPH a resonadores coplanares, fabricados a partir de una línea de transmisión superconductora, se había conseguido ya previamente. Este régimen se obtiene gracias a que el acoplo colectivo de N espines idénticos escala con $\sqrt{N}$ respecto del acoplo de un único espín. Se ha depositado el mismo tipo de muestras sobre LERs para comprobar que este nuevo diseño de resonador también permite acceder al régimen de acoplo fuerte.

Lectura del estado de qubits de espín molecular basados en radicales orgánicos con la técnica de lectura dispersiva. Primeros experimentos de manipulación coherente de qubits de espín molecular acoplados a circuitos superconductores.

La técnica de lectura dispersiva del estado de un qubit molecular de espín consiste en inferir este estado a partir de su efecto en la resonancia de un LER al que está acoplado. El sistema híbrido qubit-resonador debe estar en el régimen dispersivo, en el que la diferencia $\Delta = \omega_{\mathrm{q}} - \omega_{\mathrm{r}}$ entre la frecuencia de operación del qubit, ω_{q}, y la frecuencia del resonador, ω_{r}, es mucho mayor que el acoplo colectivo entre ambos subsistemas, G_N ($\Delta \gg G_N$). Los experimentos excitación-lectura (*pump-probe*) están compuestos de un pulso de manipulación del qubit con frecuencia cercana a ω_{q} (*pump pulse*) y uno o varios pulsos con frecuencias cercanas a ω_{r} que reconstruyen el cambio en la resonancia del LER (*probe pulse(s)*). Los primeros experimentos excitación-lectura con qubits moleculares de espín se han realizado con muestras de $\mathrm{PTM_r}$, un radical libre con espín electrónico 1/2.

Estudio del complejo [^{173}Yb(trensal)] como qudit electronuclear con 12 estados. Alta cooperatividad en transiciones nucleares acopladas a fotones en resonadores superconductores.

El complejo [^{173}Yb(trensal)], una molécula con un ion $\mathrm{Yb^{3+}}$ con espín electrónico $S = 1/2$ y el espín nuclear $I = 5/2$ del isótopo ^{173}Yb, puede codificar un qudit electronuclear con $d = (2S+1) \times (2I+1) = 12$ estados. El diseño de resonadores con frecuencias de resonancia cercanas a las de las transiciones de espín nuclear permite estudiar si la presencia del espín electrónico optimiza el acoplo del espín nuclear a campos magnéticos de microondas.

Competición entre interacciones espín-espín y espín-fotón en conjuntos de radicales libres (moleculas con espín 1/2) acopladas a líneas de transición superconductoras. Efecto de introducir anisotropía magnética al sustituir los radicales por [Ni(2-Imdipa)], con espín 1

A muy baja temperatura, las interacciones entre espines en muestras concentradas pueden cambiar las propiedades de la interacción de la muestra con fotones en circuitos superconductores. Se ha estudiado este efecto con dos tipos de moléculas: DPPH, con espín 1/2, y [Ni(2-Imdipa)], con espín 1. Esta última, con $S > 1/2$, añade un ingrediente adicional, la anisotropía magnética. La transición entre su estado fundamental y su primer estado excitado es una 'transición de reloj', más robusta frente a fluctuaciones del campo magnético que una transición normal. De esta manera, el acoplo de [Ni(2-Imdipa)] a circuitos superconductores permite explorar la competición entre interacciones entre espines y el gap de energía asociado a la transición de reloj.

Chapter 1

Introduction

Since the invention of the first working transistor in 1947 [1], the evolution of classical computation has been driven by the constant development of smaller and faster components. The corresponding exponential growth of computational power was predicted by Gordon Moore in 1965 [2]. Remarkably, his prediction has held true for decades, but eventually it may run into fundamental size limitations and the emerging quantum effects in very small physical systems. Quantum computing aims to transform this threat into an opportunity.

In 1982, Richard Feynman proposed the concept of a quantum generalization of classical computing, addressing the challenge of efficiently simulating quantum systems [3]. In a quantum computer, the classical bit is replaced by the quantum bit or *qubit*. The former can be only in one of two classical states, either 0 *or* 1, while a qubit can exist in any superposition state $|\psi\rangle := \alpha\,|0\rangle + \beta\,|1\rangle$ of two quantum states $|0\rangle$ and $|1\rangle$, enabling natural parallel operations. Moreover, multiple qubits can form collective superposition states known as entangled states. A collection of qubits has therefore access to an exponentially larger set of states than the same number of classical bits [4]. The additional possibilities that superposition states introduce to process information allow a quantum computer to efficiently solve certain complex problems such as the prime factorization of large numbers with Shor's algorithm [5], data search in large databases with Grover's algorithm [6], and the aforementioned simulation of real quantum systems proposed by Feynman. Some of these tasks are beyond the capability of classical computers in reasonable times and with finite resources.

Cold trapped ions were the first proposed physical system to encode qubits able to perform universal quantum operators, back in 1995 [7]. Nowadays, various contenders for qubits exist, such as superconducting circuits [8–10], spin

defects in semiconductors [11], photons [12], ultracold atoms [13, 14], and more, each presenting distinct strengths and weaknesses. A significant challenge in quantum computation is the phenomenon of decoherence [15], in which the interaction of the qubit with its environment destroys the information encoded in its quantum state and generates errors in the computation. Even the most advanced quantum computers, e.g. those based on superconducting circuits, are limited by unavoidable errors in manipulating a substantial number of qubits [16]. Thus, the realization of a universal, error-corrected hardware still remains distant from current capabilities.

A solution to mitigate errors is the implementation of error correction codes, which are based on redundancy. Fault-tolerant quantum computing requires additional physical qubits to encode each single logical qubit. For example, the implementation of Shor's algorithm with the surface code, a robust error correction code based on encoding logical qubits with nearest-neighbours superposition states of physical qubits in a 2-D lattice, would require as many as 10^8 physical qubits [17]. A promising alternative involves transitioning from binary qubit logic to multilevel logical units known as *qudits* [18]. The additional quantum states in a qudit (with d quantum states) have been proposed as a suitable platform to encode an error correction unit [19, 20].

A different approach that partially avoids the problem of decoherence is quantum simulation, which needs less accuracy and does not require explicit quantum gates or error correction [21]. Quantum simulators, answering the proposal by Feynman, are controllable quantum systems designed to mimic specific quantum systems of interest [22]. This is, in principle, less demanding than building a fault-tolerant quantum computer.

Microscopic spins found in molecular magnets are capable of encoding both qubits and qudits [23–26]. In addition, they are interesting due to their easily controllable purity and reproducibility, as the individual qubit/qudit properties are governed by chemistry. In the context of spin qubits, the magnetic dipolar interaction is the main source of decoherence, as spins are relatively immune to electric field fluctuations. This makes spin qubits distinct from other qubit candidates like superconducting circuits or trapped ions [27], where decoherence is mainly due to their coupling to electric fields. As a result, spin qubits can exhibit much longer coherence times, with record values beyond tens of μs for molecular spins [28, 29] and up to 30 s for impurity spins in semiconductors [30].

The challenge of developing a quantum processor based on molecular spin qubits is designing a scalable platform where the spin of each individual molecule can be initialized, controlled, and read out. A promising approach, based on circuit quantum electrodynamics (circuit-QED), involves coupling molecular

spin qubits to individual photons confined within on-chip superconducting resonators [31–33]. A proposal for the most basic quantum processor based on molecular spin qudits coupled to superconducting circuits is shown in Fig. 1.1 [34]. Two GdW_{30} molecules [35], each encoding a qudit with $d = 8$ states, are coupled to a lumped-element resonator with a tunable inductance $L(\Phi)$. The tuning of $L(\Phi)$, which modulates the photon-mediated coupling between the two qudits, is introduced by changing the magnetic flux Φ through a SQUID with an auxiliary transmission line. Each qudit has an excitation line that inputs the microwave pulses that control the qudit state, whereas its coupling to the resonator inductor allows reading out the results and introduces an effective communication channel between different qudits.

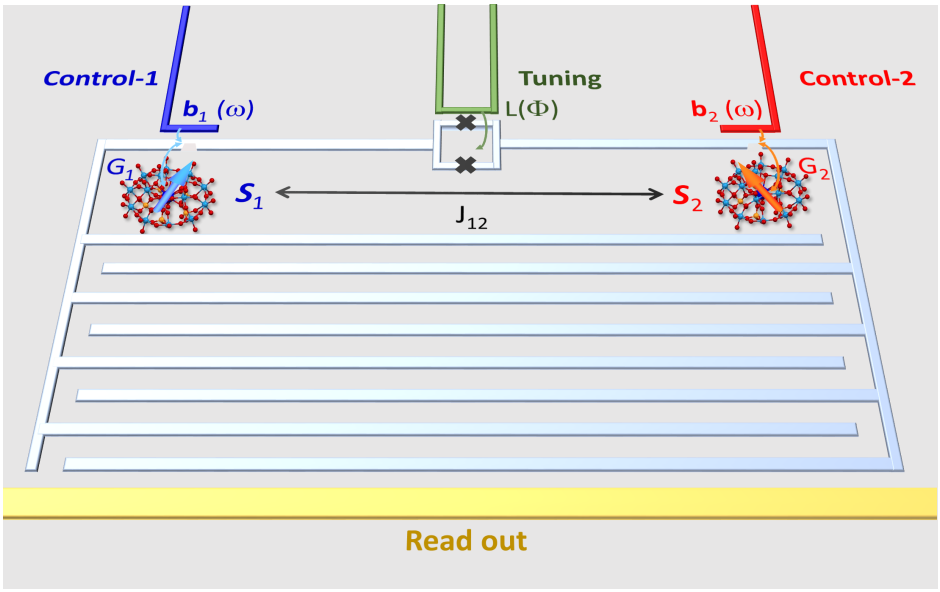

Figure 1.1: Scheme of a proposal for the most basic quantum processor based on molecular spin qudits coupled to superconducting circuits.

The crucial element is to establish a Rabi frequency Ω_R, which depends on the microwave power of control pulses, and a qubit-resonator (or qudit resonator) coupling G_1 significantly exceeding the inverse of the spin coherence time T_2. This ensures that the spin state is changed sufficiently fast ($\Omega_R T_2 \gg 1$) and that the resulting state can be readout ($G_1 T_2 \gg 1$). Unfortunately, pushing the boundaries from molecular ensembles to single molecules remains a challenging task. Recent advancements explore the fabrication of a nano-constriction in the inductor [36], which concentrates and enhances the microwave magnetic field in a very small volume, combined with small molecular deposits with Dip Pen Nanolithography (DPN) [37]. This proposal mirrors that of detecting single electron-spins in doped inorganic crystals used as sub-

strates for low-inductance superconducting resonators [38].

An alternative to enhance both the spin-photon coupling and the coherence time is based on chemical design, tailoring the spin wavefunctions encoding the qubit/qudit states to enhance their coupling to electromagnetic radiation and protect the spin states from decoherence. An interesting case is that of 'clock transitions' between spin superposition states that can arise in molecular spin systems with integer electronic spin and/or non-zero nuclear spin, which show a remarkable stability against magnetic field fluctuations [39].

Several experimental milestones are still in the way towards a physical realization of the proposal in Fig. 1.1:

- Coupling single molecular spin qubits/qudits to superconducting resonators.
- Controlling the state of molecular spin qubits/qudits.
- Reading the state of molecular spin qubits/qudits through their coupling to superconducting resonators.
- Exploring other magnetic molecules encoding molecular spin qudits.
- Characterizing the light-mediated spin-spin interactions.
- Fabricating and testing lumped-element resonators with an integrated SQUID.

In this thesis, I take the first steps towards realizing the basic ingredients of the hybrid scheme in Fig. 1.1. For this, I study experimentally some of these requirements. The outline of this work is:

- First, the experimental techniques used throughout this work are presented in chapter 2.
- Chapters 3 and 4 introduce the theoretical framework that describes the elements of the quantum processor, namely the molecular spins and the superconducting resonators, their coupling, and their measurement with microwave experiments.
- The coupling of free radical molecules with $S = 1/2$ to superconducting lumped-element resonators (LERs) is studied in chapters 5 and 6. In chapter 5, the coupling of DPPH ensembles to LERs is characterized with continuous wave experiments. Chapter 6 focuses instead on pulsed experiments on PTM_r in the dispersive regime. In these experiments, first the state of the molecular spin state is controlled with microwave

pulses, then the resulting state is read out by measuring the LER resonance frequency, which depends on the qubit state.

- Chapter 7 generalizes the experiments in chapters 5 and 6 to molecular spin qudits, with $d > 2$ spin states. In particular, the [Yb(trensal)] complex with ^{173}Yb, with electronic spin $S = 1/2$ and nuclear spin $I = 5/2$ is studied as an electro-nuclear qudit with $d = 12$ states.

- Finally, chapter 8 explores the competition of spin-spin interactions, inherent to spin ensembles unless diamagnetically diluted samples are used, with the interaction of spins with photons travelling through a waveguide and with clock transitions.

In addition to the conclusions of each individual chapter, a summary of the general conclusions is included at the end.

References

[1] J. Bardeen and W. H. Brattain, Physical Review **74**, 230 (1948).

[2] G. E. Moore, Electronics **38**, 114 (1965).

[3] R. P. Feynman, International Journal of Theoretical Physics **21**, 467 (1982).

[4] D. Deutsch and R. Jozsa, Proceedings of the Royal Society of London. Series A: Mathematical and Physical Sciences **439**, 553 (1992).

[5] P. W. Shor, in *Proceedings 35th Annual Symposium on Foundations of Computer Science* (1994), pp. 124–134.

[6] L. K. Grover, Physical Review Letters **79**, 325 (1997).

[7] J. I. Cirac and P. Zoller, Applied Physics Letters **74**, 4091 (1995).

[8] M. H. Devoret and R. J. Schoelkopf, Science **339**, 1169 (2013).

[9] F. Arute, K. Arya, R. Babbush, D. Bacon, J. C. Bardin, R. Barends, R. Biswas, S. Boixo, F. G. S. L. Brandao, D. A. Buell, et al., Nature **574**, 505 (2019).

[10] M. Kjaergaard, M. E. Schwartz, J. Braumüller, P. Krantz, J. I.-J. Wang, S. Gustavsson, and W. D. Oliver, Annual Review of Condensed Matter Physics **11**, 369 (2020).

[11] G. Burkard, T. D. Ladd, A. Pan, J. M. Nichol, and J. R. Petta, Reviews of Modern Physics **95**, 025003 (2023).

[12] P. Kok, W. J. Munro, K. Nemoto, T. C. Ralph, J. P. Dowling, and G. J. Milburn, Reviews of Modern Physics **79**, 135 (2007).

[13] M. Saffman, T. G. Walker, and K. Mølmer, Reviews of Modern Physics **82**, 2313 (2010).

[14] D. Bluvstein, S. J. Evered, A. A. Geim, S. H. Li, H. Zhou, T. Manovitz, S. Ebadi, M. Cain, M. Kalinowski, D. Hangleiter, et al., Nature **626**, 58 (2023).

[15] W. H. Zurek, Reviews of Modern Physics **75**, 715 (2003).

[16] J. Preskill, Quantum **2**, 79 (2018).

[17] A. G. Fowler, M. Mariantoni, J. M. Martinis, and A. N. Cleland, Physical Review A **86**, 032324 (2012).

[18] B. P. Lanyon, M. Barbieri, M. P. Almeida, T. Jennewein, T. C. Ralph, K. J. Resch, G. J. Pryde, J. L. O'Brien, A. Gilchrist, and A. G. White, Nature Physics **5**, 134 (2009).

[19] S. Pirandola, S. Mancini, S. L. Braunstein, and D. Vitali, Physical Review A **77**, 032309 (2008).

[20] M. Chizzini, L. Crippa, L. Zaccardi, E. Macaluso, S. Carretta, A. Chiesa, and P. Santini, Physical Chemistry Chemical Physics **24**, 20030 (2022).

[21] I. Buluta and F. Nori, Science **326**, 108 (2009).

[22] P. Scholl, M. Schuler, H. J. Williams, A. A. Eberharter, D. Barredo, K.-N. Schymik, V. Lienhard, L.-P. Henry, T. C. Lang, T. Lahaye, et al., Nature **595**, 233 (2021).

[23] E. Moreno-Pineda, C. Godfrin, F. Balestro, W. Wernsdorfer, and M. Ruben, Chemical Society Reviews **47**, 501 (2018).

[24] A. Gaita-Ariño, F. Luis, S. Hill, and E. Coronado, Nature Chemistry **11**, 301 (2019).

[25] M. Atzori and R. Sessoli, Journal of the American Chemical Society **141**, 11339 (2019).

[26] A. Chiesa, P. Santini, E. Garlatti, F. Luis, and S. Carretta, Reports on Progress in Physics **87**, 034501 (2024).

[27] C. Monroe and J. Kim, Science **339**, 1164 (2013).

[28] K. Bader, D. Dengler, S. Lenz, B. Endeward, S.-D. Jiang, P. Neugebauer, and J. van Slageren, Nature Communications **5**, 5304 (2014).

[29] J. M. Zadrozny, J. Niklas, O. G. Poluektov, and D. E. Freedman, ACS Central Science **1**, 488 (2015).

[30] J. T. Muhonen, J. P. Dehollain, A. Laucht, F. E. Hudson, R. Kalra, T. Sekiguchi, K. M. Itoh, D. N. Jamieson, J. C. McCallum, A. S. Dzurak, et al., Nature Nanotechnology **9**, 986 (2014).

[31] A. Wallraff, D. I. Schuster, A. Blais, L. Frunzio, R.-S. Huang, J. Majer, S. Kumar, S. M. Girvin, and R. J. Schoelkopf, Nature **431**, 162 (2004).

[32] J. Majer, J. M. Chow, J. M. Gambetta, J. Koch, B. R. Johnson, J. A. Schreier, L. Frunzio, D. I. Schuster, A. A. Houck, A. Wallraff, et al., Nature **449**, 443 (2007).

[33] R. J. Schoelkopf and S. M. Girvin, Nature **451**, 664 (2008).

[34] A. Chiesa, S. Roca, S. Chicco, M. C. de Ory, A. Gómez-León, A. Gomez, D. Zueco, F. Luis, and S. Carretta, Physical Review Applied **19**, 064060 (2023).

[35] M. D. Jenkins, Y. Duan, B. Diosdado, J. J. García-Ripoll, A. Gaita-Ariño, C. Giménez-Saiz, P. J. Alonso, E. Coronado, and F. Luis, Physical Review B **95**, 064423 (2017).

[36] I. Gimeno, W. Kersten, M. C. Pallarés, P. Hermosilla, M. J. Martínez-Pérez, M. D. Jenkins, A. Angerer, C. Sánchez-Azqueta, D. Zueco, J. Majer, et al., ACS Nano **14**, 8707 (2020).

[37] R. D. Piner, J. Zhu, F. Xu, S. Hong, and C. A. Mirkin, Science **283**, 661 (1999).

[38] Z. Wang, L. Balembois, M. Rančić, E. Billaud, M. Le Dantec, A. Ferrier, P. Goldner, S. Bertaina, T. Chanelière, D. Esteve, et al., Nature **619**, 276 (2023).

[39] M. Shiddiq, D. Komijani, Y. Duan, A. Gaita-Ariño, E. Coronado, and S. Hill, Nature **531**, 348 (2016).

Chapter 2

Experimental setup and techniques

This chapter presents the experimental setup and techniques used throughout this work. Most experiments here are focused on manipulating and reading molecular spin qubits and qudits coupled to superconducting resonators. The setup for these experiments consists of a superconducting chip with the molecular samples inside a dilution refrigerator, which is probed with microwaves. A transmission line and several lumped-element resonators (LERs) are patterned on the surface of the chip, on top of which the molecular spin qubits/qudits are deposited. This is the quantum processor (see section 2.1).

A dilution refrigerator cools down the processor to as low as 7 mK. Inside, a superconducting magnet generates the DC magnetic field that tunes the frequencies of the molecular spin qubits to match those of the resonators (see section 2.2). Section 2.3 introduces the microwave setup for pulse generation and detection, comprising all instruments needed to control and read the molecular spin qubit state through the LERs with microwave photons. Other complementary experimental techniques used throughout this thesis can be found in section 2.4.

2.1 Superconducting chip

Electronic Paramagnetic Resonance (EPR) is a well-established control and characterization technique of molecular electronic spins coupled to 3D cavities [1]. However, in the context of quantum computation this 3D cavity poses a problem of scalability, and it is more interesting to use instead 2D microwave integrated circuits in superconducting chips as cavities [2]. Single photons can

be confined in these systems, increasing the spin-photon coupling. The coupling enhancement moves the hybrid spin-photon system away from the weak coupling regime characteristic of EPR experiments, into the strong coupling regime that is achieved in circuit-QED.

The first proposals for coupling molecular spin qubits to superconducting circuits were based on coplanar resonators [3, 4]. These are fabricated by interrupting a transmission line patterned in a superconducting chip with gap capacitors so that the dimensions match the wavelength of microwave modes. However, with this design it is not possible to have several resonators with slightly different frequencies in the same transmission line. Each resonator is essentially a filter that reflects any microwaves with frequencies out of its bandwidth. Then, the first resonator from the input port hinders the transmission of microwaves probing the rest of resonators. Also, the design of a coplanar resonator is constrained to an interrupted line: its capacitance and inductance must be tailored so that the resonator impedance $Z = \sqrt{L/C}$ matches the impedance of the transmission line, Z_0. This last condition limits the tunability of the frequency of the resonator, which is given by $\omega_r = 1/\sqrt{LC}$.

A different chip design in which all resonators can be measured through a single transmission line is desired. This would allow, for example, the characterization of a qudit in a single chip by matching different resonators to the different transition frequencies of the qudit. The property of probing resonators with different ω_r coupled to the same transmission line is known as frequency multiplexing. A proposal for a quantum processor with this property couples the molecular spin qubits/qubits to lumped-element resonators (LERs). LERs are side coupled to the transmission line, which makes them transparent to microwaves out of their bandwidth and allows frequency multiplexing. They consist of an inductive meander and an inter-digitated capacitor patterned in the surface of a superconducting chip, as shown in Fig. 2.1.

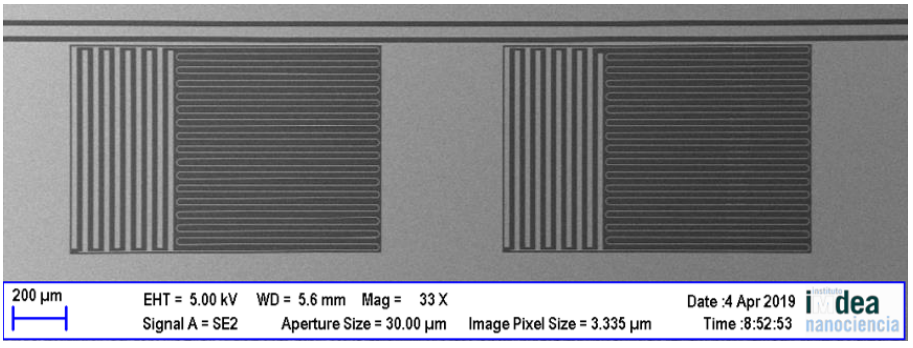

Figure 2.1: Two lumped element resonators (LERs) side coupled to a transmission line in a superconducting chip, each with two distinct parts: an inter-digitated capacitor on the left and an inductor on the right.

The inductance L and capacitance C of the LER can be tuned independently by changing the design of each of the two parts of the circuit. On top, they achieve very high quality factors ($Q \sim 10^4$ to 10^5) and, therefore, long coherence times ($\kappa^{-1} > \mu$s) [5]. Resonance frequencies are usually in the range of 1-10 GHz, matching the frequencies of the electronic spin transitions in our molecules. Inductor and capacitor are clearly separated in space in each resonator (see Fig. 2.1). This potentially allows choosing either magnetic or electric spin-photon coupling in resonance depending on where the sample is deposited.

2.1.1 Design and fabrication

Each superconducting chip consists of a transmission line with several side-coupled LERs (see Fig. 2.2). These chips were designed by Alicia Gomez and Marina Calero, from CAB (Centro de Astrobiología de Madrid), and then fabricated by Maite Magaz at Center for Nanofabricaction of IMDEA-Nanoscience [6]. They are made on 100 nm thick niobium (Nb) films deposited on top of 350 μm thick Si substrate wafers. Niobium is a superconductor below T_c = 9.26 K, with low dielectric losses.

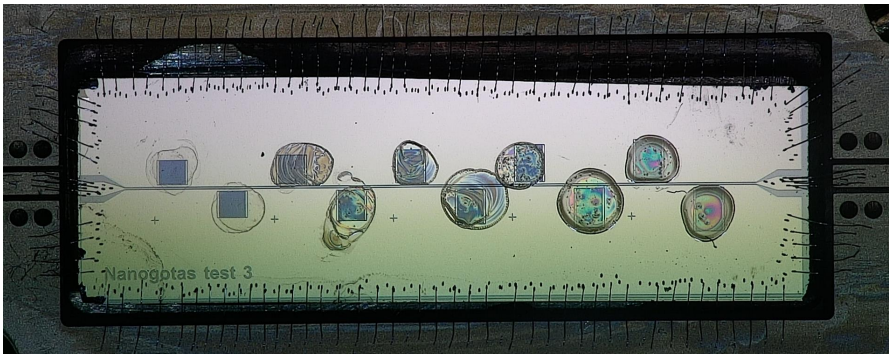

Figure 2.2: Example of a superconducting chip with ten side-coupled LERs. On top of each LER there is a sample of magnetic molecules. The chip is connected to a PCB with the wire bonding technique detailed in section 2.1.2.

First, the geometries of the transmission line and lumped-element resonators are designed with CAD software. The output vector files with the design are fed to the commercial software Sonnet for the RF simulations. An example is shown in Fig. 2.3. In these simulations, the Nb film has no thickness, but the Si substrate thickness is included. With the combination of these two software tools it is possible to tailor the parameters and characteristics of the resonators (resonance frequency, quality factors, size and shape of inductor and capacitor) so that they suit best the experiments.

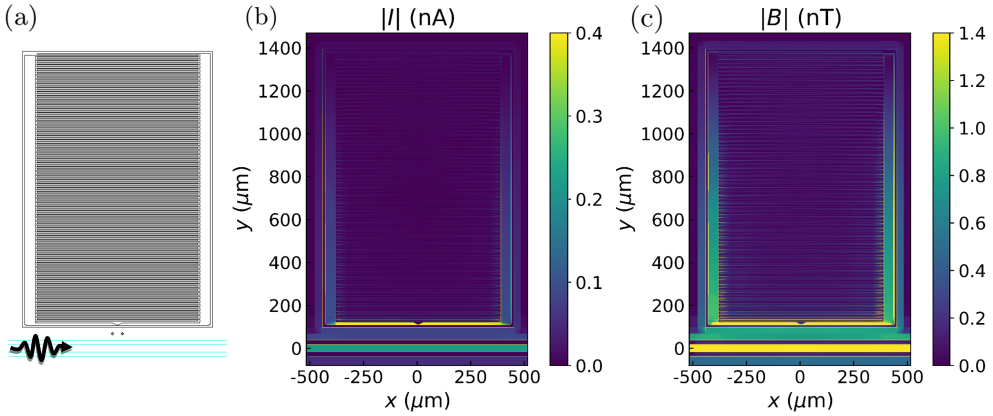

Figure 2.3: (a) Vector design of one of the LERs in Fig. 2.2. In this design, most of the LER area is the capacitor, while the inductor is only a strip at the bottom close to the transmission line. (b) Distribution of currents in the transmission line and the lumped-element circuit, simulated with Sonnet. Current is concentrated in the inductor strip. (c) Distribution of magnetic fields in a plane 100 nm above the chip surface, calculated from the simulated currents.

The fabrication process begins with the deposition of the Nb film on the Si substrate by means of DC magnetron sputtering (Fig. 2.4a). The transmission line and the LERs are then patterned in the Nb film by ultra-violet (UV) laser lithography and reactive ion etching (RIE) techniques. UV laser lithography is a maskless circuit fabrication technique to pattern a photosensitive polymer or photoresist on top a substrate with laser UV irradiation. In this case, a 405 nm wavelength laser is used to irradiate a negative photoresist deposited on top of the Nb film. The laser is fed with the vector files containing the design of the transmission line and the lumped-elements resonators.

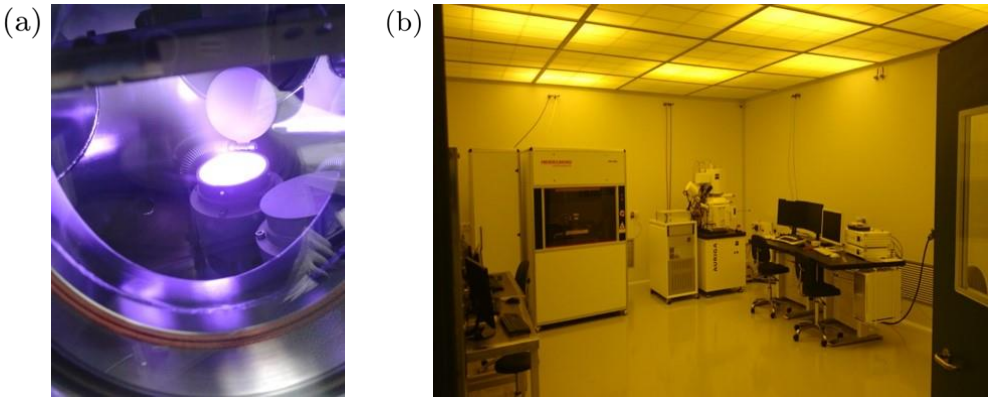

Figure 2.4: AJA Orion-5 DC magnetron sputtering system (a) and Heidelberg Maskless DWL66fs laser lithography system (b) at Center for Nanofabricaction of IMDEA-Nanoscience [7].

The non-irradiated areas of the photoresist are removed with acetone, exposing areas of the Nb film below that are then removed by RIE (Reactive Ion Etching). A beam of accelerated ions composed of a mix of SF_6 and argon gases is sent to the sample, and provides energy to drive a chemical etching reaction in the exposed Nb film. The combination of physical and chemical etching of RIE confers both good selectivity and directionality to the etching process [8]. Once the pattern is transferred to the Nb film, the remaining photoresist is removed with successive cleanings with acetone, isopropyl alcohol (IPA) and pressurized N_2 gas. The final device is then tested at room and low temperatures to check the expected properties.

2.1.2 Interface with microwave coaxial lines: PCBs and wire bonding

The transmission line in the superconducting chip is interfaced with the input and output microwave lines inside the cryostat with a PCB (Printed Circuit Board). The PCB consists of several layers of electrical conductors separated by an insulating material, with its conducting surface patterned so that it has a central line and two ground plates as in a transmission line. The superconducting chip is placed in a rectangular hole in the centre of the PCB, with its central line and grounds electrically connected to those of the PCB using $\varnothing 25$ μm 1% SiAl wires (see Figs. 2.2 and 2.5a).

(a) 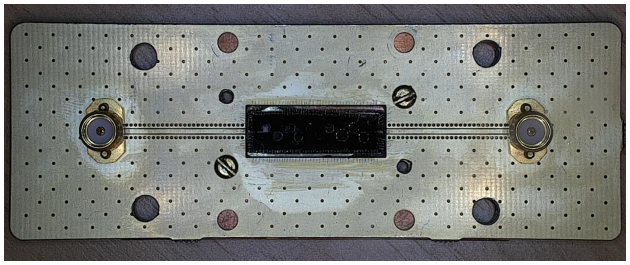 (b) 

Figure 2.5: (a) PCB with the superconducting chip placed in the rectangular hole in its centre. Figure 2.2 is a close up of this image. The PCB acts as a ground plate, except the patterned transmission line that connects the line of the chip with two female SMA adapters. First, the chip is placed on top of a oxygen-free copper holder with GE low temperature varnish to ensure good a thermal connection. Then the PCB is screwed to the holder as shown in the image. Finally, chip and PCB are electrically connected with wire bonding. (b) Hybond model 572A wire bonding machine at INMA.

Wires are bonded to the chip surface and PCB with a Hybond model 572A wire bonding machine at INMA (Instituto de Nanociencia y Materiales de Aragón) based on the wedge bonding technique (see Fig. 2.5b). The clamped

wire is first welded to the PCB and then to the chip applying ultrasounds and pressure. The capillary that holds the wire can be moved between the two bonding sites in the three spatial directions with three independent controllers.

The interface of the PCB to the coaxial lines inside the cryostat are two female SMA adapters (input and output). SMA are used instead of SMP adapters, as the former are more robust against tensions in the coaxial cables and temperature changes. These adapters are placed far from the superconducting chip, with the PCB being much larger in size than the chip. This large design keeps ground voltage inhomogeneities away from the central line and reduces their effect on the transmission.

2.2 Cryogen-free dilution refrigerator

A qubit is initialized in its ground state by cooling it far below $\hbar\omega_q/k_B$, where ω_q is the qubit operation frequency. From this initial state, the qubit state is controlled with different quantum gates. Similarly, an ensemble of quantum systems cooled to temperatures below $\Delta E/k_B$, where ΔE is the energy difference between the initial and final states, is initialized in the sense that different populations in equilibrium are obtained according to the Boltzmann distribution ($\propto 1 - e^{-\Delta E/k_B T}$). Without this non-negligible difference in population there is no significant change in the system: according to the detailed balance of absorption and stimulated emission in thermodynamic equilibrium, the rates of the two processes are the same for any transition in our quantum system if its initial and final states have the same degeneracy [9, 10]. This is sketched in Fig. 2.6.

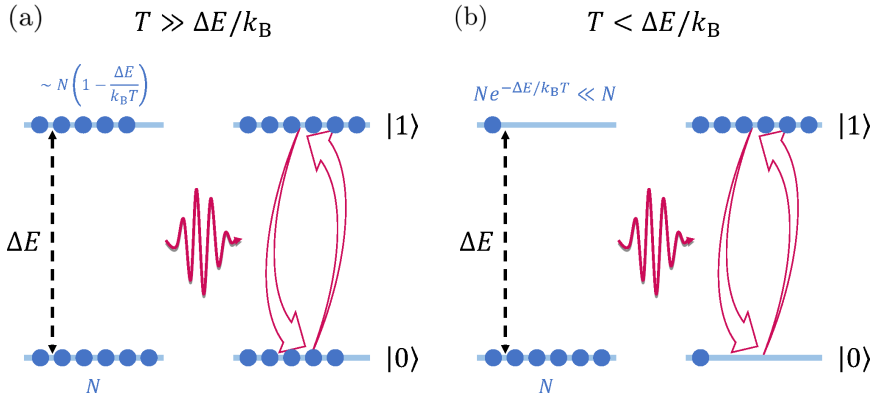

Figure 2.6: Population inversion with resonant microwave radiation at high temperatures (a), $T \gg \Delta E/k_B$, and low temperatures (b), $T < \Delta E/k_B$. The absorption and stimulated emission rates are the same, it is the difference between the initial populations of the states that makes the population inversion non negligible.

The energy differences in a magnetic molecule, when converted to transition frequencies, range from tenths of MHz in nuclear splittings to a few GHz in electronic Zeeman and zero-field splittings [11]. This demands cooling temperatures ranging from a few mK to hundreds of mK for initialization. That is, temperatures which can only be provided continuously by ^{3}He-^{4}He dilution refrigerators.

2.2.1 Operating principle of a ^{3}He-^{4}He dilution refrigerator

A dilution refrigerator is based on the cooling properties of the phase separation of a mixture of the two stable helium isotopes, ^{3}He and ^{4}He, at very low temperatures. To start the cooling cycle, an auxiliary cooling mechanism is needed to get the mixture around the temperature of liquid helium (4.2 K) or below. In a standard, not cryogen-free dilution refrigerator, this temperature is obtained by inserting the dilution circuit inside a vacuum can surrounded by a liquid helium bath. The mixture is cooled to 4.2 K with small volumes of liquid helium from the bath, and then it can be cooled further by using a 1 K pot.

The dilution refrigerator used in this work is a BlueFors LD250 Dilution Refrigerator System (Fig. 2.7), managed as a service by the Servicio de Apoyo a la Investigación (SAI) of the University of Zaragoza and accessible to all researchers [12]. It is a cryogen-free dilution refrigerator that does not need a liquid helium bath. All cooling stages of the cryostat are inside a vacuum can in order to suppress heat conduction and convection, and to thermally isolate the circuit from the environment. The vacuum can is also enclosed by a radiation shell that protects the stages from incident radiation that would otherwise heat them.

The different stages are separated by a stainless steel tubes with poor thermal conductivity, and heat switches filled with helium gas and active carbon. While the heat switch heaters are on, the helium gas thermally connects the stages. When they are turned off, helium gas is absorbed by active carbon and the stages are isolated.

To attain liquid helium temperatures, the outer stage (50 K plate) is cooled by a Cryomech Inc. Pulse Tube (PT) cooler. During this process, all cooling stages of the cryostat, from the 50 K plate to the mixing chamber, are thermally connected by heating the heat switches. After 20 hours, or 30 if the superconducting magnet is installed, a temperature of around 4.2 K si reached in the still and the mixing chamber. The heaters of the heat switches are then turned off to isolate the different stages.

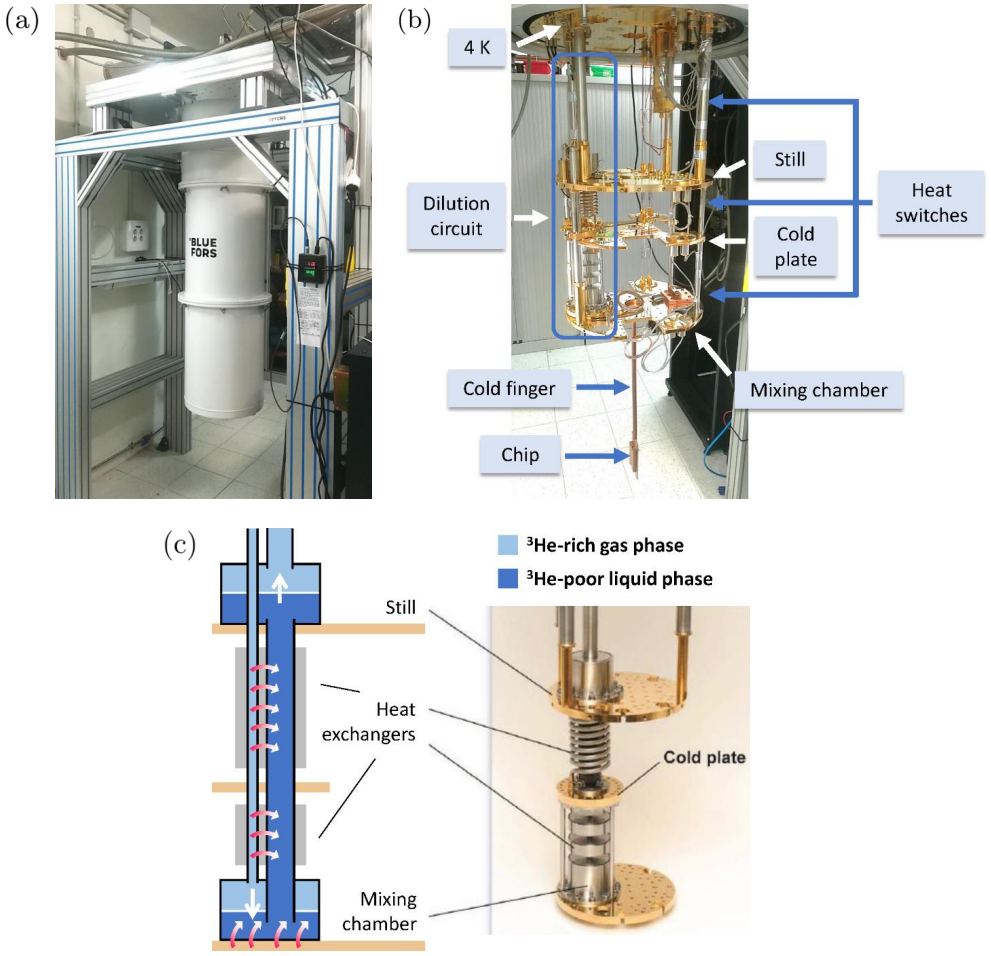

Figure 2.7: (a, b) BlueFors LD250 Dilution Refrigerator System closed (a) and open (b) to see its different cooling stages (or plates). These stages are, from highest to lowest temperature, the 50 K plate (not visible), the 4 K plate, the still, the cold plate and the mixing chamber. (c) Scheme and close-up of the dilution circuit in Fig. 2.7. The temperature of the incoming ^{3}He-rich gas flow in the condensing line decreases as it transfers heat to the ^{3}He-poor column between the mixing chamber and the still. At the mixing chamber, ^{3}He atoms borrow energy from the mixing chamber structure to cross the phase boundary, cooling it. The main limitation to the cooling power of the circuit are the heat exchangers. This is due to the thermal boundary resistance between liquid helium and the exchanger walls, known as Kapitza resistance, which increases with decreasing temperature [13, 14].

After this pre-cooling process is completed, the ^{3}He-^{4}He mixture starts flowing through the dilution circuit. The incoming mixture is pre-cooled below 4.2 K by different heat exchangers, and then compressed 2 bar to condense it. This compression is needed in cryo-free systems because ^{3}He has a condensation temperature below 4 K at atmospheric pressure. The liquid mixture fills the

circuit up to the still, with the gaseous phase of the mixture being constantly pumped out it. This evaporative cooling process lowers the temperature below 800 mK.

Below that temperature, the mixture is separated into a ^{4}He-rich (or dilute) phase and an almost pure ^{3}He gaseous phase. As ^{4}He is heavier than ^{3}He, the dilute phase remains at the bottom of the mixing chamber, while ^{3}He gas continues to flow through the dilution circuit (see Fig. 2.7c). When ^{3}He gas is pumped into the mixing chamber, it is forced to go through the phase boundary with the diluted phase to complete the circuit, taking some energy from the mixing chamber and cooling it along the samples to as low as 7 mK.

2.2.2 Superconducting magnet

The cryostat has an uniaxial superconducting magnet by American Magnetics mounted below the mixing chamber, which applies magnetic fields up to 1 T parallel to the vertical axis of the cryostat with a resolution of 10^{-4} T. The magnet is thermally connected to the 4.2 K plate and isolated from the mixing chamber. An oxygen-free copper cold finger extends below the mixing chamber and into space inside the magnet coils, placing the superconducting chip in the center of the magnet while thermalizing the sample with the mixing chamber (see Fig. 2.8a-b). A 430 power supply programmer controlling a 4Q06125PS-430 power supply outputs the current in the magnet. This programmer can be controlled from the computer.

2.2.3 Microwave coaxial lines and cryogenic amplifier

The input and output semi-rigid coaxial lines inside the cryostat send the input microwave signals to the chip and receive its transmission (see Fig. 2.8c). The input coaxial lines are made of stainless steel (SS) down to the 4 K plate, and then of a CuNi alloy down to the mixing chamber. At each cooling stage, a 10 dBm attenuator is installed in the input coaxial line, for a total of 50 dBm attenuation, limiting the input power that reaches the chip.

The output coaxial lines connecting the mixing chamber and the 4 K plate are made of a superconducting NbTi alloy. At the latter stage, they are connected to a LNF 0.3-14 GHz cryogenic Low Noise Amplifier (LNA) [15]. Superconducting coaxial lines allow a close to perfect propagation of the often very weak output signals while maintaining a proper thermal isolation. The LNA then amplifies these signals by 30 dBm at cryogenic temperatures, when the thermal noise is still low. The rest of the output coaxial lines is made of a metallic CuNi alloy.

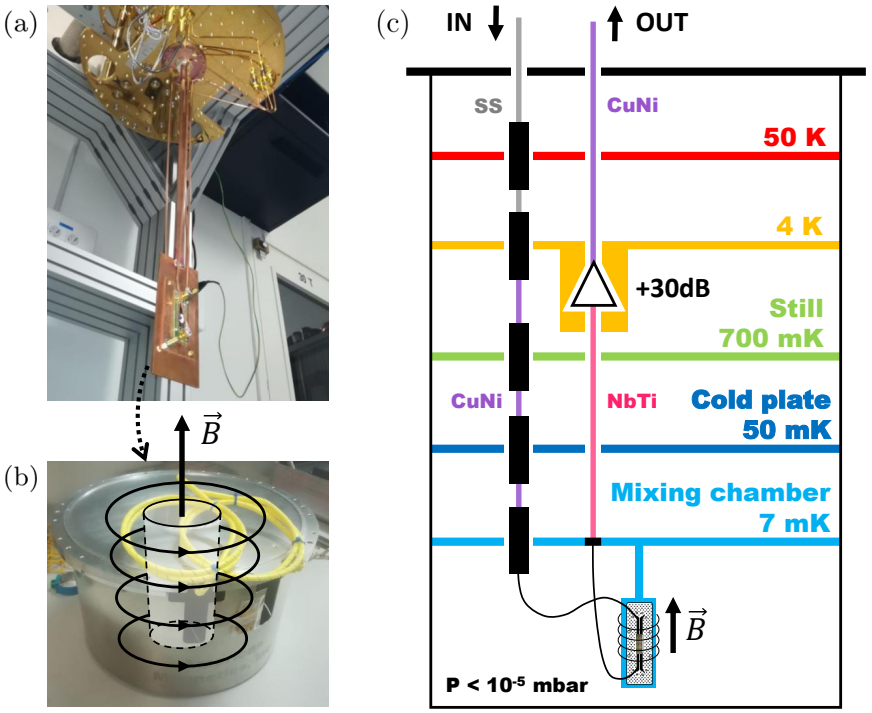

Figure 2.8: Input and output microwave coaxial lines inside the dilution refrigerator. The LNA in the output line is thermally anchored to the 4 K plate.

2.3 Microwave setup for pump-probe experiments

In pump-probe experiments, two pulse sequences are sent to the chip: the pump sequence, with short, high-power pulses exciting transitions in the spin system, and the probe sequence, with long, low-power pulses that measure the resonator frequency shift due to its strong coupling to the spins. This method of reading the spin state by measuring the resonance of the coupled resonator is known as dispersive readout. The microwave setup for these experiments has changed in the course of this thesis, the different setups will be detailed in chapter 6. All of them consist of two parts: a pulse generation stage and a readout stage.

2.3.1 Characterization with continuous wave experiments

The LER resonance and the collective spin-photon coupling must be characterized before any dispersive readout experiment. A vector network analyser (VNA) was used for this purpose, which measures the effect of frequency-swept or power-swept radio-frequency and microwave signals on the amplitude and

phase of the chip transmission. In particular, I used a Rohde & Schwarz ZVB14 model (Fig. 2.9a) provided by the Electronic Engineering and Communications Department of the University of Zaragoza, which can send and measure signals ranging from 10 MHz to 14 GHz [16].

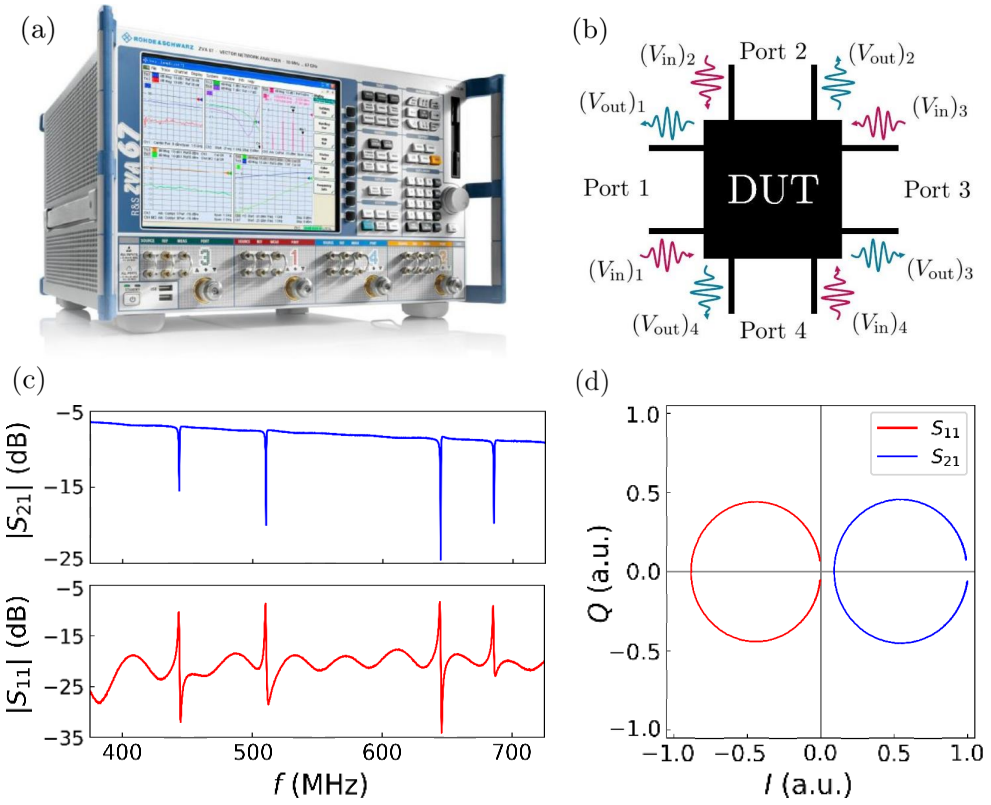

Figure 2.9: (a) Rohde & Schwarz ZVB14 model vector network analyser. (b) Definition of the inputs and outputs from the point of view of the DUT (Device Under Test) with four ports: $(V_{in})_i$ is the input wave from port i into the DUT, $(V_{out})_i$ is the output wave from the DUT into port i. (c) Module of the transmission S_{21} and reflection S_{11} scattering parameters of a transmission line with four lumped-element resonators. S_{11} and S_{21} are complex quantities that can be expressed by their module and phase or by their in-phase (I) and quadrature (Q) components (real and imaginary components). It is common to write the scattering parameters in dB units, defined as $S_{ij}(\text{dB}) := 20\log_{10}(S_{ij})$. (d) IQ plot of the calibration of the resonator at 443 MHz in (c).

The ZVB14 model has four ports, which can act both as emitters and receivers. This allows measuring the transmitted or reflected signals of a 'Device Under Test', or DUT, with up to four ports. Here, the DUT is a superconducting chip hosting LERs coupled to a single transmission line (two ports) or two transmission lines (four ports). The result of a measurement are the complex

quantities S_{ij}, the ratio between the measured signal at port i and the signal sent from port j while the other ports are decoupled from the system (see Fig. 2.9b):

$$S_{ij} = \frac{(V_{\text{out}})_i}{(V_{\text{in}})_j}\bigg|_{(V_{\text{in}})_{k\neq j}=0}. \tag{2.1}$$

In a simple transmission experiment with two ports and the input signal at port 1, the transmission and reflection of the system are given by S_{21} and S_{11}. An example of these measurements is shown in Figs. 2.9c-d.

2.3.2 Pulse generation

The pulse generation stage is a Keysight M9180A Arbitrary Waveform Generator (AWG), shown in Fig. 2.10a, with an amplifying stage [17]. It generates arbitrary pulses with a bandwidth of 5 GHz and a maximum amplitude of 1 V (10 dBm). The pulses are generated as a digital signal in the computer and then converted to an analog signal by the DAC (Digital-Analog Converter) of the AWG with a sampling rate of 12 GSa/s ($12 \cdot 10^9$ samples per second).

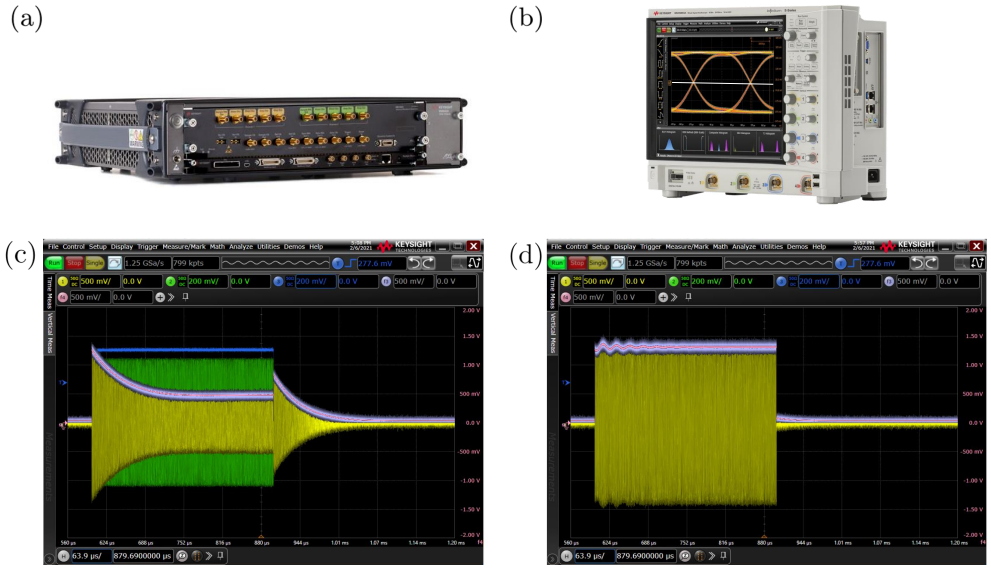

Figure 2.10: (a) Keysight M9180A AWG. (b) Keysight MSOS404A oscilloscope. (c) Raw pulse data acquired by the oscilloscope. The transmission of a pulse with carrier frequency matching the resonance frequency ω_r of a LER (yellow trace) is compared to the same pulse sent directly to the oscilloscope (green trace), showing the absorption of microwave power by the resonator. The envelope of the signal can be averaged in the oscilloscope (pink trace). The blue trace is the TTL signal that triggers the oscilloscope. (d) Same measurements for a pulse with carrier frequency detuned from ω_r.

The AWG also sends, with the same sampling rate, a pulsed TTL signal that can be used to trigger other instruments. In particular, this signal controls the microwave switch that routes the pump pulse to an additional amplifying stage, while the probe pulse is routed to an IQ mixer as the local oscillator (LO) signal and then attenuated. Both pulses are combined again in a single line before entering the cryostat.

2.3.3 Readout

After the high power excitation pulses and the low power readout pulses interact with the spins and resonators in the chip, the transmitted signals exit the cryostat and arrive at the detection stage. Before this stage, a second microwave switch separates the transmitted high power excitation pulses from the low power readout pulses. The latter are routed to the IQ mixer again, now as the RF signal.

The IQ mixer outputs two signals, I and Q (in-phase and quadrature), which are the product of the RF and LO signals, the latter shifted by 90° for the Q channel. Each of the I and Q channels outputs the sum of two signals: a high-frequency signal which oscillates with the sum of the RF and LO frequencies, and a low-frequency signal which oscillates with their absolute difference. The high-frequency signal is filtered by the bandwidth of the mixer, leaving only the low-frequency or 'demodulated' signal.

The I and Q outputs of the mixer are acquired by a Keysight MSOS404A oscilloscope shown in Fig. 2.10b. This instrument has a bandwidth of 8 GHz and is triggered by the pulsed TTL signal generated by the AWG [18]. The raw acquired data can be processed and averaged in the oscilloscope before sending it to the computer (see Fig. 2.10c-d). All microwave instruments described above, from characterization and pulse generation to measurement and data acquisition, are controlled from the computer with homemade Python scripts.

2.4 Complementary experimental techniques

Characterizing a new molecule in a microwave setup is not always a straightforward process. First, there is a limitation in frequency, as only spin transitions in the frequency range of the microwave instruments can be probed. In addition, the coupling between microwaves and the target spin system depends on the orientation of the microwave field generated by the resonator or transmission line. These limitations do not pose a problem when dealing with simple non-interacting $S = 1/2$ systems, but they become very relevant in the case

spin systems with magnetic anisotropy or when spin-spin interactions are relevant.

This section, details some experimental techniques that complement microwave experiments. Heat capacity and magnetic properties measurements were performed in services provided by the SAI (Servicio General de Apoyo a la Investigación) of the University of Zaragoza.

2.4.1 SQUID magnetometry

Magnetic measurements down to 1.9 K were carried out in a Magnetic Properties Measurement System (MPMS) by Quantum Design [19] operated by the Servicio de Apoyo a la Investigación (SAI) of the University of Zaragoza (see Fig. 2.11). The MPMS is a commercial magnetometer based on a dc-SQUID (Superconducting Quantum Interference Device) detector, which acts as a very sensitive magnetic flux to voltage transducer that allows the determination of the magnetization M of small samples at very low temperatures. Its operation is based on two quantum properties of superconductor materials: the quantization of the magnetic flux and the Josephson effect [20].

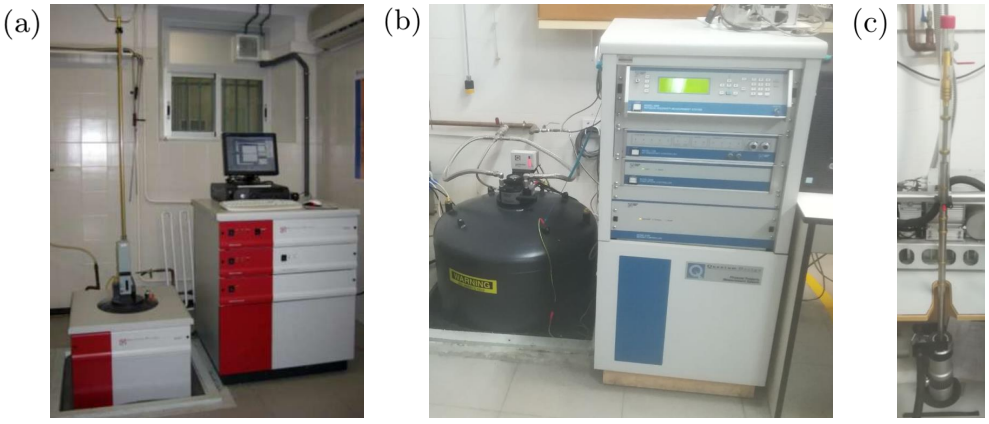

Figure 2.11: (a) MPMS-XL at SAI. (b) PPMS-9T at SAI. (c) Measurement probe of the PPMS-9T.

The sample is placed inside superconductor coils that couple the magnetic flux of the sample to the superconductor ring of the SQUID. The MPMS has a sensitivity better than 10^{-7} emu (1 emu $\leftrightarrow 10^{-3}$ A/m^2). The system has a liquid Helium cryostat that hosts the sample chamber, which allows varying temperature between 1.8 K and 350 K, and a superconducting magnet, which can generate DC magnetic fields up to 5 T.

A dc-SQUID consists of two superconductors connected in parallel by two

Josephson junctions, forming a ring (see Fig. 2.12a). Both junctions have almost the same critical intensity I_c. In the presence of a magnetic field, a magnetic flux ϕ goes through the ring, causing the phase of each junction to evolve differently. If the SQUID is polarized with an external electric current $I_b > 2I_c$, a difference of electric potential V appears between its ends, which is modulated by the net current in the ring due to phase imbalance generated by ϕ. V is an oscillating function of ϕ with a period ϕ_0, the magnetic flux quantum ($\phi_0 = h/2e \simeq 2 \cdot 10^{-15}$ Wb). In order to measure the magnetic flux ϕ generated by the sample, a feedback loop introduces an external magnetic flux $\phi_V \propto V$ opposite to ϕ which tries to maintain $\phi + \phi_V = 0$. Provided that the feedback loop keeps this condition, measuring V gives the magnetic flux $\phi = -\phi_V \propto V$. The proportionality constant $G := \phi/V$, which depends on the geometry of the SQUID, is a known calibration parameter.

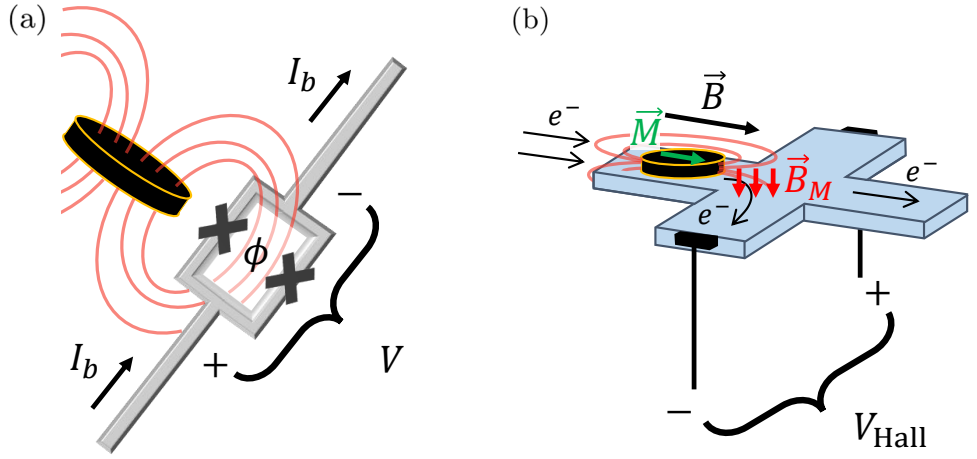

Figure 2.12: (a) Scheme of a SQUID. (b) Scheme of 'cross' magnetometer device designed to measure the Hall voltage induced by a magnetic sample.

In this thesis I carried out DC magnetic measurements, in which the MPMS applies a constant magnetic field so that sample gets a net magnetization M and generates a dipolar field. If the sample is moved across the SQUID pick-up coils, the magnetic flux changes and can be distinguished from that originated by other sources.

2.4.2 Micro-Hall magnetometry

Micro-Hall magnetometry experiments were carried out in a Physical Properties Measurement System (PPMS). The PPMS is a commercial system by Quantum Design [19] that allows performing measurements of different physical properties in a wide range of temperatures (down to 350 mK) and fields

(up to 9 or 14 T, depending on the model). In order to reach these low temperatures and high fields, the main body of the PPMS is a liquid helium dewar with a superconducting magnet, in which a measurement probe with the sample chamber and a ^{3}He cryostat is inserted.

The Micro-Hall magnetometry technique is based on the Hall effect [21]. Electrons in an electric current are deviated by a magnetic field $\vec{B}$ perpendicular to their propagation direction (defined by their velocity $\vec{v}$) via the (magnetic) Lorentz force $\vec{F} = q\vec{v} \times \vec{B} = -|e|\vec{v} \times \vec{B}$. This generates a electric current perpendicular to both $\vec{v}$ and $\vec{B}$ with an associated voltage V_{Hall}, which is the quantity that is measured.

The Micro-Hall magnetometer, sketched in Fig. 2.12b, consists of two layers of semiconductors, GaAs and $Al_{1-\alpha}Ga_{\alpha}As$, shaped in the form of a cross [22]. A two dimensional electron gas is confined at the interface between the two materials. The electrons behave as high-mobility charge carriers, which increases the Hall coefficient and the measured signal, reduces the resistivity of the device and improves the sensitivity. A current flow is introduced between two opposite ports of the 'cross' magnetometer, with a magnetic field $\vec{B}$ applied parallel to the direction of propagation of the electrons. This field does not produce a Hall voltage, as it is parallel to $\vec{v}$. Its role is to generate a magnetization $\vec{M}$ in a magnetic sample deposited on top of the magnetometer, which in turn generates an additional magnetic field $\vec{B}_M$. Part of this field is perpendicular to the device (and $\vec{v}$), producing a Hall voltage V_{Hall} proportional to the induced magnetization $\vec{M}$ in the sample between the other two ports of the magnetometer.

2.4.3 Heat capacity experiments

Heat capacity experiments were carried out in the PPMS described in the previous section. The measurements are performed with controlled pressure conditions in the sample chamber, that is, the PPMS measures the constant-pressure heat capacity, C_p:

$$C_p := \frac{dU}{dT}\Big|_{p.} \tag{2.2}$$

The sample chamber hosts a calorimeter for low-temperature heat capacity measurements [23] that consists of a sapphire disc (the sample holder), on which the sample is placed, with an integrated heater and thermometer. Sample and holder are put in mutual thermal contact with apiezon N grease. The holder is connected to a thermal reservoir with constant temperature T_0 by thin gold wires (see Fig. 2.13).

The heat capacity of the sample is measured using a relaxation technique [24]. A controlled quantity of heat power P_0 is introduced through the heater for a time t_0, which increases the temperature T_1 of both the holder and the sample. Part of the heat is transferred through the gold wires, modeled with a thermal conductivity K_1, to the thermal reservoir. The whole process is governed by the following differential equation relating the heat and temperature variation rates:

$$\frac{\partial Q(t)}{\partial t} := P_0\theta(t-t_0) = C_{\text{total}}\frac{\partial T_1(t)}{\partial t} + K_1\left[T_1(t) - T_0\right], \tag{2.3}$$

where $C_{\text{total}} = C_{\text{holder}} + C_{\text{sample}}$ is the combined heat capacity of the holder and the sample, and $\theta(t)$ is the step function.

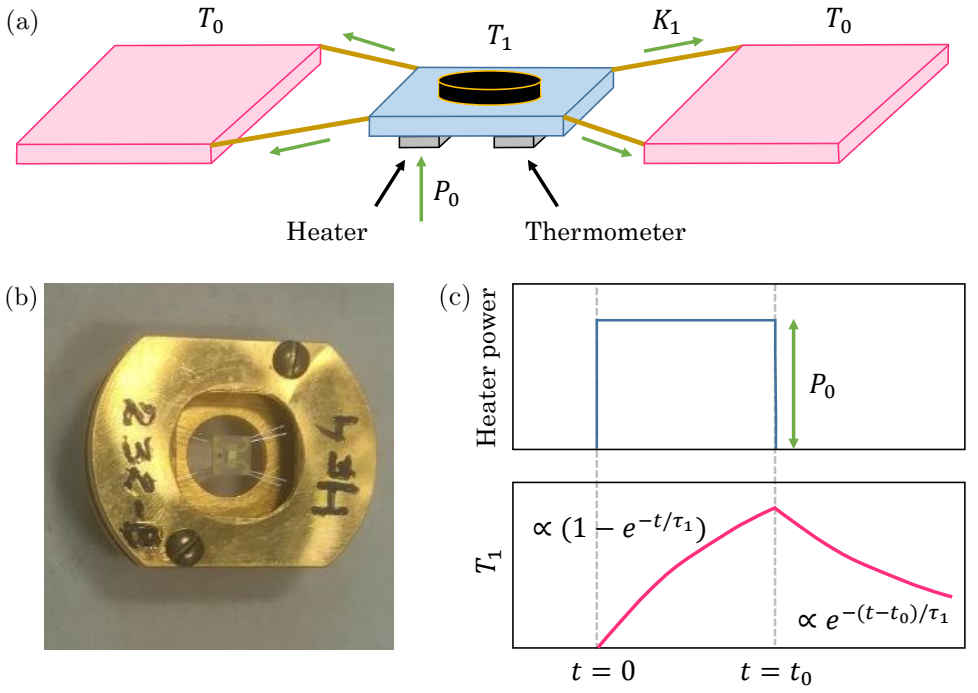

Figure 2.13: (a) Scheme of the sample holder (blue) connected to the reservoir (magenta) by thin gold wires. (b) Photo of the bulk of the calorimeter (the reservoir) with the square sample holder suspended in its centre. (c) Response of the temperature T_1 of the sample to a heat pulse at constant power P_0.

Figure 2.13c shows the solution to Eq. (2.3). It consists of an increase in the sample temperature T_1 during the heat pulse, followed by a relaxation to T_0. Both the increase and decrease are exponential functions with a time constant $\tau_1 = C_{\text{total}}/K_1$. Knowing K_1 from calibration experiments, the total heat capacity C_{total} is calculated from the measurement of τ_1. The different holders are regularly calibrated, that is, measured without sample, so that

their heat capacity C_{holder} can be subtracted from C_{total} to obtain the sample heat capacity C_{sample}.

2.4.4 Electron Paramagnetic Resonance

Electron Paramagnetic Resonance (EPR) is a spectroscopy technique in which an oscillating magnetic field induces magnetic dipole transitions between energy levels of a system of spins in a paramagnetic sample [1, 11, 25]. EPR experiments were performed in a commercial Elexsys E-580 by Brucker Corporation [26] operating in the X-band, property of the INMA (see Fig. 2.14a). The spectrometer consists of a resonant cavity that is irradiated with a microwave source. X-band cavities, which are the most common setup, have a resonance frequency around 9.8 GHz. The paramagnetic sample is placed inside the cavity, which in turn is located at the center of an electromagnet. The external DC magnetic field generated by the magnet tunes the spin transitions in the sample to the cavity frequency, which results in a resonant absorption of microwave power by the paramagnetic sample.

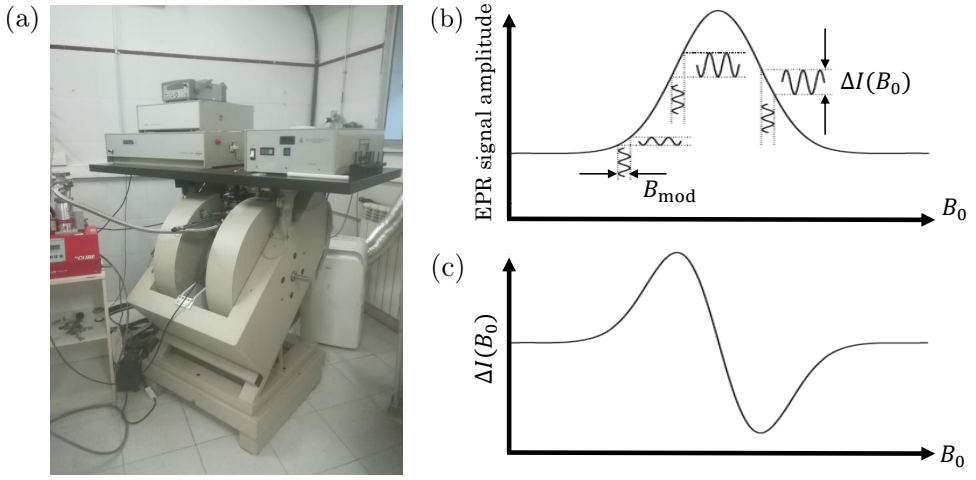

Figure 2.14: (a) Elexsys E-580 spectrometer. The bulk of the device is the electromagnet. (b) A Gaussian absorption line, measured as a function of the DC magnetic field B_0. The relation between the intensity $I(B_0)$ of the absorption line and the change $\Delta I(B_0)$ induced by the modulation field B_{mod} is shown for three fields. (c) The derivative-like lineshape that is obtained by detecting $\Delta I(B_0)$ with a lock-in amplifier. Figures (b) and (c) were taken from [1, Ch.1].

In continuous wave EPR (cw-EPR) experiment, the cavity is continuously irradiated while the DC magnetic field is swept slowly. Around each resonance condition where a spin transition frequency of the sample matches the cavity frequency, the incoming microwave radiation is absorbed by the sample. The

absorption signal is obtained with a field-modulation detection, in which a set of small coils apply a radio-frequency (RF) magnetic field modulation that results in derivative-like lineshape for each absorption signal (Figs. 2.14b-c). The cw-EPR spectrum of the sample gives information about the energies and states in the spin system and about the effective spin Hamiltonian that generates them.

A complementary technique is pulsed EPR, which measures the signal emitted by a spin system after interacting with a series of microwave pulses. This gives information on the relaxation and coherence of the spin system, as the detected signal depends on the dynamics of the spin state prepared by the pulses. The simplest pulsed EPR experiment is the measurement of the Free Induction Decay (FID), which is the signal that the spin system induces in the cavity after a microwave pulse generates a coherence between the two spin states of a given transition. This signal decays with a characteristic time T_2^* that is shorter that the phase memory time T_m of the individual spins if there is a distribution of Larmor frequencies at which the spins precess around the DC magnetic field B_0. This effect, pictured in Fig. 2.15, is known as inhomogeneous broadening. The FID measurement is usually limited by a dead time of the spectrometer after the pulse, which is needed to protect the detection circuit from the high power signal.

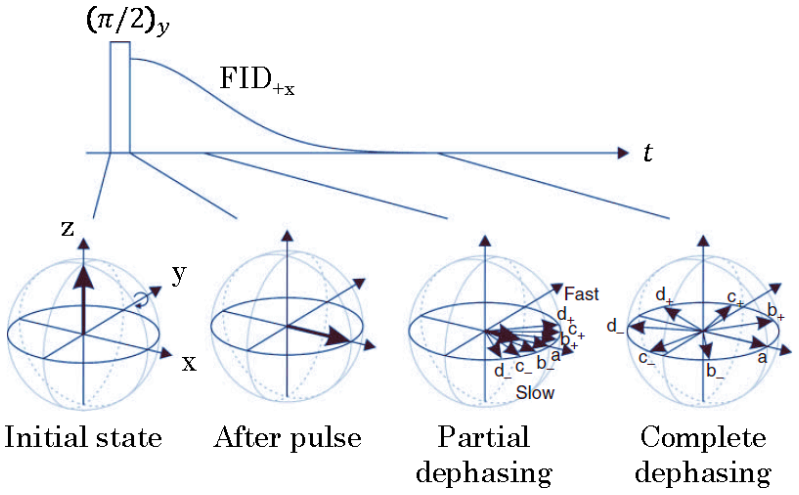

Figure 2.15: FID measurement. A microwave pulse with carrier frequency tuned to the spin transition frequency (the Larmor frequency) changes the state of the spins in the ensemble into the the xy-plane. After the pulse, spins start precessing around z with the Larmor frequency, inducing the FID signal. If there is a distribution of Larmor frequencies, the spin packet spreads in the plane (here the frame of reference is rotating around z with the average Larmor frequency). This eventually leads to a dephasing of the spins in the plane, and the decay of the FID signal. Figure taken from [1, Ch.11].

The two-pulse echo sequence, or Hahn-echo sequence, adds a second pulse that refocuses the FID signal after removing the effect of inhomogeneous broadening (see Fig. 2.16). If the second pulse is delayed by a time τ, the revival of the FID signal happens at a time τ after the second pulse (2τ from the first pulse). This revival is known as the echo signal, which decays with the single spin memory time $T_m > T_2^*$ (if spin-spin interactions are neglected). This time is obtained by measuring the echo for different delay times τ between the two pulses. The limitation of the dead time of the spectrometer is removed by choosing a long enough τ.

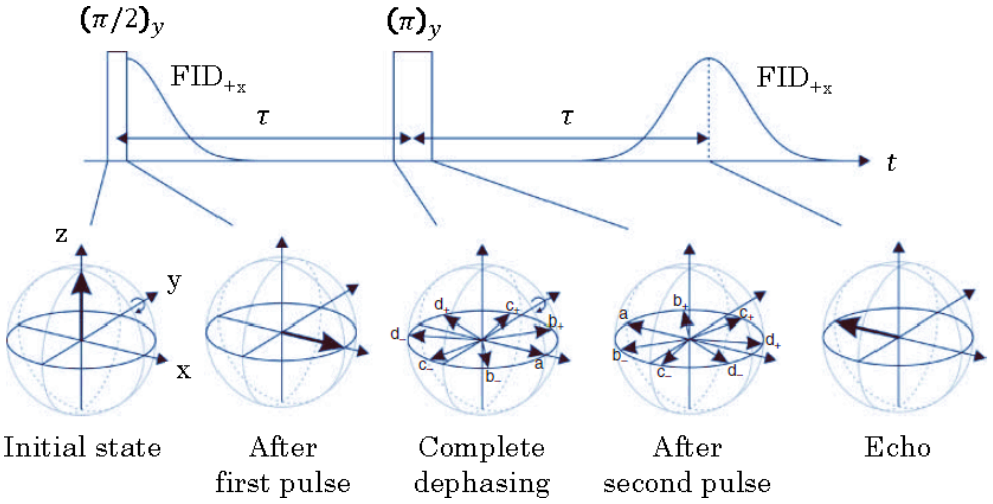

Figure 2.16: Hahn-echo experiment. A second pulse is inserted after a time τ. This pulse takes a spin state with phase $\phi(\tau)$ (in the rotating frame) into a state with phase $-\phi(\tau)$. Then, at a time 2τ from the first pulse, all spins refocus: $\phi(2\tau) = -\phi(\tau) + \phi(\tau) = 0$. This generates a revival of the FID signal, known as the echo signal. Figure taken from [1, Ch.11].

References

[1] D. Goldfarb and S. Stoll, *EPR spectroscopy: fundamentals and methods* (Wiley, 2018).

[2] A. Blais, R.-S. Huang, A. Wallraff, S. M. Girvin, and R. J. Schoelkopf, Physical Review A **69**, 062320 (2004).

[3] M. Jenkins, T. Hümmer, M. J. Martínez-Pérez, J. García-Ripoll, D. Zueco, and F. Luis, New Journal of Physics **15**, 095007 (2013).

[4] M. D. Jenkins, D. Zueco, O. Roubeau, G. Aromí, J. Majer, and F. Luis, Dalton Transactions **45**, 16682 (2016).

[5] S. Doyle, P. Mauskopf, J. Naylon, A. Porch, and C. Duncombe, Journal of Low Temperature Physics **151**, 530 (2008).

[6] B. Aja, M. C. de Ory, L. de la Fuente, E. Artal, J. P. Pascual, M. T. Magaz, D. Granados, and A. Gomez, IEEE Transactions on Microwave Theory and Techniques **69**, 578 (2021).

[7] Center for Nanofabricaction of IMDEA-Nanoscience, *Center for nanofabricaction of imdea-nanoscience*, `https://nanociencia.imdea.org/services?view=article{&}id=156`.

[8] C. Mack, *Introduction to semiconductor lithography: the science of microfabrication* (Wiley-Interscience, 2008).

[9] A. Einstein, Physikalische Zeitschrift **18**, 121 (1917).

[10] C. Cohen-Tannoudji, B. Diu, and F. Laloë, *Quantum mechanics (Second edition)* (Wiley-VCH, 2020).

[11] A. Abragam and B. Bleaney, *Electron paramagnetic resonance of transition ions* (Oxford University Press, 1970).

[12] Bluefors, *BF-LD-Series user manual* (2016).

[13] P. L. Kapitza, Physical Review **60**, 354 (1941).

[14] G. L. Pollack, Reviews of Modern Physics **41**, 48 (1969).

[15] LNF, *LNF-LNC0.3_ 14B - Datasheet* (2022).

[16] Rohde & Schwarz, *ZVB Vector Network Analyzers - Datasheet* (2011).

[17] Keysight, *M8190A Arbitrary Waveform Generator - Datasheet* (2021).

[18] Keysight, *Infiniium S-Series - Datasheet* (2022).

[19] Quantum Design, *Quantum design*, `https://qd-europe.com`.

[20] B. D. Josephson, Physics Letters **1**, 251 (1962).

[21] E. H. Hall, American Journal of Mathematics **2**, 287 (1879).

[22] A. D. Kent, S. von Molnár, S. Gider, and D. D. Awschalom, Journal of Applied Physics **76**, 6656 (1994).

[23] M. Evangelisti, F. Luis, L. J. de Jongh, and M. Affronte, Journal of Materials Chemistry **16**, 2534 (2006).

[24] G. R. Stewart, Review of Scientific Instruments **54**, 1 (1983).

[25] A. Schweiger and G. Jeschke, *Principles of pulse electron paramagnetic resonance* (Oxford University Press, 2001).

[26] Bruker Corporation, *Bruker corporation*, `https://www.bruker.com`.

Chapter 3

Background on spin systems coupled to superconducting resonators

This chapter summarizes the theoretical framework needed to describe the quantum processor. First, an effective Hamiltonian is defined for the molecular spin qubits, and their decoherence and relaxation processes are discussed (see section 3.1). A model of the lumped-element resonator that is used to read, drive/excite and control these qubits is also needed (see section 3.2).

These two quantum systems are not isolated, but coupled and entangled. The nature of this coupling and the implications of its strength compared to the qubit and resonator relaxation rates are discussed in section 3.3. Finally, section 3.4 describes the theory of the dispersive regime, when the detuning between the transition frequencies of the spin system and the resonator frequency is larger than the coupling between the two systems.

3.1 Molecular spin systems

When using molecular spin systems, the qubit/qudit states are encoded in the low energy spin states of a magnetic molecule. At very low temperatures, these are the only significantly populated states in the system. Therefore, the effective spin Hamiltonian H_S needs to account only for the low energy level structure and spin states of the molecular ground spin multiplet of the molecule. This is sketched in Fig. 3.1. The nature of the ground multiplet for each magnetic ion and the typical terms in the effective spin Hamiltonian H_S are discussed below.

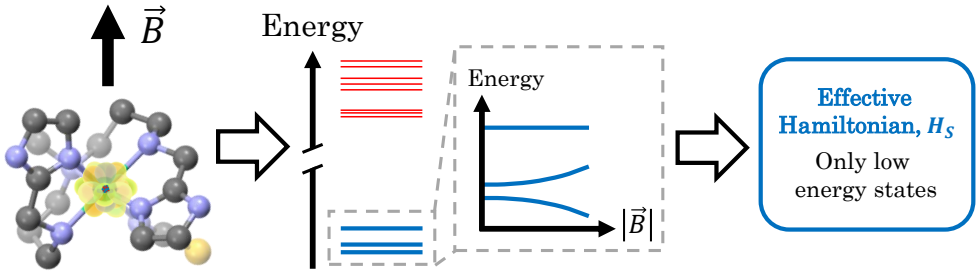

Figure 3.1: Sketch of the description of the relevant spin states of a magnetic molecule. At very low temperatures, only the ground state and a few excited states of the full Hamiltonian describing the molecular quantum states are populated. The high energy level structure is neglected, leaving an effective ground spin multiplet whose states energies depend on the applied magnetic field $\boldsymbol{B}$. The energies of these spin states at zero field and their magnetic field dependence are described by an effective spin Hamiltonian H_{S}.

3.1.1 The ground spin multiplet

The core of a magnetic molecule is composed of one or several transition metal or lanthanide magnetic ions. The ground multiplet of an isolated ion is determined by the Coulomb interaction of its electrons with the electric field of the nucleus and the repulsive interaction between electrons, as well as the spin-orbit coupling between the orbital angular momentum and the spin of each electron.

The magnetic core is surrounded by non-magnetic ligands that stabilize it and isolate from neighbouring molecules in the same crystal. The local coordination of each ion generates an electric field, known as the crystal field or ligand field, which splits the atomic orbitals and modifies the wavefunctions. The competition between the crystal field and spin-orbit interactions gives rise to a different character of the ground multiplet for transition metal and lanthanide ions.

The crystal field is the dominant interaction in transition metal ions [1, Ch.7]. The orbital contribution to the angular momentum $\mathbf{L}$ in these ions is largely quenched due to the crystal field splittings, which leads to a small magnetic anisotropy. In most cases, this means that the total spin S is a good quantum number for the ground multiplet, and the effective spin vector operator is just spin vector operator $\mathbf{S}$. The crystal field does not affect the spin states in the ground multiplet directly, but it manifests itself through spin-orbit coupling.

Lanthanide ions have large orbital angular momentum ($L = 3$), and therefore a strong spin-orbit coupling and large magnetic anisotropy. In addition,

the crystal field interaction is relatively small, as the 4f orbitals of lanthanide ions are closer to the nucleus than 3d orbitals. Following Hund's rules, the ground electronic state of a free lanthanide ion is a multiplet with a well defined total angular momentum $\mathbf{J} = \mathbf{L} + \mathbf{S}$. The vector operator $\mathbf{J}$ is treated as an effective spin, and it will be labeled $\mathbf{S}$ in what follows keeping in mind that it has an orbital angular momentum component.

3.1.2 Effective spin Hamiltonian

The effective Hamiltonian H_{S} describes the magnetic states of a molecular spin within its ground multiplet. It comprises the electronic Zeeman interaction $H_{\mathrm{el,Z}}$, the magnetic anisotropy contribution arising from the crystal field and/or spin-orbit interactions, H_{ma}, and, if the nuclear spin I of the ion is non zero, the hyperfine (H_{hf}), nuclear Zeeman ($H_{\mathrm{nu,Z}}$) and quadrupolar (H_{qp}) interactions. The latter two are usually negligible. The resulting Hamiltonian is [1, Ch.3]:

$$\begin{aligned} H_{\mathrm{S}} &= H_{\mathrm{el,Z}} + H_{\mathrm{ma}} + H_{\mathrm{hf}} + H_{\mathrm{nu,Z}} + H_{\mathrm{qp}} \\ &= \mu_{\mathrm{B}} \boldsymbol{B} \cdot \boldsymbol{g} \cdot \hat{\boldsymbol{S}} + \sum_{k,\,q} B_{kq} \hat{O}_k^q + \hat{\boldsymbol{S}} \cdot \boldsymbol{A} \cdot \hat{\boldsymbol{I}} - \mu_{\mathrm{N}} g_I \boldsymbol{B} \cdot \hat{\boldsymbol{I}} + P_{\parallel} \left(\hat{I}_z^2 - \tfrac{1}{3} I(I+1) \right), \end{aligned} \tag{3.1}$$

with the meaning of the quantities and parameters detailed below.

At high magnetic fields, the electronic Zeeman interaction between the magnetic moment of the electronic shell and the external magnetic field is the dominant term in the Hamiltonian. In a free ion, this term is $\mu_{\mathrm{B}} g_{\mathrm{e}} \boldsymbol{B} \cdot \hat{\boldsymbol{S}}$, where μ_{B} is the Bohr magneton and $g_{\mathrm{e}} \simeq 2.0$ is the free electron g-factor.[1] The effect of the magnetic anisotropy on the Zeeman interaction is modeled by replacing g_{e} with a 'tensor' $\boldsymbol{g}$.[2] In the most general case this gives all the different products of the components of $\boldsymbol{B}$ and $\hat{\boldsymbol{S}}$:

$$H_{\mathrm{el,Z}} = \mu_{\mathrm{B}} \boldsymbol{B} \cdot \boldsymbol{g} \cdot \hat{\boldsymbol{S}} \equiv \mu_{\mathrm{B}} \begin{pmatrix} B_x & B_y & B_z \end{pmatrix} \begin{pmatrix} g_{xx} & g_{xy} & g_{xz} \\ g_{yx} & g_{yy} & g_{yz} \\ g_{zx} & g_{zy} & g_{zz} \end{pmatrix} \begin{pmatrix} \hat{S}_x \\ \hat{S}_y \\ \hat{S}_z \end{pmatrix}. \tag{3.2}$$

[1] The Bohr magneton is proportional to the electron charge, and therefore a negative quantity. However, it is common practice to cancel out the negative sign of μ_{B} with the negative sign of the Zeeman interaction and define μ_{B} as positive. Note that this is not done for the nuclear magneton μ_N, which is defined to be positive (with g_I positive or negative depending on the nucleus).

[2] Although $\boldsymbol{g}$ is usually called a tensor, it is not a tensor in general. The same can be said for the hyperfine 'tensor' $\boldsymbol{A}$. The only thing that matters is whether the same choice of principal axes and basis states can be used to keep only the diagonal terms in both $\boldsymbol{g}$ and $\boldsymbol{A}$ [1, Ch.15].

In most cases the cross terms can be eliminated working in a suitable frame of reference — the principal axes — and it is enough to describe the interaction using only the diagonal terms:

$$H_{\mathrm{el,Z}} = \mu_{\mathrm{B}} \left(g_x B_x \hat{S}_x + g_y B_y \hat{S}_y + g_z B_z \hat{S}_z \right). \tag{3.3}$$

The deviation of $g_x = g_{xx}$, $g_y = g_{yy}$ and $g_z = g_{zz}$ from g_{e} depends on the strength of the magnetic anisotropy. If there is axial symmetry, which is usually assigned to the principal axis z, there are only two distinct values: the parallel g-factor $g_{\parallel} \equiv g_z$ and the perpendicular g-factor $g_{\perp} \equiv g_x = g_y$.

If the nucleus of the ion has a magnetic moment, there is also a nuclear Zeeman interaction between this moment and the magnetic field:

$$H_{\mathrm{nu,Z}} = -\mu_{\mathrm{N}} g_I \boldsymbol{B} \cdot \hat{\boldsymbol{I}} = -\mu_{\mathrm{N}} g_I \left(B_x \hat{I}_x + B_y \hat{I}_y + B_z \hat{I}_z \right). \tag{3.4}$$

Here μ_{N} is the nuclear magneton and g_I, the g-factor of the nucleus, is a dimensionless constant of the order of unity which can be positive or negative. The nuclear Zeeman interaction is much smaller than the electronic Zeeman, as the nucleus is much heavier than the electron: $\frac{\mu_{\mathrm{N}}}{\mu_{\mathrm{B}}} \propto \frac{m_{\mathrm{e}}}{m_{\mathrm{N}}} \sim 10^{-3}$.

At low fields, and in particular at zero field, magnetic anisotropy is the dominant term in the Hamiltonian. This term groups together the effects coming from the crystal field and the spin-orbit coupling. It is written as a combination of the Stevens operators $\hat{O}_k^q$, which take into account the several symmetries in the coordination sphere and how they affect the spin states, with coefficients B_{kq}:

$$H_{\mathrm{ma}} = \sum_{k,\,q} B_{kq} \hat{O}_k^q \equiv \sum_{k=2,4,6} \left(\sum_{-k \le q \le k} B_{kq} \hat{O}_k^q \right). \tag{3.5}$$

Each Stevens operator $\hat{O}_k^q$ is a combination of powers of the spin operators $\hat{S}_x$, $\hat{S}_y$ and $\hat{S}_z$ up to order k (see table 3.1).

For an effective spin S, only operators with $k \le 2S$ have non-zero matrix elements. If S is small and with low symmetry, H_{ma} can be written with only two $k = 2$ terms:

$$H_{\mathrm{ma}} = B_{20} \hat{O}_2^0 + B_{22} \hat{O}_2^2 \equiv D \left(\hat{S}_z^2 - \tfrac{1}{3} S(S+1) \right) + E \left(\hat{S}_x^2 - \hat{S}_y^2 \right), \tag{3.6}$$

where $D = 3B_{20}$ and $E = B_{22}$ are the tetragonal and orthorhombic distortion parameters.

k	q	$\hat{O}_k^q$
2	0	$3\hat{S}_z^2 - s\mathbb{I}$
	±1	$c_\pm \{\hat{S}_z,\, \hat{S}_+ \pm \hat{S}_-\}_+$
	±2	$c_\pm (\hat{S}_+^2 \pm \hat{S}_-^2)$
4	0	$35\hat{S}_z^4 - (30s-25)\,\hat{S}_z^2 + \left(3s^2-6s\right)\mathbb{I}$
	±1	$c_\pm \{7\hat{S}_z^3 - (3s+1)\,\hat{S}_z,\, \hat{S}_+ \pm \hat{S}_-\}_+$
	±2	$c_\pm \{7\hat{S}_z^2 - (s+5)\,\mathbb{I},\, \hat{S}_+^2 \pm \hat{S}_-^2\}_+$
	±3	$c_\pm \{\hat{S}_z,\, \hat{S}_+^3 \pm \hat{S}_-^3\}_+$
	±4	$c_\pm (\hat{S}_+^4 \pm \hat{S}_-^4)$
6	0	$231\hat{S}_z^6 - (315s-735)\,\hat{S}_z^4 + \left(105s^2-525s+294\right)\hat{S}_z^2 -$ $- \left(5s^3-40s^2+60s\right)\mathbb{I}$
	±1	$c_\pm \{33\hat{S}_z^5 - (30s-15)\,\hat{S}_z^3 + \left(5s^2-10s+12\right)\hat{S}_z,\, \hat{S}_+ \pm \hat{S}_-\}_+$
	±2	$c_\pm \{33\hat{S}_z^4 - (18s+123)\,\hat{S}_z^2 + \left(s^2+10s+102\right)\mathbb{I},\, \hat{S}_+^2 \pm \hat{S}_-^2\}_+$
	±3	$c_\pm \{11\hat{S}_z^3 - (3s+59)\,\hat{S}_z,\, \hat{S}_+^3 \pm \hat{S}_-^3\}_+$
	±4	$c_\pm \{11\hat{S}_z^2 - (s+38)\,\mathbb{I},\, \hat{S}_+^4 \pm \hat{S}_-^4\}_+$
	±5	$c_\pm \{\hat{S}_z,\, \hat{S}_+^5 \pm \hat{S}_-^5\}_+$
	±6	$c_\pm (\hat{S}_+^6 \pm \hat{S}_-^6)$

Table 3.1: Stevens operators from *EasySpin* documentation [2]. $\{A,B\}_+$ indicates the symmetrized product $(AB+BA)/2$, and $s = S(S+1)$, $c_+ = 1/2$, $c_- = 1/2i$.

According to Kramers theorem, at zero magnetic field, systems with half-odd electronic spin form doublets of spin states related by time-reversal symmetry [1, Ch.15]. This degeneracy, which can not be lifted by magnetic anisotropy, can be lifted in turn by the hyperfine interaction between the electronic and nuclear magnetic moments of the ion. It is in this situation when the hyperfine interaction becomes more relevant. Due to magnetic anisotropy, this interaction is mediated by a 'tensor' $\boldsymbol{A}$:[3]

$$H_{\text{hf}} = \hat{\boldsymbol{S}} \cdot \boldsymbol{A} \cdot \hat{\boldsymbol{I}} \equiv \begin{pmatrix} \hat{S}_x & \hat{S}_y & \hat{S}_z \end{pmatrix} \begin{pmatrix} A_{xx} & A_{xy} & A_{xz} \\ A_{yx} & A_{yy} & A_{yz} \\ A_{zx} & A_{zy} & A_{zz} \end{pmatrix} \begin{pmatrix} \hat{I}_x \\ \hat{I}_y \\ \hat{I}_z \end{pmatrix} . \tag{3.7}$$

In most cases the principal axes for the hyperfine interaction are the same as those for the electronic Zeeman interaction, and only the diagonal terms are needed:

$$H_{\text{hf}} = A_x \hat{S}_x \otimes \hat{I}_x + A_y \hat{S}_y \otimes \hat{I}_y + A_z \hat{S}_z \otimes \hat{I}_z \,, \tag{3.8}$$

with $A_x \equiv A_{xx}$, $A_y \equiv A_{yy}$ and $A_z \equiv A_{zz}$. For axial symmetry there are

[3] The hyperfine interaction term contains products of electronic and nuclear spin operators, which belong to different subspaces. The product of these operators is then a tensor product that is omitted here: $\hat{S}_i \hat{I}_j \equiv \hat{S}_i \otimes \hat{I}_j$.

only two hyperfine constants, which, following the notation for the electronic Zeeman interaction, are labeled $A_{\parallel} = A_z$ and $A_{\perp} = A_x = A_y$.

Finally, a quadrupolar nuclear term may be needed if $I \geq 1$:

$$H_{\mathrm{qp}} = P_{\parallel} \left(\hat{I}_z^2 - \tfrac{1}{3} I(I+1) \right). \tag{3.9}$$

3.1.3 Decoherence and relaxation processes

The molecule is surrounded by an environment that interacts with it. Then, the full Hamiltonian must include additional degrees of freedom from the environment. The decoherence and relaxation rates of the spin system are obtained by including all relevant interactions in the Hamiltonian and then tracing out all degrees of freedom except those of the spins [3, Ch.8].

The simplest case is a single spin with $S = 1/2$. Its state at a given time t is written as:

$$|\psi(t)\rangle = \cos\left(\theta(t)\right)|0\rangle + e^{i\phi(t)} \sin\left(\theta(t)\right)|1\rangle, \tag{3.10}$$

where $|0\rangle$ and $|1\rangle$ are eigenstates of $\hat{S}_z$. The ground state $|0\rangle$ and the excited state $|1\rangle$ are separated by an energy difference $\hbar\omega_{\mathrm{q}}$, where ω_{q} is the frequency of operation of the qubit. The states described by Eq. 3.10 can be plotted in the Bloch sphere, as shown in Figs. 3.2a and 3.2b: $|0\rangle$ is the north pole of the sphere, $|1\rangle$ its south pole. The state of a single spin rotates around the z-axis of its Bloch sphere at a rate ω_{q}.

Longitudinal spin relaxation is the relaxation process between different energy states of the Hamiltonian of the isolated spin system. As the total energy changes, energy conservation requires that the same energy is absorbed or provided by the environment. In a single spin $S = 1/2$, this means a jump from a state $|\psi(t)\rangle$ to the ground state $|0\rangle$ at an arbitrary time (see Fig. 3.2a).

Transverse spin relaxation is the loss of coherence of the spin system, that is, the decay of the non-diagonal terms of the density matrix $\rho(t) = |\psi(t)\rangle\langle\psi(t)|$, where $\langle\psi(t)|$ is the Hermitian conjugate of the state $|\psi(t)\rangle$. In a single spin $S = 1/2$, this means a jump to another state $|\psi'(t)\rangle$ with the same $\theta(t)$ but different $\phi(t)$ at an arbitrary time (see Fig. 3.2b). There is no energy exchange between the spin system and the environment, although the interaction with the environment is still needed.

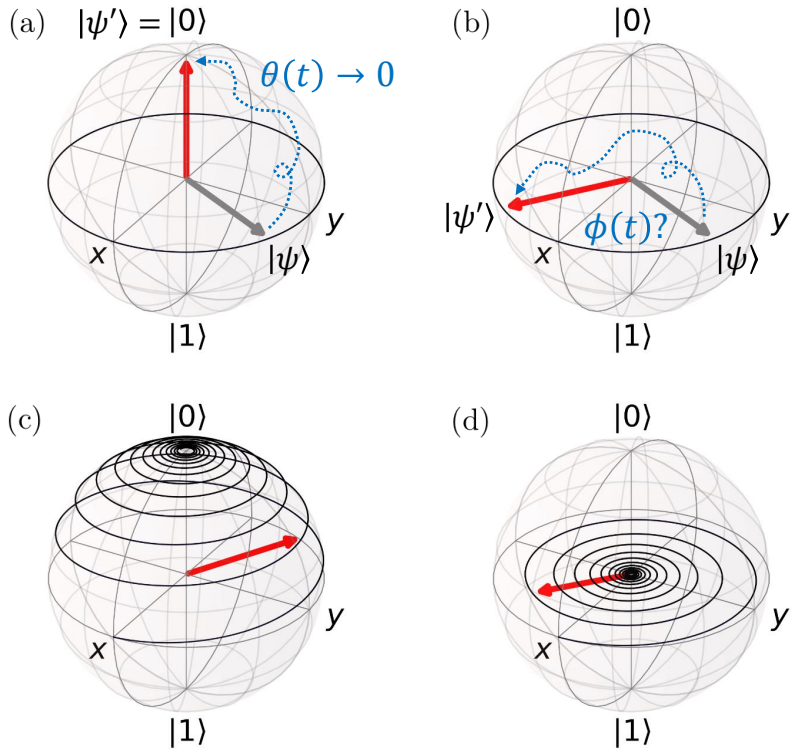

Figure 3.2: Relaxation and decoherence processes in the Bloch sphere. In the top row (a,b), the single spin description. (a) Longitudinal relaxation, where the state $|\psi\rangle$ jumps to the ground state $|\psi'\rangle = |0\rangle$. That is, $\theta(t) \to 0$, and the information in $\phi(t)$ is also lost. (b) Transverse relaxation, where the state $|\psi\rangle$ jumps to another state $|\psi'\rangle$ with the same $\theta(t)$ but different $\phi(t)$. The information in $\phi(t)$ is lost. In the bottom row (c,d), the ensemble description. The mixed state is described by a Bloch vector. (c) Longitudinal relaxation, where the z component of the Bloch vector decays with T_1. Note that the x and y components also decay (see Eq. (3.11)). (d) Transverse relaxation, where the x and y components decay with T_2'.

There is a probability for these processes to occur at a given time. This probability can be recovered by either measuring the same qubit multiple times or having several identical copies of it. The measurement of the ensemble averages of $\hat{S}_x$, $\hat{S}_y$ or $\hat{S}_z$ yields exponential decays. These three averages form the Bloch vector: $(\langle\hat{S}_x\rangle, \langle\hat{S}_y\rangle, \langle\hat{S}_z\rangle)$. The evolution of this vector in the Bloch sphere is traced for the two types of relaxation processes in Figs. 3.2c and 3.2d.

Longitudinal spin relaxation is characterized by T_1, the decay time of $\langle\hat{S}_z\rangle$, or, alternatively, its relaxation rate T_1^{-1}. In solids, the dominant contribution to T_1^{-1} is spin-lattice relaxation, driven by the interaction between the spins and electric field fluctuations caused by lattice vibrations (phonons). Besides, if the spin system is strongly coupled to a resonator, it is possible that T_1^{-1} is

enhanced by the spin-photon interaction at energies (or frequencies) close to the spin-resonator resonance. This is known as the Purcell effect [4, Ch.4].

Transverse spin relaxation is characterized by the decay rate of $\langle \hat{S}_x \rangle$ and $\langle \hat{S}_y \rangle$. One decoherence mechanism is provided by the energy conserving flip-flop process: two spins exchange states, destroying phase ($\phi(t)$) correlation. The contribution by flip-flop processes is measured by T_2'. The total transverse spin relaxation rate T_2^{-1} includes also the contribution from longitudinal spin relaxation, which is half as efficient in destroying coherence than flip-flop processes as it only involves one spin:[4]

$$\frac{1}{T_2} = \frac{1}{T_2'} + \frac{1}{2T_1}. \tag{3.11}$$

In solid state systems T_2 is often not well defined, as the number of coherently coupled spins can change depending on the experiment that is performed. Instead of using T_2, it is common practice to define characteristic transverse decay times associated to each experiment. One of these parameters is the phase memory time T_m, the inverse of the homogeneous half-width of the spin transition. It is measured as the decay time of the echo signal after a Hahn echo sequence ($\pi/2$ and π pulses, see section 2.4.4) as a function of the delay time τ between the two pulses.[5] Another relevant parameter is T_2^*, which is the inverse of the inhomogeneous half-width of the transition and can be measured directly from the spectrum.

3.1.4 The molecular spin qubit

The Hamiltonian of a two-level system encoding a qubit with a frequency of operation ω_q is:

$$H_\mathrm{q} = \frac{\hbar\omega_\mathrm{q}}{2}\hat{\sigma}_z. \tag{3.12}$$

Here $\hat{\sigma}_z$ is one of the three Pauli matrices:

$$\hat{\sigma}_x = \begin{pmatrix} 0 & 1 \\ 1 & 0 \end{pmatrix}, \qquad \hat{\sigma}_y = \begin{pmatrix} 0 & -i \\ i & 0 \end{pmatrix}, \qquad \hat{\sigma}_z = \begin{pmatrix} 1 & 0 \\ 0 & -1 \end{pmatrix}, \tag{3.13}$$

which obey $\hat{\sigma}_j\hat{\sigma}_k = \delta_{jk}\mathbb{I} + i\epsilon_{jkl}\hat{\sigma}_l$.[6]

[4] Note in Fig. 3.2c that the longitudinal spin relaxation process implies a decay in $\langle \hat{S}_x \rangle$ and $\langle \hat{S}_y \rangle$.

[5] T_m is often called T_2, but in general T_m is a lower bound to T_2 as it includes the instantaneous diffusion effect during the pulses.

[6] ϵ_{jkl} is the Levi-Civita symbol.

The simplest physical system with this Hamiltonian is the spin of a free electron biased with an static magnetic field $\boldsymbol{B}$. The isotropic Zeeman interaction of its spin 1/2 with the magnetic field gives the Hamiltonian:

$$H_{\mathrm{S}} = \mu_{\mathrm{B}} g_{\mathrm{e}} B \hat{S}_z = \frac{\mu_{\mathrm{B}} g_{\mathrm{e}} B}{2} \hat{\sigma}_z, \tag{3.14}$$

where g_{e} is the g-factor of the free electron and $\hat{z}$ is the orientation of the magnetic field ($\boldsymbol{B} := B\,\hat{z}$). Here $\hat{S}_z = \hat{\sigma}_z/2$ is a dimensionless spin operator.[7] The frequency of operation of the free electron qubit is then $\omega_{\mathrm{q}} = \mu_{\mathrm{B}} g_{\mathrm{e}} B/\hbar$.

Free-radicals provide the closest example of a free electron in an organic molecule. One atom in these molecules loses an electron, leaving an unpaired electron with spin 1/2 and almost no anisotropy. This situation is described by Hamiltonian (3.14), now with a g-factor g_{S} that will be very similar to but not exactly g_{e}.

In a more complex molecule, like an organic ligand hosting a magnetic ion with effective spin 1/2, the most general case is an anisotropic Zeeman interaction with the magnetic field. This sets two different frames of reference in an experiment: the principal axes of the magnetic anisotropy of the molecule ($\boldsymbol{x}_{\mathbf{mol}}$, $\boldsymbol{y}_{\mathbf{mol}}$ and $\boldsymbol{z}_{\mathbf{mol}}$) and the laboratory axes defined by the magnetic field ($\boldsymbol{x}_{\mathbf{lab}}$, $\boldsymbol{y}_{\mathbf{lab}}$ and $\boldsymbol{z}_{\mathbf{lab}}$, with $\boldsymbol{z}_{\mathbf{lab}}$ parallel to $\boldsymbol{B}$).

The effect of the magnetic anisotropy on the spin Hamiltonian for a spin 1/2 is that there may be different g-values for the three principal axes in the diagonal tensor $\boldsymbol{g}$ of the Zeeman interaction. The simplest setup is then applying the magnetic field along one of the principal axes, replacing g_{e} by the corresponding g-value in Eq. (3.14). If the magnetic field is applied in any other direction, either $\boldsymbol{g}$ is written in the laboratory frame of reference (which will be non-diagonal) or $\boldsymbol{z}_{\mathbf{lab}}$ is written in the frame of reference of the principal axes in order to find the effective g-value for $\boldsymbol{z}_{\mathbf{lab}}$.

3.1.5 The molecular spin qudit

A molecular spin qudit is encoded in a magnetic molecule with more than two spin states. This can be achieved by using a magnetic ion with electronic spin greater than 1/2 or using a magnetic ion with non-zero nuclear spin. Each value of the magnetic field $\boldsymbol{B}$ yields a set of d eigenstates $\{|\alpha\rangle\}$. In this basis, the qudit Hamiltonian (the spin Hamiltonian of the magnetic molecule, with

[7] The true spin operators $\hat{S}_j = \hbar\hat{\sigma}_j/2$ (with $j = x,\ y,\ z$) fulfill the angular momentum algebra and represent a spin 1/2. Using dimensionless spin operators (dividing by $\hbar$) is just a convention to have the spin Hamiltonian parameters in units of energy

all necessary terms) takes the simple diagonal form:

$$H_{\mathrm{q}} = \sum_{\alpha=0}^{d-1} E_\alpha \hat{X}^{\alpha,\alpha}, \tag{3.15}$$

Here $\hat{X}^{\alpha,\alpha} \equiv |\alpha\rangle \langle\alpha|$ is the projector of the eigenstate $|\alpha\rangle$ with energy eigenvalue E_α. States are labeled in increasing order in energy so that $E_\beta > E_\alpha$ if $\beta > \alpha$.

3.2 Lumped-element resonators

Lumped-element resonators or LERs can be seen as superconducting LC circuits, with two well defined parts: an inductor and a capacitor (see Fig. 2.1 in chapter 2). The inductor is composed of either a single straight conductor or a conductor with several turns in one side of the resonator, which give rise to an inductance L. The inter-digitated capacitor has a capacitance C. The resonance frequency of the circuit is given by:

$$\omega_{\mathrm{r}} = \frac{1}{\sqrt{LC}}. \tag{3.16}$$

The quantization of a LER as an LC circuit is obtained starting at classical circuit theory, expressed in terms of flux ϕ or charge q, which derives from an effective Lagrangian. The associated Hamiltonian is quantized using canonically conjugate variables [5].

3.2.1 The classical LC resonator

The Kirchhoff's voltage and current laws for the LC resonator are (see Fig. 3.3a):

$$\begin{aligned} V(t) - L\dot{I}(t) &= 0\,, \\ I(t) + C\dot{V}(t) &= 0\,. \end{aligned} \tag{3.17}$$

Integrating in time the voltage law and combining it with the current law yields a single equation in terms of the flux ϕ, which is related to V as $\dot{\phi} = V$:

$$\ddot{\phi}(t) = -\omega_{\mathrm{r}}^2 \phi(t). \tag{3.18}$$

This is the equation of motion of a resonator with frequency ω_{r}. It can be derived from the classical Lagrangian for the LC circuit:

$$L_{\mathrm{R}} = \frac{1}{2} C\dot{\phi}^2 - \frac{1}{2L}\phi^2, \tag{3.19}$$

or the associated Hamiltonian:

$$H_{\mathrm{R}} = q\dot{\phi} - L_{\mathrm{R}} = \frac{1}{2C}q^2 + \frac{1}{2L}\phi^2, \tag{3.20}$$

where the charge $q = \partial L_{\mathrm{R}}/\partial\dot{\phi}$, defined in terms of current as $\dot{q} = I$, is the canonical conjugate variable of ϕ.[8]

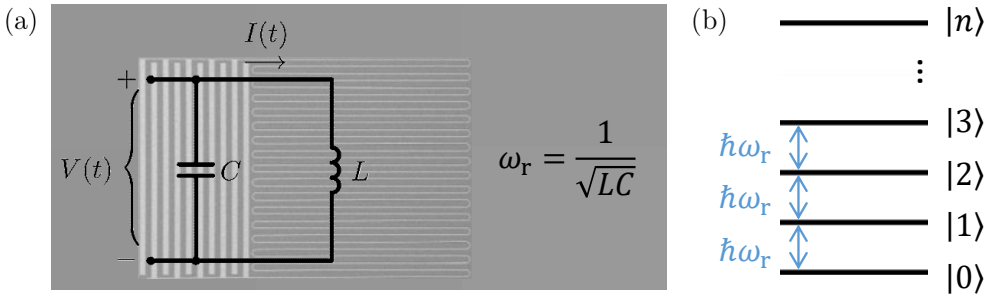

Figure 3.3: (a) Parallel LC circuit representing a lumped-element resonator with frequency ω_{r}. $V(t)$ is the voltage in the capacitor and in the inductor. Taking $I(t)$ as the current in the inductor, the current in the capacitor is $-I(t)$. (b) Energy spectrum of the quantized resonator. The eigenstates $|n\rangle$ of the system are labeled by the number of photons confined in the resonator, n. The energy difference associated to adding one photon to the system is always $\hbar\omega_{\mathrm{r}}$.

3.2.2 Quantization of the LC resonator

The LC circuit can be quantized as the harmonic oscillator. The canonical conjugate variables ϕ and q are now two non-commuting operators $\hat{\phi}$ and $\hat{q}$, with $[\hat{\phi}, \hat{q}] = i\hbar$.[9] From $\hat{\phi}$ and $\hat{q}$, the dimensionless annihilation $\hat{a}$ and creation $\hat{a}^\dagger$ operators are defined as:

$$\hat{a} := \sqrt{\frac{1}{2\hbar Z}}\left(\hat{\phi} + iZ\hat{q}\right) \quad , \quad \hat{a}^\dagger := \sqrt{\frac{1}{2\hbar Z}}\left(\hat{\phi} - iZ\hat{q}\right). \tag{3.21}$$

Here $Z = \sqrt{L/C}$ is the impedance of the resonator, and $\sqrt{\hbar Z}$ has flux units. These operators obey bosonic commutation rules, with $[\hat{a}, \hat{a}^\dagger] = 1$. Using $\hat{a}$ and $\hat{a}^\dagger$, the textbook Hamiltonian of the quantum harmonic oscillator is obtained:

$$H_{\mathrm{R}} = \hbar\omega_{\mathrm{r}}\left(\hat{a}^\dagger\hat{a} + \frac{1}{2}\right). \tag{3.22}$$

[8] The Poisson bracket of ϕ and q gives $\{\phi, q\}_{\mathrm{PB}} = 1$. The bracket is defined, for any pair of variables $A(\phi, q)$ and $B(\phi, q)$ that are functions of the canonical conjugate variables ϕ and q, as $\{A(\phi,q), B(\phi,q)\}_{\mathrm{PB}} = \frac{\partial A}{\partial\phi}\frac{\partial B}{\partial q} - \frac{\partial A}{\partial q}\frac{\partial B}{\partial\phi}$.

[9] The Poisson bracket of two canonical conjugate variables is promoted to the commutator of the operators that represent them (with a factor $i\hbar$): $\{\phi, q\}_{\mathrm{PB}} = 1 \rightarrow [\hat{\phi}, \hat{q}] = i\hbar$

The eigenstates $|n\rangle$ of H_R are Fock states labeled by non-negative integer numbers n indicating the number of excitations — confined photons — in the resonator. These excitations are annihilated and created by $\hat{a}$ and $\hat{a}^\dagger$, respectively:

$$\hat{a}\,|n\rangle = \sqrt{n}\,|n-1\rangle \quad , \quad \hat{a}^\dagger\,|n\rangle = \sqrt{n+1}\,|n+1\rangle\,, \tag{3.23}$$

and the number operator $\hat{n} = \hat{a}^\dagger\hat{a}$ has the number of excitations as eigenvalues: $\hat{n}\,|n\rangle = n\,|n\rangle$. The energies E_n of the system are then:

$$E_n = \left(n + \frac{1}{2}\right)\hbar\omega_\mathrm{r}. \tag{3.24}$$

The energy spectrum is shown in Fig. 3.3b. Note that in the absence of excitations ($n = 0$), the energy of the resonator is not zero: $E_0 = \hbar\omega_\mathrm{r}/2$. This is the energy of the quantum fluctuations associated to the vacuum state $|0\rangle$.

The time evolution of the expectation value of $\hat{a}$ is given by $\langle\hat{a}\rangle = \langle\psi|\,a\,|\psi\rangle$, where $|\psi\rangle$ is the wavefunction of the resonator. It can also be written as $\langle\hat{a}\rangle = \langle\psi|\,a\,|\psi\rangle = \mathrm{Tr}\,\hat{a}\rho$, where $\rho = |\psi\rangle\langle\psi|$ is the density matrix.[10] Then, the time evolution of $\langle\hat{a}\rangle$ reads:

$$\frac{\mathrm{d}}{\mathrm{d}\,t}\langle\hat{a}\rangle = -\frac{i}{\hbar}\,\mathrm{Tr}\,(\hat{a}\,[H_\mathrm{R},\rho]) = -i\omega_\mathrm{r}\langle\hat{a}\rangle \quad \Rightarrow \quad \langle\hat{a}\rangle(t) = \langle\hat{a}\rangle(0)e^{-i\omega_\mathrm{r}t}. \tag{3.25}$$

Here I used the Schrödinger picture, where only the density matrix is time dependent obeying the von Neumann equation $\dot{\rho} = -i\,[H_\mathrm{R},\rho]\,/\hbar$.[11] If the resonator is not completely isolated there will be a leaking of photons to the environment. This is modeled with a decay rate κ for $\langle\hat{a}\rangle$ (and $\langle\hat{a}^\dagger\rangle$):[12]

$$\frac{\mathrm{d}}{\mathrm{d}\,t}\langle\hat{a}\rangle = -i\omega_\mathrm{r}\langle\hat{a}\rangle - \kappa\langle\hat{a}\rangle \quad \Rightarrow \quad \langle\hat{a}\rangle(t) = \langle\hat{a}\rangle(0)e^{-(i\omega_\mathrm{r}+\kappa)t}. \tag{3.26}$$

The relative strength of ω_r and the decay rate of photons in the cavity (associated to $\hat{n}$), which is twice the decay rate κ for $\langle\hat{a}\rangle$ and $\langle\hat{a}^\dagger\rangle$, is encapsulated in the quality factor Q:

$$Q := \frac{\omega_\mathrm{r}}{2\kappa}. \tag{3.27}$$

3.3 Coupling molecular spin qubits to lumped-element resonators

If molecular spin qubits were directly coupled to the transmission line, their interaction time with the photons sent through the line would be too short

[10] Given a matrix A, $\mathrm{Tr}\,A$ is the sum of its diagonal elements: $\mathrm{Tr}\,A = \sum_i A_{ii}$.

[11] $\frac{\mathrm{d}}{\mathrm{d}\,t}\langle\hat{a}\rangle = \mathrm{Tr}\,\hat{a}\dot{\rho} = -\frac{i}{\hbar}\,\mathrm{Tr}\,\hat{a}\,[H_\mathrm{R},\rho] = -i\omega_\mathrm{r}\langle\left[\hat{a},\hat{a}^\dagger\right]\hat{a}\rangle = -i\omega_\mathrm{r}\langle\hat{a}\rangle$

[12] This decay is justified with a quantum master equation in the next chapter.

for them to interact coherently. In order to have longer interaction times, spins are coupled to photons inside a cavity or resonator. Section 3.3.1 models the interaction between a single molecular spin qubit and a lumped element resonator.

Unfortunately, this model can not be applied directly to describe the experiments, as they are not performed on single molecules yet. The coupling G_1 of each molecular spin to the resonator is still too weak for quantum applications, its enhancement being a subject of current research [6]. However, it is still possible to test large ensembles of molecules. This gives a collective coupling G_N that enhances the single molecule coupling by a factor $\sqrt{N}$, where N is the number of spins in the ensemble. The simplest case is an ensemble of spin 1/2 molecules, like in free radicals, which were reviewed in section 3.3.2. Finally, section 3.3.3 generalizes the results for higher spin ensembles.

3.3.1 Molecular spin qubit-resonator coupling

A molecular spin qubit couples to a resonator via the interaction of the magnetic moment of the molecule with the zero-point magnetic field $\boldsymbol{B_0}$ of the resonator, that is, the field generated by the vacuum state $|0\rangle$ of the resonator [7]. Both subsystems exchange excitations at the single qubit-resonator coupling rate G_1, with $\hbar G_1$ being the matrix element of the Zeeman interaction (see Eq. (3.2)) generated by the field $\boldsymbol{B_0}$ at the position $\boldsymbol{r}$ of the molecule [8]:

$$\hbar G_1 := \langle \mathrm{g} | \, \mu_\mathrm{B} \boldsymbol{B_0}(\boldsymbol{r}) \cdot \boldsymbol{g} \cdot \hat{\boldsymbol{S}} \, | \mathrm{e} \rangle \, . \tag{3.28}$$

Here $|\mathrm{g}\rangle$ (ground state) and $|\mathrm{e}\rangle$ (excited state) are the eigenstates of the qubit Hamiltonian of Eq. (3.12), with new labels in order to avoid confusion between qubit and resonator states. The z axis is defined by the orientation of the static magnetic field $\boldsymbol{B}$.

The simplest case is an isotropic spin 1/2, with qubit frequency $\omega_\mathrm{q} = \mu_\mathrm{B} g_\mathrm{S} B/\hbar$ and coupling:

$$\begin{aligned} \hbar G_1 :=& \frac{\mu_\mathrm{B} g_\mathrm{S}}{2} \langle \mathrm{g} | \left[B_{0,\,x}(\boldsymbol{r}) \hat{\sigma_x} + B_{0,\,y}(\boldsymbol{r}) \hat{\sigma_y} + B_{0,\,z}(\boldsymbol{r}) \hat{\sigma_z} \right] | \mathrm{e} \rangle \\ =& \frac{\mu_\mathrm{B} g_\mathrm{S}}{2} \left[B_{0,\,x}(\boldsymbol{r}) - i B_{0,\,y}(\boldsymbol{r}) \right] , \end{aligned} \tag{3.29}$$

that is, only the components of $\boldsymbol{B_0}(\boldsymbol{r})$ perpendicular to $\boldsymbol{B}$ contribute to the complex coupling. In the case of a single qubit, there is freedom to choose molecular x axis as the orientation of $\boldsymbol{B_0}(\boldsymbol{r})$ and write a real G_1:

$$\hbar G_1 := \frac{\mu_\mathrm{B} g_\mathrm{S} B_{0,\,\perp}(\boldsymbol{r})}{2}, \tag{3.30}$$

where $B_{0,\perp}(\boldsymbol{r})$ is the projection of $\boldsymbol{B_0}(\boldsymbol{r})$ in the plane perpendicular to $\boldsymbol{B}$.

Another common situation with a simple description is a molecule with axial symmetry, with a longitudinal g-value $g_\parallel$ and a perpendicular g-value $g_\perp$ (see section 3.1.2). If the magnetic field $\boldsymbol{B}$ is applied parallel to the symmetry axis with $g_\parallel$, the qubit frequency is $\omega_\mathrm{q} = \mu_\mathrm{B} g_\parallel B$, and the qubit-resonator coupling is:

$$\hbar G_1 := \frac{\mu_\mathrm{B} g_\perp B_{0,\perp}(\boldsymbol{r})}{2}. \tag{3.31}$$

While qubit and resonator exchange excitations at the rate G_1, each subsystem looses coherence. The qubit coherence decays at a rate γ (the inverse of T_2 or T_m, see section 3.1.3) and the resonator field at a rate κ (see section 3.2.2). This is sketched in Fig. 3.4. In order to use the qubit-resonator system for quantum computing, the qubit must be operated coherently. This requires that $G_1 \gg \kappa, \gamma$ so that both qubit and resonator field remain coherent for long enough time for G_1 to perform the operation. When this condition is fulfilled, the qubit-resonator system is said to be in the strong coupling regime.

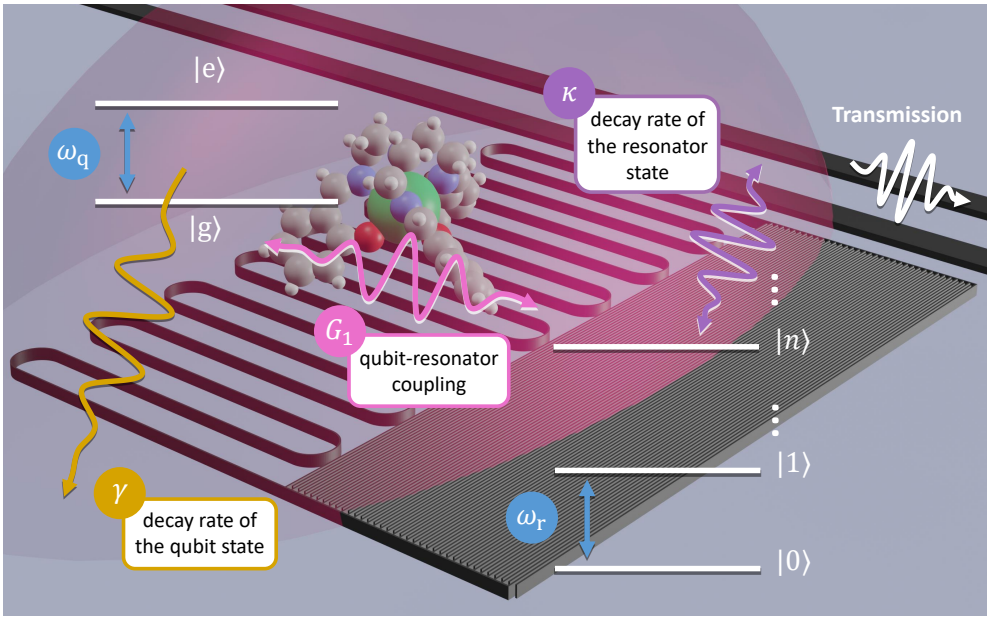

Figure 3.4: Scheme of the qubit-resonator coupling. The spin/qubit can be in any complex superposition of its two eigenstates |g⟩ (ground) and |e⟩ (excited). The energy difference $\hbar\omega_\mathrm{q}$ between |g⟩ and |e⟩ determines the frequency of operation ω_q of the qubit. The coherence of the encoded state decays with γ (without including the interaction with the resonator). The resonator can be in any superposition of its eigenstates, labeled by the number n of photons in the cavity. The state of the resonator decays into the transmission line at a rate κ. The two subsytems, qubit and resonator, exchange excitations at a rate G_1.

The quantum Rabi model gives a Hamiltonian for the closed (lossless) qubit-resonator system [5]:

$$H_{\text{Rabi}} = \frac{\hbar\omega_{\text{q}}}{2}\hat{\sigma}_z + \hbar\omega_{\text{r}}\hat{a}^\dagger\hat{a} + \hbar\sigma_x\left(G_1\hat{a} + G_1^*\hat{a}^\dagger\right), \tag{3.32}$$

where $\hat{\sigma}_x$ and $\hat{\sigma}_z$ are the Pauli matrices from Eq. (3.13). Here I keep a complex coupling G_1 that can be extended to qubit ensembles.

Typically, the qubit-resonator coupling rate $|G_1|$ is much lower than both ω_{q} and ω_{r}. Using the rotating wave approximation, which neglects the counter-rotating terms in Eq. (3.32) that do not preserve the number of excitations in the qubit-resonator system,[13] yields the so-called Jaynes-Cummings Hamiltonian [9, Ch.2]:

$$H_{\text{JC}} = \frac{\hbar\omega_{\text{q}}}{2}\hat{\sigma}_z + \hbar\omega_{\text{r}}\hat{a}^\dagger\hat{a} + \hbar\left(G_1\hat{\sigma}_+\hat{a} + G_1^*\hat{\sigma}_-\hat{a}^\dagger\right). \tag{3.33}$$

Hamiltonian (3.33) is the starting point for any description of the system. The ground state of the JC model is $|\psi_{0,\,\text{g}}\rangle \equiv |0\rangle \otimes |\text{g}\rangle$, the tensor product of the Fock state of zero photons in the resonator, $|0\rangle$, and the ground state of the qubit, $|\text{g}\rangle$.[14] with energy $E_{0,\,\text{g}} = -\frac{\hbar\omega_{\text{q}}}{2}$. The excited states are pairs of hybridized qubit-resonator states $|\psi_{n,\,\pm}\rangle$, known as polaritons.[15] These states are symmetric (+) and antisymmetric (−) superpositions of the $|\psi_{n,\,\text{g}}\rangle \equiv |n\rangle \otimes |\text{g}\rangle$ and $|\psi_{n-1,\,\text{e}}\rangle \equiv |n-1\rangle \otimes |\text{e}\rangle$ states, where $|\text{e}\rangle$ is the excited state of the qubit.[16]

The energy gap between the polaritonic states is $\hbar$ times the Rabi frequency Ω_n. Shifting the zero of energy to $E_{0,\,\text{g}}$, this gives [9, Ch.6]:

$$E_{n,\,\pm} = n\hbar\omega_{\text{r}} + \frac{\hbar\Delta}{2} \pm \frac{\hbar\Omega_n}{2}, \qquad \Omega_n \equiv \sqrt{\Delta^2 + 4n|G_1|^2}. \tag{3.34}$$

These energies are controlled by the frequency detuning $\Delta = \omega_{\text{q}} - \omega_{\text{r}}$ between the spin and resonator characteristic frequencies. The corresponding polaritonic states $|\psi_{n,\,\pm}\rangle$ are (see Fig. 3.5):

$$|\psi_{n,\,\pm}\rangle = \frac{1}{\sqrt{2}}\left(\sqrt{1 \mp \frac{\Delta}{\Omega_n}}\,|\psi_{n,\,\text{g}}\rangle \pm \sqrt{1 \pm \frac{\Delta}{\Omega_n}}\,|\psi_{n-1,\,\text{e}}\rangle\right). \tag{3.35}$$

[13] Writing $\hat{\sigma}_x = \hat{\sigma}_+ + \hat{\sigma}_-$, this means dropping terms with $\hat{\sigma}_+\hat{a}^\dagger$ or $\hat{\sigma}_-\hat{a}$ and keeping the terms with $\hat{\sigma}_+\hat{a}$ or $\hat{\sigma}_-\hat{a}^\dagger$.

[14] Obeying $\hat{\sigma}_z\,|\text{g}\rangle = -\,|\text{g}\rangle \;\Rightarrow\; |\text{g}\rangle = \begin{pmatrix}0\\1\end{pmatrix}$.

[15] The total number of excitations in the qubit-resonator system, given by the number operator $\hat{\mathcal{N}} := \hat{a}^\dagger\hat{a} + \hat{\sigma}_+\hat{\sigma}_-$, label the pairs of polaritonic states. However, it is common to find the states labeled with the same letter n as for the number of excitations in the resonator, instead of a new letter $\mathcal{N}$ for the total number of excitations.

[16] Obeying $\hat{\sigma}_z\,|\text{e}\rangle = +\,|\text{e}\rangle \;\Rightarrow\; |\text{e}\rangle = \begin{pmatrix}1\\0\end{pmatrix}$.

In resonance ($\Delta = 0$), these are symmetric and antisymmetric superpositions:

$$|\psi_{n,\pm}\rangle = \frac{1}{\sqrt{2}}\left(|\psi_{n,\mathrm{g}}\rangle \pm |\psi_{n-1,\mathrm{e}}\rangle\right) . \tag{3.36}$$

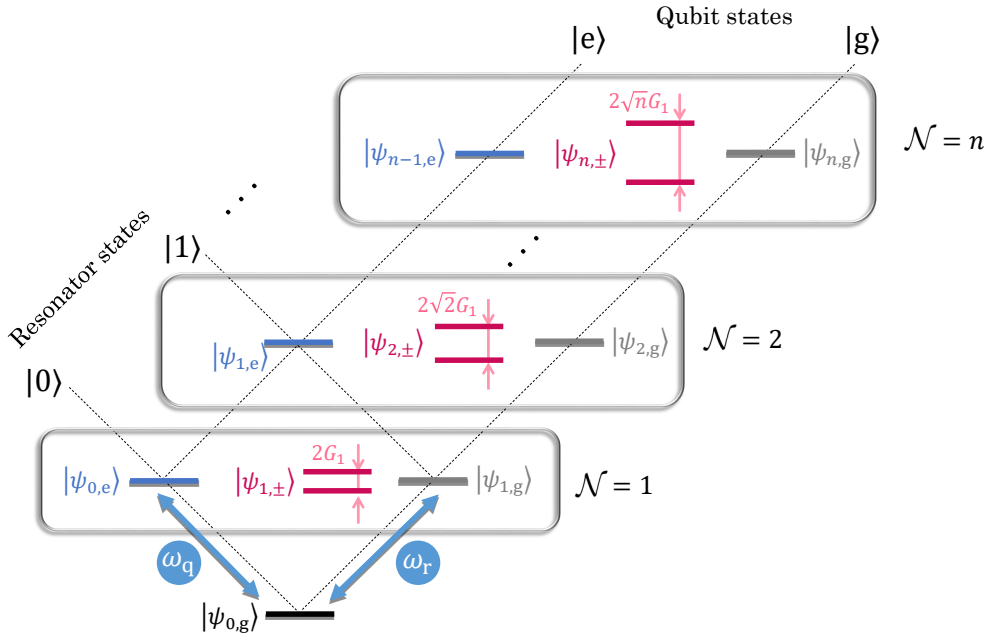

Figure 3.5: Scheme of the Jaynes-Cummings 'ladder'. Ignoring the coupling, the energy of the system is increased by either exciting the resonator with frequency ω_r (up and right in the ladder) or the qubit with frequency ω_q (up and left in the ladder). States with the same total number of excitations, $\mathcal{N}$, are drawn at the same height in the ladder. In general, these states will have different energies if $\Delta = \omega_\mathrm{q} - \omega_\mathrm{r} \neq 0$, but have the same energy in the resonant case ($\Delta = 0$). This two-fold degeneracy is lifted if the systems are coupled, with a pair of polaritonic states forming for each $\mathcal{N}$.

3.3.2 Spin 1/2 ensembles

In current experiments, an ensemble of molecules is deposited on the resonator in order to have an enhanced collective spin-resonator coupling. The case of an ensemble of magnetic molecules with spin 1/2, like in free radicals, is described by extending the Jaynes-Cummings model to N qubits:[17]

$$H_\mathrm{TC} = \sum_{i=1}^{N} \frac{\hbar\omega_{\mathrm{q},i}}{2}\hat{\sigma}_{z,i} + \hbar\omega_\mathrm{r}\hat{a}^\dagger\hat{a} + \sum_{i=1}^{N}\hbar\left(G_{1,i}\,\hat{\sigma}_{+,i}\,\hat{a} + G_{1,i}^*\,\hat{\sigma}_{-,i}\,\hat{a}^\dagger\right) . \tag{3.37}$$

[17] Here, a single-spin operator (like $\hat{\sigma}_{z,i}$) written alone is omitting the tensor product with the identities of the subspaces of the spins with labels different than i: $\hat{\sigma}_{z,i} \to \hat{\sigma}_{z,i} \otimes (... \otimes \mathbb{I}_{j\neq i} \otimes ...)$.

This is the Tavis-Cummings Hamiltonian [10]. Imposing that all qubits share the same frequency of operation ω_q and qubit-resonator coupling G_1 yields:

$$H_{\text{RWA Dicke}} = \frac{\hbar\omega_\mathrm{q}}{2}\hat{S}_z + \hbar\omega_\mathrm{r}\hat{a}^\dagger\hat{a} + \hbar\left(G_1\hat{S}_+\hat{a} + G_1^*\hat{S}_-\hat{a}^\dagger\right), \tag{3.38}$$

with the collective spin operators $\hat{S}_z = \sum_{i=1}^{N}\hat{\sigma}_{z,i}$ and $\hat{S}_\pm = \sum_{i=1}^{N}\hat{\sigma}_{\pm,i}$. Hamiltonian (3.38) can be also seen as the result of using a rotating wave approximation in the Dicke model [11].

Because these collective operators fulfill the angular momentum algebra, the Holstein-Primakoff [12, Ch.6] approximation can be applied in the limit of large N, defining the bosonic operators $\hat{b} := \frac{1}{\sqrt{N}}\hat{S}_-$ and $\hat{b}^\dagger := \frac{1}{\sqrt{N}}\hat{S}_+$. The resulting Hamiltonian is just that of two coupled resonators [9, Ch.2]:

$$H_\mathrm{eff} = \hbar\omega_\mathrm{r}\hat{a}^\dagger\hat{a} + \hbar\omega_\mathrm{q}\hat{b}^\dagger\hat{b} + \hbar G_N\left(\hat{a}^\dagger\hat{b} + \hat{a}\hat{b}^\dagger\right), \tag{3.39}$$

with an enhanced coupling:

$$G_N \equiv |G_1|\sqrt{N}. \tag{3.40}$$

Note that if there are any inhomogeneities in the magnetic field felt by each spin, the decay rate of the spin ensemble coherence will be the inverse of T_2^* (see section 3.1.3), which is larger than the rate γ of each individual spin. Then, the strong coupling condition compares an enhanced G_N with an also larger $\Gamma := 1/T_2^*$.

Hamiltonian (3.39) can be rewritten in terms of the normal modes $\hat{c}_+$ and $\hat{c}_-$:

$$H_\mathrm{eff} = \hbar\omega_+\hat{c}_+^\dagger\hat{c}_+ + \hbar\omega_-\hat{c}_-^\dagger\hat{c}_-, \tag{3.41}$$

with:

$$\begin{aligned}\omega_\pm &= \omega_\mathrm{r} + \frac{\Delta}{2} \pm \frac{\Omega}{2}, \qquad \Omega \equiv \sqrt{\Delta^2 + 4G_N^2},\\ \hat{c}_\pm &= \frac{1}{\sqrt{2}}\left(\sqrt{1 \mp \frac{\Delta}{\Omega}}\ \hat{a}\ \pm\ \sqrt{1 \pm \frac{\Delta}{\Omega}}\ \hat{b}\right).\end{aligned} \tag{3.42}$$

The system is characterized by two frequencies, ω_+ and ω_-, which are shown in Fig. 3.6 as a function of the detuning $\Delta = \omega_\mathrm{q} - \omega_\mathrm{r}$.

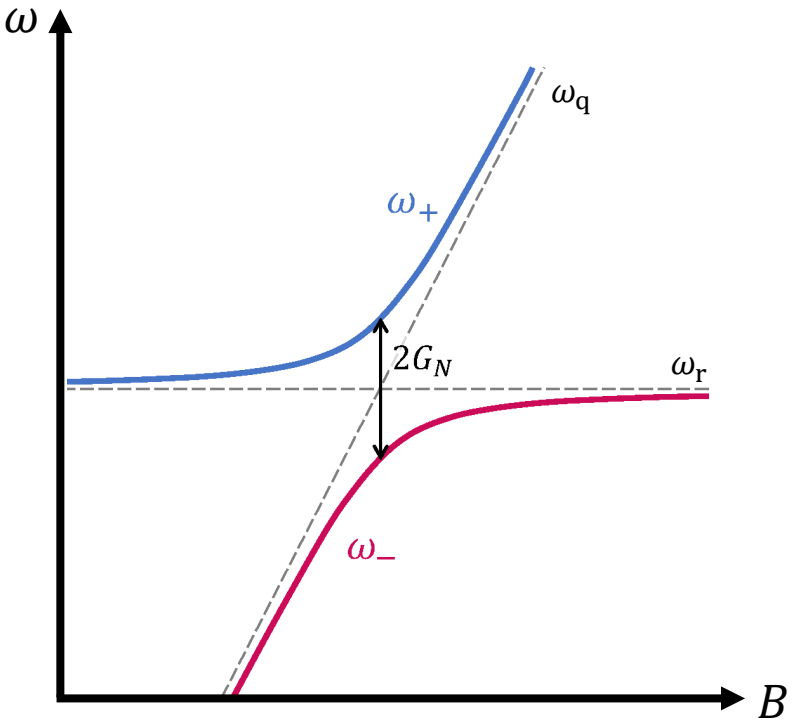

Figure 3.6: Frequency spectrum relevant to transmission experiments, plotted against applied magnetic field B. The two branches correspond to transitions with excitation energies $\hbar\omega_\pm$ (see Eq. (3.42)). When the qubit and the resonator are in resonance ($\omega_\mathrm{q} = \omega_\mathrm{r}$), the two frequencies are just $\omega_\pm = \omega_\mathrm{r} \pm G_N$. The ensemble frequency ω_q is tuned by varying B.

The ground state of the system is $|\psi_{0,\mathrm{g}}\rangle \equiv |0\rangle \otimes |\mathrm{g}\rangle_1 \otimes ... \otimes |\mathrm{g}\rangle_N$. Similarly, the $|\psi_{n,\mathrm{g}}\rangle$ states are the product of the ensemble ground state with the Fock state of n photons in the resonator. For each n there is also the product of the resonator state with an excited state of the ensemble, which is a completely symmetric state in the excitation of any qubit (recall that $\hat{b}^\dagger = \frac{1}{\sqrt{N}} \sum_i \hat{\sigma}_{+,i}$):

$$|\psi_{n,\mathrm{e}}\rangle \equiv \hat{b}^\dagger |\psi_{n,\mathrm{g}}\rangle = |n\rangle \otimes \frac{1}{\sqrt{N}} \sum_{i=1}^{N} |\mathrm{e}\rangle_i \otimes \left(... \otimes |\mathrm{g}\rangle_{j\neq i} \otimes ... \right). \tag{3.43}$$

These are known as Dicke states, or superradiant modes, which couple to cavity photons. As in the Jaynes-Cummings Hamiltonian (3.33), the spin-photon coupling generates two polaritonic states $|\psi_{n,\pm}\rangle$ for each $n \geq 1$, superpositions of $|\psi_{n,\mathrm{g}}\rangle$ and $|\psi_{n-1,\mathrm{e}}\rangle$, with the their corresponding creation operators $\hat{c}_+^\dagger$ and $\hat{c}_-^\dagger$.

Higher excitations of the spin ensemble, which are obtained with the creation operator $\hat{b}^\dagger \propto \hat{S}_+$, are completely symmetric states of more than one

excited spin. The k-th excitation of the ensemble of N spins is then the completely symmetric state with $m_S = -S + k$, where $S = N/2$ is the total spin of the ensemble. The remaining degrees of freedom of the ensemble, which do not couple to the resonator, are the $2^N - (N+1)$ non-symmetric dark states, $\binom{N}{k} - 1$ for each k-th excited symmetric state [11]. This description is valid as long as N is kept much larger than the number of photons, n [4, Ch.4].

The action of $\hat{b}^\dagger$ on the k-th excitation $|k\rangle \equiv |S, m_S = -S + k\rangle$ is similar to the action of the creation operator $a^\dagger$ of a quantum harmonic oscillator, provided that $k \ll N$ (see Fig. 3.7).

$$\begin{aligned}\hat{b}^\dagger |k\rangle \equiv & \frac{1}{\sqrt{N}} \hat{S}_+ |S, m_S = -S + k\rangle \\ = & \frac{1}{\sqrt{N}} \sqrt{S(S+1) - (-S+k)(-S+k+1)}\, |S, m_S + 1 = -S + k + 1\rangle \\ \equiv & \sqrt{\frac{N-k}{N}} \sqrt{k+1}\, |k+1\rangle \quad \rightarrow \quad \sqrt{k+1}\, |k+1\rangle \quad \text{if} \quad k \ll N.\end{aligned} \tag{3.44}$$

At low temperatures, $k \ll N$ when $n \ll N$, as the origin of the excitations are the photons in the resonator. Then, the harmonic description for the ensemble is valid. This is typically the case in microwave transmission experiments.

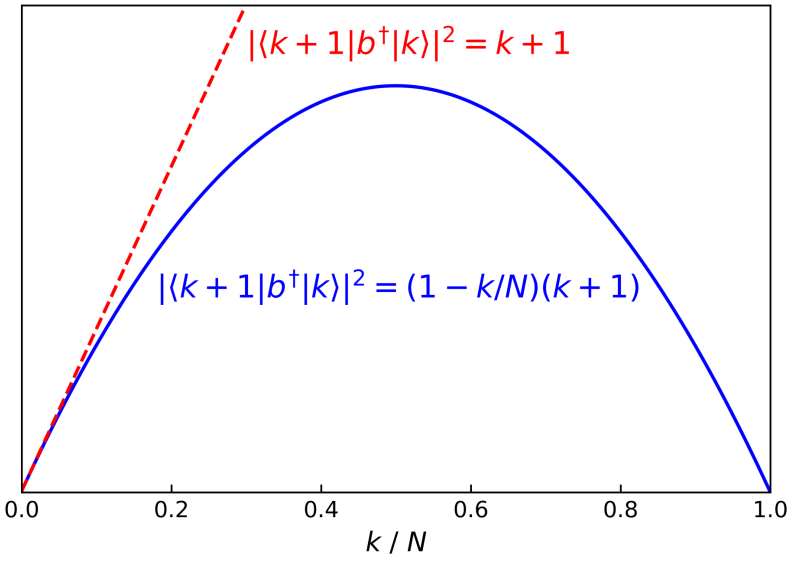

Figure 3.7: Squared matrix element of $\hat{b}^\dagger$ between the k-th and $(k+1)$-th excitations, as a function of k/N. The true parabolic dependence (blue solid line) is closely matched by that of the creation operator (red dashed line) only for small k/N (≤ 0.1).

Let us return again to the Tavis-Cummings Hamiltonian (3.37). It is worthy pointing out that, even with an inhomogeneous coupling, it is possible to arrive

at the simple Hamiltonian (3.39) [13]. Assuming again that there is at least a homogeneous qubit frequency ω_{q}, the collective operators b and $b^\dagger$ are redefined for inhomogeneous coupling as:

$$\hat{b} := \frac{1}{G_N}\sum_{i=1}^{N} G_{1,i}^{*}\,\hat{\sigma}_{-,i}, \qquad \hat{b}^\dagger := \frac{1}{G_N}\sum_{i=1}^{N} G_{1,i}\,\hat{\sigma}_{+,i}, \tag{3.45}$$

with $G_N \equiv G_{1,\mathrm{RMS}}\sqrt{N}$. $G_{1,\mathrm{RMS}}$ is the root mean square of the absolute values of the N different couplings:[18]

$$G_N \equiv G_{1,\mathrm{RMS}}\sqrt{N}, \qquad G_{1,\mathrm{RMS}} = \sqrt{\frac{1}{N}\sum_{i=1}^{N}|G_{1,i}|^2}. \tag{3.46}$$

Working in the limit of few excited qubits, and restricting the excitations to generalized Dicke states, the operators b and $b^\dagger$ in Eq. (3.45) fulfill approximately the bosonic commutation relations, arriving again at Hamiltonian (3.39). This time the superradiant modes are generalized Dicke states of the form:

$$|\psi_{n,\mathrm{e}}\rangle \equiv |n\rangle \otimes \frac{1}{G}\sum_{i=1}^{N} G_{1,i}\,|\mathrm{e}\rangle_i \otimes \Big(... \otimes |\mathrm{g}\rangle_{j\neq i} \otimes ...\Big). \tag{3.47}$$

3.3.3 Generalization to a higher spin ensemble

Let us consider now a spin system with more than two states ($d > 2$), coming from either a magnetic ion with electronic spin $S > 1/2$ or the coupling to a nuclear spin. The results from previous sections are generalized by working in the eigenbasis $\{|\alpha\rangle\}$ of the spin Hamiltonian [14]. In this basis, the spin Hamiltonian takes the simple diagonal form of Eq. (3.15), and the Jaynes-Cummings Hamiltonian (3.33) is extended to an arbitrary spin system as:

$$\begin{aligned} H_{\mathrm{JC}} = &\sum_{\alpha=0}^{d-1} E_\alpha \hat{X}^{\alpha\alpha} + \hbar\omega_{\mathrm{r}}\hat{a}^\dagger\hat{a} \\ &+ \hbar\sum_{\alpha=0}^{d-1}\sum_{\beta>\alpha}\Big((G_1)_{\beta\alpha}\hat{X}^{\beta\alpha}\,\hat{a} + (G_1)_{\alpha\beta}\hat{X}^{\alpha\beta}\,\hat{a}^\dagger\Big), \end{aligned} \tag{3.48}$$

where $\mathbf{G_1}$ is an Hermitian matrix encoding the coupling strengths of the different transitions, and $\hat{X}^{\alpha\beta} \equiv |\alpha\rangle\langle\beta|$ are Hubbard operators, also known

[18] If the absolute values of all couplings are the same in Eq. (3.46), the definition from Eq. (3.40) is recovered.

as level-shift operators [15, Ch.I.3], a generalization of the projection operators. For instance, for $S = 1/2$ ($d = 2$): $\hat{X}^{1,0} = |1\rangle\langle 0| = |\mathrm{e}\rangle\langle \mathrm{g}| = \hat{\sigma}_+$ and $\hat{X}^{0,1} = |0\rangle\langle 1| = |\mathrm{g}\rangle\langle \mathrm{e}| = \hat{\sigma}_-$.[19]

Similarly, the Tavis-Cummings Hamiltonian (3.37) can be generalized for an ensemble of arbitrary spin systems:

$$\begin{aligned} H_{\mathrm{TC}} = & \sum_{i=1}^{N}\sum_{\alpha=0}^{d-1} E_\alpha \hat{X}_i^{\alpha,\alpha} + \hbar\omega_{\mathrm{r}}\hat{a}^\dagger\hat{a} \\ & + \hbar\sum_{i=1}^{N}\sum_{\alpha=0}^{d-1}\sum_{\beta>\alpha}\left((G_{1,\,i})_{\beta\alpha}\hat{X}_i^{\beta,\alpha}\hat{a} + (G_{1,\,i})_{\alpha\beta}\hat{X}_i^{\alpha,\beta}\hat{a}^\dagger\right), \end{aligned} \tag{3.49}$$

where all spins are assumed to have the same energy spectrum $\{E_\alpha\}$, but the spin-index dependence in the couplings $(G_{1,\,i})_{\alpha\beta}$ is kept.

3.4 Dispersive regime

Consider now the situation in which qubit and resonator have very different frequencies, hindering the exchange of excitations between them and therefore suppressing a decoherence mechanism of the qubit. This regime is known as the dispersive regime [16]. Taking the limit $|G_1/\Delta| \ll 1$ in the definition of the eigenstates of the Jaynes-Cummings Hamiltonian (3.35) gives:

$$\begin{aligned} |\psi_{n,\,+}\rangle &\simeq \begin{cases} \left|\dfrac{G_1\sqrt{n}}{\Delta}\right| |\psi_{n,\,\mathrm{g}}\rangle + |\psi_{n-1,\,\mathrm{e}}\rangle & \text{if } \Delta > 0 \\ |\psi_{n,\,\mathrm{g}}\rangle + \left|\dfrac{G_1\sqrt{n}}{\Delta}\right| |\psi_{n-1,\,\mathrm{e}}\rangle & \text{if } \Delta < 0 \end{cases} \\ |\psi_{n,\,-}\rangle &\simeq \begin{cases} |\psi_{n,\,\mathrm{g}}\rangle - \left|\dfrac{G_1\sqrt{n}}{\Delta}\right| |\psi_{n-1,\,\mathrm{e}}\rangle & \text{if } \Delta > 0 \\ \left|\dfrac{G_1\sqrt{n}}{\Delta}\right| |\psi_{n,\,\mathrm{g}}\rangle - |\psi_{n-1,\,\mathrm{e}}\rangle & \text{if } \Delta < 0\,. \end{cases} \end{aligned} \tag{3.50}$$

In resonance ($\Delta = 0$), these states were the completely hybridized qubit-resonator states from Eq. (3.36), with a decay rate $(\kappa+\gamma)/2$. Conversely, the states in Eq. (3.50) have predominantly an excitation in either the qubit or the resonator.

Let us assume $\Delta > 0$ in what follows. The state $|\psi_{n,\,+}\rangle$ becomes mainly a qubit-only excitation in the dispersive regime, while the state $|\psi_{n,\,-}\rangle$ is in

[19] Following the notation used in previous sections for the ground and excited states of a spin 1/2. Note that in that case $\mathbf{G_1}$ was already Hermitian, with $(G_1)_{10} \to G_1$ and $(G_1)_{01} \to G_1^*$

turn mainly a resonator-only excitation. Then $|\psi_{n,+}\rangle$ has a decay rate $\Gamma_{n,+} \simeq \gamma + \left(\frac{g_1\sqrt{n}}{\Delta}\right)^2 \kappa$, while $|\psi_{n,-}\rangle$ has a decay rate $\Gamma_{n,-} \simeq \kappa + \left(\frac{g_1\sqrt{n}}{\Delta}\right)^2 \gamma$, with γ and κ exchanging roles [17, 18]. $|\psi_{n,+}\rangle$ has an enhanced lifetime in the dispersive regime compared to the resonant case. This is known as the *Purcell effect* [19]. Besides, the qubit has a small influence on state $|\psi_{n,-}\rangle$. The following sections describe how the state of the qubit can be inferred by measuring its effect on $|\psi_{n,-}\rangle$.

3.4.1 Qubit coupled to a resonator

Using the rotating wave approximation, the starting point is Hamiltonian (3.33). In the dispersive regime, the spin-resonator coupling is a perturbation $\hat{V}$ of the Hamiltonian H_0 describing the two isolated systems:

$$\begin{aligned} H_{\mathrm{JC}} &\equiv H_0 + \hat{V}, \\ H_0 &= \frac{\hbar\omega_{\mathrm{q}}}{2}\hat{\sigma}_z + \hbar\omega_{\mathrm{r}}\hat{a}^\dagger\hat{a}, \\ \hat{V} &= \hbar\left(G_1\hat{\sigma}_+\hat{a} + G_1^*\hat{\sigma}_-\hat{a}^\dagger\right). \end{aligned} \tag{3.51}$$

Now, a Schrieffer-Wolff transformation $H' = e^{\hat{\theta}_{\mathrm{SW}}} H e^{-\hat{\theta}_{\mathrm{SW}}}$ is applied, changing to a basis where H becomes diagonal to first order in the perturbation $\hat{V}$. The anti-Hermitian[20] generator $\hat{\theta}_{\mathrm{SW}}$ of the transformation is chosen so as to fulfill the condition $\hat{V} + \left[\hat{\theta}_{\mathrm{SW}}, H_0\right] = 0$, obtaining [20]:

$$H' = H_0 + \frac{1}{2}\left[\hat{\theta}_{\mathrm{SW}}, \hat{V}\right] + \frac{1}{3}\left[\hat{\theta}_{\mathrm{SW}}, \left[\hat{\theta}_{\mathrm{SW}}, \hat{V}\right]\right] + ... \tag{3.52}$$

In this case, the condition is fulfilled by (note the minus sign) [16]:

$$\hat{\theta}_{\mathrm{SW}} = \frac{1}{\Delta}\left(G_1\hat{\sigma}_+\hat{a} - G_1^*\hat{\sigma}_-\hat{a}^\dagger\right), \tag{3.53}$$

where $\Delta \equiv \omega_{\mathrm{q}} - \omega_{\mathrm{r}}$ is the frequency detuning between the qubit and the resonator. In the dispersive regime, this detuning is much larger than the qubit-resonator coupling ($|G_1| \ll |\Delta|$). Therefore, the expansion of H' can be truncated to the lowest order in $\hat{\theta}_{\mathrm{SW}}$ (lowest order in G_1/Δ):

$$H' \simeq H_0 + \frac{1}{2}\left[\hat{\theta}_{\mathrm{SW}}, \hat{V}\right], \tag{3.54}$$

giving (plus an omitted constant term):[21]

$$H'_{\mathrm{JC}} \simeq \frac{\hbar}{2}\left(\omega_{\mathrm{q}} + \chi\right)\hat{\sigma}_z + \hbar\left(\omega_{\mathrm{r}} + \chi\hat{\sigma}_z\right)\hat{a}^\dagger\hat{a}, \tag{3.55}$$

[20] The generator $\hat{\theta}_{\mathrm{SW}}$ is anti-Hermitian to render $e^{\hat{\theta}_{\mathrm{SW}}}$ unitary.

[21] I used Eq. (3.54) combined with $[\hat{a}, \hat{a}^\dagger] = 1$, $[\hat{\sigma}_+, \hat{\sigma}_-] = \hat{\sigma}_z$, $2\hat{\sigma}_+\hat{\sigma}_- = \mathbb{I} + \hat{\sigma}_z$ and $2\hat{\sigma}_-\hat{\sigma}_+ = \mathbb{I} - \hat{\sigma}_z$.

with:

$$\chi := \frac{|G_1|^2}{\Delta} . \tag{3.56}$$

The term $(\omega_\mathrm{r}+\chi\hat{\sigma}_z)\hat{a}^\dagger\hat{a}$ implies that the frequency of the resonator depends on the state of the qubits: the bare resonator frequency ω_r is shifted by either $+\chi$ or $-\chi$. Thus, the state of the qubits can be inferred from a measurement of the resonator. The frequency of operation of the qubit is also shifted by the coupling: $\omega_\mathrm{q} \mapsto \omega_\mathrm{q} + \chi$. However, this shift does not depend on the state of the resonator.

Equation (3.55) is valid as long as the condition for the rotating wave approximation ($|\Delta| \ll \omega_\mathrm{q} + \omega_\mathrm{r}$) assumed in the Jaynes-Cummings model (Eq. (3.33)) is fulfilled. However, a system with a large qubit-resonator coupling requires an also large detuning to be in the dispersive regime, and this may not be a good approximation anymore. A similar derivation that is valid for the whole dispersive regime is obtained by including the counter-rotating terms from the Rabi Hamiltonian (3.32) in the perturbation $\hat{V}$ [21]:

$$\hat{V} = \hbar \left(G_1\hat{\sigma}_+ + G_1^*\hat{\sigma}_-\right)\left(a + a^\dagger\right). \tag{3.57}$$

Using the extended generator:

$$\hat{\theta}_\mathrm{SW} = \frac{1}{\Delta}\left(G_1\hat{\sigma}_+\hat{a} - G_1^*\hat{\sigma}_-\hat{a}^\dagger\right) + \frac{1}{\Delta + 2\omega_\mathrm{r}}\left(G_1\hat{\sigma}_+\hat{a}^\dagger - G_1^*\hat{\sigma}_-\hat{a}\right), \tag{3.58}$$

yields:[22]

$$H'_\mathrm{Rabi} \simeq \frac{\hbar}{2}\left(\omega_\mathrm{q} + \chi'\right)\hat{\sigma}_z + \hbar\left(\omega_\mathrm{r} + \chi'\hat{\sigma}_z\right)\hat{a}^\dagger\hat{a} + \frac{\hbar}{2}\chi'\hat{\sigma}_z\left[a^2 + (a^\dagger)^2\right], \tag{3.59}$$

with:

$$\chi' := |G_1|^2\left(\frac{1}{\Delta} + \frac{1}{\Delta + 2\omega_\mathrm{r}}\right) =: \frac{|G_1|^2}{\Delta'} . \tag{3.60}$$

Here $\Delta' = F(\Delta/\omega_\mathrm{r})\,\Delta$ is a modified detuning, with:

$$F(x) := \frac{1 + \frac{1}{2}x}{1 + x} . \tag{3.61}$$

If the cavity photons are weakly perturbed by the interaction with the spins, second-order photons processes can be neglected [14], dropping the term with a^2 and $(a^\dagger)^2$ in Hamiltonian (3.59). This leaves the same terms obtained with the rotating wave approximation, now with a modified detuning Δ' (and dispersive shift χ'). For a small detuning $\Delta \ll \omega_\mathrm{r}$ ($x = \Delta/\omega_\mathrm{r} \ll 1$), Δ' is similar to Δ. However, a very large detuning ($x \gg 1$) gives $\Delta' \simeq \Delta/2$, and the rotating wave approximation may overestimate $|G_1|$ by a factor $\sqrt{2}$.

[22] Same as for Eq. (3.55). I also used that $\hat{\sigma}_+^2 = \hat{\sigma}_-^2 = 0$.

3.4.2 Spin 1/2 ensembles

This section extends the description of the dispersive regime to ensembles of many spin 1/2 systems. Assuming the rotating wave approximation is valid, the starting point is the Tavis-Cummings Hamiltonian (3.37):

$$\begin{aligned} H_{\mathrm{TC}} &\equiv H_0 + \hat{V}, \\ H_0 &= \sum_{i=1}^{N} \frac{\hbar\omega_{\mathrm{q},\,i}}{2}\hat{\sigma}_{z,\,i} + \hbar\omega_{\mathrm{r}}\hat{a}^{\dagger}\hat{a}\,, \\ \hat{V} &= \sum_{i=1}^{N} \hbar\left(G_{1,i}\hat{\sigma}_{+,\,i}\hat{a} + G_{1,i}^{*}\hat{\sigma}_{-,\,i}\hat{a}^{\dagger}\right). \end{aligned} \tag{3.62}$$

The generator of the Schrieffer-Wolff transformation for the Tavis-Cummings Hamiltonian is [21]:

$$\hat{\theta}_{\mathrm{SW}} = \sum_{i=1}^{N} \frac{1}{\Delta_i}\left(G_{1,i}\hat{\sigma}_{+,\,i}\hat{a} - G_{1,i}^{*}\hat{\sigma}_{-,\,i}\hat{a}^{\dagger}\right), \tag{3.63}$$

where $\Delta_i \equiv \omega_{\mathrm{q},\,i} - \omega_{\mathrm{r}}$ is the frequency detuning between the qubit and the resonator. Using once more Eq. (3.54) yields the generalization to N qubits of Hamiltonian (3.55):

$$\begin{aligned} H'_{\mathrm{TC}} \simeq \frac{\hbar}{2}\sum_{i=1}^{N}\left(\omega_{\mathrm{q},\,i} + \chi_i\right)\hat{\sigma}_{z,\,i} + \hbar\left(\omega_{\mathrm{r}} + \sum_{i=1}^{N}\chi_i\hat{\sigma}_{z,\,i}\right)\hat{a}^{\dagger}\hat{a} \\ + \hbar\sum_{i=1}^{N}\sum_{j>i}\left(J_{ij}\hat{\sigma}_{+,\,i}\hat{\sigma}_{-,\,j} + J_{ij}^{*}\hat{\sigma}_{-,\,i}\hat{\sigma}_{+,\,j}\right), \end{aligned} \tag{3.64}$$

with the parameters:

$$J_{ij} := \frac{G_{1,i}G_{1,j}^{*}}{2}\left(\frac{1}{\Delta_i} + \frac{1}{\Delta_j}\right), \qquad \chi_i := J_{ii} \equiv \frac{|G_{1,i}|^2}{\Delta_i}. \tag{3.65}$$

If all qubits have roughly the same coupling $G_{1,i}$, the dispersive shift is enhanced by the number of qubits N. Also, a new term appears: a transverse exchange interaction between the qubits of strength $|J_{ij}|$ just by being coupled to the same resonator [16, 22].

As with single qubits, a Hamiltonian that is valid for the whole dispersive regime is obtained by including the counter-rotating terms in the perturbation $\hat{V}$:

$$\hat{V} = \hbar\sum_{i=1}^{N}\left(G_{1,i}\hat{\sigma}_{+,\,i} + G_{1,i}^{*}\hat{\sigma}_{-,\,i}\right)\left(a + a^{\dagger}\right). \tag{3.66}$$

The generator is now:

$$\begin{aligned}\hat{\theta}_{\mathrm{SW}} = \sum_{i=1}^{N} \Bigg[& \frac{1}{\Delta_i} \left(G_{1,i} \hat{\sigma}_{+,\,i}\, \hat{a} - G_{1,i}^{*} \hat{\sigma}_{-,\,i}\, \hat{a}^{\dagger} \right) \\ & + \frac{1}{\Delta_i + 2\omega_{\mathrm{r}}} \left(G_{1,i} \hat{\sigma}_{+,\,i}\, \hat{a}^{\dagger} - G_{1,i}^{*} \hat{\sigma}_{-,\,i}\, \hat{a} \right) \Bigg],\end{aligned} \tag{3.67}$$

giving:

$$\begin{aligned}H' \simeq & \frac{\hbar}{2} \sum_{i=1}^{N} \left(\omega_{\mathrm{q},\,i} + \chi_i' \right) \hat{\sigma}_{z,\,i} + \hbar \Big(\omega_{\mathrm{r}} + \sum_{i=1}^{N} \chi_i' \hat{\sigma}_{z,\,i} \Big) \hat{a}^{\dagger} \hat{a} \\ & + \frac{\hbar}{2} \sum_{i=1}^{N} \chi_i' \hat{\sigma}_{z,\,i} \left[a^2 + (a^{\dagger})^2 \right] + 4\hbar \sum_{i=1}^{N} \sum_{j>i} \left(2J_{ij} - J_{ij}' \right) \hat{\sigma}_{x',\,i}(\varphi_i)\, \hat{\sigma}_{x',\,j}(\varphi_j)\end{aligned}, \tag{3.68}$$

with:

$$\hat{\sigma}_{x',\,i}(\varphi_i) := \cos(\varphi_i)\, \hat{\sigma}_{x,\,i} - \sin(\varphi_i)\, \hat{\sigma}_{y,\,i} \qquad , \qquad G_{1,i} := |G_{1,i}| e^{i\varphi_i}, \tag{3.69}$$

and:

$$\begin{aligned}J_{ij} &:= \frac{|G_{1,i}||G_{1,j}|}{2} \left(\frac{1}{\Delta_i} + \frac{1}{\Delta_j} \right), \\ J_{ij}' &:= \frac{|G_{1,i}||G_{1,j}|}{2} \left(\frac{1}{\Delta_i} + \frac{1}{\Delta_j} + \frac{1}{\Delta_i + 2\omega_{\mathrm{r}}} + \frac{1}{\Delta_j + 2\omega_{\mathrm{r}}} \right) \\ &=: \frac{|G_{1,i}||G_{1,j}|}{2} \left(\frac{1}{\Delta_i'} + \frac{1}{\Delta_j'} \right), \\ \chi_i' &:= J_{ii}' = |G_{1,i}|^2 \left(\frac{1}{\Delta_i} + \frac{1}{\Delta_i + 2\omega_{\mathrm{r}}} \right) =: \frac{|G_{1,i}|^2}{\Delta_i'}.\end{aligned} \tag{3.70}$$

Here a modified detuning $\Delta_i' := F(\Delta_i/\omega_{\mathrm{r}})\, \Delta_i$ was defined for each qubit (recall the definition of $F(x)$ in Eq. 3.61)).

Equation (3.68) is similar to the single qubit Hamiltonian (3.59), but with an enhanced dispersive shift and a qubit-qubit interaction mediated by the resonator. As in the single qubit case, the use of the rotating wave approximation changes the dispersive shift. The type of photon-mediated spin-spin interactions is also different [21].[23]

[23] An isotropic XY interaction in Eq. (3.64) if the rotating wave approximation is assumed. An 'Ising-like' interaction in Eq. (3.68) without it.

3.4.3 Generalization to higher spin systems

For a higher spin system ($d > 2$), only a single qudit is considered in order to simplify the calculation (see Eq. (3.48)). The previous section already showed that the effect of having multiple particles is that the total dispersive shift increases linearly with the number of spins, N, and that these N spins are effectively coupled through the resonator.

A qudit with d states can have up to $d(d-1)$ different non-zero transition frequencies (positive and negative), and up to the same number of detunings from the resonator frequency ω_r. For the transition between states $|\alpha\rangle$ and $|\beta\rangle$, this detuning is:

$$\Delta_{\alpha\beta} = \frac{E_\alpha - E_\beta}{\hbar} - \omega_\mathrm{r}. \tag{3.71}$$

In general, the condition for the rotating wave approximation will not hold simultaneously for all transitions. The ensemble-resonator coupling of Eq. (3.48) must be rewritten to include the counter-rotating terms:

$$\hat{V} = \hbar \sum_{\alpha=0}^{d-1} \sum_{\beta\neq\alpha} \Lambda_{\alpha\beta} \hat{X}^{\alpha,\beta} \left(a + a^\dagger \right), \tag{3.72}$$

with $\Lambda_{\alpha\beta}$ Hermitian. The generator of the Schrieffer-Wolff transformation is now [14]:

$$\hat{\theta}_\mathrm{SW} = \sum_{\alpha=0}^{d-1} \sum_{\beta\neq\alpha} \Lambda_{\alpha\beta} \hat{X}^{\alpha,\beta} \left(\frac{1}{\Delta_{\alpha\beta}} \hat{a} + \frac{1}{\Delta_{\alpha\beta} + 2\omega_\mathrm{r}} \hat{a}^\dagger \right), \tag{3.73}$$

and one obtains:

$$\begin{aligned} H' \simeq & \sum_{\alpha=0}^{d-1} E_\alpha \hat{X}^{\alpha,\alpha} + \hbar\omega_\mathrm{r} \hat{a}^\dagger \hat{a} \\ & + \hbar \sum_{\alpha=0}^{d-1} \sum_{\beta_1\neq\alpha} \sum_{\beta_2\neq\alpha} \left(J_{\alpha\beta_1\beta_2} + J'_{\alpha\beta_1\beta_2} \hat{a}^\dagger \hat{a} \right) \hat{X}^{\beta_1,\beta_2} \\ & + \frac{\hbar}{2} \sum_{\alpha=0}^{d-1} \sum_{\beta_1\neq\alpha} \sum_{\beta_2\neq\alpha} \left(\frac{1}{\Delta_{\beta_1\alpha}} + \frac{1}{\Delta_{\beta_2\alpha} + 2\omega_\mathrm{r}} \right) \left(\Lambda_{\beta_1\alpha} \Lambda_{\alpha\beta_2} \hat{a}^2 \hat{X}^{\beta_1,\beta_2} + \mathrm{h.c.} \right). \end{aligned} \tag{3.74}$$

Here I defined the parameters:

$$\begin{aligned} J_{\alpha\beta_1\beta_2} :=& \frac{\Lambda_{\beta_1\alpha}\Lambda_{\alpha\beta_2}}{2}\left(\frac{1}{\Delta_{\beta_1\alpha}}+\frac{1}{\Delta_{\beta_2\alpha}}\right), \\ J'_{\alpha\beta_1\beta_2} :=& \frac{\Lambda_{\beta_1\alpha}\Lambda_{\alpha\beta_2}}{2}\left(\frac{1}{\Delta_{\beta_1\alpha}}+\frac{1}{\Delta_{\beta_2\alpha}}+\frac{1}{\Delta_{\beta_1\alpha}+2\omega_\mathrm{r}}+\frac{1}{\Delta_{\beta_2\alpha}+2\omega_\mathrm{r}}\right) \\ =:& \frac{\Lambda_{\beta_1\alpha}\Lambda_{\alpha\beta_2}}{2}\left(\frac{1}{\Delta'_{\beta_1\alpha}}+\frac{1}{\Delta'_{\beta_2\alpha}}\right), \end{aligned} \tag{3.75}$$

with the modified detunings $\Delta'_{\beta\alpha} := F(\Delta_{\beta\alpha}/\omega_\mathrm{r})\,\Delta_{\beta\alpha}$.

An ensemble weakly perturbed by the interaction with the cavity can be described by keeping only the dominant diagonal terms with $\hat{a}^\dagger\hat{a}$ over $\hat{a}^2$ or $(\hat{a}^\dagger)^2$, and with $\beta_1 = \beta_2$:

$$H' \simeq \sum_{\alpha=0}^{d-1}(E_\alpha+\chi_\alpha)\,\hat{X}^{\alpha,\alpha} + \hbar\left(\omega_\mathrm{r}+\sum_{\alpha=0}^{d-1}\chi'_\alpha\hat{X}^{\alpha,\alpha}\right)\hat{a}^\dagger\hat{a}\,, \tag{3.76}$$

with the dispersive shifts χ_α and χ'_α defined in terms of $J_{\alpha\beta_1\beta_2}$ and $J'_{\alpha\beta_1\beta_2}$:

$$\begin{aligned} \chi_\alpha &:= \sum_{\beta\neq\alpha}\frac{|\Lambda_{\alpha\beta}|^2}{\Delta_{\alpha\beta}} = \sum_{\beta\neq\alpha} J_{\beta\alpha\alpha}\,, \\ \chi'_\alpha &:= \sum_{\beta\neq\alpha}\frac{|\Lambda_{\alpha\beta}|^2}{\Delta'_{\alpha\beta}} = \sum_{\beta\neq\alpha} J'_{\beta\alpha\alpha}\,. \end{aligned} \tag{3.77}$$

The results obtained for a qubit in section 3.4.1 are retrieved by taking $d = 2$ (which implies that $\beta_1 = \beta_2$) and following the definitions for a spin 1/2: $\hat{X}^{1,0} = \hat{\sigma}_+$, $\Lambda_{1,0} = G_1$, $\omega_\mathrm{q} = \frac{E_1-E_0}{\hbar}$.

References

[1] A. Abragam and B. Bleaney, *Electron paramagnetic resonance of transition ions* (Oxford University Press, 1970).

[2] S. Stoll, *EasySpin documentation*, `https://easyspin.org/easyspin/documentation/index.html`.

[3] A. Schweiger and G. Jeschke, *Principles of pulse electron paramagnetic resonance* (Oxford University Press, 2001).

[4] S. Haroche and J.-M. Raimond, *Exploring the quantum: atoms, cavities and photons* (Oxford University Press, 2006).

[5] J. García Ripoll, *Quantum information and quantum optics* (Cambridge University Press, 2022).

[6] I. Gimeno Alonso, Ph.D. thesis, Universidad de Zaragoza (2023).

[7] J. H. Wesenberg, A. Ardavan, G. A. D. Briggs, J. J. L. Morton, R. J. Schoelkopf, D. I. Schuster, and K. Mølmer, Physical Review Letters **103**, 070502 (2009).

[8] M. Jenkins, T. Hümmer, M. J. Martínez-Pérez, J. García-Ripoll, D. Zueco, and F. Luis, New Journal of Physics **15**, 095007 (2013).

[9] S. M. Barnett and P. M. Radmore, *Methods in theoretical quantum optics* (Oxford Science Publications, 1997).

[10] M. Tavis and F. W. Cummings, Physical Review **170**, 379 (1968).

[11] P. Kirton, M. M. Roses, J. Keeling, and E. G. Dalla Torre, Advanced Quantum Technologies **2**, 1800043 (2019).

[12] D. I. Khomskii, *Basic aspects of the theory of the quantum theory of solids: order and elementary excitations* (Cambridge University Press, 2010).

[13] T. Hümmer, G. M. Reuther, P. Hänggi, and D. Zueco, Physical Review A **85**, 052320 (2012).

[14] A. Gómez-León, F. Luis, and D. Zueco, Physical Review Applied **17**, 064030 (2022).

[15] D. Gamliel and H. Levanon, *Stochastic processes in magnetic resonance* (World Scientific, 1995).

[16] A. Blais, R.-S. Huang, A. Wallraff, S. M. Girvin, and R. J. Schoelkopf, Physical Review A **69**, 062320 (2004).

[17] M. Boissonneault, J. M. Gambetta, and A. Blais, Physical Review A **79**, 013819 (2009).

[18] G. M. Reuther, D. Zueco, F. Deppe, E. Hoffmann, E. P. Menzel, T. Weißl, M. Mariantoni, S. Kohler, A. Marx, E. Solano, et al., Physical Review B **81**, 144510 (2010).

[19] E. M. Purcell, H. C. Torrey, and R. V. Pound, Physical Review **69**, 37 (1946).

[20] J. R. Schrieffer and P. A. Wolff, Physical Review **149**, 491 (1966).

[21] D. Zueco, G. M. Reuther, S. Kohler, and P. Hänggi, Physical Review A **80**, 033846 (2009).

[22] J. Majer, J. M. Chow, J. M. Gambetta, J. Koch, B. R. Johnson, J. A. Schreier, L. Frunzio, D. I. Schuster, A. A. Houck, A. Wallraff, et al., Nature **449**, 443 (2007).

Chapter 4

Measurement of the quantum processor

The quantum processor described in the previous chapter is not completely isolated: it interacts with its environment. In particular, a description of its interaction with the microwave photons that are sent through the transmission line to measure the properties of the circuit is needed. This is the focus of this chapter.

First, a brief description of the transmission line is given in section 4.1. Input-output theory (section 4.2) relates the signals that are sent through the line to the evolution of some coupled quantum system. The effect of the transmission line in this evolution is modeled with a quantum master equation (section 4.3). In the remaining sections, this formalism is applied to different quantum systems, from lumped-element resonators to spin ensembles.

4.1 Transmission line

A coplanar transmission line consists of a central line with a ground plane at each side (see Fig. 4.1). This is modeled as two parallel conductors — central line and ground — with voltages and currents varying in magnitude and phase over their length. An infinitesimal piece of this conductor pair, with length Δz, can be treated as a lumped element with infinitesimal changes in voltage and current (see Fig. 4.2). Each of these pieces is assigned a series resistance and inductance, and shunt conductance and capacitance per unit length.

In a superconducting line, the series resistance and shunt conductance can be considered to be small, and it can be described by an ideal lossless line. This is modeled with a series inductance l per unit length, representing the

total self-inductance of the two conductors, and a shunt capacitance c per unit length between them if they are in close proximity (see Fig. 4.2). The impedance of this line is $Z_0 = \sqrt{l/c}$.

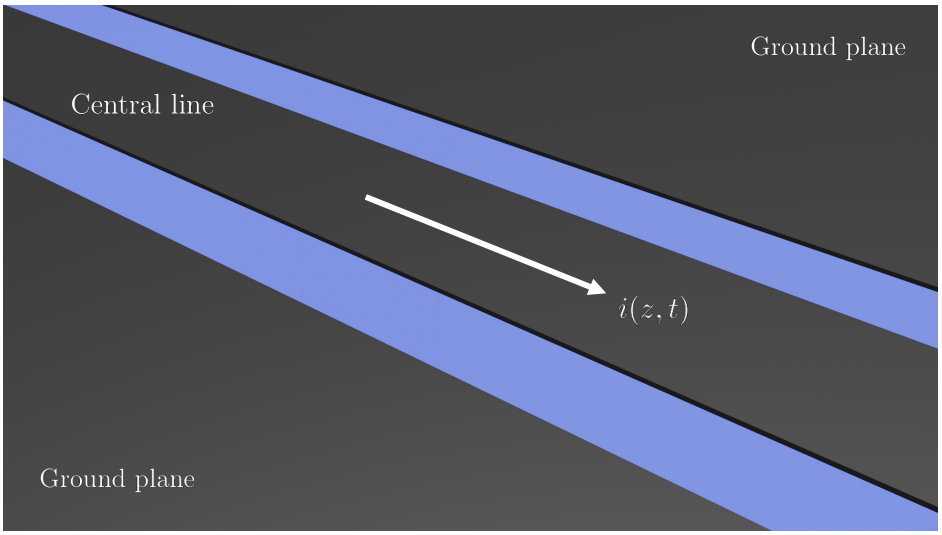

Figure 4.1: Drawing of a superconducting transmission line. The central line and the ground planes at the sides are made of a superconducting material deposited on top of an isolating substrate (blue).

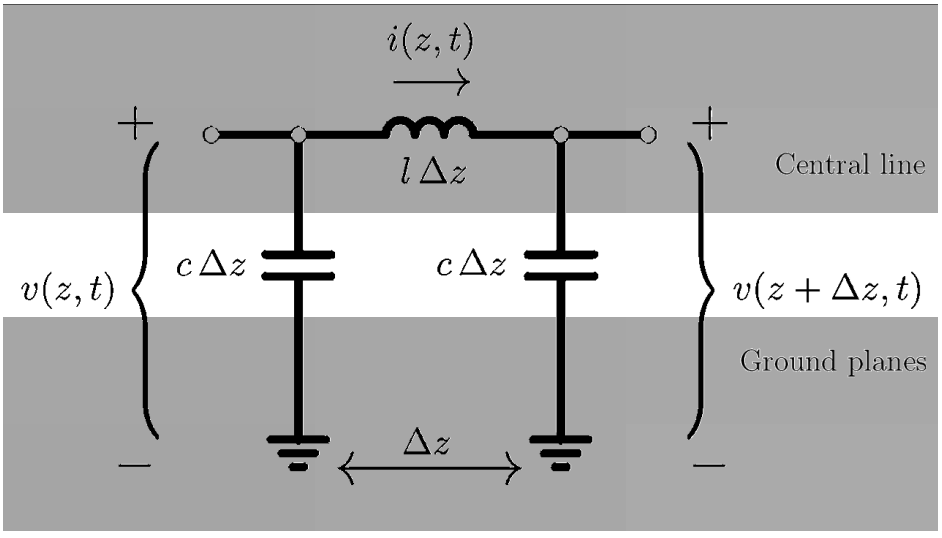

Figure 4.2: Lumped element circuit representing an infinitesimal segment of the transmission line of Fig. 4.1.

4.1.1 The classical transmission line

The Kirchhoff's voltage and current laws for each lumped element are:

$$\begin{aligned} v(z,t) - l\,\Delta z\,\frac{\partial i(z,t)}{\partial t} - v(z+\Delta z,t) = 0, \\ i(z,t) - c\,\Delta z\,\frac{\partial v(z+\Delta z,t)}{\partial t} - i(z+\Delta z,t) = 0. \end{aligned} \tag{4.1}$$

Taking the limit $\Delta z \to 0$ yields a pair of differential equations — the telegrapher equations of a lossless line — for voltage and current in the line:

$$\begin{aligned} \frac{\partial v(z,t)}{\partial z} &= -l\,\frac{\partial i(z,t)}{\partial t}, \\ \frac{\partial i(z,t)}{\partial z} &= -c\,\frac{\partial v(z,t)}{\partial t}, \end{aligned} \tag{4.2}$$

which for solutions of the form $v(z,t) = V(z)e^{i\omega t}$ and $i(z,t) = I(z)e^{i\omega t}$ gives:

$$\begin{aligned} \frac{\partial^2 V(z)}{\partial z^2} &= -|k|^2\,V(z), \\ \frac{\partial^2 I(z)}{\partial z^2} &= -|k|^2\,I(z), \end{aligned} \tag{4.3}$$

where $|k| = \omega\sqrt{lc}$ is the wave vector modulus. This means that the one-dimensional line has two solutions with $\pm|k|$ and phase velocity $v_\mathrm{p} = \pm\omega/|k| = \pm 1/\sqrt{lc}$ for each frequency ω.

Kirchhoff's laws (Eq. (4.1)) can be rewritten in terms of the flux $\phi(z,t)$ and the charge $q(z,t)$, which are related to $v(z,t) = \dot{\phi}(z,t)$ and $i(z,t) = \dot{q}(z,t)$, by integrating in time the voltage law, and then combined into a single equation for $\phi(z,t)$:

$$\ddot{\phi}(z,t) = \left(\frac{v_\mathrm{p}}{\Delta z}\right)^2 \Big\{\,[\phi(z+\Delta z,t) - \phi(z,t)] + [\phi(z-\Delta z,t) - \phi(z,t)]\,\Big\}. \tag{4.4}$$

This is just the discrete version of a wave equation for $\phi(z,t)$ with phase velocity v_p:

$$\frac{\partial^2 \phi(z,t)}{\partial t^2} = v_\mathrm{p}^2\,\frac{\partial^2 \phi(z,t)}{\partial z^2}. \tag{4.5}$$

Defining $\phi_n(t) = \phi(z,t)$ and $\phi_{n\pm1}(t) = \phi(z \pm \Delta z, t)$, Eq. (4.4) is now:

$$\ddot{\phi}_n(t) = \left(\frac{v_\mathrm{p}}{\Delta z}\right)^2 \Big\{\,[\phi_{n+1}(t) - \phi_n(t)] + [\phi_{n-1}(t) - \phi_n(t)]\,\Big\}. \tag{4.6}$$

These are the equations of motion that can be derived from the Lagrangian L_{B} or Hamiltonian H_{B} of an array of N coupled resonators with periodic boundary conditions ($\phi_{N+1} = \phi_1$):

$$\begin{aligned} L_{\mathrm{B}} &= \frac{1}{2}\, c\, \Delta z \sum_{n=1}^{N} \dot{\phi}_n^2 - \frac{1}{2}\, \frac{1}{l\, \Delta z} \sum_{n=1}^{N} (\phi_{n+1} - \phi_n)^2 \,, \\ H_{\mathrm{B}} &= \frac{1}{2}\, \frac{1}{c\, \Delta z} \sum_{n=1}^{N} q_n^2 + \frac{1}{2}\, \frac{1}{l\, \Delta z} \sum_{n=1}^{N} (\phi_{n+1} - \phi_n)^2 \,, \end{aligned} \tag{4.7}$$

where the charge $q_n := \partial\, L_{\mathrm{B}} / \partial \dot{\phi}_n$ is the conjugate canonical variable of the flux ϕ_n.

Let us consider the limit $\Delta z \to 0$. The charge density $\rho(z)$ is defined as:

$$\rho(z) := \lim_{\Delta z \to 0} \frac{q_n}{\Delta z}. \tag{4.8}$$

Taking the limit $\Delta z \to 0$ in Eq. (4.7) gives [1, Ch.11]:[1]

$$\begin{aligned} L_{\mathrm{B}} &= \int dz\, \mathcal{L}_{\mathrm{B}}(z) = \int dz \left[\frac{1}{2}\, c\, \dot{\phi}^2(z) - \frac{1}{2l} \left(\frac{\partial \phi(z)}{\partial z} \right)^2 \right], \\ H_{\mathrm{B}} &= \int dz\, \mathcal{H}_{\mathrm{B}}(z) = \int dz \left[\frac{1}{2c} \rho^2(z) + \frac{1}{2l} \left(\frac{\partial \phi(z)}{\partial z} \right)^2 \right], \end{aligned} \tag{4.9}$$

where $\mathcal{L}_{\mathrm{B}}(z)$ and $\mathcal{H}_{\mathrm{B}}(z)$ are the Lagrange and Hamilton densities. $\phi(z)$ and $\rho(z)$ are canonically conjugate fields related by $\rho(z) = \delta\, L_{\mathrm{B}} / \delta \dot{\phi}(z)$.[2]

4.1.2 Quantization of the transmission line

The quantization of the LC resonator was described in section 3.2.2. Similarly, here the pairs of conjugate canonical variables ϕ_n and q_n are promoted to pairs of non-commuting operators $\hat{\phi}_n$ and $\hat{q}_n$ with $[\hat{\phi}_m, \hat{q}_n] = i\hbar\delta_{mn}$. In the limit $\Delta z \to 0$, the pair of $\hat{\phi}(z)$ and $\hat{\rho}(z)$ fulfills that $[\hat{\phi}(z), \hat{q}(z')] = i\hbar\delta(z - z')$,[3]

[1] Rewrite L_{B} and H_{B} in Eq. (4.7) in terms of $\dot{\phi}_n$, $(\phi_{n+1} - \phi_n)/\Delta z$ and $q_n/\Delta z$. This leaves a factor Δz inside the sums in n. Taking the limit $\Delta z \to 0$ gives $\sum_n (\Delta z) \to \int dz$ and: $\dot{\phi}_n \to \dot{\phi}(z)$, $\quad \frac{\phi_{n+1} - \phi_n}{\Delta z} \to \frac{\partial \phi(z)}{\partial z}$, $\quad \frac{q_n}{\Delta z} \to \rho(z)$.

[2] $\frac{\delta\, L_{\mathrm{B}}}{\delta \dot{\phi}(z)}$ is a functional derivative, defined as $\lim_{\Delta z \to 0} \left(\frac{L_{\mathrm{B}}[\dot{\phi}(z + \Delta z)] - L_{\mathrm{B}}[\dot{\phi}(z)]}{\Delta z} \right)$.

[3] $[\hat{\phi}(z), \hat{\rho}(z')] = \lim_{\Delta z \to 0} \left[\hat{\phi}_m, \frac{\hat{q}_n}{\Delta z} \right] = \lim_{\Delta z \to 0} \left(i\hbar \frac{\delta_{mn}}{\Delta z} \right) = i\hbar\delta(z - z')$.

and the Hamilton density $\mathcal{H}_{\mathrm{B}}(z)$ reads:

$$\mathcal{H}_{\mathrm{B}}(z) = \frac{1}{2c}\hat{\rho}^2(z) + \frac{1}{2l}\left(\frac{\partial\hat{\phi}(z)}{\partial z}\right)^2. \tag{4.10}$$

Let us define the Fourier transforms of the field operators $\hat{\phi}(z)$ and $\hat{\rho}(z)$:

$$\hat{\phi}_k := \frac{1}{\sqrt{L}}\int_0^l dz\, e^{ikz}\hat{\phi}(z), \qquad \hat{\rho}_k := \frac{1}{\sqrt{L}}\int_0^l dz\, e^{-ikz}\hat{q}(z), \tag{4.11}$$

where $L = N\Delta z$ is the length of the line. Then:

$$\hat{\phi}(z) = \frac{1}{\sqrt{L}}\sum_k e^{-ikz}\hat{\phi}_k, \qquad \hat{q}(z) = \frac{1}{\sqrt{L}}\sum_k e^{ikz}\hat{\rho}_k, \tag{4.12}$$

with $k = 2\pi m/L$, where m is an integer. Inserting the definitions of Eq. (4.12) in Eq. (4.10) gives a Hamiltonian that is a sum of independent oscillators with different k:

$$H_{\mathrm{B}} = \int \mathrm{d}\, z\ \mathcal{H}_{\mathrm{B}}(z) = \sum_k \left(\frac{1}{2c}\hat{\rho}_k\hat{\rho}_{-k} + \frac{1}{2l}k^2\hat{\phi}_k\hat{\phi}_{-k}\right). \tag{4.13}$$

The creation and annihilation operators $\hat{a}_k^\dagger$ and $\hat{a}_k$ can be defined for each oscillator:

$$\hat{a}_k := \sqrt{\frac{|k|}{2\hbar Z_0}}\left(\hat{\phi}_k + i\frac{Z_0}{|k|}\hat{\rho}_{-k}\right), \qquad \hat{a}_k^\dagger := \sqrt{\frac{|k|}{2\hbar Z_0}}\left(\hat{\phi}_{-k} - i\frac{Z_0}{|k|}\hat{\rho}_k\right), \tag{4.14}$$

to obtain:

$$H_{\mathrm{B}} = \sum_k \hbar\omega_k\, \hat{a}_k^\dagger\hat{a}_k + \text{constant}. \tag{4.15}$$

The sum in k includes positive and negative wave numbers. Each pair $+|k|$, $-|k|$ shares the same positive frequency $\omega_k = |k|/\sqrt{lc}$. Then the sum in k can be rewritten as a sum in frequency:[4]

$$H_{\mathrm{B}} = \sum_\omega \hbar\omega\, \left(\hat{r}_\omega^\dagger\hat{r}_\omega + \hat{l}_\omega^\dagger\hat{l}_\omega\right) + \text{constant}, \tag{4.16}$$

where the subscript k in ω_k has been dropped. Hamiltonian (4.16) distinguishes between right- ($\hat{a}_k \to \hat{r}_\omega$, $k > 0$) and left-moving ($\hat{a}_k \to \hat{l}_\omega$, $k < 0$) photons with different operators to highlight that they commute ($[\hat{r}_\omega, \hat{l}_\omega^\dagger] = [\hat{a}_k, \hat{a}_{-k}^\dagger] =$

[4]The constant in H_{B} (the zero-point energy) diverges because there are infinitely many modes. This does not matter in an experiment, where only energy differences are measured [2, Ch.4].

0): the two types of photons have the same frequency but opposite momentum, therefore they are represented by different quantum states.

An infinite transmission line will have all possible values for k (and ω) instead of just those that fulfill the condition $k = 2\pi m/L$. Then, the sum in Eq. (4.16) is replaced by an integral over ω:[5]

$$H_{\mathrm{B}} = \int \mathrm{d}\,\omega\,\hbar\omega\,\left(\hat{r}_\omega^\dagger \hat{r}_\omega + \hat{l}_\omega^\dagger \hat{l}_\omega\right) + \text{constant}. \tag{4.17}$$

4.2 Input-output theory

In the superconducting chip, the transmission line is coupled to a quantum system like a superconducting resonator or an ensemble of magnetic molecules (see Fig. 4.3a). This quantum system is probed by sending photons through the line, which are scattered by the system. The effect that this has on the dynamics of the outgoing photons in the system-line setup is obtained by measuring the transmission and reflection of the chip.

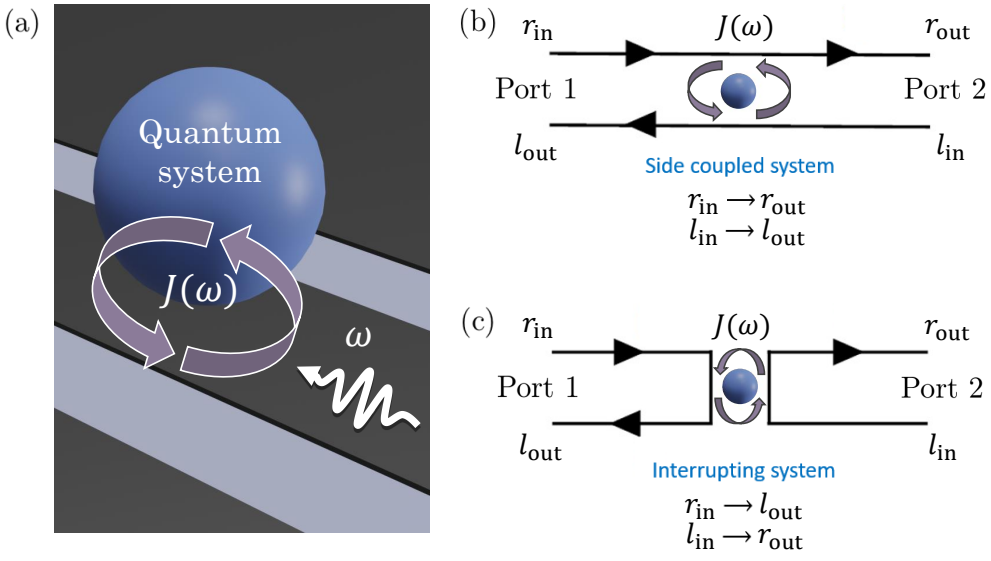

Figure 4.3: (a) Drawing of a quantum system coupled to a transmission line with a spectral function $J(\omega)$. (b, c) Input-output for (b) side coupled and (c) interrupting systems. Note that in the case of interrupting systems the roles of $\langle \hat{r}_{\mathrm{out}} \rangle$ and $\langle \hat{l}_{\mathrm{out}} \rangle$ are exchanged in Eq. (4.24). Lumped-element resonators read out via a transmission line are an example of a side coupled system.

[5] With $\hat{r}_\omega$ and $\hat{l}_\omega$ redefined as $\lim_{\Delta\omega\to 0}\left(\frac{\hat{r}_\omega}{\Delta\omega}\right)$ and $\lim_{\Delta\omega\to 0}\left(\frac{\hat{l}_\omega}{\Delta\omega}\right)$.

The general Hamiltonian describing a quantum system and a discrete collection of resonant modes in waveguide, with an interaction between the two subsystems, can be written as:

$$\begin{aligned} H &= H_{\mathrm{S}} + H_{\mathrm{B}} + H_1 \\ &= H_{\mathrm{S}} + \sum_n \hbar\omega_n \left(\hat{r}^\dagger_{\omega_n}\hat{r}_{\omega_n} + \hat{l}^\dagger_{\omega_n}\hat{l}_{\omega_n}\right) + \hbar\hat{S}\sum_n G_1(\omega_n)\left(\hat{r}^\dagger_{\omega_n} + \hat{l}^\dagger_{\omega_n} + \hat{r}_{\omega_n} + \hat{l}_{\omega_n}\right), \end{aligned} \tag{4.18}$$

where the index n labels the modes (ω_n) of the waveguide. $\hat{S}$ is the system coupling operator, with a non-chiral — the same for both types of photons — coupling $G_1(\omega_n)$.[6] In the continuous limit, a spectral function $J(\omega)$ is defined [3, Ch.17]:[7]

$$J(\omega) = \lim_{\Delta\omega\to 0}\left(\frac{1}{\Delta\omega}\sum_{\omega<\omega_n<\omega+\Delta\omega}|G_1(\omega_n)|^2\right). \tag{4.19}$$

With this definition, the continuous limit of Eq. (4.18) reads:

$$\begin{aligned} H &= H_{\mathrm{S}} + H_{\mathrm{B}} + H_1 \\ &= H_{\mathrm{S}} + \int \mathrm{d}\,\omega\ \hbar\omega\left(\hat{r}^\dagger_\omega\hat{r}_\omega + \hat{l}^\dagger_\omega\hat{l}_\omega\right) + \hbar\hat{S}\int \mathrm{d}\,\omega\ \sqrt{J(\omega)}\left(\hat{r}^\dagger_\omega + \hat{l}^\dagger_\omega + \hat{r}_\omega + \hat{l}_\omega\right), \end{aligned} \tag{4.20}$$

4.2.1 Input-output relations

The time evolution of the expectation values of $\hat{r}_\omega$ and $\hat{l}_\omega$ are computed assuming decoupled initial conditions:

$$\begin{aligned} \frac{\mathrm{d}}{\mathrm{d}\,t}\langle\hat{r}_\omega\rangle(t) &= -i\omega\langle\hat{r}_\omega\rangle(t) - i\sqrt{J(\omega)}\langle\hat{S}\rangle(t), \\ \frac{\mathrm{d}}{\mathrm{d}\,t}\langle\hat{l}_\omega\rangle(t) &= -i\omega\langle\hat{l}_\omega\rangle(t) - i\sqrt{J(\omega)}\langle\hat{S}\rangle(t). \end{aligned} \tag{4.21}$$

The solutions to these equations are:

$$\begin{aligned} \langle\hat{r}_\omega\rangle(t_1)e^{i\omega t_1} &= \langle\hat{r}_\omega\rangle(t_0)e^{i\omega t_0} - i\sqrt{J(\omega)}\int_{t_0}^{t_1}\mathrm{d}\,\tau\langle\hat{S}\rangle(\tau)e^{i\omega\tau}, \\ \langle\hat{l}_\omega\rangle(t_1)e^{i\omega t_1} &= \langle\hat{l}_\omega\rangle(t_0)e^{i\omega t_0} - i\sqrt{J(\omega)}\int_{t_0}^{t_1}\mathrm{d}\,\tau\langle\hat{S}\rangle(\tau)e^{i\omega\tau}, \end{aligned} \tag{4.22}$$

where t_0 marks the time in which the incident wave packet is injected in the line, and t_1 is any time after the interaction between the wave packet and

[6] The subscript in $G_1(\omega_n)$ indicates that it is the coupling for a single system, similar to the single spin-resonator coupling that was derived in section 3.3 of chapter 3.

[7] In reference [3, Ch.17] the spectral function $J(\omega)$ is called the 'strength function' $g(\omega)$.

the scatterers has already occurred. The expectation values of the input and output fields are defined as [4, Ch.3]:

$$\begin{aligned}
\langle \hat{r}_{\rm in}\rangle(t) &:= \int_0^\infty \frac{\mathrm{d}\,\omega}{\sqrt{2\pi}} \langle \hat{r}_\omega\rangle(t_0) e^{-i\omega(t-t_0)},\\
\langle \hat{l}_{\rm in}\rangle(t) &:= \int_0^\infty \frac{\mathrm{d}\,\omega}{\sqrt{2\pi}} \langle \hat{l}_\omega\rangle(t_0) e^{-i\omega(t-t_0)},\\
\langle \hat{r}_{\rm out}\rangle(t) &:= \int_0^\infty \frac{\mathrm{d}\,\omega}{\sqrt{2\pi}} \langle \hat{r}_\omega\rangle(t_1) e^{-i\omega(t-t_1)},\\
\langle \hat{l}_{\rm out}\rangle(t) &:= \int_0^\infty \frac{\mathrm{d}\,\omega}{\sqrt{2\pi}} \langle \hat{l}_\omega\rangle(t_1) e^{-i\omega(t-t_1)}.
\end{aligned} \tag{4.23}$$

Then, taking $t_0 \to -\infty$ and $t_1 \to \infty$, Eq. (4.22) reads:

$$\begin{aligned}
\langle \hat{r}_{\rm out}\rangle(t) &= \langle \hat{r}_{\rm in}\rangle(t) - i\int_0^\infty \frac{\mathrm{d}\,\omega}{\sqrt{2\pi}} e^{-i\omega t}\sqrt{J(\omega)} \int_{-\infty}^\infty \mathrm{d}\,\tau e^{i\omega\tau}\langle \hat{S}\rangle(\tau),\\
\langle \hat{l}_{\rm out}\rangle(t) &= \langle \hat{l}_{\rm in}\rangle(t) - i\int_0^\infty \frac{\mathrm{d}\,\omega}{\sqrt{2\pi}} e^{-i\omega t}\sqrt{J(\omega)} \int_{-\infty}^\infty \mathrm{d}\,\tau e^{i\omega\tau}\langle \hat{S}\rangle(\tau).
\end{aligned} \tag{4.24}$$

Equation (4.24) is a central result, linking the input and output fields through the dynamics of the operator $\hat{S}$ that describes a system that is side coupled to the transmission line. If the system interrupts the line, then the roles of $\langle \hat{r}_{\rm out}\rangle$ and $\langle \hat{l}_{\rm out}\rangle$ are exchanged (see Figs. 4.3b-c).

Port 1 in Figs. 4.3b-c is the input port. The scattering parameters S_{21} (transmission) and S_{11} (reflection) from Eq. (2.1) in chapter 2 can be written in terms of the input and output fields as:

$$S_{21}(t) := \frac{\langle \hat{r}_{\rm out}\rangle(t)}{\langle \hat{r}_{\rm in}\rangle(t)}, \qquad S_{11}(t) := \frac{\langle \hat{l}_{\rm out}\rangle(t)}{\langle \hat{r}_{\rm in}\rangle(t)}, \tag{4.25}$$

with $\langle \hat{l}_{\rm in}\rangle(t) = 0$ (no input in port 2). Then, from Eq. (4.24) it follows that $S_{21} = 1 + S_{11}$.

4.2.2 Coherent drive

A simple form of the input-output relations in Eq. (4.24) is obtained if the input field is a coherent drive of frequency $\omega_{\rm d}$:

$$\langle \hat{r}_{\rm in}\rangle(t) = \alpha_{\rm in} e^{-i\omega_{\rm d} t}. \tag{4.26}$$

The coupling of $\hat{S}$ to this field is:[8]

$$H_1 = \hbar\,\hat{S}\left(\sqrt{2\pi J(\omega_{\rm d})}\alpha_{\rm in} e^{-i\omega_{\rm d} t}\right). \tag{4.27}$$

[8] Comparing with the coupling term in Hamiltonian (4.20), note the $\sqrt{2\pi}$ factor here from the definition of the input fields in Eq. (4.23).

Once the transient state of $\langle \hat{S} \rangle$ decays, only the driven state remains:

$$\langle \hat{S} \rangle(t) \simeq \chi_{\hat{S}}(\omega_{\mathrm{d}}) \sqrt{2\pi J(\omega_{\mathrm{d}})} \alpha_{\mathrm{in}} e^{-i\omega_{\mathrm{d}} t}, \tag{4.28}$$

where the susceptibility $\chi_{\hat{S}}(\omega_{\mathrm{d}})$ encodes the frequency dependence of the system response to the coherent driving. Inserting this expression for $\langle \hat{S} \rangle(t)$ in the input-output relations yields:

$$\begin{aligned} \langle \hat{r}_{\mathrm{out}} \rangle(t) &= \langle \hat{r}_{\mathrm{in}} \rangle(t) - 2\pi J(\omega_{\mathrm{d}}) \chi_{\hat{S}}(\omega_{\mathrm{d}}) \langle \hat{r}_{\mathrm{in}} \rangle(t), \\ \langle \hat{l}_{\mathrm{out}} \rangle(t) &= \langle \hat{l}_{\mathrm{in}} \rangle(t) - 2\pi J(\omega_{\mathrm{d}}) \chi_{\hat{S}}(\omega_{\mathrm{d}}) \langle \hat{r}_{\mathrm{in}} \rangle(t), \end{aligned} \tag{4.29}$$

where $J(\omega_{\mathrm{d}})$ is considered to be a smooth function. Then $J(\omega_{\mathrm{d}}) \simeq J(\Omega_{\mathrm{S}})$ for driving frequencies ω_{d} close to a resonant frequency Ω_{S} of the system.

A typical experiment inputs a coherent drive into the system, obtaining the input-output relations from Eq. (4.29). All that is needed is the susceptibility $\chi_{\hat{S}}(\omega_{\mathrm{d}})$ for each particular system and coupling operator $\hat{S}$. Ignoring the dissipation of the quantum system into the line (or other pathways of dissipation), the function $\chi_{\hat{S}}(\omega_{\mathrm{d}})$ diverges whenever ω_{d} is in resonance with a frequency Ω_{S} of the system. However, this is not what happens in experiments: every resonance has a finite height and width due to dissipation. The next section describes how this dissipation is modeled in a quantum system.

4.3 Dissipation of the quantum system through the transmission line

Hamiltonian (4.20) allows calculating the time evolution of the density matrix ρ that describes the coupled waveguide and quantum system:

$$\dot{\rho} = -\frac{i}{\hbar}[H, \rho] = -\frac{i}{\hbar}[H_{\mathrm{S}}, \rho] - \frac{i}{\hbar}[H_{\mathrm{B}}, \rho] - \frac{i}{\hbar}[H_1, \rho]. \tag{4.30}$$

A description of the evolution of the quantum system needs a self-contained equation for the density matrix of the quantum system alone (ρ_{S}) — the quantum master equation — which will inevitably be approximate. The effect of the coupling to the transmission line will enter in this equation as a decay of the elements of ρ_{S} to those in thermal equilibrium at the temperature T of the transmission line.

4.3.1 Time-dependent perturbation theory in the interaction picture

The unperturbed Hamiltonian H_0 contains only the terms of the quantum system (H_S) and the transmission line (H_B):

$$H_0 := H_\mathrm{S} + H_\mathrm{B}\,. \tag{4.31}$$

The evolution of the density matrix is then given by:

$$\dot{\rho} = -\frac{i}{\hbar}\left[H_0, \rho\right] - \frac{i}{\hbar}\left[H_1, \rho\right]. \tag{4.32}$$

The interaction picture defines a new density matrix $\rho^{(\mathrm{I})}$:

$$\rho^{(\mathrm{I})}(t) := e^{i\,H_0\,t/\hbar}\rho(t)e^{-i\,H_0\,t/\hbar}. \tag{4.33}$$

This change removes the first term from Eq. (4.32):[9]

$$\dot{\rho}^{(\mathrm{I})} = \frac{i}{\hbar}\left[H_0, \rho^{(\mathrm{I})}\right] + e^{i\,H_0\,t/\hbar}\dot{\rho}\,e^{-i\,H_0\,t/\hbar} = -\frac{i}{\hbar}\left[H_1(t), \rho^{(\mathrm{I})}\right], \tag{4.34}$$

but now H_1 evolves, according to the interaction picture, with H_0:

$$H_1(t) = e^{i\,H_0\,t/\hbar}\,H_1\,e^{-i\,H_0\,t/\hbar}. \tag{4.35}$$

The formal solution to Eq. (4.34) is found by integration:

$$\rho^{(\mathrm{I})}(t) = \rho^{(I)}(t_0) - \frac{i}{\hbar}\int_{t_0}^{t}\mathrm{d}\,t'\left[H_1(t'), \rho^{(\mathrm{I})}(t')\right]. \tag{4.36}$$

[9] This step uses the product rule of differentiation combined with the fact that H_0 commutes with $e^{\pm i\,H_0\,t/\hbar}$ (which are only functions of H_0 and time) but not with ρ or $\dot{\rho}$:

$$\begin{aligned}\dot{\rho}^{(\mathrm{I})} &= \frac{\mathrm{d}}{\mathrm{d}\,t}\left(e^{i\,H_0\,t/\hbar}\rho(t)e^{-i\,H_0\,t/\hbar}\right) = (i\,H_0)\rho^{(\mathrm{I})} + e^{i\,H_0\,t/\hbar}\dot{\rho}\,e^{-i\,H_0\,t/\hbar} + \rho^{(\mathrm{I})}(-i\,H_0)\\ &= \frac{i}{\hbar}\left[H_0, \rho^{(\mathrm{I})}\right] + e^{i\,H_0\,t/\hbar}\dot{\rho}\,e^{-i\,H_0\,t/\hbar}.\end{aligned}$$

Inserting Eq. (4.32) in the second term and using again that H_0 commutes with $e^{\pm i\,H_0\,t/\hbar}$ but not with $\dot{\rho}$ or H_1 gives:

$$\begin{aligned}e^{i\,H_0\,t/\hbar}\dot{\rho}\,e^{-i\,H_0\,t/\hbar} &= -\frac{i}{\hbar}e^{i\,H_0\,t/\hbar}\left[H_0, \rho\right]e^{-i\,H_0\,t/\hbar} - \frac{i}{\hbar}e^{i\,H_0\,t/\hbar}\left[H_1, \rho\right]e^{-i\,H_0\,t/\hbar}\\ &= -\frac{i}{\hbar}\left[H_0, \rho^{(\mathrm{I})}\right] - \frac{i}{\hbar}\left[e^{i\,H_0\,t/\hbar}\,H_1\,e^{-i\,H_0\,t/\hbar}, \rho^{(\mathrm{I})}\right].\end{aligned}$$

This equation can be approximated by an infinite series of powers of H_1 by iteration.[10] If the interaction term is assumed to be small, the series can be truncated to second order in H_1:

$$\begin{aligned}\rho^{(\mathrm{I})}(t) &= \rho^{(\mathrm{I})}(t_0) - \frac{i}{\hbar}\int_{t_0}^{t} \mathrm{d}\,t' \left[H_1(t'), \rho^{(\mathrm{I})}(t_0) - \frac{i}{\hbar}\int_{t_0}^{t'} \mathrm{d}\,t'' \left[H_1(t''), \rho^{(\mathrm{I})}(t'')\right]\right] \\ &\simeq \rho^{(\mathrm{I})}(t_0) - \frac{i}{\hbar}\int_{t_0}^{t} \mathrm{d}\,t' \left[H_1(t'), \rho^{(\mathrm{I})}(t_0)\right] \\ &\quad - \frac{1}{\hbar^2}\int_{t_0}^{t} \mathrm{d}\,t' \int_{t_0}^{t'} \mathrm{d}\,t'' \left[H_1(t'), \left[H_1(t''), \rho^{(\mathrm{I})}(t_0)\right]\right],\end{aligned} \tag{4.37}$$

where $\rho^{(\mathrm{I})}(t'')$ was approximated by $\rho^{(\mathrm{I})}(t_0)$ in the last term to keep an equation of second order in H_1. The time derivative of Eq. (4.37) is:

$$\dot{\rho}^{(\mathrm{I})}(t) = -\frac{i}{\hbar}\left[H_1(t), \rho^{(\mathrm{I})}(t_0)\right] - \frac{1}{\hbar^2}\int_{t_0}^{t} \mathrm{d}\,t' \left[H_1(t), \left[H_1(t'), \rho^{(\mathrm{I})}(t_0)\right]\right], \tag{4.38}$$

where all the time-dependence is inside the evolution of H_1.

4.3.2 Tracing the line

The trace of $\dot{\rho}^{(\mathrm{I})}$ is the sum of all diagonal elements of $\dot{\rho}^{(\mathrm{I})}$ in any basis:

$$\mathrm{Tr}\,\dot{\rho}^{(\mathrm{I})} = \sum_n \sum_m \dot{\rho}^{(\mathrm{I})}_{nm}\delta_{nm} = \sum_n \dot{\rho}^{(I)}_{nn}, \tag{4.39}$$

where n (m) is an index that labels the basis states. An equation for the density matrix of the system alone is obtained by tracing out the degrees of freedom of the line. Let us label the basis states with the pair of indices n_S, n_B (m_S, m_B), one for the system and the other for the line. Then, the trace over the line is:

$$\begin{aligned}(\dot{\rho}^{(\mathrm{I})}_\mathrm{S})_{n_\mathrm{S}m_\mathrm{S}} &= (\underset{\mathrm{B}}{\mathrm{Tr}}\ \dot{\rho}^{(\mathrm{I})})_{n_\mathrm{S}m_\mathrm{S}} \\ &= \sum_{n_\mathrm{B}}\sum_{m_\mathrm{B}} \dot{\rho}^{(\mathrm{I})}_{n_\mathrm{S}n_\mathrm{B}m_\mathrm{S}m_\mathrm{B}}\delta_{n_\mathrm{B}m_\mathrm{B}} \\ &= \sum_{n_\mathrm{B}} \dot{\rho}^{(\mathrm{I})}_{n_\mathrm{S}n_\mathrm{B}m_\mathrm{S}n_\mathrm{B}}.\end{aligned} \tag{4.40}$$

Equation (4.38) needs to be written in such a way that it can be easily traced over the line states. Consider that H_1 is of the form $H_1 := \hat{S}\otimes\hat{B}$, where

[10] A 'Dyson-like' series is built for $\rho^{(\mathrm{I})}(t)$ similar to the Dyson series for the time-evolution operator in the interaction picture.

$\hat{S}$ is an operator of the system and $\hat{B}$ is an operator of the line. This is true for Hamiltonian (4.20), with:

$$\hat{B} = \hbar \int \mathrm{d}\,\omega \, \sqrt{J(\omega)} \left(\hat{r}_\omega^\dagger + \hat{l}_\omega^\dagger + \hat{r}_\omega + \hat{l}_\omega \right). \tag{4.41}$$

Besides, the line is in its thermal equilibrium state, with:

$$\rho_{\mathrm{B}}^{\mathrm{e}} = Z^{-1} e^{-\beta \int \mathrm{d}\,\omega \, \hbar\omega \left(\hat{r}_\omega^\dagger \hat{r}_\omega + \hat{l}_\omega^\dagger \hat{l}_\omega \right)}, \tag{4.42}$$

where $\beta = 1/k_{\mathrm{B}}T$, and Z is a normalization factor, the partition function. Assuming decoupled initial conditions, that is, that at the initial time t_0 the system-line density matrix is the product $\rho_{\mathrm{S}}(t_0) \otimes \rho_{\mathrm{B}}(t_0)$ of the density matrix of the system times the density matrix of the line, generates products of line operators with $\rho_{\mathrm{B}}^{\mathrm{e}}$ that can be traced out. The time evolution of the interaction term can be then written as $H_1(t) = \hat{S}(t) \otimes \hat{B}(t)$, with:

$$\begin{aligned} \hat{S}(t) &= e^{i\, H_{\mathrm{S}}\, t/\hbar} \hat{S} e^{-i\, H_{\mathrm{S}}\, t/\hbar}, \\ \hat{B}(t) &= e^{i\, H_{\mathrm{B}}\, t/\hbar} \hat{B} e^{-i\, H_{\mathrm{B}}\, t/\hbar}, \end{aligned} \tag{4.43}$$

where $\hat{S}$ evolves with H_{S} and $\hat{B}$ with H_{B} because each term of the unperturbed Hamiltonian H_0 acts on a different Hilbert space.

Defining $\langle\theta\rangle_{\mathrm{e}} := \underset{\mathrm{B}}{\mathrm{Tr}} \, (\theta \rho_{\mathrm{B}}^{\mathrm{e}})$, where θ is any combination of line operators, tracing the degrees of freedom of the line from $\dot{\rho}^{(\mathrm{I})}(t)$ reads:

$$\begin{aligned} \dot{\rho}_{\mathrm{S}}^{(\mathrm{I})}(t) = \underset{\mathrm{B}}{\mathrm{Tr}} \left(\dot{\rho}^{(\mathrm{I})}(t) \right) = &- \frac{i}{\hbar} \left[\hat{S}(t), \rho_S^{(\mathrm{I})}(t_0) \right] \langle \hat{B}(t) \rangle_{\mathrm{e}} \\ &- \frac{1}{\hbar^2} \int_{t_0}^{t} \mathrm{d}\,t' \left[\hat{S}(t), \hat{S}(t') \rho_{\mathrm{S}}^{(\mathrm{I})}(t_0) \right] \langle \hat{B}(t) \hat{B}(t') \rangle_{\mathrm{e}} \\ &+ \frac{1}{\hbar^2} \int_{t_0}^{t} \mathrm{d}\,t' \left[\hat{S}(t), \rho_{\mathrm{S}}^{(\mathrm{I})}(t_0) \hat{S}(t') \right] \langle \hat{B}(t') \hat{B}(t) \rangle_{\mathrm{e}}. \end{aligned} \tag{4.44}$$

For the line operator considered in Eq. (4.41), $\langle \hat{B}(t) \rangle_{\mathrm{e}} = 0$.[11] The remaining terms have the two-time correlators $\langle \hat{B}(t) \hat{B}(t') \rangle_{\mathrm{e}}$:[12]

$$\begin{aligned} \langle \hat{B}(t) \hat{B}(t') \rangle_{\mathrm{e}} = 2\hbar^2 \int \mathrm{d}\,\omega J(\omega) \Big[&\bar{n}(\omega, T) e^{i\omega(t-t')} \\ &+ (\bar{n}(\omega, T) + 1) e^{-i\omega(t-t')} \Big]. \end{aligned} \tag{4.45}$$

[11] The density matrix of the line in equilibrium, $\rho_{\mathrm{B}}^{\mathrm{e}}$, is diagonal in the basis of eigenstates of H_{B}, while the coupling line operator $\hat{B}$ from Eq. (4.41) does not have any terms in the diagonal in this same basis. It follows that the trace of the product of $\hat{B}$ times $\rho_{\mathrm{B}}^{\mathrm{e}}$ is zero.

[12] Actually they depend only on the time difference.

Here $\bar{n}(\omega, T)$ is the bosonic occupation number for thermal photons of frequency ω in the transmission line at temperature T:

$$\bar{n}(\omega, T) \equiv \langle \hat{l}_\omega^\dagger \hat{l}_\omega \rangle_{\mathrm{e}} = \langle \hat{r}_\omega^\dagger \hat{r}_\omega \rangle_{\mathrm{e}} = \frac{1}{e^{\beta\hbar\omega} - 1}. \tag{4.46}$$

4.3.3 Secular and rotating wave approximations

The evolution of $\hat{S}$ can be written using its spectral decomposition in the frequencies Ω_{S} [4, Ch.3]. Each component $\hat{S}(\Omega_{\mathrm{S}})$ evolves with frequency Ω_{S}:

$$\hat{S} = \sum_{\Omega_{\mathrm{S}}} \hat{S}(\Omega_{\mathrm{S}}) \quad \rightarrow \quad \hat{S}(t) = \sum_{\Omega_{\mathrm{S}}} \hat{S}(\Omega_{\mathrm{S}}) e^{i\Omega_S t}, \tag{4.47}$$

and the commutators in Eq. (4.44) read:

$$\begin{aligned}
\left[\hat{S}(t), \hat{S}(t')\rho_{\mathrm{S}}^{(\mathrm{I})}(t_0)\right] &= \sum_{\Omega_{\mathrm{S}}} \sum_{\Omega'_{\mathrm{S}}} \left[\hat{S}(\Omega_{\mathrm{S}}), \hat{S}(\Omega'_{\mathrm{S}})\rho_S^{(\mathrm{I})}(t_0)\right] e^{i\Omega_{\mathrm{S}}(t-t')} e^{i(\Omega_{\mathrm{S}}+\Omega'_{\mathrm{S}})t'}, \\
\left[\hat{S}(t), \rho_{\mathrm{S}}^{(\mathrm{I})}(t_0)\hat{S}(t')\right] &= \sum_{\Omega_{\mathrm{S}}} \sum_{\Omega'_S} \left[\hat{S}(\Omega_{\mathrm{S}}), \rho_{\mathrm{S}}^{(\mathrm{I})}(t_0)\hat{S}(\Omega'_{\mathrm{S}})\right] e^{i\Omega_{\mathrm{S}}(t-t')} e^{i(\Omega_{\mathrm{S}}+\Omega'_{\mathrm{S}})t'}.
\end{aligned} \tag{4.48}$$

They contain fast oscillating terms except when $\Omega'_{\mathrm{S}} \simeq -\Omega_{\mathrm{S}}$. In the secular approximation, only terms with $\Omega'_{\mathrm{S}} = -\Omega_{\mathrm{S}}$ are kept. If the spectral decomposition of $\hat{S}$ is non-degenerate, that is, if all frequencies Ω_{S} are different:

$$\begin{aligned}
\left[\hat{S}(t), \hat{S}(t')\rho_{\mathrm{S}}^{(\mathrm{I})}(t_0)\right] &\simeq \sum_{\Omega_{\mathrm{S}}} \left[\hat{S}(\Omega_{\mathrm{S}}), \hat{S}(-\Omega_{\mathrm{S}})\rho_{\mathrm{S}}^{(\mathrm{I})}(t_0)\right] e^{i\Omega_{\mathrm{S}}(t-t')}, \\
\left[\hat{S}(t), \rho_{\mathrm{S}}^{(\mathrm{I})}(t_0)\hat{S}(t')\right] &\simeq \sum_{\Omega_{\mathrm{S}}} \left[\hat{S}(\Omega_{\mathrm{S}}), \rho_{\mathrm{S}}^{(\mathrm{I})}(t_0)\hat{S}(-\Omega_{\mathrm{S}})\right] e^{i\Omega_{\mathrm{S}}(t-t')}.
\end{aligned} \tag{4.49}$$

Inserting the commutators above and the expression for the two-time correlators (see Eq. (4.45)) back in Eq. (4.44) for $\dot{\rho}_{\mathrm{S}}^{(\mathrm{I})}(t)$ gives fast oscillating terms except for $\Omega_{\mathrm{S}} \simeq \omega$ in $e^{i(\Omega_{\mathrm{S}}-\omega)(t-t')}$, and $\Omega_{\mathrm{S}} \simeq -\omega$ in $e^{i(\Omega_{\mathrm{S}}+\omega)(t-t')}$. In the rotating wave approximation, these fast oscillating terms are neglected, leaving only terms with $e^{\pm i(\Omega_{\mathrm{S}}-\omega)(t-t')}$, where $\Omega_{\mathrm{S}}, \omega > 0$.

4.3.4 Markovian regime

The memory function of the line is defined as the Fourier transform of the spectral function $J(\omega)$. If $J(\omega)$ is a smooth function over a broad range of frequencies around each Ω_{S}, this memory function decays with a very short

characteristic time τ_c [5, App.B].[13] In the Markovian regime, the timescale of the decay of the memory function of the line is smaller than any timescale of the system (given by the different times Ω_S^{-1}). That is, the line immediately loses all memory of its interaction with the system.

In this regime, the integrand of the time integral vanishes quickly for $\tau = t' - t_0 \gg \tau_c$, and the upper limit of the integral can be extended to infinity:[14]

$$\begin{aligned}\int_{t_0}^{\infty} \mathrm{d}\, t'\, e^{\pm i(\Omega_S-\omega)t'} &= e^{\pm i(\Omega_S-\omega)t_0} \int_0^{\infty} \mathrm{d}\,\tau\, e^{\pm i(\omega-\Omega_S)\tau} \\ &= e^{\pm i(\Omega_S-\omega)t_0}\Big[\pi\delta(\Omega_S-\omega) \pm i\mathcal{PV}\Big(\frac{1}{\Omega_S-\omega}\Big)\Big],\end{aligned} \tag{4.50}$$

with $\mathcal{PV}$ the principal value [6, App.7]. The principal value generates a shift — the Lamb shift — that diverges with the previous approximations. In practice, this shift is small, and can be included in the frequencies Ω_S. This leaves only the term with $\delta(\Omega_S - \omega)$, which gives the master equation for $\rho_S^{(I)}$:

$$\dot{\rho}_S^{(I)}(t) = \sum_{\Omega_S>0} \Gamma(\Omega_S)\Big[\bar{n}(\Omega_S,T)\mathcal{D}(\Omega_S) + (\bar{n}(\Omega_S,T)+1)\mathcal{D}(-\Omega_S)\Big], \tag{4.51}$$

with $\Gamma(\Omega_S) = 2\pi J(\Omega_S)$ and:

$$\mathcal{D}(\Omega_S) := 2\hat{S}(\Omega_S)\rho_S^{(I)}(t_0)\hat{S}(-\Omega_S) - \Big\{\hat{S}(-\Omega_S)\hat{S}(\Omega_S), \rho_S^{(I)}(t_0)\Big\}, \tag{4.52}$$

where $\{\hat{A},\hat{B}\} = \hat{A}\hat{B} + \hat{B}\hat{A}$ is the standard anti-commutator of $\hat{A}$ and $\hat{B}$.

4.3.5 Back to the Schrödinger picture

Equation (4.51) is a master equation for the density matrix of the system in the interaction picture. However, a master equation in the Schrödinger picture, with all the time dependence encoded in the density matrix ρ_S and not in the system operators, is desired instead. Inserting $\rho_S(t) = e^{-i\,H_S\,t/\hbar}\rho_S^{(I)}(t)e^{i\,H_S\,t/\hbar}$ in Eq. (4.51) gives the quantum master equation in the Schrödinger picture:

$$\begin{aligned}\dot{\rho}_S(t) &= -\frac{i}{\hbar}\,[H_S,\rho_S(t)] + e^{-i\,H_S\,t/\hbar}\dot{\rho}_S^{(I)}(t)e^{i\,H_S\,t/\hbar} \\ &= -\frac{i}{\hbar}\,[H_S,\rho_S(t)] + \mathcal{R}(t),\end{aligned} \tag{4.53}$$

[13] Consider that the spectral function is a very wide resonance. Its Fourier transform — the memory function — is an exponential decay with a very short characteristic time that is inversely proportional to the width of the spectral function.

[14] The integration variable is changed from t' to $\tau = t' - t_0$, the elapsed time since the interaction started.

with the relaxation operator:

$$\mathcal{R}(t) := \sum_{\Omega_S>0} \Gamma(\Omega_S)\Big(\bar{n}(\Omega_S,T)\mathcal{D}(\Omega_S,t) + (\bar{n}(\Omega_S,T)+1)\mathcal{D}(-\Omega_S,t)\Big), \tag{4.54}$$

and the dissipators:

$$\begin{aligned}\mathcal{D}(\Omega_S,t) &:= e^{-i\,H_S\,t/\hbar}\mathcal{D}(\Omega_S)e^{i\,H_S\,t/\hbar} \\ &= 2\hat{S}(\Omega_S)\rho_S(t)\hat{S}(-\Omega_S) - \Big\{\hat{S}(-\Omega_S)\hat{S}(\Omega_S),\rho_S(t)\Big\}.\end{aligned} \tag{4.55}$$

Here I used that the phases from $\hat{S}(\Omega_S)$ and $\hat{S}(-\Omega_S)$ in each term cancel out and that, at the time t_0 when the interaction started, $\rho_S(t_0) = \rho_S^{(I)}(t_0)$.

4.4 Measurement of a lumped-element resonator

4.4.1 Dynamics of a resonator without driving

One of the simplest applications of the quantum master equation is a resonator coupled to a transmission line. The system coupling operator of Hamiltonian (4.20) is now $\hat{S} = \hat{a} + \hat{a}^\dagger$. The time-evolution of $\langle\hat{S}\rangle$ without interactions is $\langle\hat{S}\rangle(t) = \langle\hat{a}\rangle e^{-i\omega_r t} + \langle\hat{a}^\dagger\rangle e^{i\omega_r t}$ (see section 3.2.2), where ω_r is the resonator frequency as defined in Eq. (3.16). The spectral decomposition of $\hat{S}$ is then given by $\hat{S}(\omega_r) = \hat{a}^\dagger$ and $\hat{S}(-\omega_r) = \hat{a}$. The sum in Ω_S in Eq. (4.54) has only one term with $\Omega_S = \omega_r$:

$$\mathcal{R}(t) = \Gamma(\omega_r)\Big[\bar{n}(\omega_r,T)\mathcal{D}(\omega_r,t) + (\bar{n}(\omega_r,T)+1)\mathcal{D}(-\omega_r,t)\Big], \tag{4.56}$$

with:

$$\begin{aligned}\mathcal{D}(\omega_r,t) &= 2\hat{a}^\dagger\rho(t)\hat{a} - \Big\{\hat{a}\hat{a}^\dagger,\rho(t)\Big\}, \\ \mathcal{D}(-\omega_r,t) &= 2\hat{a}\rho(t)\hat{a}^\dagger - \Big\{\hat{a}^\dagger\hat{a},\rho(t)\Big\},\end{aligned} \tag{4.57}$$

where $\rho(t)$ is the density matrix of the resonator. The time evolution of the expectation value of the annihilation operator is then given by the Hamiltonian

of the resonator, $H_{\mathrm{R}} = \hbar\omega_{\mathrm{r}}\hat{a}^{\dagger}\hat{a}$, and the relaxation operator $\mathcal{R}(t)$:[15]

$$\begin{aligned}\frac{\mathrm{d}}{\mathrm{d}\,t}\langle\hat{a}\rangle(t) &= \mathrm{Tr}\left(\hat{a}\dot{\rho}(t)\right)\\ &= -\frac{i}{\hbar}\,\mathrm{Tr}\left(\hat{a}\left[H_{\mathrm{R}},\rho(t)\right]\right) + \mathrm{Tr}\left(\hat{a}\mathcal{R}(t)\right)\\ &= -i\omega_{\mathrm{r}}\langle\hat{a}\rangle(t) - \kappa_{\mathrm{c}}\langle\hat{a}\rangle(t),\end{aligned} \tag{4.58}$$

with $\kappa_{\mathrm{c}} := \Gamma(\omega_{\mathrm{r}}) = 2\pi J(\omega_{\mathrm{r}})$, having the dimensions of frequency.

In practice, there are also internal losses (κ_{i}), giving a total decay rate $\kappa := \kappa_{\mathrm{i}} + \kappa_{\mathrm{c}}$. The complete time evolution reads (recall Eq. (3.26) in chapter 3):

$$\frac{\mathrm{d}}{\mathrm{d}\,t}\langle\hat{a}\rangle = -i\omega_{\mathrm{r}}\langle\hat{a}\rangle - \kappa\langle\hat{a}\rangle \;\;\Rightarrow\;\; \langle\hat{a}\rangle(t) = \langle\hat{a}\rangle(0)e^{-(i\omega_{\mathrm{r}}+\kappa)t}. \tag{4.59}$$

Sometimes, the dimensionless quality factors Q, Q_{i} and Q_{c} are used instead of the decay rates κ, κ_{i} and κ_{c}:

$$Q := \frac{\omega_{\mathrm{r}}}{2\kappa}, \qquad Q_{\mathrm{i}} := \frac{\omega_{\mathrm{r}}}{2\kappa_{\mathrm{i}}}, \qquad Q_{\mathrm{c}} := \frac{\omega_{\mathrm{r}}}{2\kappa_{\mathrm{c}}}. \tag{4.60}$$

The time evolution of the expectation value of the number of photons in the cavity, $\hat{n} = \hat{a}^{\dagger}\hat{a}$, is:[16]

$$\begin{aligned}&\frac{\mathrm{d}}{\mathrm{d}\,t}\langle\hat{n}\rangle = -2\kappa\left[\langle\hat{n}\rangle - \bar{n}(\omega_{\mathrm{r}},T)\right] \;\;\Rightarrow\\ \Rightarrow\;\; &\langle\hat{n}\rangle(t) = \langle\hat{n}\rangle(0)e^{-2\kappa t} + \bar{n}(\omega_{\mathrm{r}},T)\left(1-e^{-2\kappa t}\right),\end{aligned} \tag{4.61}$$

with a decay rate that is twice the decay rate of $\langle\hat{a}\rangle$. At very long times ($t \gg \kappa^{-1}$), $\langle\hat{n}\rangle \to \bar{n}(\omega_{\mathrm{r}},T)$, and $\langle\hat{a}\rangle \to 0$. That is, the number of photons in the resonator will be the number of thermal photons, and the coherence of the state of the resonator will be zero.

4.4.2 Driving the resonator

Following the definitions in section 4.2.2, the coupling Hamiltonian of the resonator to a coherent drive field reads:

$$H_{\mathrm{drive}} = \hbar\sqrt{\kappa_{\mathrm{c}}}\alpha_{\mathrm{in}}(\hat{a}+\hat{a}^{\dagger})e^{-i\omega_{\mathrm{d}}t}. \tag{4.62}$$

Including this term in the quantum master equation of $\langle\hat{a}\rangle$ gives:

$$\frac{\mathrm{d}}{\mathrm{d}\,t}\langle\hat{a}\rangle = -\left(i\omega_{\mathrm{r}}+\kappa\right)\langle\hat{a}\rangle - i\sqrt{\kappa_{\mathrm{c}}}\alpha_{\mathrm{in}}e^{-i\omega_{\mathrm{d}}t}, \tag{4.63}$$

[15] $\mathrm{Tr}\,\hat{a}\mathcal{D}(\omega_{\mathrm{r}},t)$ and $\mathrm{Tr}\,\hat{a}\mathcal{D}(-\omega_{\mathrm{r}},t)$ can be easily computed by using the commutation rule $\left[\hat{a},\hat{a}^{\dagger}\right]=1$ to transform the sums of products of $\hat{a}$ and $\hat{a}^{\dagger}$ into only $\hat{a}$.

[16] Again, using $\left[\hat{a},\hat{a}^{\dagger}\right]=1$.

with the solution:

$$\langle \hat{a} \rangle(t) = \langle \hat{a} \rangle(0) e^{-(i\omega_\mathrm{r}+\kappa)t} - i\sqrt{\kappa_\mathrm{c}} \frac{1 - e^{-(i(\omega_\mathrm{r}-\omega_\mathrm{d})+\kappa)t}}{i(\omega_\mathrm{r}-\omega_\mathrm{d})+\kappa} \alpha_\mathrm{in} e^{-i\omega_\mathrm{d}t}. \tag{4.64}$$

The first term in Eq. (4.64) is the transient state of the resonator. If the coherent drive signal starts long enough ($t \gg \kappa^{-1}$) since the last excitation of the resonator, then $\langle \hat{a} \rangle(0) = 0$. The remaining term is the emerging driven state with frequency ω_d:

$$\langle \hat{a} \rangle(t) \simeq \chi_{\hat{a}}(\omega_\mathrm{d}) \sqrt{\kappa_\mathrm{c}} \langle \hat{r}_\mathrm{in} \rangle(t) \quad , \quad \chi_{\hat{a}}(\omega_\mathrm{d}) = \frac{-i}{i(\omega_\mathrm{r}-\omega_\mathrm{d})+\kappa}, \tag{4.65}$$

where $\chi_{\hat{a}}$ is the susceptibility of $\hat{a}$.

Substituting Eq. 4.65 in the input-output relations (Eq. (4.29)):

$$\begin{aligned} \langle \hat{r}_\mathrm{out} \rangle(t) &= \langle \hat{r}_\mathrm{in} \rangle(t) \, \left(1 - i\kappa_\mathrm{c} \chi_{\hat{a}}(\omega_\mathrm{d})\right), \\ \langle \hat{l}_\mathrm{out} \rangle(t) &= \langle \hat{r}_\mathrm{in} \rangle(t) \, \left(-i\kappa_\mathrm{c} \chi_{\hat{a}}(\omega_\mathrm{d})\right), \end{aligned} \tag{4.66}$$

and using the definition of scattering parameters from Eq. (4.25) yields:

$$\begin{aligned} S_{21}(\omega_\mathrm{d}) &= 1 - i\kappa_\mathrm{c} \chi_{\hat{a}}(\omega_\mathrm{d}) = 1 - \frac{\kappa_\mathrm{c}}{i(\omega_\mathrm{r}-\omega_\mathrm{d})+\kappa}, \\ S_{11}(\omega_\mathrm{d}) &= -i\kappa_\mathrm{c} \chi_{\hat{a}}(\omega_\mathrm{d}) = -\frac{\kappa_\mathrm{c}}{i(\omega_\mathrm{r}-\omega_\mathrm{d})+\kappa}. \end{aligned} \tag{4.67}$$

4.5 Measurement of a spin 1/2 ensemble

Before diving into the model for the measurement of a hybrid system of a spin ensemble coupled to a resonator, let us describe a simpler case in which the ensemble is directly coupled to the transmission line.

4.5.1 Dynamics of a single spin without driving

Consider a single spin coupled to the transmission line. The system coupling operator of Hamiltonian (4.20) is now $\hat{S} = \hat{\sigma}_+ + \hat{\sigma}_-$. The evolution of the expectation value of $\sigma_\pm$ with the Hamiltonian of a single spin, $H_\mathrm{S} = \hbar\omega_\mathrm{q}\hat{\sigma}_z/2$, is:

$$\frac{\mathrm{d}}{\mathrm{d}\,t}\langle \hat{\sigma}_\pm \rangle = -\frac{i}{\hbar} \mathrm{Tr}\left(\hat{\sigma}_\pm \left[H_\mathrm{S}, \rho\right]\right) = \pm\omega_\mathrm{q} \langle \hat{\sigma}_\pm \rangle \quad \rightarrow \quad \langle \hat{\sigma}_\pm \rangle(t) = \langle \hat{\sigma}_\pm \rangle(0) e^{\pm i\omega_\mathrm{q} t}, \tag{4.68}$$

where $\rho(t)$ is the density matrix of the spin. Then, the time-evolution of $\langle\hat{S}\rangle$ without interactions is $\langle\hat{S}\rangle(t) = \langle\hat{\sigma}_+\rangle e^{i\omega_\mathrm{q}t} + \langle\hat{\sigma}_-\rangle e^{-i\omega_\mathrm{q}t}$, and its spectral decomposition is given by $\hat{S}(\omega_\mathrm{q}) = \hat{\sigma}_+$ and $\hat{S}(-\omega_\mathrm{q}) = \hat{\sigma}_-$. The sum in Ω_S in Eq. (4.54) has only one term with $\Omega_\mathrm{S} = \omega_\mathrm{q}$:

$$\mathcal{R}(t) = \Gamma(\omega_\mathrm{q})\Big[\bar{n}(\omega_\mathrm{q},T)\mathcal{D}(\omega_\mathrm{q},t) + (\bar{n}(\omega_\mathrm{q},T)+1)\mathcal{D}(-\omega_\mathrm{q},t)\Big], \tag{4.69}$$

with the dissipators:

$$\begin{aligned}\mathcal{D}(\omega_\mathrm{q},t) &= 2\hat{\sigma}_+\rho(t)\hat{\sigma}_- - \Big\{\hat{\sigma}_-\hat{\sigma}_+,\rho(t)\Big\},\\ \mathcal{D}(-\omega_\mathrm{q},t) &= 2\hat{\sigma}_-\rho(t)\hat{\sigma}_+ - \Big\{\hat{\sigma}_+\hat{\sigma}_-,\rho(t)\Big\}.\end{aligned} \tag{4.70}$$

The time evolution of the coherences $\hat{\sigma}_\pm$ reads:[17]

$$\begin{aligned}\frac{\mathrm{d}}{\mathrm{d}\,t}\langle\hat{\sigma}_\pm\rangle &= \mathrm{Tr}\left(\hat{\sigma}_\pm\dot{\rho}(t)\right)\\ &= -\frac{i}{\hbar}\,\mathrm{Tr}\left(\hat{\sigma}_\pm\left[H_\mathrm{S},\rho(t)\right]\right) + \mathrm{Tr}\left(\hat{\sigma}_\pm\mathcal{R}(t)\right)\\ &= \pm i\omega_\mathrm{q}\langle\hat{\sigma}_\pm\rangle - \Gamma_\perp\langle\hat{\sigma}_\pm\rangle,\end{aligned} \tag{4.71}$$

with $\Gamma_\perp := (2\bar{n}(\omega_\mathrm{q},T)+1)\,G_1^{(\mathrm{line})}$, where $G_1^{(\mathrm{line})} := \Gamma(\omega_\mathrm{q}) = 2\pi J(\omega_\mathrm{q})$. In practice, there are also internal losses ($\gamma_\perp = T_2^{-1}$), for a total decay rate $\Gamma_\perp := \gamma_\perp + (2\bar{n}(\omega_\mathrm{q},T)+1)\,G_1^{(\mathrm{line})}$. Solving the differential equation, one obtains:

$$\langle\hat{\sigma}_\pm\rangle(t) = \langle\hat{\sigma}_\pm\rangle(0)e^{(\pm i\omega_\mathrm{q}-\Gamma_\perp)t}. \tag{4.72}$$

Similarly, the time evolution of $\langle\hat{\sigma}_z\rangle$ is:

$$\frac{\mathrm{d}}{\mathrm{d}\,t}\langle\hat{\sigma}_z\rangle = \mathrm{Tr}\left(\hat{\sigma}_z\mathcal{R}(t)\right) = -\Gamma_\parallel\left(\langle\hat{\sigma}_z\rangle + (\Delta P)_\mathrm{e}\right), \tag{4.73}$$

where internal losses ($\gamma_\parallel = T_1^{-1}$) are already included in $\Gamma_\parallel := \gamma_\parallel + 2(2\bar{n}(\omega_\mathrm{q},T)+1)\,G_1^{(\mathrm{line})}$. Only the relaxation term of the quantum master equation is relevant here, as $\hat{\sigma}_z$ commutes with H_S. $(\Delta P)_\mathrm{e} = (2\bar{n}(\omega_\mathrm{q},T)+1)^{-1} = \tanh\left(\hbar\omega_\mathrm{q}/2k_\mathrm{B}T\right)$ is the population difference between the ground and excited spin states in thermal equilibrium. At long times ($t \gg \Gamma_\perp^{-1}, \Gamma_\parallel^{-1}$), the coherences $\langle\hat{\sigma}_\pm\rangle$ vanish and $\langle\hat{\sigma}_z\rangle$ decays to its value in thermal equilibrium, $-(\Delta P)_\mathrm{e}$.

[17] The time evolution of $\hat{\sigma}_\pm$ is encoded in the off-diagonal terms of the density matrix, that is, the spin coherence.

4.5.2 Driving a single spin

The interaction of a spin with the coherent drive of Eq. (4.26) is:

$$H_{\rm drive} = \hbar\sqrt{G_1^{\rm (line)}}\alpha_{\rm in}e^{-i\omega_{\rm d}t}(\hat{\sigma}_+ + \hat{\sigma}_-). \tag{4.74}$$

Including this term in the quantum master equations of $\langle\hat{\sigma}_\pm\rangle$ and $\langle\hat{\sigma}_z\rangle$ one obtains:

$$\begin{aligned}
\frac{\rm d}{{\rm d}\,t}\langle\hat{\sigma}_\pm\rangle &= \pm\, i\omega_{\rm q}\langle\hat{\sigma}_\pm\rangle - \Gamma_\perp\langle\hat{\sigma}_\pm\rangle \mp i\sqrt{G_1^{\rm (line)}}\alpha_{\rm in}e^{-i\omega_{\rm d}t}\langle\hat{\sigma}_z\rangle,\\
\frac{\rm d}{{\rm d}\,t}\langle\hat{\sigma}_z\rangle &= -\,\Gamma_\parallel\,(\langle\hat{\sigma}_z\rangle + (\Delta P)_{\rm e})\\
&\quad - i\sqrt{G_1^{\rm (line)}}\alpha_{\rm in}e^{-i\omega_{\rm d}t}\langle\hat{\sigma}_+\rangle + i\sqrt{G_1^{\rm (line)}}\alpha_{\rm in}e^{-i\omega_{\rm d}t}\langle\hat{\sigma}_-\rangle.
\end{aligned} \tag{4.75}$$

Instead of solving these equations, let us consider the typical transmission experiment. By the time the driving starts, the free evolution of the spin has relaxed to $\langle\hat{\sigma}_\pm\rangle = 0$ and $\langle\hat{\sigma}_z\rangle = -(\Delta P)_{\rm e}$. Also, the spin-line coupling $G_1^{\rm (line)}$ is very small compared to the decay rates $\Gamma_\perp$ and $\Gamma_\parallel$. It can be assumed then that $\langle\hat{\sigma}_z\rangle(t) \simeq -(\Delta P)_{\rm e}$ at all times. With this approximation, the equation for $\langle\hat{\sigma}_\pm\rangle$ reads:

$$\frac{\rm d}{{\rm d}\,t}\langle\hat{\sigma}_\pm\rangle = \pm i\omega_{\rm q}\langle\hat{\sigma}_\pm\rangle - \Gamma_\perp\langle\hat{\sigma}_\pm\rangle \pm i\sqrt{G_1^{\rm (line)}}(\Delta P)_{\rm e}\alpha_{\rm in}e^{-i\omega_{\rm d}t}. \tag{4.76}$$

In particular, for positive $\omega_{\rm d}$ I am interested in the expectation value of $\hat{\sigma}_-$. Assuming that $\langle\hat{\sigma}_-\rangle(0) = 0$:

$$\langle\hat{\sigma}_-\rangle(t) = -i\sqrt{G_1^{\rm (line)}}(\Delta P)_{\rm e}\frac{1 - e^{-(i(\omega_{\rm q}-\omega_{\rm d})+\Gamma_\perp)t}}{i(\omega_{\rm q}-\omega_{\rm d})+\Gamma_\perp}\alpha_{\rm in}e^{-i\omega_{\rm d}t}, \tag{4.77}$$

and at long times ($t \gg \Gamma_\perp^{-1}$):

$$\langle\hat{\sigma}_-\rangle(t) \simeq \chi_{\hat{\sigma}_-}(\omega_{\rm d})\sqrt{G_1^{\rm (line)}}\langle\hat{r}_{\rm in}\rangle(t) \quad , \quad \chi_{\hat{\sigma}_-}(\omega_{\rm d}) = \frac{-i(\Delta P)_{\rm e}}{i(\omega_{\rm q}-\omega_{\rm d})+\Gamma_\perp}, \tag{4.78}$$

where $\chi_{\hat{a}}$ is the susceptibility of $\hat{a}$.

The equations for the outputs of the coherent drive are:

$$\begin{aligned}
\langle\hat{r}_{\rm out}\rangle(t) &= \langle\hat{r}_{\rm in}\rangle(t)\,\left(1 - iG_1^{\rm (line)}\chi_{\hat{\sigma}_-}(\omega_{\rm d})\right),\\
\langle\hat{l}_{\rm out}\rangle(t) &= \langle\hat{r}_{\rm in}\rangle(t)\,\left(-iG_1^{\rm (line)}\chi_{\hat{\sigma}_-}(\omega_{\rm d})\right).
\end{aligned} \tag{4.79}$$

Following the definitions from Eq. (4.25), the scattering parameters S_{21} and S_{11} are given by:

$$\begin{aligned} S_{21}(\omega_\mathrm{d}) &= 1 - iG_1^{(\mathrm{line})}\chi_{\hat{\sigma}_-}(\omega_\mathrm{d}) = 1 - \frac{G_1^{(\mathrm{line})}(\Delta P)_\mathrm{e}}{i(\omega_\mathrm{q}-\omega_\mathrm{d})+\Gamma_\perp}, \\ S_{11}(\omega_\mathrm{d}) &= -iG_1^{(\mathrm{line})}\chi_{\hat{\sigma}_-}(\omega_\mathrm{d}) = -\frac{G_1^{(\mathrm{line})}(\Delta P)_\mathrm{e}}{i(\omega_\mathrm{q}-\omega_\mathrm{d})+\Gamma_\perp}. \end{aligned} \tag{4.80}$$

4.5.3 Driving a spin 1/2 ensemble

Obtaining similar expressions for the reflection and transmission of a spin 1/2 ensemble is not as simple as taking the product of the single-spin scattering parameters S_{11} or S_{21} of all spins in the ensemble. These parameters were defined with an input field coming from port 1, $\langle\hat{r}_\mathrm{in}\rangle$, and no input field from port 2. Conversely, S_{12} and S_{22} consider only an input from port 2, $\langle\hat{l}_\mathrm{in}\rangle$. Assuming a non-chiral coupling, $S_{12} = S_{21}$ and $S_{22} = S_{11}$. Together, these four parameters form the two-port scattering matrix $\boldsymbol{S}$:

$$\boldsymbol{S} = \begin{pmatrix} S_{11} & S_{12} \\ S_{21} & S_{22} \end{pmatrix}, \tag{4.81}$$

which relates the outputs from both ports to their inputs:

$$\begin{pmatrix} \langle\hat{l}_\mathrm{out}\rangle \\ \langle\hat{r}_\mathrm{out}\rangle \end{pmatrix} = \boldsymbol{S} \begin{pmatrix} \langle\hat{l}_\mathrm{in}\rangle \\ \langle\hat{r}_\mathrm{in}\rangle \end{pmatrix}. \tag{4.82}$$

The scattering matrix $\boldsymbol{S}$ relates the inputs and outputs of the system. In order to see the effect of the reflection and transmission of each spin on the reflection and transmission of other spins in the ensemble, a description with the transfer matrix $\boldsymbol{T}$ in needed. The transfer matrix relates the input and output in port 1 to those of port 2 (see Fig. 4.3):

$$\begin{pmatrix} \langle\hat{r}_\mathrm{out}\rangle \\ \langle\hat{l}_\mathrm{in}\rangle \end{pmatrix} = \boldsymbol{T} \begin{pmatrix} \langle\hat{r}_\mathrm{in}\rangle \\ \langle\hat{l}_\mathrm{out}\rangle \end{pmatrix} = \begin{pmatrix} T_{11} & T_{12} \\ T_{21} & T_{22} \end{pmatrix} \begin{pmatrix} \langle\hat{r}_\mathrm{in}\rangle \\ \langle\hat{l}_\mathrm{out}\rangle \end{pmatrix}. \tag{4.83}$$

The elements of the transfer matrix are related to those of the scattering matrix. Defining $\theta := S_{11}/S_{21}$:

$$\theta(\omega_\mathrm{d}) := \frac{S_{11}(\omega_\mathrm{d})}{S_{21}(\omega_\mathrm{d})} = \frac{-G_1^{(\mathrm{line})}(\Delta P)_\mathrm{e}}{i\left(\omega_\mathrm{q}-\omega_\mathrm{d}\right) + \left[\Gamma_\perp - G_1^{(\mathrm{line})}(\Delta P)_\mathrm{e}\right]}, \tag{4.84}$$

the single spin transfer matrix $\boldsymbol{T}$ is written as:

$$\boldsymbol{T} = \begin{pmatrix} 1+\theta & \theta \\ -\theta & 1-\theta \end{pmatrix} = \mathbb{I} + \theta\boldsymbol{\epsilon}, \qquad \boldsymbol{\epsilon} = \begin{pmatrix} 1 & 1 \\ -1 & -1 \end{pmatrix}, \tag{4.85}$$

where I used that $S_{21} = 1 + S_{11}$.

The ensemble is modeled as an array of N spins. Their collective transfer matrix is just the product of all the single-spin transfer matrices: $\boldsymbol{T} = \prod_{j=1}^{N} \boldsymbol{T_j}$. That is, the fields in port 2 for one spin become the fields in port 1 for the next one. For N spins, $\boldsymbol{T}$ will be a series of powers of $\boldsymbol{\epsilon}$ up to order N. However, $\boldsymbol{\epsilon}^2 = 0$, and only terms up to first order in $\boldsymbol{\epsilon}$ are non-zero. The collective transfer matrix is then similar to that of a single spin:

$$\boldsymbol{T} = \mathbb{I} + \left(\sum_{j=1}^{N} \theta_j \right) \boldsymbol{\epsilon} \equiv \mathbb{I} + \theta\boldsymbol{\epsilon}, \tag{4.86}$$

with:

$$\theta(\omega_\mathrm{d}) := \sum_{j=1}^{N} \theta_j(\omega_\mathrm{d}) = -\sum_{j=1}^{N} \frac{G_{1,\,j}^{(\mathrm{line})}(\Delta P)_\mathrm{e}}{i\,(\omega_\mathrm{q} - \omega_\mathrm{d}) + \left[\Gamma_{\perp,\,j} - G_{1,\,j}^{(\mathrm{line})}(\Delta P)_\mathrm{e}\right]}. \tag{4.87}$$

S_{11} and S_{21} are retrieved using again that $S_{21} = 1 + S_{11}$ and $\theta = S_{11}/S_{21}$:

$$S_{21}(\omega_\mathrm{d}) = \frac{1}{1-\theta(\omega_\mathrm{d})}, \qquad S_{11}(\omega_\mathrm{d}) = \frac{\theta(\omega_\mathrm{d})}{1-\theta(\omega_\mathrm{d})}. \tag{4.88}$$

At very low temperatures ($T \ll \hbar\omega_\mathrm{q}/k_\mathrm{B}$), the population difference between the ground and excited states is approximately one, $(\Delta P)_\mathrm{e} \simeq 1$. Then, using that $\Gamma_{\perp,\,j} = \gamma_\perp + G_{1,\,j}^{(\mathrm{line})}$:

$$\theta(\omega_\mathrm{d}) \simeq -\frac{G_N^{(\mathrm{line})}(\Delta P)_\mathrm{e}}{i\,(\omega_\mathrm{q} - \omega_\mathrm{d}) + \gamma_\perp}, \tag{4.89}$$

with:

$$G_N^{(\mathrm{line})} = \sum_{j=1}^{N} G_{1,\,j}^{(\mathrm{line})}. \tag{4.90}$$

In practice, if there is inhomogeneous broadening the coherence time T_2 is substituted by T_2^* in $\gamma_\perp$. Inserting $\theta(\omega_\mathrm{d})$ back in the expressions for the scattering parameters gives:

$$\begin{aligned} S_{21}(\omega_\mathrm{d}) &= 1 - \frac{G_N^{(\mathrm{line})}(\Delta P)_\mathrm{e}}{i(\omega_\mathrm{q} - \omega_\mathrm{d}) + \gamma_\perp + G_N^{(\mathrm{line})}(\Delta P)_\mathrm{e}}, \\ S_{11}(\omega_\mathrm{d}) &= -\frac{G_N^{(\mathrm{line})}(\Delta P)_\mathrm{e}}{i(\omega_\mathrm{q} - \omega_\mathrm{d}) + \gamma_\perp + G_N^{(\mathrm{line})}(\Delta P)_\mathrm{e}}. \end{aligned} \tag{4.91}$$

4.6 Measurement of a spin 1/2 ensemble-resonator system

The previous sections described the measurement of a lumped-element resonator and the measurement of a spin 1/2 ensemble. This section describes the measurement of the hybrid system of a spin 1/2 ensemble coupled to a lumped-element resonator. This system is modeled by the Tavis-Cummings Hamiltonian (3.37). However, let us consider first the single spin case.

4.6.1 Spin-resonator system

For a single spin, the spin-resonator system is described by Jaynes-Cummings Hamiltonian (3.33). I assume that there is no direct coupling between the spin and the transmission line, only a resonator-line coupling. The quantum master equations for $\langle\hat{a}\rangle$, $\langle\hat{\sigma}_-\rangle$ and $\langle\hat{\sigma}_z\rangle$ without driving read:[18]

$$\begin{aligned}
\frac{\mathrm{d}}{\mathrm{d}\,t}\,\langle\hat{a}\rangle &= -(i\omega_\mathrm{r}+\kappa)\langle\hat{a}\rangle - iG_1^*\langle\hat{\sigma}_-\rangle,\\
\frac{\mathrm{d}}{\mathrm{d}\,t}\langle\hat{\sigma}_-\rangle &= -(i\omega_\mathrm{q}+\gamma_\perp)\langle\hat{\sigma}_-\rangle + iG_1\langle\hat{\sigma}_z\hat{a}\rangle,\\
\frac{\mathrm{d}}{\mathrm{d}\,t}\langle\hat{\sigma}_z\rangle &= -\gamma_\parallel\left(\langle\hat{\sigma}_z\rangle + (\Delta P)_\mathrm{e}\right) - 2iG_1\langle\hat{\sigma}_+\hat{a}\rangle + 2iG_1^*\langle\hat{\sigma}_-\hat{a}^\dagger\rangle,
\end{aligned} \tag{4.92}$$

where I wrote $\gamma_\perp$ and $\gamma_\parallel$ instead of $\Gamma_\perp$ and $\Gamma_\parallel$ because now the spin is not coupled to the transmission line. The coupling of the spin with its environment takes $\langle\hat{\sigma}_z\rangle$ to its equilibrium value $-(\Delta P)_\mathrm{e}$ at long times ($t \gg \gamma_\parallel^{-1} = T_1$).

These equations look very similar to Eq. (4.75) for a spin coupled to a line with coherent driving, now with the resonator field playing the role of the input field on the spin. However, there is an important difference: spin and resonator are entangled, so this drive is entering into the spin equations as the correlators $\langle\hat{\sigma}_z\hat{a}\rangle$, $\langle\hat{\sigma}_+\hat{a}\rangle$ and $\langle\hat{\sigma}_-\hat{a}^\dagger\rangle$. In fact, computing the quantum master equations for these correlators generates an infinite hierarchy of coupled equations for higher order correlators of spin and resonator operators. Thus, the infinite system of equations must be truncated in order to obtain approximate solutions.

4.6.2 Ensemble-resonator system

Luckily, there is a justification for the truncation of the system of equations if an ensemble of N spins coupled to the resonator is considered instead of

[18] The equations for $\langle\hat{a}^\dagger\rangle$ and $\langle\hat{\sigma}_+\rangle$ are just the Hermitian conjugates of those of $\langle\hat{a}\rangle$ and $\langle\hat{\sigma}_-\rangle$.

a single spin, with a quantum master equation for every single spin in the ensemble [7]:

$$\begin{aligned}
\frac{\mathrm{d}}{\mathrm{d}\,t}\langle\hat{a}\rangle &= -(i\omega_\mathrm{r}+\kappa)\langle\hat{a}\rangle - i\sum_{k=1}^{N} G_{1,\,k}^{*}\langle\hat{\sigma}_{-,\,k}\rangle,\\
\frac{\mathrm{d}}{\mathrm{d}\,t}\langle\hat{\sigma}_{-,\,k}\rangle &= -(i\omega_\mathrm{q}+\gamma_\perp)\langle\hat{\sigma}_{-,\,k}\rangle + iG_{1,\,k}\langle\hat{\sigma}_{z,\,k}\hat{a}\rangle,\\
\frac{\mathrm{d}}{\mathrm{d}\,t}\langle\hat{\sigma}_{z,\,k}\rangle &= -\gamma_\parallel\left(\langle\hat{\sigma}_{z,\,k}\rangle + (\Delta P)_\mathrm{e}\right) - 2iG_{1,\,k}\langle\hat{\sigma}_{+,\,k}\hat{a}\rangle + 2iG_{1,\,k}^{*}\langle\hat{\sigma}_{-,\,k}\hat{a}^\dagger\rangle,
\end{aligned} \tag{4.93}$$

where $\gamma_\perp$ is now the inverse of T_2^* if there is inhomogeneous broadening. In the semi-classical limit ($N\to\infty$), the correlators $\langle\hat{\sigma}_{z,\,j}\hat{a}\rangle$, $\langle\hat{\sigma}_{+,\,j}\hat{a}\rangle$ and $\langle\hat{\sigma}_{-,\,j}\hat{a}^\dagger\rangle$ can be approximated by the factorizations $\langle\hat{\sigma}_{z,\,j}\rangle\langle\hat{a}\rangle$, $\langle\hat{\sigma}_{+,\,j}\rangle\langle\hat{a}\rangle$ and $\langle\hat{\sigma}_{-,\,j}\rangle\langle\hat{a}^\dagger\rangle$ [8]:

$$\begin{aligned}
\frac{\mathrm{d}}{\mathrm{d}\,t}\langle\hat{a}\rangle &= -(i\omega_\mathrm{r}+\kappa)\langle\hat{a}\rangle - i\sum_{j=1}^{N} G_{1,\,j}^{*}\langle\hat{\sigma}_{-,\,j}\rangle,\\
\frac{\mathrm{d}}{\mathrm{d}\,t}\langle\hat{\sigma}_{-,\,j}\rangle &= -(i\omega_\mathrm{q}+\gamma_\perp)\langle\hat{\sigma}_{-,\,j}\rangle + iG_{1,\,j}\langle\hat{\sigma}_{z,\,j}\rangle\langle\hat{a}\rangle,\\
\frac{\mathrm{d}}{\mathrm{d}\,t}\langle\hat{\sigma}_{z,\,j}\rangle &= -\gamma_\parallel\left(\langle\hat{\sigma}_{z,\,j}\rangle + (\Delta P)_\mathrm{e}\right)\\
&\quad - 2iG_{1,\,j}\langle\hat{\sigma}_{+,\,j}\rangle\langle\hat{a}\rangle + 2iG_{1,\,j}^{*}\langle\hat{\sigma}_{-,\,j}\rangle\langle\hat{a}^\dagger\rangle.
\end{aligned} \tag{4.94}$$

At long times all the coherences $\langle\hat{\sigma}_{-,\,j}\rangle$ vanish, and therefore all $\langle\hat{\sigma}_{z,\,j}\rangle$ relax to their equilibrium value $-(\Delta P)_\mathrm{e}$.

4.6.3 Driving the ensemble-resonator system

Let us assume that $\langle\hat{a}\rangle = \langle\hat{\sigma}_{-,\,j}\rangle = 0$ and $\langle\hat{\sigma}_{z,\,j}\rangle = -(\Delta P)_\mathrm{e}$ when the driving starts. Also, if the single spin-photon couplings $G_{1,\,k}$ are small enough, each $\langle\hat{\sigma}_{z,\,j}\rangle$ remains close to its equilibrium value during all the measurement. Then, introducing the driving only in the resonator (see Eq. (4.27)) yields:

$$\begin{aligned}
\frac{\mathrm{d}}{\mathrm{d}\,t}\langle\hat{a}\rangle &= -(i\omega_\mathrm{r}+\kappa)\langle\hat{a}\rangle - i\sum_{j=1}^{N} G_{1,\,j}^{*}\langle\hat{\sigma}_{-,\,j}\rangle - i\sqrt{\kappa_\mathrm{c}}\alpha_\mathrm{in}e^{-i\omega_\mathrm{d}t},\\
\frac{\mathrm{d}}{\mathrm{d}\,t}\langle\hat{\sigma}_{-,\,j}\rangle &= -(i\omega_\mathrm{q}+\gamma_\perp)\langle\hat{\sigma}_{-,\,j}\rangle - iG_{1,\,j}(\Delta P)_\mathrm{e}\langle\hat{a}\rangle.
\end{aligned} \tag{4.95}$$

A collective ladder operator $\hat{\sigma}_-$ can be defined as (recall the operator $\hat{b}$ in Eq. (3.45) of chapter 3):

$$\hat{\sigma}_- := \frac{1}{G_N}\sum_{j=1}^{N} G_{1,j}^{*}\,\hat{\sigma}_{-,\,j}\,, \tag{4.96}$$

with $G_N = G_{1,\mathrm{rms}}\sqrt{N}$. $G_{1,\mathrm{rms}}$ is the root mean square of the N different couplings as defined in Eq. (3.46) of chapter 3. Substituting in Eq. (4.95), one finds:

$$\begin{aligned}\frac{\mathrm{d}}{\mathrm{d}\,t}\langle\hat{a}\rangle &= -(i\omega_\mathrm{r}+\kappa)\langle\hat{a}\rangle - iG_N\langle\hat{\sigma}_-\rangle - i\sqrt{\kappa_\mathrm{c}}\alpha_\mathrm{in}e^{-i\omega_\mathrm{d}t},\\ \frac{\mathrm{d}}{\mathrm{d}\,t}\langle\hat{\sigma}_-\rangle &= -(i\omega_\mathrm{q}+\gamma_\perp)\langle\hat{\sigma}_-\rangle - iG_N(\Delta P)_\mathrm{e}\langle\hat{a}\rangle,\end{aligned} \tag{4.97}$$

or, in matrix form:

$$\frac{\mathrm{d}}{\mathrm{d}\,t}\boldsymbol{x}(t) = \boldsymbol{M}\boldsymbol{x}(t) + \boldsymbol{f}(t)e^{-i\omega_\mathrm{d}t}, \tag{4.98}$$

with the definitions:

$$\boldsymbol{x}(t) := \begin{pmatrix}\langle\hat{a}\rangle(t)\\ \langle\hat{\sigma}_-\rangle(t)\end{pmatrix}, \qquad \boldsymbol{f}(t) := \begin{pmatrix}-i\sqrt{\kappa_\mathrm{c}}\alpha_\mathrm{in}(t)\\ 0\end{pmatrix} \tag{4.99}$$

and:

$$\boldsymbol{M} := -\begin{pmatrix}(i\omega_\mathrm{r}+\kappa) & iG_N\\ iG_N(\Delta P)_\mathrm{e} & (i\omega_\mathrm{q}+\gamma_\perp)\end{pmatrix}. \tag{4.100}$$

The solution of Eq. (4.98) is:

$$\boldsymbol{x}(t) = e^{\boldsymbol{M}t}\boldsymbol{x}(0) + \int_0^t d\tau e^{\boldsymbol{M}(t-\tau)}e^{-i\omega_\mathrm{d}\tau}\boldsymbol{f}(\tau)\ . \tag{4.101}$$

As in the dynamics of the bare resonator, see Eq. (4.64), the first term of the solution is the transient state of the system, and the second term that is the emerging driven state with frequency ω_d. The driving $\boldsymbol{f}(t)$ is time-dependent in general, with $\alpha_\mathrm{in}(t)$ being the envelope of the input signal. For a square pulse, $\boldsymbol{f}(t)$ is constant, and the response can be easily obtained by computing the eigenvalues λ_n and eigenvectors $\boldsymbol{q}_n$ of $\boldsymbol{M}$:

$$\begin{aligned}\boldsymbol{x}_\mathbf{pulse}(t) &= \sum_{n=1,2}\boldsymbol{q}_n\boldsymbol{q}_n^*\left(e^{\lambda_n t}\boldsymbol{x}(0) + \frac{e^{(\lambda_n+i\omega_\mathrm{d})t}-1}{\lambda_n+i\omega_\mathrm{d}}\boldsymbol{f}\right),\\ \boldsymbol{x}_\mathbf{decay}(t) &= \sum_{n=1,2}\boldsymbol{q}_n\boldsymbol{q}_n^*e^{\lambda_n t}\boldsymbol{x}_\mathbf{pulse}(T)\,.\end{aligned} \tag{4.102}$$

For long times only the driven state remains, yielding the scattering parameters S_{11} and S_{21}:

$$\begin{aligned}S_{21}(\omega_\mathrm{d}) &= 1 - \frac{\kappa_\mathrm{c}}{i(\omega_\mathrm{r}-\omega_\mathrm{d})+\kappa+\dfrac{G_N^2(T)}{i(\omega_\mathrm{q}-\omega_\mathrm{d})+\gamma_\perp}}\ ,\\ S_{11}(\omega_\mathrm{d}) &= -\frac{\kappa_\mathrm{c}}{i(\omega_\mathrm{r}-\omega_\mathrm{d})+\kappa+\dfrac{G_N^2(T)}{i(\omega_\mathrm{q}-\omega_\mathrm{d})+\gamma_\perp}}\ ,\end{aligned} \tag{4.103}$$

with a temperature dependent coupling $G_N(T)$:

$$G_N^2(T) := G_N^2(\Delta P)_{\rm e}. \tag{4.104}$$

$G_N \equiv G_N(T=0)$ is the limit of the coupling at zero temperature. At very low temperatures, $(\Delta P)_{\rm e} \simeq 1$, and the ensemble-resonator is equivalent to a system of two coupled resonators with a coupling rate G_N.

4.6.4 Weak and strong coupling

Section 3.3 in chapter 3 described how the qubit-resonator (or spin-resonator, or spin ensemble-resonator) system formed pairs of polaritonic states, that is, superpositions of qubit/spin/ensemble states and resonator states. In resonance, the energies of the states of each pair are split by twice the coupling between the subsystems.

Consider the case of the ensemble-resonator system. The strength of the coupling gives two distinct regimes, defined by opposite limits of the ratio between $G_N\sqrt{(\Delta P)_{\rm e}}$ and $\gamma_\perp$. In the strong coupling regime ($G_N\sqrt{(\Delta P)_{\rm e}}/\gamma_\perp > 1$), the ensemble-resonator coupling is faster than the decoherence rate of the ensemble, which is typically much faster than the decoherence rate of the resonator, κ. Conversely, the decoherence of the ensemble is the dominant process in the weak coupling regime ($G_N\sqrt{(\Delta P)_{\rm e}}/\gamma_\perp \ll 1$).

Let us study $S_{21}(\omega_{\rm d})$ in these two regimes. The transmission is minimum when the imaginary part of the denominator in Eq. (4.103) vanishes. That is, when:

$$(\omega_{\rm r}-\omega_{\rm d})(\omega_{\rm q}-\omega_{\rm d})^2 + (\omega_{\rm r}-\omega_{\rm d})\gamma_\perp^2 + (\omega_{\rm d}-\omega_{\rm q})G_N^2(\Delta P)_{\rm e} = 0\,. \tag{4.105}$$

In the strong coupling regime, strong enough so that $G_N\sqrt{(\Delta P)_{\rm e}}/\gamma_\perp \gg 1$, the second term in Eq. (4.105) is neglected:

$$(\omega_{\rm r}-\omega_{\rm d})(\omega_{\rm q}-\omega_{\rm d}) \simeq G_N^2(\Delta P)_{\rm e}\,, \tag{4.106}$$

which gives:

$$\omega_{\rm d,\pm} = \frac{\omega_{\rm r}+\omega_{\rm q}}{2} \pm \sqrt{\left(\frac{\omega_{\rm r}-\omega_{\rm q}}{2}\right)^2 + G_N^2(\Delta P)_{\rm e}}. \tag{4.107}$$

In resonance ($\omega_{\rm r} = \omega_{\rm q}$), the system has two normal modes with frequencies $\omega_{\rm d,\pm} = \omega_{\rm r} \pm G_N\sqrt{(\Delta P)_{\rm e}}$. The transmission shows two minima at $\omega_{\rm d,\pm}$ (see Eq. (3.42) and Fig. 3.6 in chapter 3). Substituting $\omega_{\rm d,\pm}$ as the driving frequency in the real part of the denominator gives that the half width of each of the two

peaks in resonance is $\kappa + \gamma_\perp$. For any ω_r and ω_q, the two minima appear at the frequencies defined by Eq. (3.42) and shown in Fig. 3.6.

In the weak coupling regime, only a minimum of the transmission is found instead of two, with resonance frequency and half width similar to those of the bare resonator. Substituting $\omega_\mathrm{q} - \omega_\mathrm{d}$ by $\omega_\mathrm{q} - \omega_\mathrm{r}$ in the transmission, the imaginary part of the denominator vanishes when $\omega_\mathrm{d} = \tilde{\omega}_\mathrm{r}$, while the half width $\tilde{\kappa}$ of the resonance is given by the real part of the denominator:

$$\begin{aligned} \tilde{\omega}_\mathrm{r} :=& \omega_\mathrm{r} + \left[\frac{G_N^2 (\Delta P)_\mathrm{e}}{(\omega_\mathrm{q} - \omega_\mathrm{r})^2 + \gamma_\perp^2}\right](\omega_\mathrm{r} - \omega_\mathrm{q}), \\ \tilde{\kappa} :=& \kappa + \left[\frac{G_N^2 (\Delta P)_\mathrm{e}}{(\omega_\mathrm{q} - \omega_\mathrm{r})^2 + \gamma_\perp^2}\right]\gamma_\perp. \end{aligned} \tag{4.108}$$

In many transmission experiments, the hybrid system is in between these two regimes ($G_N\sqrt{(\Delta P)_\mathrm{e}}/\gamma_\perp \sim 1$), with the coupling slightly below $\gamma_\perp$ but large enough to reach the high-cooperativity regime. In this regime, defined by a cooperativity $C := G_N^2(\Delta P)_\mathrm{e}/\gamma_\perp\kappa$ larger than one, the coupling is strong in the sense that at resonance nearly every photon entering the cavity is coherently transferred into the qubits/spins [9]. While strong coupling ensures a double peak in the transmission, this is not necessarily the case for high-cooperativity (see Fig. 4.4).

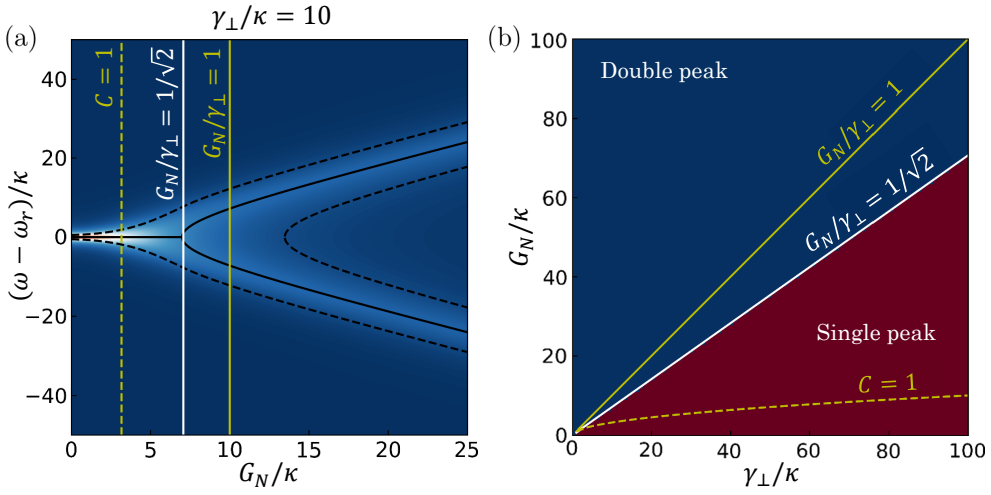

Figure 4.4: (a) Transmission of the spin ensemble-resonator system as a function of the coupling G_N (including $(\Delta P)_\mathrm{e}$, that is, $G_N \propto \sqrt{(\Delta P)_\mathrm{e}}$) and the detuning from the frequency of the resonator, ω_r, both normalized by the resonator decoherence rate κ. The ratio of the spin decoherence rate $\gamma_\perp$ to κ is 10. The minima of the transmission at different values of G_N trace the solid black lines, with the points at half height of the peaks trace the dashed lines. Note the bifurcation point at $G_N/\gamma_\perp = 1/\sqrt{2}$. (b) Number of transmission minima for different values of G_N/κ and Γ/κ. The single peak and double peak regions are separated by the $G_N/\gamma_\perp = 1/\sqrt{2}$ line.

4.7 Generalization to high spin systems

This last section generalizes the transmission formulas from previous sections to higher spin ensembles. The simplest case is a single spin $S > 1/2$ directly coupled to a transmission line.

4.7.1 Single spin $S > 1/2$ coupled to a transmission line

The system coupling operator of Hamiltonian (4.20) is now:

$$\hat{S} = \sum_{\alpha=0}^{2S} \sum_{\beta>\alpha} \left(\hat{X}^{\alpha\beta} + \hat{X}^{\beta\alpha} \right). \tag{4.109}$$

Computing the time evolution of the expectation value of each $\hat{X}^{\alpha\beta}$ with the Hamiltonian of a single spin $S > 1/2$ (recall Eq. (3.15) in chapter 3) gives:

$$\begin{aligned} \frac{\mathrm{d}}{\mathrm{d}\,t}\langle \hat{X}^{\alpha\beta} \rangle &= -\frac{i}{\hbar} \operatorname{Tr}\left(\hat{X}^{\alpha\beta} \left[H_{\mathrm{S}}, \rho \right] \right) = -\frac{i}{\hbar} \operatorname{Tr}\left(\hat{X}^{\alpha\beta} \sum_{\gamma=0}^{2S} E_\gamma \left[\hat{X}^{\gamma\gamma}, \rho \right] \right) \\ &= i \frac{E_\alpha - E_\beta}{\hbar} \langle \hat{X}^{\alpha\beta} \rangle, \end{aligned} \tag{4.110}$$

where $\rho(t)$ is the density matrix of the spin. The solution of this equation for $\langle \hat{X}^{\alpha\beta} \rangle$ is just:

$$\langle \hat{X}^{\alpha\beta} \rangle = \langle \hat{X}^{\alpha\beta} \rangle(0) e^{i \frac{E_\alpha - E_\beta}{\hbar} t}, \tag{4.111}$$

as expected from the definition of the level shift operators $\hat{X}^{\alpha\beta}$. The time-evolution of $\langle \hat{S} \rangle$ without interactions is then:

$$\langle \hat{S} \rangle(t) = \sum_{\alpha=0}^{2S} \sum_{\beta>\alpha} \left(\langle \hat{X}^{\alpha\beta} \rangle e^{-i\omega_{\alpha\beta} t} + \langle \hat{X}^{\beta\alpha} \rangle e^{i\omega_{\alpha\beta} t} \right), \tag{4.112}$$

with the (positive) frequencies $\omega_{\alpha\beta}$:[19]

$$\omega_{\alpha\beta} = \frac{E_\beta - E_\alpha}{\hbar}. \tag{4.113}$$

Assuming a non-degenerate frequency spectrum, that is, that all frequencies $\omega_{\alpha\beta}$ are different, the spectral decomposition of $\hat{S}$ is given by all $\hat{S}(\omega_{\alpha\beta}) = \hat{X}^{\beta\alpha}$

[19] Remember that α and β were chosen in $\hat{S}$ so that $E_\beta > E_\alpha$.

and $\hat{S}(-\omega_{\alpha\beta}) = \hat{X}^{\alpha\beta}$. The sum in $\Omega_{\rm S}$ in Eq. (4.54) runs over all the different frequencies $\omega_{\alpha\beta}$:

$$\mathcal{R}(t) = \sum_{\alpha=0}^{2S} \sum_{\beta>\alpha} \Gamma(\omega_{\alpha\beta}) \Big(\bar{n}(\omega_{\alpha\beta}, T) \mathcal{D}(\omega_{\alpha\beta}, t) + (\bar{n}(\omega_{\alpha\beta}, T) + 1) \mathcal{D}(-\omega_{\alpha\beta}, t) \Big), \tag{4.114}$$

with:[20]

$$\begin{aligned} \mathcal{D}(\omega_{\alpha\beta}, t) &= 2\hat{X}^{\beta\alpha} \rho(t) \hat{X}^{\alpha\beta} - \Big\{ \hat{X}^{\alpha\alpha}, \rho(t) \Big\}, \\ \mathcal{D}(-\omega_{\alpha\beta}, t) &= 2\hat{X}^{\alpha\beta} \rho(t) \hat{X}^{\beta\alpha} - \Big\{ \hat{X}^{\beta\beta}, \rho(t) \Big\}, \end{aligned} \tag{4.115}$$

where $\rho(t)$ is again the density matrix of the spin. Let us consider first the time evolution of the expectation value of the coherence $\hat{X}^{\alpha\beta}$ (with $\beta > \alpha$):

$$\begin{aligned} \frac{\mathrm{d}}{\mathrm{d}\,t} \langle \hat{X}^{\alpha\beta} \rangle &= \mathrm{Tr} \left(\hat{X}^{\alpha\beta} \dot{\rho}(t) \right) \\ &= -\frac{i}{\hbar} \mathrm{Tr} \left(\hat{X}^{\alpha\beta} \left[H_{\rm S}, \rho(t) \right] \right) + \mathrm{Tr} \left(\hat{X}^{\alpha\beta} \mathcal{R}(t) \right) \\ &= -i\omega_{\alpha\beta} \langle \hat{X}^{\alpha\beta} \rangle - \Gamma_{\perp,\alpha\beta} \langle \hat{X}^{\alpha\beta} \rangle, \end{aligned} \tag{4.116}$$

with $\Gamma_{\perp,\alpha\beta} := \gamma_{\perp,\alpha\beta} + \Gamma_\alpha + \Gamma_\beta$, where $\gamma_{\perp,\alpha\beta}$ is the inverse of the coherence time T_2 of the $\alpha \to \beta$ transition without coupling to the transmission line. The decay rates Γ_α are:

$$\Gamma_\alpha := \sum_{\gamma<\alpha} (G_1^{(\rm line)})_{\gamma\alpha} (\bar{n}(\omega_{\gamma\alpha}, T) + 1) + \sum_{\gamma>\alpha} (G_1^{(\rm line)})_{\alpha\gamma} \bar{n}(\omega_{\alpha\gamma}, T). \tag{4.117}$$

Here the couplings $(G_1^{(\rm line)})_{\alpha\beta}$ were identified to the rates $\Gamma(\omega_{\alpha\beta}) = 2\pi J(\omega_{\alpha\beta})$ in $\mathcal{R}(t)$. Solving the differential equation, one obtains:

$$\langle \hat{X}^{\alpha\beta} \rangle(t) = \langle \hat{X}^{\alpha\beta} \rangle(0) e^{\left(-i\omega_{\alpha\beta} - \Gamma_{\perp,\alpha\beta}\right)t}. \tag{4.118}$$

The same derivation can be done for $\langle \hat{X}^{\beta\alpha} \rangle$:

$$\langle \hat{X}^{\beta\alpha} \rangle(t) = \langle \hat{X}^{\beta\alpha} \rangle(0) e^{\left(i\omega_{\alpha\beta} - \Gamma_{\perp,\alpha\beta}\right)t}, \tag{4.119}$$

with the same decay rate $\Gamma_{\perp,\alpha\beta}$.

[20] The last term of the dissipators $\mathcal{D}(\pm\omega_{\alpha\beta}, t)$ was written using that $\hat{X}^{\alpha\beta}\hat{X}^{\beta\alpha} = \hat{X}^{\alpha\alpha}$ and $\hat{X}^{\beta\alpha}\hat{X}^{\alpha\beta} = \hat{X}^{\beta\beta}$.

The quantum master equation for the population $\langle \hat{X}^{\alpha\alpha} \rangle$ gives:[21]

$$\begin{aligned}\frac{\mathrm{d}}{\mathrm{d}\,t}\langle \hat{X}^{\alpha\alpha}\rangle &= \mathrm{Tr}\left(\hat{X}^{\alpha\alpha}\dot{\rho}(t)\right)\\ &= \mathrm{Tr}\left(\hat{X}^{\alpha\alpha}\mathcal{R}(t)\right)\\ &= 2\sum_{\gamma<\alpha}(G_1^{(\mathrm{line})})_{\gamma\alpha}(\bar{n}(\omega_{\gamma\alpha},T)+1)\langle \hat{X}^{\gamma\gamma}\rangle\\ &\quad + 2\sum_{\gamma>\alpha}(G_1^{(\mathrm{line})})_{\alpha\gamma}\bar{n}(\omega_{\alpha\gamma},T)\langle \hat{X}^{\gamma\gamma}\rangle\\ &\quad - 2\Gamma_\alpha\langle \hat{X}^{\alpha\alpha}\rangle.\end{aligned} \tag{4.120}$$

This is a system of $2S+1$ coupled first order linear differential equations. In general, $\langle \hat{X}^{\alpha\alpha}\rangle(t)$ will not be an exponential decay but a sum of exponential decays. Still, the steady state $\langle \hat{X}^{\alpha\alpha}\rangle_{\mathrm{ss}}$, the value to which $\langle \hat{X}^{\alpha\alpha}\rangle$ decays at long times, can be easily obtained. Taking $\frac{\mathrm{d}}{\mathrm{d}\,t}\langle \hat{X}^{\alpha\alpha}\rangle = 0$, one finds that the steady states of the populations are related by:

$$\begin{aligned}\langle \hat{X}^{\alpha\alpha}\rangle_{\mathrm{ss}} = \frac{1}{\Gamma_\alpha}\Big(&\sum_{\gamma<\alpha}(G_1^{(\mathrm{line})})_{\gamma\alpha}(\bar{n}(\omega_{\gamma\alpha},T)+1)\langle \hat{X}^{\gamma\gamma}\rangle_{\mathrm{ss}}\\ &+\sum_{\gamma>\alpha}(G_1^{(\mathrm{line})})_{\alpha\gamma}\bar{n}(\omega_{\alpha\gamma},T)\langle \hat{X}^{\gamma\gamma}\rangle_{\mathrm{ss}}\Big),\end{aligned} \tag{4.121}$$

with the solution:

$$\langle \hat{X}^{\alpha\alpha}\rangle_{\mathrm{ss}} = \frac{e^{-E_\alpha/k_{\mathrm{B}}T}}{Z(T)} =: \langle \hat{X}^{\alpha\alpha}\rangle_{\mathrm{e}}, \tag{4.122}$$

with $Z(T) = \sum_\gamma e^{-E_\gamma/k_{\mathrm{B}}T}$. That is, the population $\langle \hat{X}^{\alpha\alpha}\rangle$ relaxes to its value $\langle \hat{X}^{\alpha\alpha}\rangle_{\mathrm{e}}$ in thermal equilibrium, as expected.

4.7.2 Driving a single spin $S > 1/2$ through the transmission line

The interaction of a single spin $S > 1/2$ with a coherent drive is given by:

$$\begin{aligned}H_{\mathrm{drive}} = \hbar\sum_{\alpha=0}^{2S}\sum_{\beta>\alpha}\Big(&\sqrt{(G_1^{(\mathrm{line})})_{\alpha\beta}}\langle \hat{X}^{\alpha\beta}\rangle\\ &+\sqrt{(G_1^{(\mathrm{line})})_{\beta\alpha}}\langle \hat{X}^{\beta\alpha}\rangle\Big)\alpha_{\mathrm{in}}e^{-i\omega_{\mathrm{d}}t}.\end{aligned} \tag{4.123}$$

As with a spin 1/2, let us assume that the populations have already decayed to their values in thermal equilibrium before the driving starts, and

[21] Only the relaxation term of the quantum master equation remains, as $\hat{X}^{\alpha\alpha}$ commutes with H_{S}.

that the couplings $(G_1^{(\mathrm{line})})_{\alpha\beta}$ are small enough so the deviation from these values is negligible. Defining the difference of population in thermal equilibrium $(\Delta P_{\alpha\beta})_\mathrm{e} := \langle\hat{X}^{\alpha\alpha}\rangle_\mathrm{e} - \langle\hat{X}^{\beta\beta}\rangle_\mathrm{e}$, one obtains for the coherences $\langle\hat{X}^{\alpha\beta}\rangle$:

$$\begin{aligned}
\frac{\mathrm{d}}{\mathrm{d}\,t}\langle\hat{X}^{\alpha\beta}\rangle &= \mathrm{Tr}\left(\hat{X}^{\alpha\beta}\dot{\rho}(t)\right) \\
&= -\frac{i}{\hbar}\,\mathrm{Tr}\,\hat{X}^{\alpha\beta}\left[H_\mathrm{S},\rho(t)\right] + \mathrm{Tr}\,\hat{X}^{\alpha\beta}\mathcal{R}(t) \\
&\quad -\frac{i}{\hbar}\,\mathrm{Tr}\left(\hat{X}^{\alpha\beta}\left[H_\mathrm{drive},\rho(t)\right]\right) \\
&= -(i\omega_{\alpha\beta}+\Gamma_{\perp,\alpha\beta})\langle\hat{X}^{\alpha\beta}\rangle \\
&\quad - i\sqrt{(G_1^{(\mathrm{line})})_{\alpha\beta}}(\Delta P_{\alpha\beta})_\mathrm{e}\alpha_\mathrm{in}e^{-\omega_\mathrm{d}t} \\
&\quad - i\alpha_\mathrm{in}e^{-\omega_\mathrm{d}t}\sum_{\gamma\neq\alpha,\beta}\sqrt{(G_1^{(\mathrm{line})})_{\beta\gamma}}\langle\hat{X}^{\alpha\gamma}\rangle \\
&\quad + i\alpha_\mathrm{in}e^{-\omega_\mathrm{d}t}\sum_{\gamma\neq\alpha,\beta}\sqrt{(G_1^{(\mathrm{line})})_{\gamma\alpha}}\langle\hat{X}^{\gamma\beta}\rangle.
\end{aligned} \tag{4.124}$$

In a transmission measurement probing the transition $\alpha \leftrightarrow \beta$, the driving frequency ω_d will be close to the transition frequency $\omega_{\alpha\beta}$ and far from the frequencies of other spin transitions, assuming that the spin frequency spectrum is non-degenerate. Then, none of the terms in the last two rows of Eq. (4.124) oscillate with frequencies close to ω_d or $\omega_{\alpha\beta}$. Dropping these terms, one obtains:

$$\frac{\mathrm{d}}{\mathrm{d}\,t}\langle\hat{X}^{\alpha\beta}\rangle \simeq -(i\omega_{\alpha\beta}+\Gamma_{\perp,\alpha\beta})\langle\hat{X}^{\alpha\beta}\rangle - i\sqrt{(G_1^{(\mathrm{line})})_{\alpha\beta}}(\Delta P_{\alpha\beta})_\mathrm{e}\alpha_\mathrm{in}e^{-\omega_\mathrm{d}t}, \tag{4.125}$$

and, if all coherences have already decayed to zero before driving the system, the following scattering parameters S_{21} and S_{11} are obtained at long times ($t \gg 1/\Gamma_{\perp,\alpha\beta}$):

$$\begin{aligned}
S_{21}(\omega_\mathrm{d}\simeq\omega_{\alpha\beta}) &= 1 - \frac{(G_1^{(\mathrm{line})})_{\alpha\beta}(\Delta P_{\alpha\beta})_\mathrm{e}}{i(\omega_{\alpha\beta}-\omega_\mathrm{d})+\Gamma_{\perp,\alpha\beta}}, \\
S_{11}(\omega_\mathrm{d}\simeq\omega_{\alpha\beta}) &= -\frac{(G_1^{(\mathrm{line})})_{\alpha\beta}(\Delta P_{\alpha\beta})_\mathrm{e}}{i(\omega_{\alpha\beta}-\omega_\mathrm{d})+\Gamma_{\perp,\alpha\beta}}.
\end{aligned} \tag{4.126}$$

4.7.3 Driving a spin $S > 1/2$ ensemble through the transmission line

Following the steps in section 4.5.3, the transmission and reflection scattering parameters for a higher spin ensemble coupled to the transmission line are:

$$\begin{aligned} S_{21}(\omega_\mathrm{d} \simeq \omega_{\alpha\beta}) &= \frac{1}{1-\theta(\omega_\mathrm{d} \simeq \omega_{\alpha\beta})}, \\ S_{11}(\omega_\mathrm{d} \simeq \omega_{\alpha\beta}) &= \frac{\theta(\omega_\mathrm{d} \simeq \omega_{\alpha\beta})}{1-\theta(\omega_\mathrm{d} \simeq \omega_{\alpha\beta})}, \end{aligned} \tag{4.127}$$

with:

$$\begin{aligned} \theta(\omega_\mathrm{d} \simeq \omega_{\alpha\beta}) &= \sum_{j=1}^{N} \theta_j(\omega_\mathrm{d} \simeq \omega_{\alpha\beta}) \\ &= -\sum_{j=1}^{N} \frac{(G_{1,\,j}^{(\mathrm{line})})_{\alpha\beta}(\Delta P_{\alpha\beta})_\mathrm{e}}{\left[(\Gamma_{\perp,\,j})_{\alpha\beta} - (G_{1,\,j}^{(\mathrm{line})})_{\alpha\beta}(\Delta P_{\alpha\beta})_\mathrm{e}\right] + i\,(\omega_{\alpha\beta} - \omega_\mathrm{d})}. \end{aligned} \tag{4.128}$$

This can be simplified if $(\Delta P_{\alpha\beta})_\mathrm{e} \simeq 1$, which will not hold in general for transitions between excited states, or if the coupling $(G_{1,\,j}^{(\mathrm{line})})_{\alpha\beta}$ to the transmission line is much smaller than the total losses $(\Gamma_{\perp,\,j})_{\alpha\beta}$:

$$\theta(\omega_\mathrm{d} \simeq \omega_{\alpha\beta}) \simeq -\frac{(G_N^{(\mathrm{line})})_{\alpha\beta}(\Delta P_{\alpha\beta})_\mathrm{e}}{\gamma_{\perp,\,\alpha\beta} + i\,(\omega_{\alpha\beta} - \omega_\mathrm{d})}, \tag{4.129}$$

with:

$$(G_N^{(\mathrm{line})})_{\alpha\beta} = \sum_{j=1}^{N} (G_1^{(\mathrm{line})})_{\alpha\beta}. \tag{4.130}$$

Substituting in Eq. (4.127), the transmission and reflection parameters read:

$$\begin{aligned} S_{21}(\omega_\mathrm{d} \simeq \omega_{\alpha\beta}) &= \frac{\gamma_{\perp,\,\alpha\beta} + i\,(\omega_{\alpha\beta} - \omega_\mathrm{d})}{\gamma_{\perp,\,\alpha\beta} + (G_N^{(\mathrm{line})})_{\alpha\beta}(\Delta P_{\alpha\beta})_\mathrm{e} + i\,(\omega_{\alpha\beta} - \omega_\mathrm{d})}, \\ S_{11}(\omega_\mathrm{d} \simeq \omega_{\alpha\beta}) &= -\frac{(G_N^{(\mathrm{line})})_{\alpha\beta}(\Delta P_{\alpha\beta})_\mathrm{e}}{\gamma_{\perp,\,\alpha\beta} + (G_N^{(\mathrm{line})})_{\alpha\beta}(\Delta P_{\alpha\beta})_\mathrm{e} + i\,(\omega_{\alpha\beta} - \omega_\mathrm{d})}. \end{aligned} \tag{4.131}$$

4.7.4 Driving a spin $S > 1/2$ ensemble-resonator system

As with spin 1/2 ensembles, a large number of spins is needed in order to factorize the correlators that appear in the equations of the time evolution

of the expectation values of the resonator and the spin operators in a hybrid ensemble-resonator system (see sections 4.6.1 and 4.6.2). This system is described by the generalized Tavis-Cummings Hamiltonian (3.49). Assuming that the ensemble is not directly coupled to the transmission line, sending a coherent drive to the resonator gives the following quantum master equations for $\langle \hat{a} \rangle$ and each $\langle \hat{X}_j^{\alpha\beta} \rangle$:

$$\begin{aligned} \frac{\mathrm{d}}{\mathrm{d}\,t}\langle \hat{a} \rangle &= -(i\omega_\mathrm{r} + \kappa)\langle \hat{a} \rangle - i \sum_{j=1}^{N} \sum_{\alpha=0}^{2S} \sum_{\beta>\alpha} (G_{1,\,j})_{\alpha\beta} \langle \hat{X}_j^{\alpha\beta} \rangle - i\sqrt{\kappa_\mathrm{c}}\alpha_\mathrm{in} e^{-i\omega_\mathrm{d} t}, \\ \frac{\mathrm{d}}{\mathrm{d}\,t}\langle \hat{X}_j^{\alpha\beta} \rangle &\simeq -(i\omega_{\alpha\beta} + \gamma_{\perp,\alpha\beta})\langle \hat{X}_j^{\alpha\beta} \rangle - i(G_{1,\,j})_{\beta\alpha}(\Delta P_{\alpha\beta})_\mathrm{e} \langle \hat{a} \rangle. \end{aligned} \tag{4.132}$$

Here the populations $\langle \hat{X}_j^{\alpha\alpha} \rangle$ have been replaced by their values in thermal equilibrium, which is valid for small single spin couplings $(G_{1,\,j})_{\beta\alpha}$.

For each transition, a collective operator $\hat{X}^{\alpha\beta}$ can be defined:

$$\hat{X}^{\alpha\beta} := \frac{1}{(G_N)_{\alpha\beta}} \sum_{j=1}^{N} (G_{1,\,j})_{\alpha\beta}\, \hat{X}_j^{\alpha\beta}, \tag{4.133}$$

with $(G_N)_{\alpha\beta} = (G_{1,\,\mathrm{rms}})_{\alpha\beta}\sqrt{N}$:

$$(G_{1,\,\mathrm{rms}})_{\alpha\beta} = \sqrt{\frac{1}{N} \sum_{j=1}^{N} |(G_{1,\,j})_{\alpha\beta}|^2}\,. \tag{4.134}$$

Substituting in Eq. (4.132), one obtains:

$$\begin{aligned} \frac{\mathrm{d}}{\mathrm{d}\,t}\langle \hat{a} \rangle &= -(i\omega_\mathrm{r} + \kappa)\langle \hat{a} \rangle - i \sum_{\alpha=0}^{2S} \sum_{\beta>\alpha} (G_N)_{\alpha\beta} \langle \hat{X}^{\alpha\beta} \rangle - i\sqrt{\kappa_\mathrm{c}}\alpha_\mathrm{in} e^{-i\omega_\mathrm{d} t}, \\ \frac{\mathrm{d}}{\mathrm{d}\,t}\langle \hat{X}^{\alpha\beta} \rangle &\simeq -(i\omega_{\alpha\beta} + \gamma_{\perp,\alpha\beta})\langle \hat{X}^{\alpha\beta} \rangle - i(G_N)_{\alpha\beta}(\Delta P_{\alpha\beta})_\mathrm{e} \langle \hat{a} \rangle. \end{aligned} \tag{4.135}$$

At long times, these equations yield the following scattering parameters [10]:

$$S_{21}(\omega_\mathrm{d}) = 1 - \frac{\kappa_\mathrm{c}}{i(\omega_\mathrm{r} - \omega_\mathrm{d}) + \kappa + \sum\limits_{\alpha=0}^{2S} \sum\limits_{\beta>\alpha} \dfrac{(G_N)_{\alpha\beta}^2 (\Delta P_{\alpha\beta})_\mathrm{e}}{i(\omega_{\alpha\beta} - \omega_\mathrm{d}) + \gamma_{\perp,\alpha\beta}}}\,, \tag{4.136}$$

$$S_{11}(\omega_\mathrm{d}) = -\frac{\kappa_\mathrm{c}}{i(\omega_\mathrm{r} - \omega_\mathrm{d}) + \kappa + \sum\limits_{\alpha=0}^{2S} \sum\limits_{\beta>\alpha} \dfrac{(G_N)_{\alpha\beta}^2 (\Delta P_{\alpha\beta})_\mathrm{e}}{i(\omega_{\alpha\beta} - \omega_\mathrm{d}) + \gamma_{\perp,\alpha\beta}}}\,.$$

Or, driving a resonator close to resonance with an specific transition $\alpha \leftrightarrow \beta$:

$$S_{21}(\omega_{\mathrm{d}} \simeq \omega_{\alpha\beta}) = 1 - \frac{\kappa_{\mathrm{c}}}{i(\omega_{\mathrm{r}} - \omega_{\mathrm{d}}) + \kappa + \dfrac{(G_N)^2_{\alpha\beta}(\Delta P_{\alpha\beta})_{\mathrm{e}}}{i(\omega_{\alpha\beta} - \omega_{\mathrm{d}}) + \gamma_{\perp,\alpha\beta}}}\,,$$
$$S_{11}(\omega_{\mathrm{d}} \simeq \omega_{\alpha\beta}) = -\frac{\kappa_{\mathrm{c}}}{i(\omega_{\mathrm{r}} - \omega_{\mathrm{d}}) + \kappa + \dfrac{(G_N)^2_{\alpha\beta}(\Delta P_{\alpha\beta})_{\mathrm{e}}}{i(\omega_{\alpha\beta} - \omega_{\mathrm{d}}) + \gamma_{\perp,\alpha\beta}}}\,. \tag{4.137}$$

The discussion of Eq. (4.137) in the weak and strong regimes is similar to the one in section 4.6.4.

References

[1] H. Goldstein, *Classical Mechanics* (Addison-Wesley, 1959).

[2] W. Greiner and J. Reinhardt, *Field quantization* (Springer, 1996).

[3] N. G. van Kampen, *Stochastic processes in physics and chemistry (Revised and enlarged edition)* (North-Holland, 1992).

[4] I. F. Quijandría Díaz, Ph.D. thesis, Universidad de Zaragoza (2016).

[5] J. García Ripoll, *Quantum information and quantum optics* (Cambridge University Press, 2022).

[6] S. M. Barnett and P. M. Radmore, *Methods in theoretical quantum optics* (Oxford Science Publications, 1997).

[7] S. Weichselbaumer, M. Zens, C. W. Zollitsch, M. S. Brandt, S. Rotter, R. Gross, and H. Huebl, Physical Review Letters **125**, 137701 (2020).

[8] M. Zens, D. O. Krimer, and S. Rotte, Physical Review A **100**, 013856 (2019).

[9] D. I. Schuster, A. P. Sears, E. Ginossar, L. DiCarlo, L. Frunzio, J. J. L. Morton, H. Wu, G. A. D. Briggs, B. B. Buckley, D. D. Awschalom, et al., Physical Review Letters **105**, 140501 (2010).

[10] A. Gómez-León, F. Luis, and D. Zueco, Physical Review Applied **17**, 064030 (2022).

Chapter 5

Strong coupling of organic free-radical molecules to lumped-element resonators

Chapter 2 introduced superconducting lumped-element resonators (LERs) as a suitable platform for controlling and measuring molecular spin qubits. LERs have several interesting properties as compared to coplanar resonators. Several LERs with different resonance frequencies ω_r can be coupled to the same readout transmission line, which allows measuring them independently (frequency multiplexing). Also, the impedance $Z = \sqrt{L/C}$ of the LER is independent from the transmission line impedance $Z_0 = 50\ \Omega$. This gives more freedom in the fabrication of low-inductance LERs (small L) in order to enhance the spin-photon coupling [1, 2].

While coplanar resonators have been already used to reach the strong coupling regime with molecular spin ensembles [3–5], with LERs this regime has been achieved only with non-molecular spin ensembles [6]. In this chapter I explore whether strong coupling can be achieved with molecular spin qubits coupled to LERs, in particular organic free radicals that realize model $S = 1/2$ systems [7]. These experiments illustrate the basic characteristics of a hybrid spin-LER platform.

5.1 Chip design and characterization

5.1.1 Chip design

I have used two superconducting chips, labeled *Test 1* and *Test 2*, made of a 100 nm-thick niobium (Nb) film deposited on top of a silicon substrate (see section 2.1.1 in chapter 2). Niobium is superconducting below $T_c = 9.26$ K. Twelve LERs with different resonance frequencies ω_r were patterned in the surface of each chip, side-coupled to the same transmission line. I labeled them from 1 to 12 from lowest to highest ω_r. Figure 5.1 shows both chip designs.

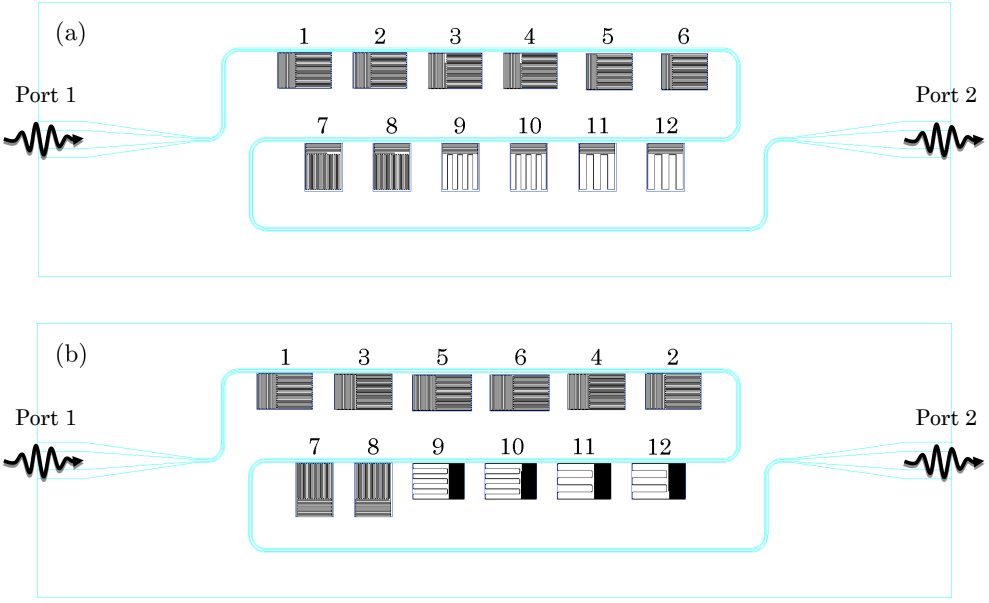

Figure 5.1: Vector file design of (a) *Test 1* and (b) *Test 2*. All twelve LERs (black) in each chip are side-coupled to a single transmission line (blue), and labeled in increasing ω_r. The ordering in the top row in *Test 2* is different from the ordering in *Test 1* so that some pairs of resonators with similar frequencies (LERs 1 and 2, and LERs 3 and 4) are farther apart.

Chips *Test 1* and *Test 2* were fabricated to explore different LER designs and test how different parameters affect the spin-photon coupling and the transmission characteristics. LER designs are shown in Figs. 5.2 and 5.3. Most of the resonators have both inductive and capacitive coupling to the transmission line, that is, they have parts of both the meandering inductor and the inter-digitated capacitor very close to the line (Fig. 5.2). The rest are placed so that only the inductor or the capacitor is close to the line, which gives either an inductive or capacitive resonator-line coupling (Fig. 5.3).

There also LERs with different geometric inductance L_{geo} in order to see its effect on the spin-resonator coupling. Between resonators with a similar design, their resonance frequency is tuned by increasing or decreasing the length of the last finger of the inter-digitated capacitor.

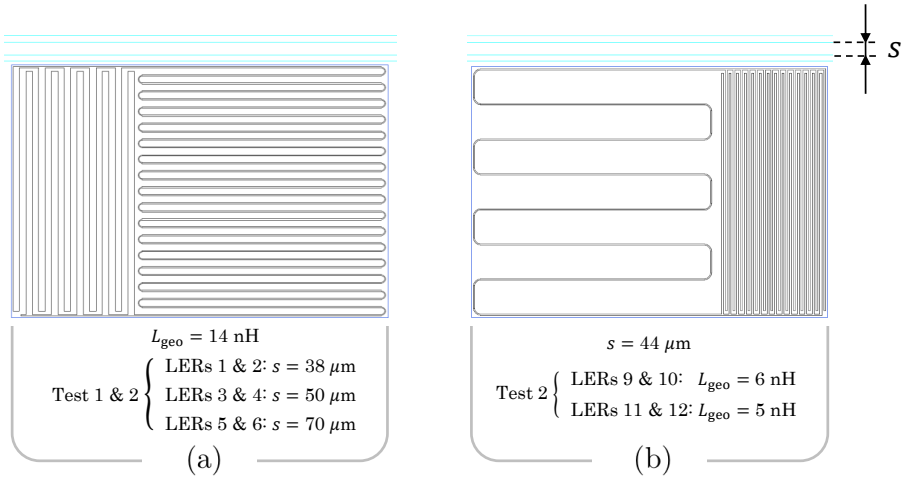

Figure 5.2: Examples of resonator designs having both inductive and capacitive coupling to the transmission line. The magnitude of this coupling is controlled by s, the shortest distance between the borders of the resonator and the central line of the transmission line. Higher line-resonator couplings are expected for shorter s. There are LERs with high (a) and low (b) geometric inductance L_{geo}.

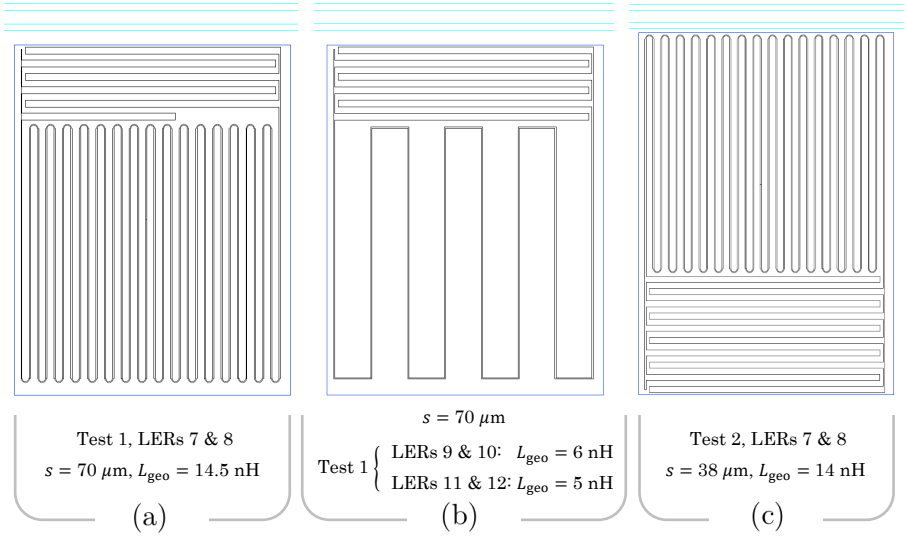

Figure 5.3: Examples of resonator designs with only capacitive coupling (a, b) or with only inductive coupling (c) to the transmission line. Designs (a) and (c) have a higher geometric inductance L_{geo} than design (b).

The ensemble-resonator coupling depends on the microwave magnetic field generated by the resonator, which in resonance is concentrated around the inductor. I used the 3D-MLSI software [8], which solves London equations for thin superconducting films with a finite element method, to compute the current distribution in the inductor in resonance. The magnetic field distribution on top of the inductor is computed using this current distribution. It is mainly contained within the plane perpendicular to the longer induction lines of the LER (see Fig. 5.4a). In a sample of free-radicals molecules with spin 1/2, only the microwave magnetic field perpendicular to the static magnetic $\boldsymbol{B_{dc}}$ contributes to the coupling (see section 3.3.1, and in particular Eq. (3.30)). Then, the best configuration in the experiment is to apply $\boldsymbol{B_{dc}}$ parallel to the longer inductor lines, as shown in Fig. 5.4a.

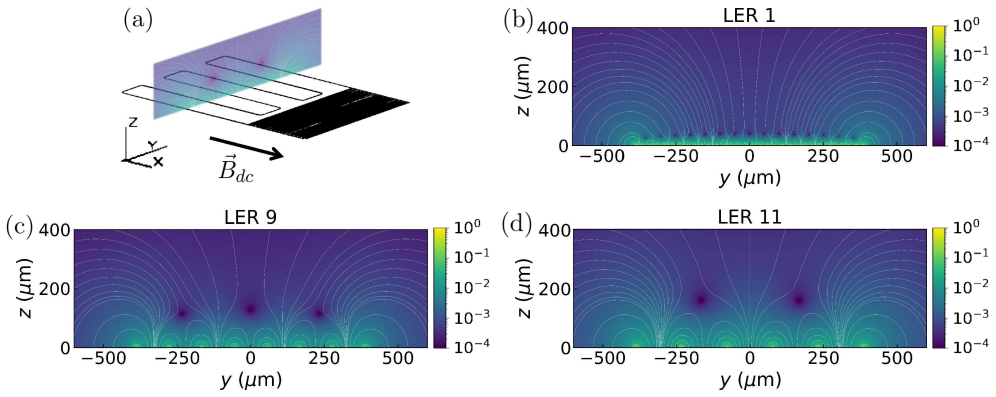

Figure 5.4: (a) Orientation of the plane containing the microwave magnetic field generated by the longer inductor lines with respect to the resonator design. The coupling is maximum if the static field $\boldsymbol{B_{dc}}$ is applied perpendicular to this plane (parallel to the inductor lines). (b-d) Maps showing the amplitude of the magnetic field within this plane generated by vacuum fluctuations in the resonator at the resonance frequency ω_r. The field distributions of three resonators in *Test 2* with different geometric inductance L_{geo} are shown: LER 1 (b), LER 9 (c), and LER 11 (d). Maps are normalized by the maximum field within the plane in each case: 3.05 nT for LER 1, 4.22 nT for LER 9 and 3.08 nT for LER 11. White solid lines show the field lines.

Figures 5.4b, 5.4c and 5.4d show the distribution of the magnetic field in the plane perpendicular to the inductor lines above LERs 1, 9 and 11 of *Test 2*. These resonators have different geometric inductance L_{geo}: 14 nH for LER 1, 6 nH for LER 9 and 5 nH for LER 11. The magnetic field generated by LER 1 is localized within a few microns above the inductor lines. This small mode volume is better suited for samples place very close to the chip surface. Conversely, LERs 9 and 11, with lower L_{geo}, generate a magnetic field distribution that spreads further from the surface (large mode volume), which is better for larger samples.

5.1.2 Characterization of *Test 1*

Prior to the experiments with spin samples, LERs in *Test 1* were characterized with transmission experiments at 17 mK and zero magnetic field. Each LER has a resonance, that is, a dip in transmission (S_{21}) centered around its resonance frequency ω_r. Figure 5.5) shows all the resonances in this chip except for LER 10. The results were fitted with the model for S_{21} around ω_r given by Eq. (4.67) in chapter 4, which is reproduced here for clarity:

$$S_{21}(\omega_d) = 1 - \frac{\kappa_c}{i(\omega_r - \omega_d) + \kappa}, \tag{5.1}$$

where ω_d is the input (driving) frequency and κ comprises the total losses of the photon mode, including internal losses (κ_i) and the line-resonator coupling (κ_c). Figures showing experimental results are shown in terms of the regular input frequency $f = \omega_d/2\pi$.

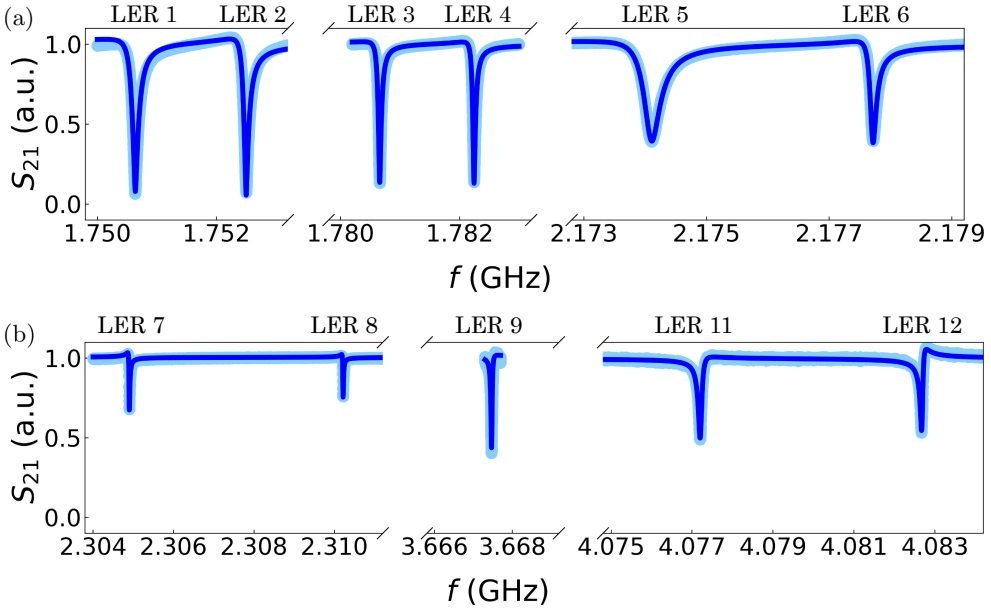

Figure 5.5: Module of the microwave transmission S_{21} (light blue dots) of *Test 1*, measured at 17 mK and zero magnetic field near the resonance frequency ω_r of each LER (except LER 10). Solid blue line shows the fit of the resonances of each pair of LERs, ordered in increasing resonance frequency: LERs 1 to 6 (a), and LERs 7 to 12 (b).

The asymmetry of the resonances arises from the coupling of the mode of the resonator to modes in a slightly mismatched transmission line [9, 10], in which is known as a Fano resonance [11], or due to memory effects of the

transmission line beyond the Markovian regime (see section 4.3.4) [12]. Instead of including a description of the modes in the line, a simpler model can be used: the Diameter Correction Method (DCM), which describes the asymmetry in S_{21} with only one additional parameter [13]. In the DCM model the line-resonator coupling rate κ_c is a complex quantity with module $|\kappa_c|$ and argument ϕ_c. Only the real part of κ_c contributes to κ:

$$\kappa := \mathrm{Re}(\kappa_c) + \kappa_i = |\kappa_c| \cos\phi_c + \kappa_i, \tag{5.2}$$

while its imaginary part accounts for the resonance asymmetry. The resonance visibility is defined as the ratio:

$$\eta := \mathrm{Re}(\kappa_c)/\kappa = 1 - \kappa_i/\kappa. \tag{5.3}$$

The results of the fit of the resonances with Eq. (5.1) yields the parameters listed in table 5.1. All the resonance frequencies are shifted to lower frequencies (between 70 and 120 MHz) compared to the results from simulations with Sonnet (see table A.1 in Appendix A). This shift is associated with contributions to the resonator inductance and capacitance that these simulations do not take into account. The inductance of the resonator is increased by the kinetic inductance L_k due to the inertia of superconducting electrons at high frequencies. The capacitance is also increased due to parasitic capacitances with other elements in the chip (the ground planes or the transmission line). All resonances are also broadened, with higher κ_i, in the experimental setup compared to the simulations.

LER	$\omega_r/2\pi$ (GHz)	$\kappa/2\pi$ (kHz)	$\lvert\kappa_c\rvert/2\pi$ (kHz)	ϕ_c (°)
1	$1.7506246 \pm 2 \cdot 10^{-7}$	89.3 ± 0.2	84.7 ± 0.3	-8.5 ± 0.1
2	$1.7524814 \pm 2 \cdot 10^{-7}$	70.7 ± 0.2	68.7 ± 0.3	-18.5 ± 0.1
3	$1.78065512 \pm 7 \cdot 10^{-8}$	42.7 ± 0.1	37.6 ± 0.1	-8.6 ± 0.1
4	$1.78223735 \pm 6 \cdot 10^{-8}$	38.2 ± 0.1	33.8 ± 0.1	-13.7 ± 0.1
5	$2.1740753 \pm 4 \cdot 10^{-7}$	199.6 ± 0.4	124.6 ± 0.3	-13.3 ± 0.1
6	$2.1776990 \pm 2 \cdot 10^{-7}$	74.5 ± 0.2	47.3 ± 0.2	-21.9 ± 0.1
7	$2.30489941 \pm 7 \cdot 10^{-8}$	12.7 ± 0.1	4.57 ± 0.03	-30.1 ± 0.2
8	$2.31021363 \pm 8 \cdot 10^{-8}$	10.0 ± 0.1	2.67 ± 0.03	-28.5 ± 0.3
9	$3.66747128 \pm 6 \cdot 10^{-8}$	22.1 ± 0.1	12.70 ± 0.04	11.0 ± 0.1
10	–	–	–	–
11	$4.0772129 \pm 2 \cdot 10^{-7}$	61.6 ± 0.2	31.4 ± 0.1	15.9 ± 0.1
12	$4.0826920 \pm 2 \cdot 10^{-7}$	42.3 ± 0.2	21.6 ± 0.1	33.8 ± 0.2

Table 5.1: Fitting parameters of the experimental results of Fig. 5.5 with Eq. (5.1). ω_r is the resonance frequency of the LER. κ is the decay rate of the photon mode and comprises the total losses of the resonator. These include internal losses (κ_i) and the line-resonator coupling (κ_c). Using DCM, κ_c is complex-valued with module $|\kappa_c|$ and argument ϕ_c.

Figure 5.6 shows the module of the line-resonator coupling, $|\kappa_c|$ for each resonator. LERs with inductive coupling (LERs 1 to 6) display higher line-resonator coupling rates than those with only capacitive coupling (LERs 7 to 12). The magnetic field generated by the inductor extends farther than the electric field, which is typically confined close to the superconducting surface of the capacitor fingers, enhancing the line-resonator coupling. In fact, LERs 1 to 6 are over-coupled, with a visibility larger than 0.5 ($\eta > 0.5$), while those with only capacitive coupling are either critically coupled ($\eta = 0.5$) or under-coupled ($\eta < 0.5$). In particular, LERs 7 and 8 have by far the lowest line-resonator coupling rates and are clearly under-coupled.

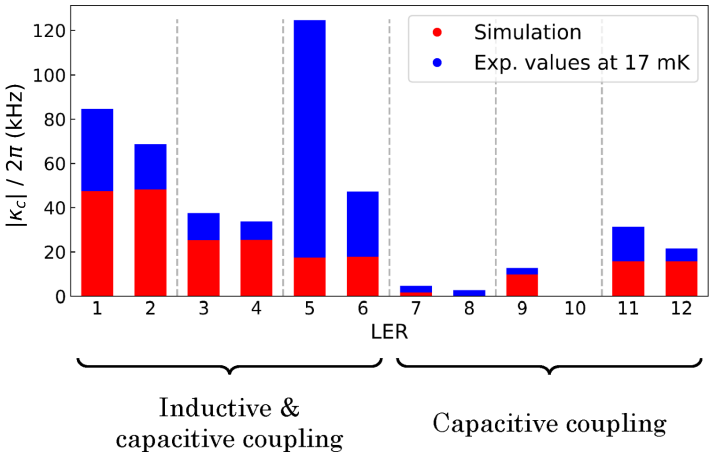

Figure 5.6: Absolute value of the complex line-coupling κ_c of LERs in *Test 1*.

Resonators LERs 1 and 2, which are closer to the transmission line than LERs 3 and 4, show higher line-resonator coupling rates than the latter. However, there is no clear dependence on the resonator-line distance s if LERs 5 and 6 are included, which have also the same design. This broadening of LER 5 (or LER 6, depending on the design) has been repeatedly observed in experiments with chip designs akin to *Test 1* or *Test 2*.

5.1.3 Characterization of *Test 2*

The resonances in *Test 2* span a much narrower frequency range than those in *Test 1*. As with *Test 1*, these resonances were characterized with transmission experiments at 17 mK and zero magnetic field and fitted with Eq. (5.1). This chip was also characterized at 4.2 K in order to see the effect of temperature on the resonances. Figures 5.7 and 5.8 show the resonances at 17 mK at 4.2 K respectively, with the fitting parameters listed in tables 5.2 and 5.3.

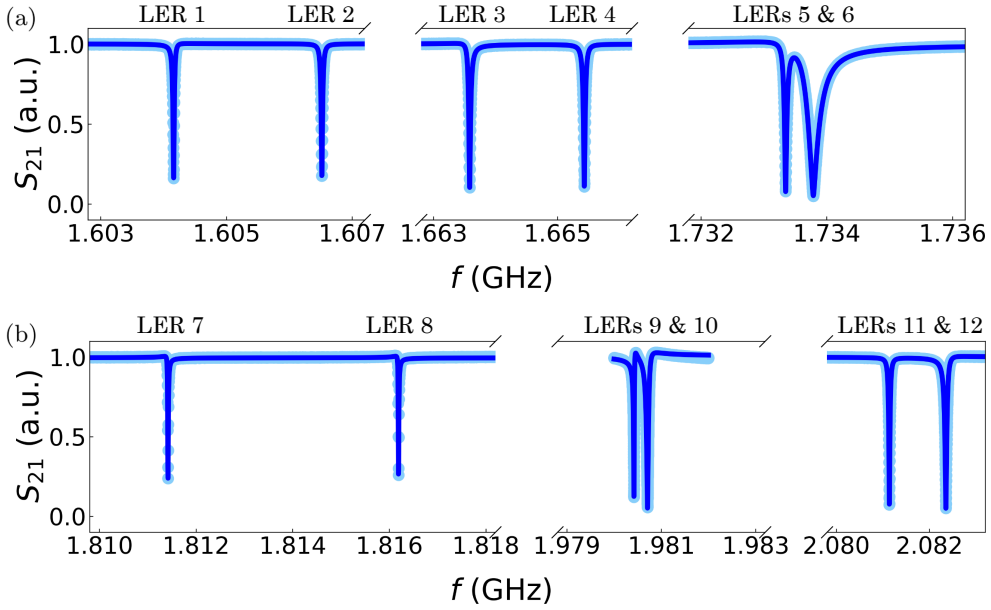

Figure 5.7: Microwave transmission (light blue dots) of *Test 2* measured at 17 mK near the resonance frequencies of all LERs. Solid blue line shows the fit of the resonances of each pair of LERS, ordered in increasing resonance frequency: LERs 1 to 6 (a), and LERs 7 to 12 (b).

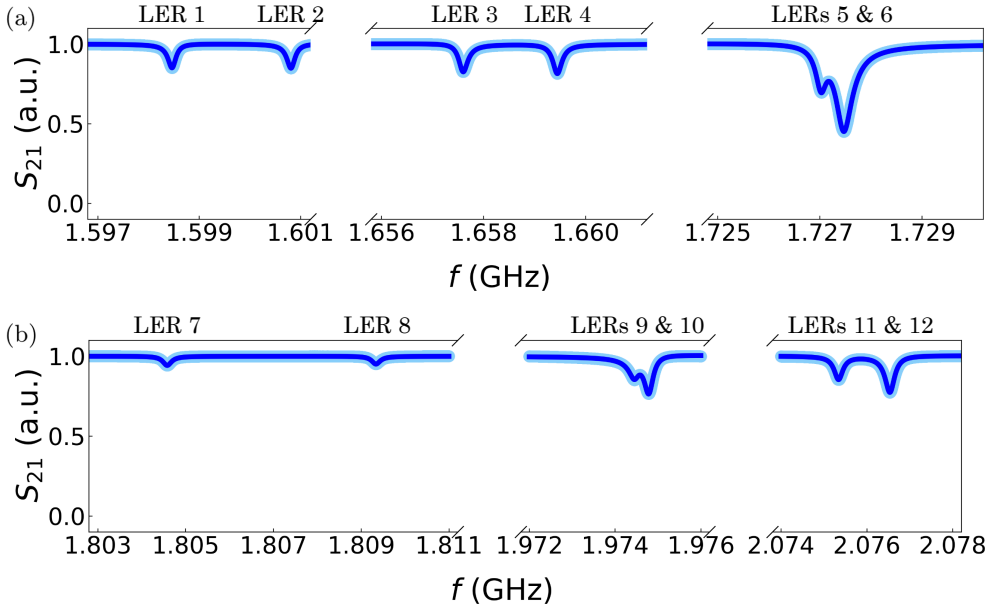

Figure 5.8: Microwave transmission (light blue dots) of *Test 2* measured at 4.2 K near the resonance frequencies of all LERs. The solid blue line shows the fit of the resonances of each pair of LERs, ordered in increasing resonance frequency: LERs 1 to 6 (a), and LERs 7 to 12 (b).

LER	$\omega_r/2\pi$ (GHz)	$\kappa/2\pi$ (kHz)	$\lvert\kappa_c\rvert/2\pi$ (kHz)	ϕ_c (°)
1	$1.60416155 \pm 1 \cdot 10^{-8}$	16.51 ± 0.01	13.87 ± 0.01	4.92 ± 0.03
2	$1.60651821 \pm 1 \cdot 10^{-8}$	18.17 ± 0.01	15.08 ± 0.02	-0.45 ± 0.03
3	$1.66357945 \pm 1 \cdot 10^{-8}$	24.10 ± 0.01	21.86 ± 0.02	-5.54 ± 0.02
4	$1.66543185 \pm 1 \cdot 10^{-8}$	23.72 ± 0.01	21.07 ± 0.02	0.25 ± 0.02
5	$1.73334419 \pm 5 \cdot 10^{-8}$	33.4 ± 0.1	31.5 ± 0.1	15.0 ± 0.1
6	$1.7337608 \pm 1 \cdot 10^{-7}$	152.4 ± 0.1	149.0 ± 0.2	-14.14 ± 0.03
7	$1.81141912 \pm 3 \cdot 10^{-8}$	9.75 ± 0.03	7.62 ± 0.03	-9.5 ± 0.1
8	$1.81619219 \pm 2 \cdot 10^{-8}$	8.82 ± 0.02	6.88 ± 0.03	-10.3 ± 0.1
9	$1.98042651 \pm 3 \cdot 10^{-8}$	11.68 ± 0.03	10.56 ± 0.04	27.1 ± 0.1
10	$1.98071604 \pm 4 \cdot 10^{-8}$	34.94 ± 0.04	34.2 ± 0.1	7.94 ± 0.05
11	$2.08114007 \pm 1 \cdot 10^{-8}$	21.65 ± 0.01	20.04 ± 0.02	1.72 ± 0.02
12	$2.08235739 \pm 1 \cdot 10^{-8}$	36.75 ± 0.02	35.10 ± 0.03	4.80 ± 0.01

Table 5.2: Parameters from the fit of the experimental results in Fig. 5.7 with Eq. (5.1).

LER	$\omega_r/2\pi$ (GHz)	$\kappa/2\pi$ (kHz)	$\lvert\kappa_c\rvert/2\pi$ (kHz)	ϕ_c (°)
1	$1.59847075 \pm 6 \cdot 10^{-8}$	99.7 ± 0.1	14.91 ± 0.01	7.11 ± 0.03
2	$1.60081773 \pm 6 \cdot 10^{-8}$	102.3 ± 0.1	15.62 ± 0.01	4.29 ± 0.03
3	$1.65759532 \pm 9 \cdot 10^{-8}$	112.4 ± 0.1	19.74 ± 0.02	-7.89 ± 0.03
4	$1.65944270 \pm 8 \cdot 10^{-8}$	113.6 ± 0.1	20.85 ± 0.02	-4.24 ± 0.03
5	$1.7270242 \pm 3 \cdot 10^{-7}$	132.7 ± 0.2	33.9 ± 0.1	16.5 ± 0.1
6	$1.7274524 \pm 2 \cdot 10^{-7}$	238.7 ± 0.2	132.3 ± 0.1	-10.98 ± 0.04
7	$1.8045798 \pm 1 \cdot 10^{-7}$	121.7 ± 0.1	7.00 ± 0.01	-2.02 ± 0.05
8	$1.8093356 \pm 2 \cdot 10^{-7}$	119.1 ± 0.2	5.83 ± 0.01	-2.7 ± 0.1
9	$1.9744671 \pm 6 \cdot 10^{-7}$	144.3 ± 0.6	16.7 ± 0.1	26.2 ± 0.3
10	$1.9747926 \pm 3 \cdot 10^{-7}$	137.7 ± 0.3	33.2 ± 0.1	4.2 ± 0.1
11	$2.0753418 \pm 1 \cdot 10^{-7}$	127.6 ± 0.1	18.36 ± 0.03	1.81 ± 0.05
12	$2.0765439 \pm 1 \cdot 10^{-7}$	142.8 ± 0.1	32.49 ± 0.03	3.83 ± 0.03

Table 5.3: Parameters from the fit of the experimental results in Fig. 5.8 with Eq. (5.1).

The changes in transmission with temperature are those expected for superconducting lumped-element resonators [14]. Although the DC-resistance of a superconductor is zero below T_c ($\sim$ 9.2 K for Nb), its AC-impedance can be still non-zero. In particular, this impedance increases with frequency and temperature, even below T_c, and makes for the increase of around one order of magnitude in the internal losses of the resonator, κ_i, between 17 mK and 4.2 K (from 10–35 kHz to 100–145 kHz). This increase in κ_i accounts for the wider line-shapes — higher κ — with lower visibility, while κ_c is temperature-

independent. There is also a decrease in ω_r of about 6 MHz in all resonances as temperature is increased. The penetration depth of the superconducting material increases with temperature, which in turn increases the resonator inductance L. The magnitude of the shift in the resonance frequency $\omega_r = 1/\sqrt{LC}$ depends on the contribution of this effect to the total L.

5.2 DPPH samples

5.2.1 The DPPH radical

2,2-diphenyl-1-picrylhydrazyl (DPPH) is an organic free radical molecule with spin 1/2 that is widely used as an standard in Electron Paramagnetic Resonance (EPR) [15]. Each DPPH molecule consists of a hydracyl radical bridging a picryl group and two phenyl groups (see Fig. 5.9). The spin 1/2 of the unpaired electron of the radical behaves nearly as the spin of a free electron. It is described by a spin Hamiltonian that is just an isotropic electronic Zeeman term with a g-factor $g_S = 2.004$ just above the value for a free electron [16]:

$$H = \mu_B g_S B \hat{S}_z = \frac{\mu_B g_S B}{2} \hat{\sigma}_z. \tag{5.4}$$

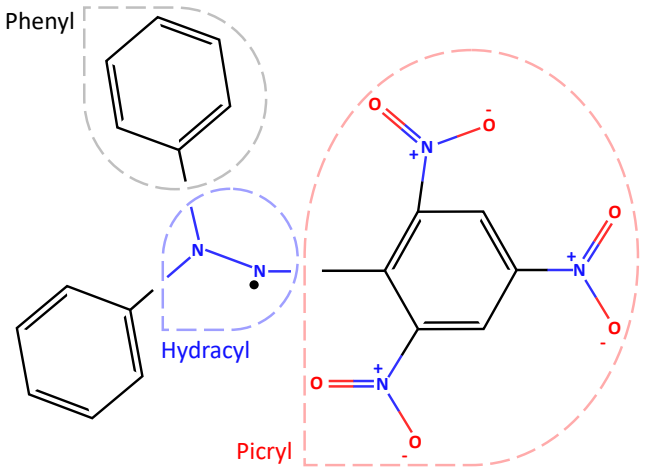

Figure 5.9: Chemical structure of DPPH, adapted from [17]. The unpaired electron, pictured as a black dot, that gives the effective spin 1/2 of the molecule is localized in the nitrogen atom of the hydracyl group closest to the picryl group.

The spin 1/2 is biased by a static field $\boldsymbol{B}_{\mathbf{dc}}$ of magnitude B, which tunes its transition frequency $\omega_q = \mu_B g_S B/\hbar$. As stated in section 5.1.1, a spin 1/2 couples only to oscillating fields perpendicular to $\boldsymbol{B}_{\mathbf{dc}}$. The coupling is the modulation of the isotropic electronic Zeeman term by these components.

5.2.2 Sample characterization

All experiments in this chapter used DPPH in powder form, as purchased from Sigma Aldrich (reference D9132), pressed into a 1 mm wide, 0.2 mm thick pellets. Solvent-free DPPH is known to have at least two different crystal structures, usually labeled DPPH-I and DPPH-III. Information on their crystal lattice parameters was reported in 1965 [18, 19], but a full structural determination was not performed until 2010 [16]. The results of X-ray diffraction experiments on these samples, shown in Fig. 5.10a, suggest that they exhibit the DPPH-III structure (Fig. 5.10b).

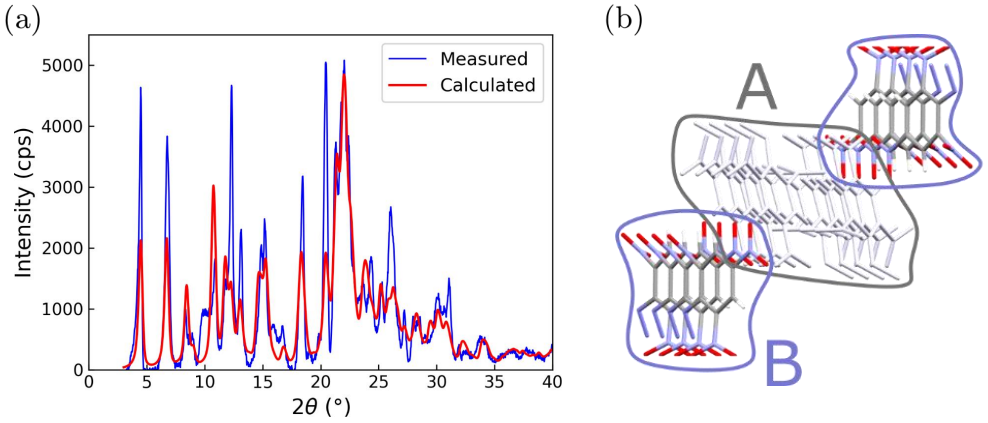

Figure 5.10: (a) X-ray diffraction experiment on our powder samples (blue solid line) and calculated spectrum for DPPH-III (red solid line). (b) Picture of the two subspecies, labeled A and B, present in the structure of the sample (DPPH-III). They are distinguished by the formation of dimers (A) or spin chains (B) at low temperatures.

Information on the magnetic response of DPPH was obtained by a combination of magnetic, heat capacity and magnetic resonance experiments. In all these, the DPPH powder pellets were glued to the sample holder with apiezon N grease in order to improve its thermalization.

Magnetic measurements were performed between 1.7 K and 300 K using a commercial SQUID magnetometer. The dc susceptibility χ was measured with a magnetic field $B = 0.1$ T. Magnetization isotherms were also measured at fixed temperatures by varying B from 0 to 5 T. Measurements for temperatures lower than 1.7 K were performed with a home-made micro-Hall magnetometer, based on a high-mobility $2D$ electron gas created at the interface between GaAs and GaInAs semiconducting layers, coupled to a ^{3}He cryostat. A few microns wide DPPH sample was placed close to one of the three Hall crosses patterned onto the device. The net Hall voltage, proportional to the sample

magnetic moment, was recorded between 0.35 K and 5 K with a $B = 0.1$ T magnetic field applied along the plane of the sensor. The bare device signal was measured independently and then subtracted from the experimental data, with the results showing no thermal hysteresis.

The dc-magnetic susceptibility χ and heat capacity c_P of powdered DPPH samples are shown in Figs. 5.11a and 5.11b. From room temperature down to about 35 K, χ follows a Curie-Weiss law $\chi = C/(T - \theta)$, with C the Curie constant and θ the Weiss temperature, see the inset of Fig. 5.11a. The constant $C = 0.320 \pm 0.001$ emu K/mol Oe measured in this region is smaller, by a factor $x \equiv C/C_{S=1/2} \cong 0.85$, than the value $C_{S=1/2} = N_A g_S^2/4k_B = 0.375$ emu K/mol Oe that would be expected for isolated $S = 1/2$ with $g_S = 2.004$. This suggests that a fraction of DPPH molecules are in their oxidized form, which is diamagnetic ($S = 0$).

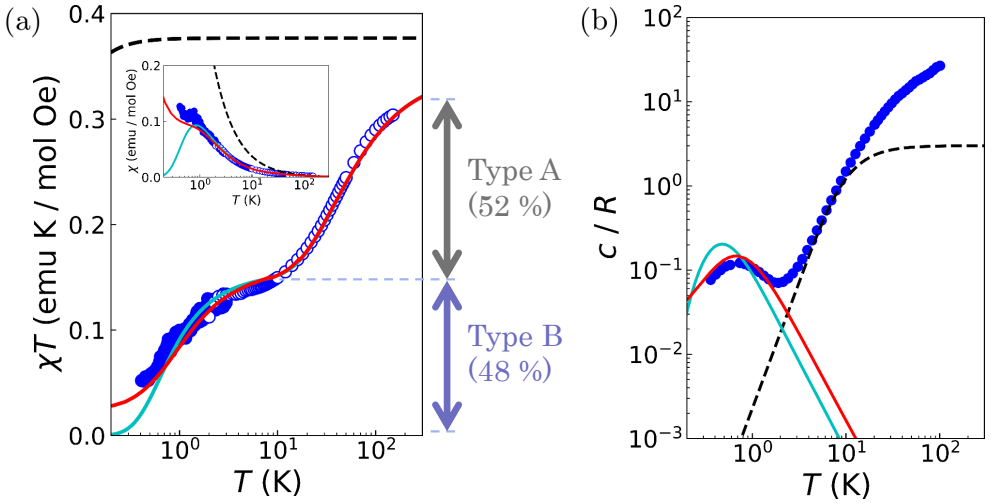

Figure 5.11: (a) Dependence of the χT product (where χ is magnetic susceptibility) of a DPPH powder sample with temperature, measured at $\mu_0 H = 0.1$ T. Hollow blue dots are SQUID measurements, while solid blue dots are Hall voltage measurements. Solid lines consist of the contribution from a model of AF dimers from type A molecules and the contribution from type B molecules. For the latter, the cyan solid line is a model of AF dimers, while the red solid line is a model of AF chains. As a reference, the dashed black line shows the expected χT for a fully paramagnetic DPPH sample. Inset: χ vs. temperature. (b) Temperature dependence of the heat capacity at $\mu_0 H = 0$ T of a powder sample of DPPH (blue dots). The contribution from type B molecules appears at low temperatures. A model of infinite AF chains (red solid line) follows the experimental data much better than the model of AF dimers (cyan solid line). Black dashed line is the Debye model for the lattice heat capacity, with $\theta_D = 47$ K.

The finite negative $\theta = -21$ K reflects the existence of relatively strong antiferromagnetic (AF) interactions. These interactions lead to the drop in the χT product, proportional to the effective magnetic moment squared, which is observed experimentally (Fig. 5.11a). A quite similar behaviour has been observed in diverse DPPH derivatives [16, 20, 21]. It is associated with the coupling between nearest neighbour molecules, which tend to form AF dimers with an $S = 0$ ground state. In the DPPH-III structure, such spin dimers are formed by DPPH molecules belonging to the A crystal sublattice [16].

This picture agrees also with the results of magnetic resonance experiments. Continuous wave EPR measurements (cw-EPR) were performed with a Bruker Biospin ELEXSYS E-580 spectrometer operating in the X-band (9–10 GHz). A DPPH pellet was glued with vacuum grease onto a diamagnetic holder and introduced in the EPR cavity. A single narrow line was measured, shown in Fig. 5.12a, in agreement with a spin $S = 1/2$ and $g_S = 2.004$. The line intensity I shows a paramagnetic behaviour, with the IT product behaving very much as χT (see Fig. 5.12b). The spin resonance line is homogeneously broadened as temperature is decreased from room temperature to 4 K. It is known that, in the paramagnetic phase of DPPH, exchange interactions tend to suppress the inhomogenous broadening associated with dipole-dipole interactions [22] via the exchange narrowing mechanism [23].

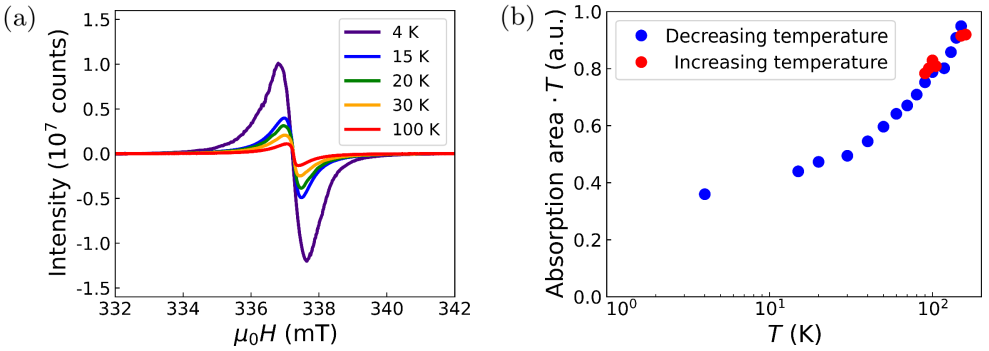

Figure 5.12: (a) cw-EPR of a powder sample of DPPH at 4, 15, 20, 30, 100 K. The complete set of measurements span from 4 K to room temperature. (b) Product of absorption area and temperature. The cw-EPR spectra were initially measured going from room temperature down to 4 K (blue dots), then a few measurements were carried out at high temperatures going back to room temperature (red dots). No hysteresis is observed.

Time-domain EPR measurements of the Free Induction Decay (FID) were carried out at 7.7 K (Fig. 5.13a) and at room temperature (Fig. 5.13b). This signal is the decay of the magnetization of the sample after a single excitation pulse, without refocusing. When homogeneous broadening is dominant, there

is no echo signal, and T_m is obtained as the characteristic time constant of the decay of the FID. The fit of the two signals is compatible with a homogeneous broadening $\gamma_\perp/2\pi = 1/2\pi T_m \cong 4.8$ MHz at 7.7 K, and $\gamma_\perp/2\pi = 4.3$ MHz at room temperature, which correspond to phase memory times $T_m = 33.5$ ns and 37 ns respectively.

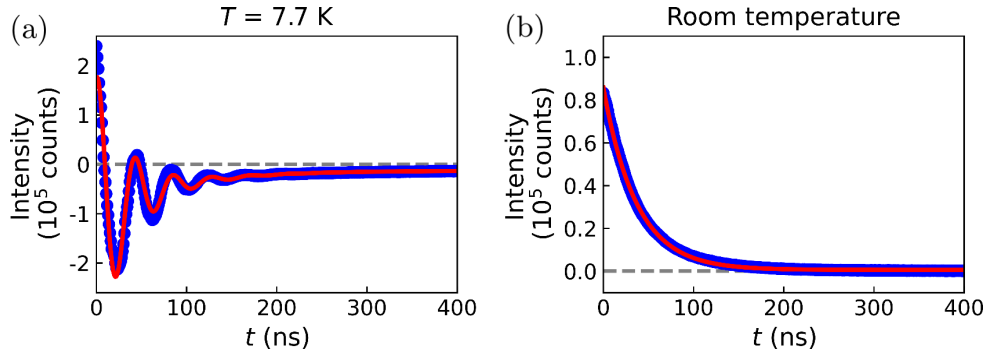

Figure 5.13: FID signal of a DPPH powder sample measured at 7.7 K (a) and at room temperature (b). Experimental data (blue dots) is fitted with an oscillating decay with two decay rates (bi-exponential). I assign the faster rate with T_m, yielding $T_m = 33.5$ ns at 7.7 K and 37 ns at room temperature.

Below 10 K, χT shows a second drop, as seen in Fig. 5.11a. In this temperature region, χ follows also a Curie-Weiss law, but with a smaller C and a much smaller $\theta = -0.65$ K. This behaviour probably reflects the weaker interactions between spins in sublattice B of DPPH-III. The response remains paramagnetic down to very low-T, with no clear indication of a phase transition. It is consistent with the formation of either AF dimers or low dimensional (1D) antiferromagnetic chains.

In order to decide between these two alternatives, the specific heat of the samples was measured with a commercial physical properties measurement platform that uses the relaxation method [24]. The temperature was varied between 0.35 K and 200 K and magnetic fields between 0 and 2 T were applied parallel to the sample plane. Above 2 K, specific heat data measured at zero field (Fig. 5.11b) are dominated by a large contribution arising from lattice and molecular vibrations. At lower temperatures, an additional contribution shows up, which depends on magnetic field as shown in Fig. 5.14. Therefore, it reflects spin excitations. The broad shape of this anomaly confirms that no phase transition to long-range magnetic order takes place in this temperature region. The data agree well with predictions for the specific heat of infinite AF chains at zero magnetic field [25], and seem to rule out the formation of dimers within the B sublattice of DPPH.

Figure 5.14 shows the temperature dependence of the heat capacity at increasing magnetic fields. Without an extension of the model of infinite AF chains to include an applied magnetic field, the measured heat capacity was tentatively described with a model of finite AF chains. At low fields, this model fits the measured heat capacity, while the paramagnetic theory fails. Conversely, for $\mu_0 H > 1$ T the paramagnetic theory is a good description of the system: magnetic order is broken by the application of a strong enough magnetic field. At intermediate fields ($\mu_0 H = 1$ T), a model of finite AF chains is not enough to represent accurately the measured heat capacity.

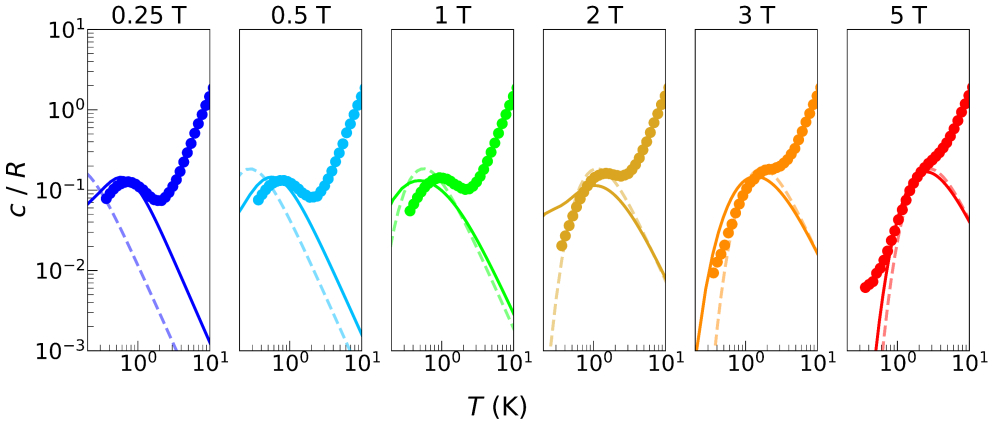

Figure 5.14: Molar specific heat of a powder DPPH sample measured at 0.25, 0.5, 1, 2, 3 and 5 T. The experimental results (dots) are compared with a theory of AF chains (solid lines) and the paramagnetic theory for spin 1/2 (dashed lines).

The above interpretation is also compatible with the magnetic susceptibility data. The dc susceptibility of finite chains of N $S = 1/2$ spins coupled by a Heisenberg AF coupling was calculated. Figure 5.11a shows how the experimental χT can be described by the combination of two contributions: one arising from AF dimers of A-type DPPH molecules and another one resulting from AF chains formed within the B sub-lattice. The low-T susceptibility can be accounted for with a model that considers only small-N chains because the contribution per spin to the total susceptibility tends to vanish as $N \to \infty$. The uncompensated spins in odd-N chains are responsible for the incomplete cancellation of χT as $T \to 0$. The origin of finite size chains can be associated with the presence of about 15 % of diamagnetic DPPH molecules, which are randomly distributed over the crystal lattice.

Finally, for completeness, Fig. 5.15a shows the magnetization isotherms that were measured in the same experiment as the dc-magnetic susceptibility from Fig. 5.11a. The magnetization of each spin 1/2 is expected to saturate to μ_B at high fields. However, as discussed in the measurement of χT, $\sim 15\%$

of the sample is already diamagnetic at high temperatures, and at 10 K the A-type DPPH molecules have already formed diamagnetic dimers. Normalizing by the total number of molecules in the sample, a lower saturation value for the magnetization is obtained. The remaining contribution from B-type DPPH molecules is fitted with a scaled paramagnetic theory for spins 1/2. At the lower measured temperatures (0.5, 1 and 2 K) and low fields, this theory fails due to the onset of antiferromagnetic interactions in lattice B, which oppose the onset of magnetization due to the applied magnetic field see (5.15b).

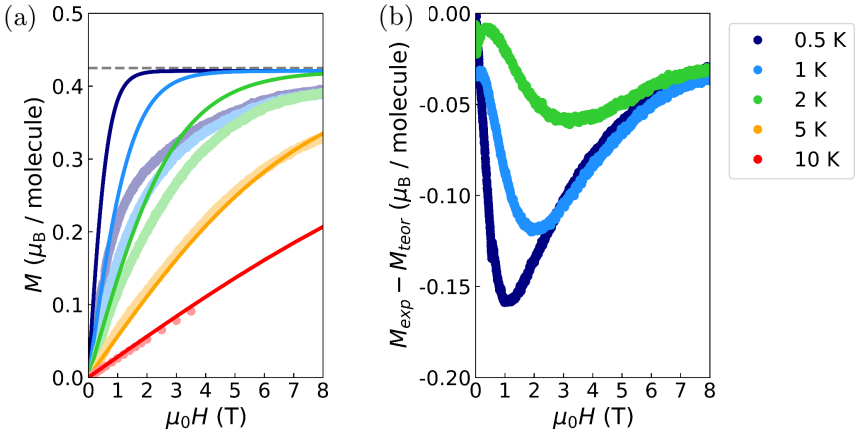

Figure 5.15: (a) Field-dependent magnetization isotherms of a DPPH powder sample measured at 0.5, 1, 2, 5 and 10 K (dots), in units of Bohr magnetons (μ_B) per molecule. The dashed line is the saturation value of the magnetization per molecule taking into account that a 15% of the sample is diamagnetic. Solid lines are the paramagnetic theory of a spin 1/2. (b) Difference between measured magnetization and the predicted magnetization with the paramagnetic theory of a spin 1/2 at 0.5, 1 and 2 K.

5.3 Coupling of DPPH to LERs in *Test 1*

5.3.1 Effect of the resonator geometry and orientation on its visibility

The transmission experiments to study the coupling of DPPH samples to LERs were carried out at 4.2 K. At this temperature, A-type DPPH molecules have formed AF dimers, but B-type DPPH molecules still remain paramagnetic. However, LERs in *Test 1* were only characterized at 17 mK right after fabrication. Figure 5.16 shows the transmission of these resonators at 4.2 K. Only the resonances of LERs 1 to 6 were detected at zero magnetic field, which were fitted with Eq. (5.1). The fitting parameters are listed in table 5.4.

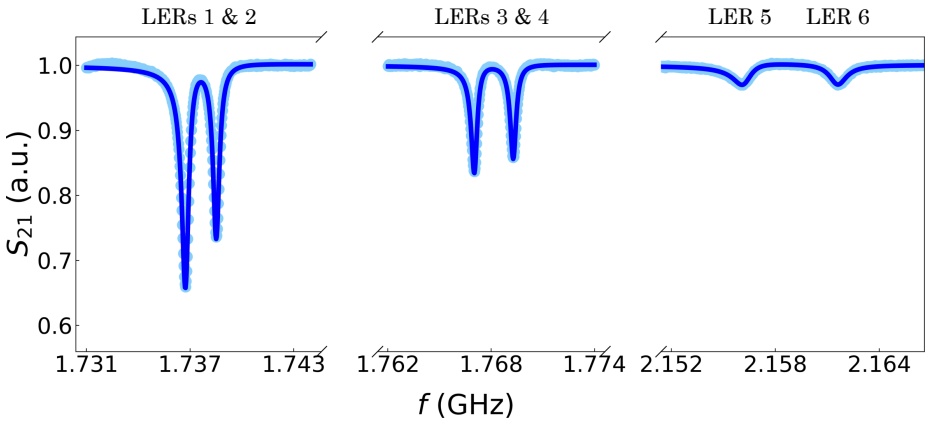

Figure 5.16: Transmission (light blue dots) of the lumped-element resonators in chip *Test 1* at 4.2 K and zero magnetic field. The solid blue line shows the fit of the resonances of LERs 1 to 6, ordered in increasing resonance frequency.

LER	$\omega_r/2\pi$ (GHz)	$\kappa/2\pi$ (kHz)	$\lvert\kappa_c\rvert/2\pi$ (kHz)	ϕ_c (°)
1	$1.736763 \pm 2 \cdot 10^{-6}$	273.2 ± 1.9	93.7 ± 0.8	9.6 ± 0.3
2	$1.738524 \pm 2 \cdot 10^{-6}$	243.0 ± 2.2	65.3 ± 0.7	1.1 ± 0.4
3	$1.767044 \pm 2 \cdot 10^{-6}$	219.15 ± 1.98	36.3 ± 0.4	9.4 ± 0.4
4	$1.769291 \pm 2 \cdot 10^{-6}$	214.7 ± 2.2	31.2 ± 0.4	2.6 ± 0.4
5	$2.156230 \pm 6 \cdot 10^{-6}$	636.8 ± 5.5	20.3 ± 0.2	26.4 ± 0.4
6	$2.161580 \pm 6 \cdot 10^{-6}$	608.7 ± 5.6	18.9 ± 0.2	-6.6 ± 0.4

Table 5.4: Parameters from the fit of the transmission of the lumped-element resonators in chip *Test 1* at 4.2 K and zero magnetic field.

The resonances are shifted to lower frequencies by $\sim$ 14 MHz as the temperature increases from 17 mK to 4.2 K. They are also broadened, with κ increasing by one order of magnitude with respect to to its value at 17 mK in every resonator. These are the same features observed in the temperature dependence of the resonances in *Test 2* (see section 5.1.3). It is not surprising then that the resonances of LERs 7 to 12 in *Test 1* at 4.2 K may be too weak to be detected: their visibility at 17 mK was already much smaller than that of their counterparts in *Test 2*, and now they are further broadened by temperature.

Note that LERs 7 to 12 are rotated 90° with respect to LERs 1 to 6 in *Test 1* (see Fig. 5.1), with only capacitive line-resonator coupling. This suggests that this kind of coupling alone is not enough to measure the resonators far from the millikelvin regime (4.2 K, in this case). For that reason, *Test 2* was designed with only two rotated LERs (7 and 8), both of them with inductive resonator-line coupling.

5.3.2 Strong coupling of a DPPH ensemble to a LER

LERs 1 to 6 can be grouped in three pairs with similar frequencies: LERs 1 and 2, LERs 3 and 4, and LERs 5 and 6. They all share the design of type (a) resonators in Fig. 5.2. In this section I present the transmission of one LER of each pair coupled to the same DPPH sample, which was moved from one resonator to the next between experiments (see Fig. 5.17).

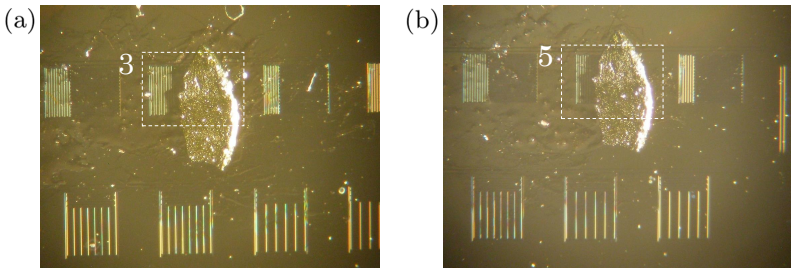

Figure 5.17: Photo of the same sample of DPPH powder placed on top of the inductor LER 3 (a) and then on top of the inductor of LER 5 (b).

The sample is a DPPH powder pellet with a thickness of ∼100 μm and an area ($\sim$ 1 mm^2) slightly larger than the size of the resonators, covering the whole inductor. This large sample can be easily handled and moved between LERs. With a molecular density of $\sim 2 \times 10^{27}$ molecules/m^3 for DPPH-III [26], there are roughly $N \sim 10^{17}$ spins in this sample. The sample was initially placed on top of LER 1 with Paratone oil.

Figure 5.18a shows the hybrid spins-LER system resonance around the resonator frequency ω_r of LER 1 for different magnetic fields. The coupling between the sample spins and the resonator mode becomes apparent when the field-dependent transition frequency of a spin 1/2, $\omega_\mathrm{q} = \mu_\mathrm{B} g_\mathrm{S} B/\hbar$, is close to ω_r. The spin-photon resonance field B_res is defined by the condition $\omega_\mathrm{r} = \omega_\mathrm{q} = \mu_\mathrm{B} g_\mathrm{S} B_\mathrm{res}/\hbar$. The experiment is modeled as the transmission (S_{21}) of a resonator coupled to an ensemble of non-interacting spins. This is described in Eq. (4.103) from chapter 4, which is reproduced here for clarity:

$$S_{21}(\omega_\mathrm{d}) = 1 - \frac{\kappa_\mathrm{c}}{i(\omega_\mathrm{r} - \omega_\mathrm{d}) + \kappa + \dfrac{G_N^2 \Delta P}{i(\omega_\mathrm{q} - \omega_\mathrm{d}) + \gamma_\perp}} \,. \tag{5.5}$$

Apart from the previously characterized LER parameters (ω_r, κ, and κ_c), Eq. (5.18) depends on the spin transition frequency, ω_q, the decoherence rate of the spin ensemble, $\gamma_\perp$, and the collective spin-photon G_N. The population

difference ΔP between the spin down and spin up states at temperature T is included in what follows in a temperature dependent coupling $G_N \propto \sqrt{\Delta P}$. In a microwave transmission experiment, S_{21} is measured for different regular input frequencies $f = \omega_\mathrm{d}/2\pi$ and magnetic fields B (tuning ω_q). LER parameters resulting from the least-squares fit are listed in table A.2 in Appendix A. The g-factor g_S and the coupling G_N for $\gamma_\perp/2\pi = 6.5 \pm 0.5$ MHz are reported in table 5.5. This value of $\gamma_\perp$ is consistent with previous reported values for DPPH pellets coupled to superconducting resonators [27, Ch.7].

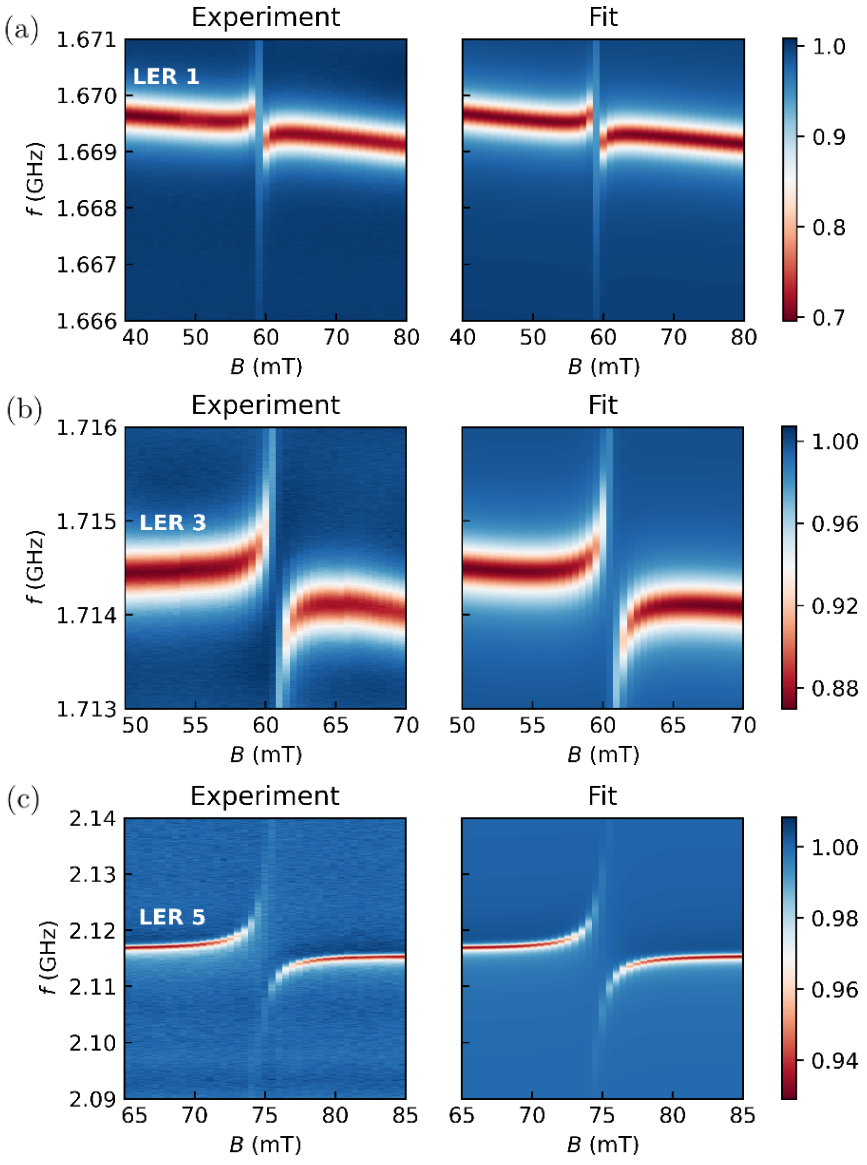

Figure 5.18: Transmission of *Test 1* LER 1 (a), LER 3 (b) and LER 5 (c) coupled to the same DPPH powder sample (see Fig. 5.17).

LER	g_S	$G_N/2\pi$ (MHz)	$G_N/\gamma_\perp$	C
1	$2.02058 \pm 5 \cdot 10^{-5}$	2.586 ± 0.003	0.40 ± 0.03	4.0 ± 0.3
3	$2.01953 \pm 5 \cdot 10^{-5}$	3.758 ± 0.003	0.58 ± 0.04	10.6 ± 0.8
5	$2.01928 \pm 4 \cdot 10^{-5}$	12.491 ± 0.004	1.9 ± 0.1	57.9 ± 4.5

Table 5.5: Parameters from the fit of the magnetic field dependent resonances of LERs 1, 3 and 5 in chip *Test 1* at $T = 4.2$ K shown in Fig. 5.18. The same DPPH was coupled to each of the three resonators. G_N is the collective spin-photon coupling defined by Eq. (4.104), measured at 4.2 K. The cooperativity is defined as $C = G_N^2/\gamma_\perp\kappa$ (see section 4.6.4).

The same sample was moved to LERs 3 and 5 (see Fig. 5.17), and transmission experiments were carried out the same way around their corresponding ω_r and B_{res} (Figs. 5.18b and 5.18c). These experiments were fitted with Eq. (5.5), see table A.2 in Appendix A and table 5.5. All measurements were fitted with the same decoherence rate $\gamma_\perp$, which is intrinsic to the sample.

The collective spin-photon coupling of LER 5 reaches both the strong coupling and high cooperativity regimes, defined by $G_N/\gamma_\perp > 1$ and $C = G_N^2/\gamma_\perp\kappa > 1$ respectively. The strong spin-photon coupling of LER 5, together with the high coupling of the resonator to the readout line, enables the detection of two transmission dips in resonance ($B = B_{res}$). Figure 5.19 shows these two dips at the measured field closest to the resonance field.

In LERs 1 and 3, the collective spin-photon coupling is nearly high enough to achieve the strong collective coupling regime, with $G_N/\gamma_\perp$ close to one. High cooperativity is achieved, with $C = G_N^2/\gamma_\perp\kappa = 4$ and 10.6 respectively. A single broadened dip in transmission is observed, as $G_N/\gamma_\perp < 1/\sqrt{2}$ (see Fig. 4.4 in chapter 4). Both LERs have an inductor design similar to that LER 5,[1] therefore one would expect a similar collective spin-photon coupling G_N to that of LER 5. Instead, the measured G_N for LER 5 is significantly higher.

A possible explanation for the different G_N values could be associated to the magnitude of the microwave field, rather than with the its distribution, which depends only the inductor design. This field scales with the square root of the resonance frequency ω_r [6, App.]. However, this effect alone cannot explain the change in G_N. Let us take the resonators with highest (LER 5) and lowest (LER 1) spin-resonator coupling. The effect of their different resonance frequencies accounts for an increase by a factor 1.13 in G_N from LER 1 to LER 5. Instead, an increase by a factor 4.83 is measured. Therefore, other effects

[1] Figure 5.4 shows the field distribution for LER 1 in chip *Test 2*. The design of this resonator is similar to the design of the resonators that are being discussed here (LERs 1 to 6 in chip *Test 1*).

may be more relevant to the change in G_N.

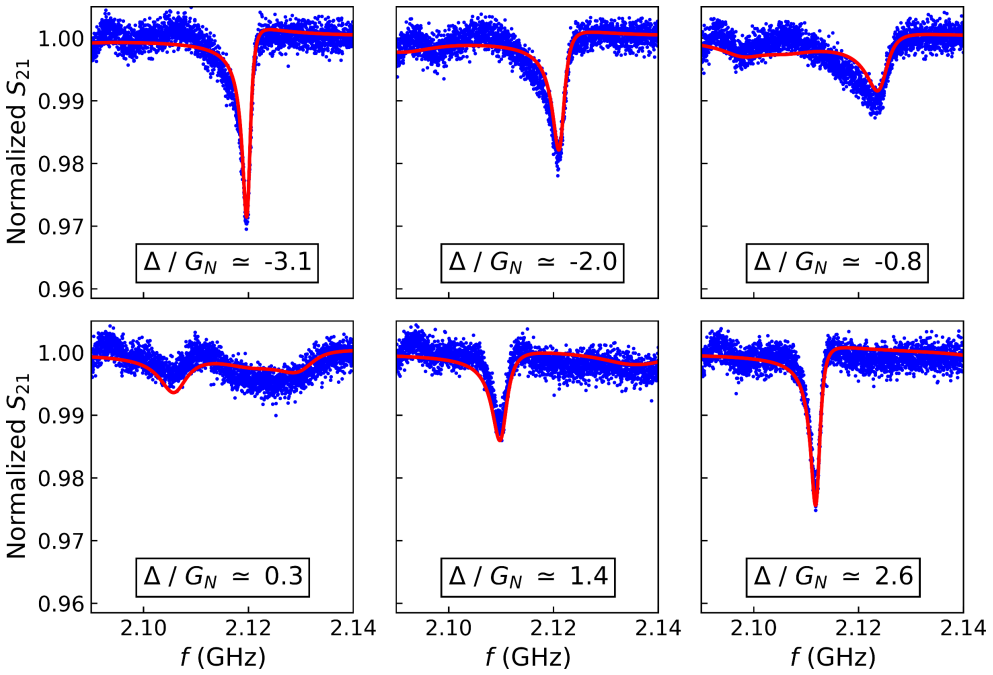

Figure 5.19: Transmission of *Test 1* LER 5 coupled to a DPPH sample for three different detunings $\Delta = \omega_q - \omega_r$ (blue dots). Δ is given in units of the collective coupling G_N. The theoretical transmission with the fit parameters from table A.2 in Appendix A and table 5.5 is also shown (red solid lines). The ensemble-resonator coupling of LER 5 is high enough to be in the strong coupling regime. Two peaks can be seen in the transmission for $|\Delta/G_N| < 1$. These two peaks look slightly different because $\Delta \neq 0$.

In this experimental setup, the position of the sample has a large effect on the coupling: it determines which volume of the inhomogeneous magnetic field generated by the resonator is actually filled with spins. The reason for this is that the intensity of the microwave field decays very rapidly as the sample moves away from the surface (see Fig. 5.4) [28]. Any irregularities in the sample, as well as the layer of oil that is needed to stick the samples to the surface of the chip, create a gap of the order of a few micrometres at the sample-chip interface [29]. In these measurements, the rapid increase in the coupling suggests that the gap was closing as the sample was moved from the first resonator (LER 1) to the last one (LER 5), see Fig. 5.20. This can be explained by the sample leaving part of the oil layer between the sample and the chip surface as it was moved from one resonator to the next. Still, there is a non-negligible gap in LER 5 that might be due to irregularities in the sample surface.

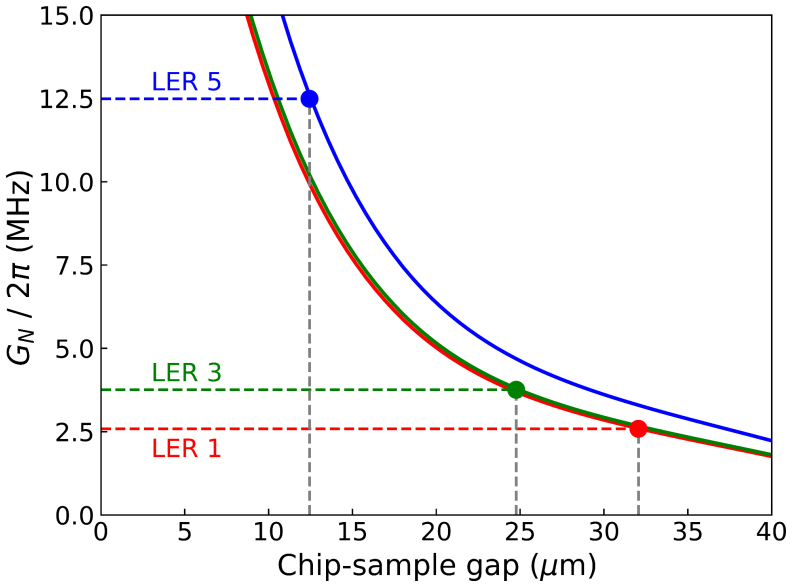

Figure 5.20: Simulation of the coupling of the magnetic field generated by the inductor of resonators 1, 3 and 5 to a sample of DPPH as a function of the sample-resonator gap (solid lines). A comparison with the experimental G_N (horizontal dashed lines) gives an estimation of the gap in each LER (vertical dashed lines). The gap decreases as the sample is moved from LER 1 to 3 and then to 5 as part of the oil layer between sample and chip surface remains attached to the chip surface.

5.3.3 Effect of the magnetic field orientation

Three different DPPH samples were deposited on LERs 7, 8 and 9. Only one of the six missing resonators (7 to 12) was identified, most probably LER 7 (labeled LER 7 in what follows), through its coupling to the DPPH sample (see Fig. 5.21, the largest sample is on top of LER 7). This resonator has a very small coupling κ_c to the transmission line compared to its total losses κ, which explains why its visibility is so low at $T \simeq 4.2$ K.

The design of LER 7 is rotated 90° with respect to the design of LERs 1 to 6. The microwave magnetic field generated by its inductor has then some components parallel to the readout transmission line (the chip axis). Therefore, the geometry that was used to measure the spin-photon coupling in the case of LERs 1, 3 and 5, with the magnetic field applied along the chip axis, is not ideal. For this reason, the resonance of LER 7 was measured with magnetic fields applied at various angles θ from the chip axis. The results are shown in Figs. 5.22 and 5.23. The parameters obtained from the fit of these measurements with Eq. (5.5) are given in table 5.6).

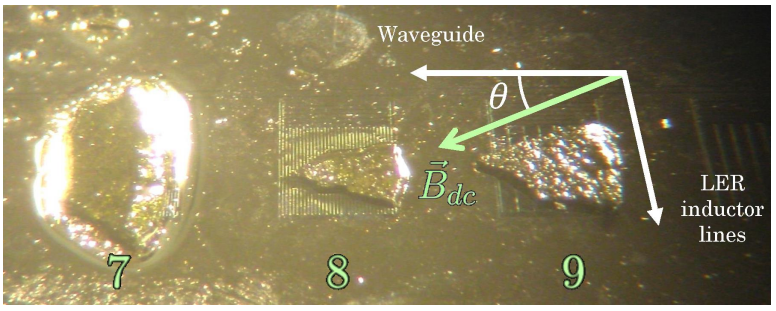

Figure 5.21: Photo of three DPPH powder samples on top of LERs 7 (below the largest sample), 8 and 9. Only one resonance was measured (attributed to LER 7 or 8, based on their expected resonance frequency). From the large ensemble coupling it can be assumed that it belongs to LER 7, which hosts the largest sample. The other two resonances are difficult to measure due to the combination of low resonator-line coupling (like LER 7) and low ensemble-resonator coupling (smaller samples). The direct spin ensemble to transmission line coupling observed for low θ values comes from the large sample located on LER 7, which covers part of the transmission line.

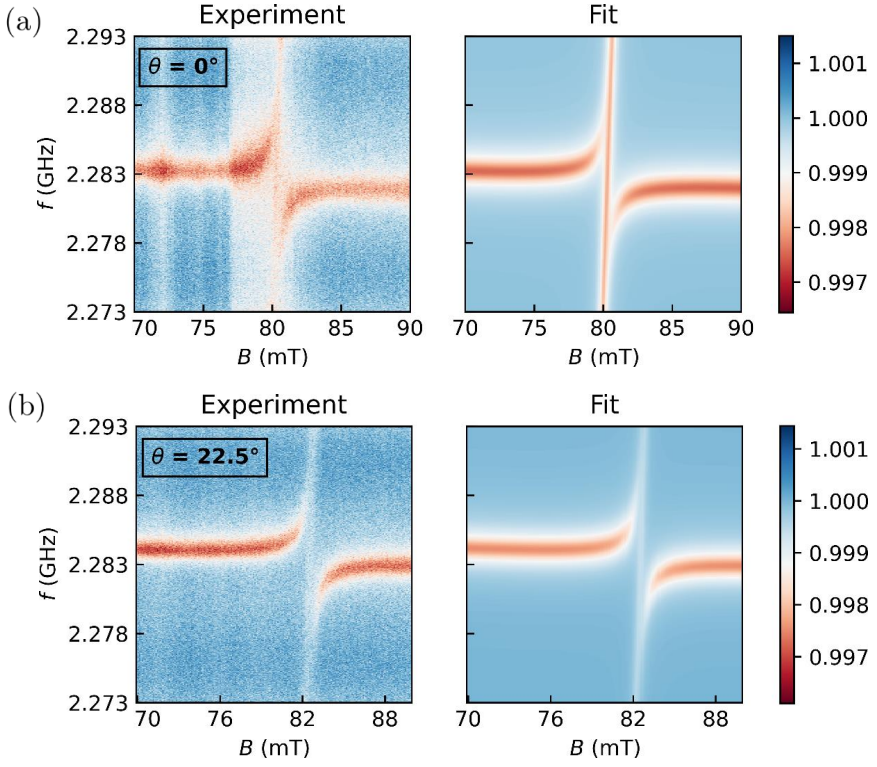

Figure 5.22: Transmission of LER 7 of chip *Test 1* coupled to a DPPH sample when the magnetic field is applied parallel to the transmission line of the chip (a) or at an angle of 22.5° from the transmission line (b). See table 5.6 for the fit parameters.

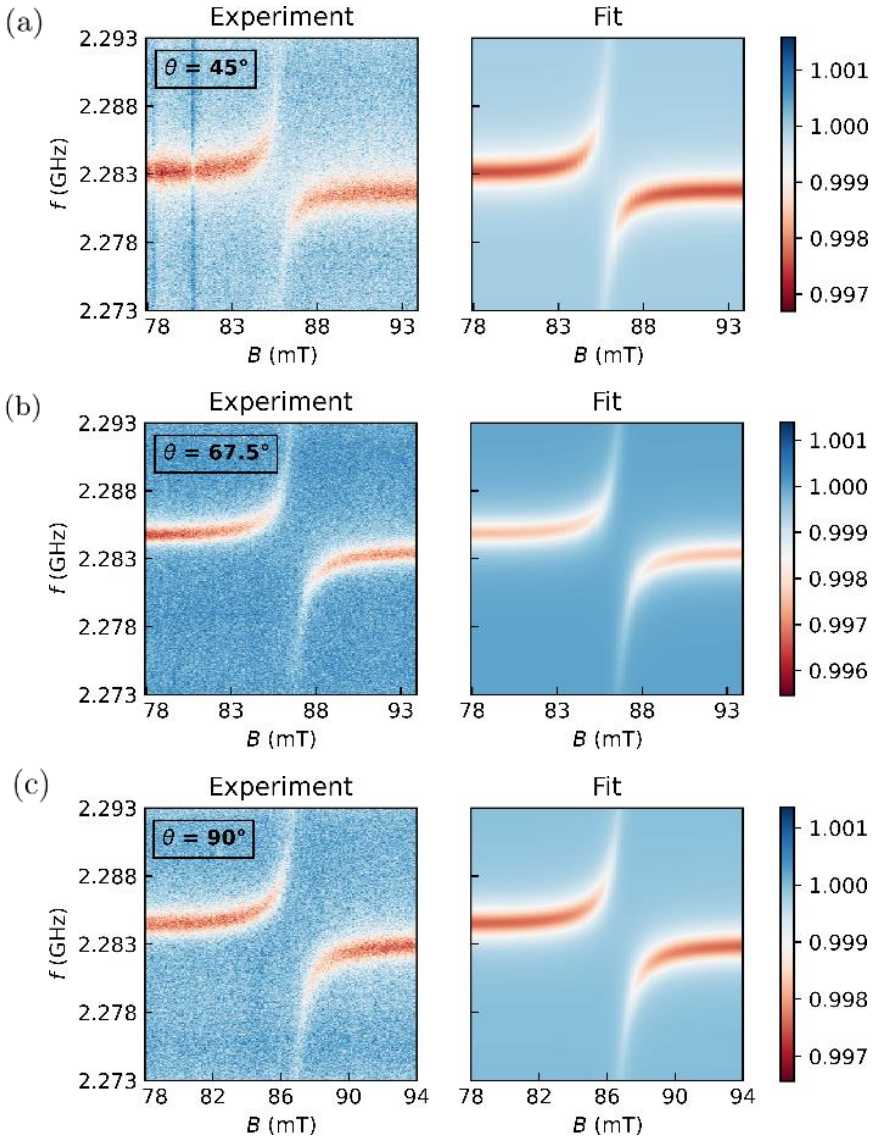

Figure 5.23: Transmission of LER 7 of chip *Test 1* coupled to a DPPH sample when the magnetic field is applied at an angle of 45° (a), 67.5° (b) or 90.0° (c) from the transmission line. See table 5.6 for the fit parameters.

The ensemble-resonator coupling is in the strong regime ($G_N > \gamma_\perp$). G_N increases as the magnetic field is rotated from $\theta = 0°$, when it is parallel to the transmission line, to $\theta = 90°$, when it is parallel to the resonator inductor lines. The microwave magnetic field generated by the inductor lines lies mainly in the plane perpendicular to them (see Fig. 5.4), and only the components of this oscillating field perpendicular to the static field contribute to the coupling. The maximum coupling is obtained then for $\theta = 90°$. At $\theta = 0°$, when part of the

microwave magnetic field is parallel to the static magnetic field, the ensemble-resonator coupling is lower. It is still non-zero thanks to the microwave field component perpendicular to the surface of the chip. A sufficiently large sample covers enough of the resonator field volume so that the in-plane and out-plane components of the microwave field contribute equally to the coupling. From the definition of the ensemble-resonator coupling (Eq. (3.46) in chapter 3), losing half of the contributions when the in-plane componenents are parallel to static magnetic field should give rise to a factor $1/\sqrt{2}$ (∼70%) of the maximum coupling. This agrees very well with the measured G_N (see Fig. 5.24), and it is an effect that was also observed with DPPH pellets on coplanar resonators [27, Ch.7].

θ (°)	g_S	$G_N/2\pi$ (MHz)	$G_N/\gamma_\perp$	C
0.0	$2.03001 \pm 2 \cdot 10^{-5}$	7.53 ± 0.01	1.032 ± 0.004	8.87 ± 0.04
22.5	$1.97559 \pm 7 \cdot 10^{-5}$	7.43 ± 0.01	1.017 ± 0.004	8.62 ± 0.04
45.0	$1.90015 \pm 7 \cdot 10^{-5}$	8.47 ± 0.01	1.160 ± 0.004	11.21 ± 0.05
67.5	$1.88166 \pm 6 \cdot 10^{-5}$	9.19 ± 0.01	1.259 ± 0.005	13.2 ± 0.1
90.0	$1.87924 \pm 6 \cdot 10^{-5}$	10.15 ± 0.01	1.39 ± 0.01	16.1 ± 0.1

Table 5.6: Parameters from the fit of the transmission of LER 7 in chip *Test 1* at different orientations of the magnetic field. All experiments were fitted with the same ensemble decoherence rate $\gamma_\perp = 7.30 \pm 0.03$ MHz, and the same resonator parameters except the resonance frequency ω_r: $\kappa/2\pi = 876.22 \pm 0.96$ kHz, $|\kappa_c|/2\pi = 2.175 \pm 0.003$ kHz and $\phi_c = (-4.05 \pm 0.05)°$. The average fitted resonance frequency is $\omega_r/2\pi = 2.2838 \pm 7 \cdot 10^{-4}$ GHz.

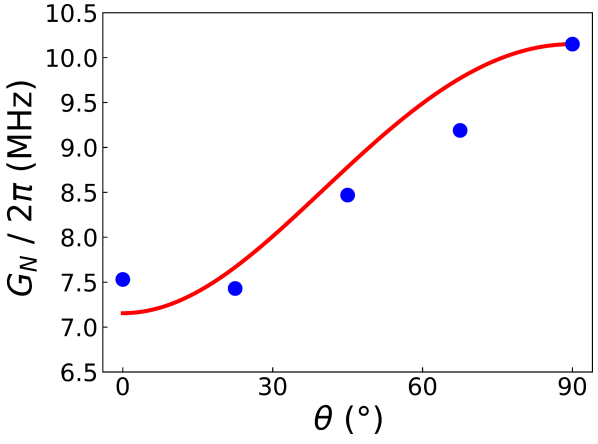

Figure 5.24: Collective spin-photon coupling between LER 7 and the DPPH sample as a function of the angle θ that the static magnetic field $\boldsymbol{B}_{\mathbf{dc}}$ makes with the transmission line (see Fig. 5.21). Blue dots mark the values obtained from the fit of the experiments. Red solid lines are the estimated coupling from the simulation of the microwave magnetic field generated by the resonator.

At $\theta = 0°$ and $\theta = 22.5°$, the contribution from spins in the ensemble that are directly coupled transmission line can be also seen clearly. Figure 5.25 shows how subtracting the fit of the ensemble-resonator coupling from the experimental data leaves only the absorption signal of DPPH coupled the transmission line. The ensemble-line coupling is maximum for $\theta = 0°$, as the transmission line is perpendicular to the inductor lines of LER 7. From the simulation of the field generated by the waveguide, the same dependence with θ as in the case of the resonator was expected, only switching the roles of the orientations defined by $\theta = 0°$ and $\theta = 90°$. Instead, the line-resonator coupling vanished quickly for $\theta > 0°$ (see Fig. 5.26).

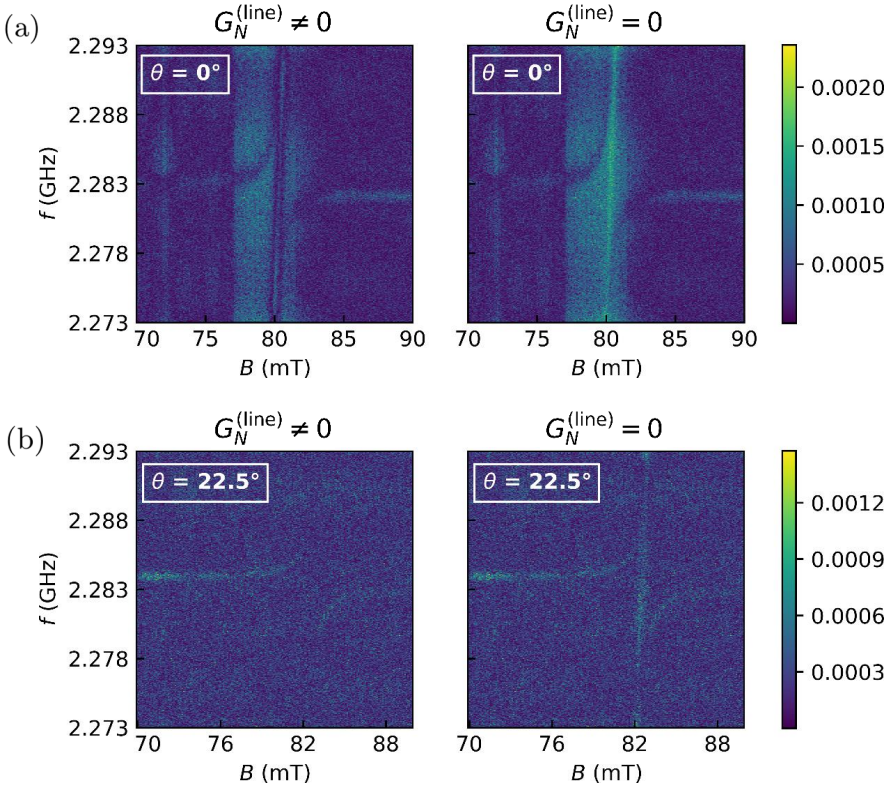

Figure 5.25: Absolute value of the difference between experimental transmission and its fit with the model, for $G_N^{(line)} \neq 0$ and $G_N^{(line)} = 0$. The two angles θ with higher $G_N^{(line)}$ are compared: (a) $\theta = 0°$ and (b) $\theta = 22.5°$. Subtracting the transmission of the fitted model with $G_N^{(line)} = 0$ removes only the transmission of the coupled resonator and leaves the transmission of the line coupled to the ensemble.

A tentative explanation to this unexpectedly drastic angular dependence of the ensemble-line coupling is the competition between the coupling rates of spins to the resonator field and the line field. Where the line field is higher,

the direct coupling of the spins to the input signal through the line is observed. However, if the resonator field is higher, then the hybrid spin-resonator system is measured (as an ensemble-resonator system). The line field is in general much weaker than the resonator field, and it is only stronger in the part of the sample that sits just on top of the central line of the waveguide. In this region, there is only an in-plane oscillating magnetic field perpendicular to the line. The out-of-plane component does not contribute to the coupling, which explains the vanishing of the coupling when the static magnetic field is aligned with the in-plane component.

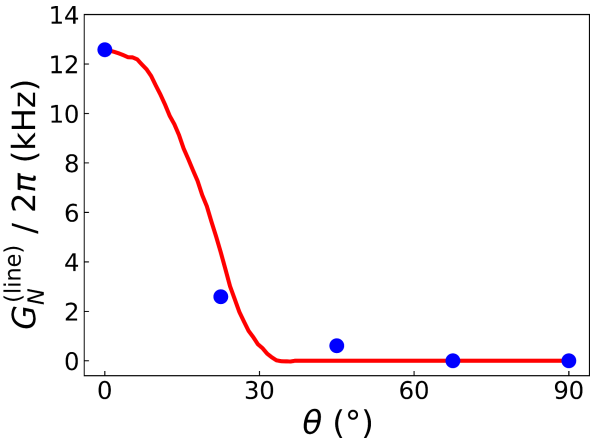

Figure 5.26: Collective spin-photon coupling of the DPPH sample to the transmission line as a function of the angle θ that the static magnetic field $\boldsymbol{B}_{\mathbf{dc}}$ makes with the transmission line (see Fig. 5.21). Blue dots mark the values obtained from the fit of the experiments. Red solid lines are the estimated coupling from the simulation of the microwave magnetic field generated by the transmission line. A lower bound was imposed to the microwave magnetic field of the line that contributes to the coupling. This is a simple model for the suppression of the direct ensemble-line coupling where the resonator field is higher than the line field.

There is another effect that the orientation of the static magnetic field has on the transmission: for each θ, a different resonance field B_{res} is measured. The drift in B_{res} is shown in Fig. 5.27 by plotting the effective g-value at each angle θ. The change in the resonator characteristic frequency between different angles is not more than 0.1%, thus not enough to account for the dispersion of 7% in the effective g-factor. This is unexpected, as the effect of anisotropy in the g-tensor of free-radical electrons is usually very small, and I am using a powder sample. The comparison of the experimental effective g-values with those expected if magnetic anisotropy is introduced (neglecting that the sample is a powder) rules out that the change in the g-values is due to an anisotropic g-tensor.

Another possible source of the error is the vector magnet. In particular, I suspect it is a problem of the magnet axis that is used to rotate the static field in the plane of the chip surface (x-axis in the magnet frame of reference). It is not a current to field conversion error, which would appear as an anisotropic g-tensor. The results from Fig. 5.27 can be explained with a zero-point error of around 7 mT in the magnet x-axis due to an error in the magnet calibration. This problem has been previously reported in previous experiments with the x-axis of the magnet [27, Ch.7]. These experiments have therefore allowed us to detect it and correct it.

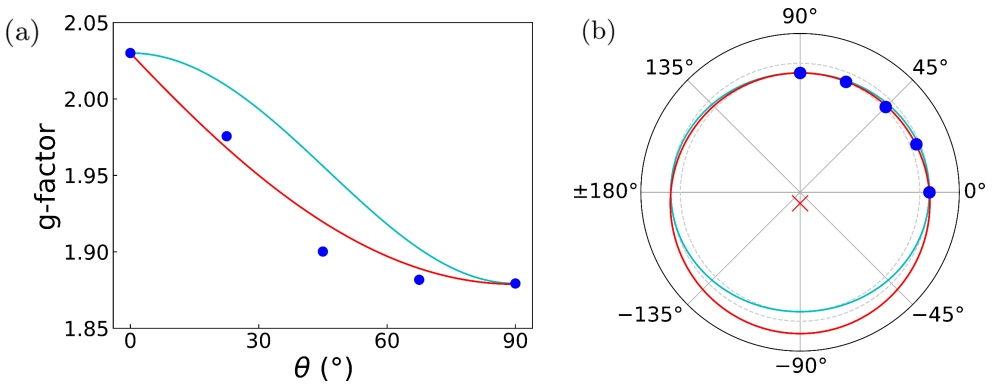

Figure 5.27: (a) g-factor (blue dots) for different angles θ between the static magnetic field $\boldsymbol{B}_{\mathbf{dc}}$ and the orientation of the transmission line. Solid lines are the g-factor that would be measured with an anisotropic g-tensor (neglecting that the sample is a powder) or if there was a scale error in one of the components of the field generated by the vector magnet (cyan), or a zero-point error in this same field component (red). (b) The same plot in polar coordinates, with the zero-point error marked with a red cross.

5.4 Coupling of DPPH to LERs in *Test 2*

5.4.1 Testing the bare resonator response with magnetic field

The resonators of chip *Test 2* were measured at 4 K before depositing the DPPH samples. Note that in this chip LERs 7 and 8 are in the same orientation in which their resonances could not be initially detected in *Test 1* (see Fig. 5.1), but now with the inductor placed closer to the transmission line. This geometry provides a higher coupling of the resonator to the transmission line, improving the visibility of the resonator response. Still, the resonator-line coupling in this configuration is much smaller than that obtained with the longer parts of the inductor lines placed parallel to the transmission lines.

The bare resonator responses were measured for magnetic fields up to 100

mT (see Fig. 5.28), which are enough to perform the coupling experiments shown below. The effect of high static magnetic fields parallel to the chip surface in the resonances is akin to an increase in temperature (see section 5.1.3) [30]. As the magnetic field increases, the resonances shift towards lower frequencies. Also, the resonances of LERs 7 and 8 broaden with magnetic field, but the line-resonator coupling rate κ_c remains nearly constant. Therefore, the increase in κ is associated with an increase in the internal decay rate κ_i.

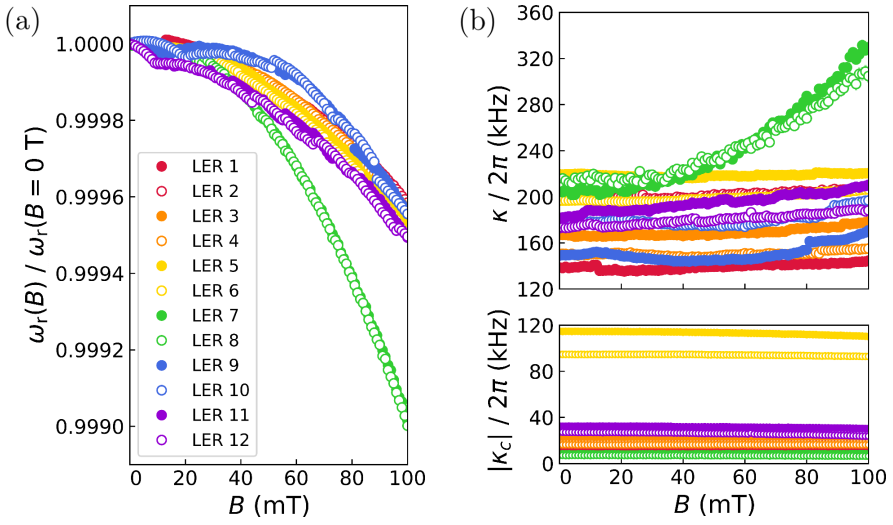

Figure 5.28: (a) Drift with magnetic field of the resonance frequencies of *Test2* LERs. (b) Change with magnetic field of the total decay rate κ and the module of the line-resonator coupling rate κ_c for the same set of resonators.

5.4.2 Frequency shift by sample deposition

In the first run of experiments with the *Test 2* chip, a DPPH powder sample was placed on top of six of the twelve resonators: LERs 1, 4, 5, 8, 10 and 12, as shown in Fig. 5.29. The resonance frequencies measured at zero field for all twelve resonators are listed in table A.4 in Appendix , with the relative shift from the resonance frequencies of the bare resonators plotted in Fig. 5.30. LERs hosting a DPPH sample show larger frequency shifts, enough to swap the order in frequency in each pair of LERs.[2] LERs 4, 8, 10 and 12 show the largest shifts. Figure 5.29 shows that the samples on these resonators were deposited with more oil. I therefore assign the shift to the increase in the resonator capacitance as the space between capacitor fingers is filled with the oil (with a relative permittivity $\epsilon_r > 1$).

[2]I know that there is a swap in some pairs because only one resonator of each pair is coupled to an ensemble in the transmission measurements around the resonance field B_{res}.

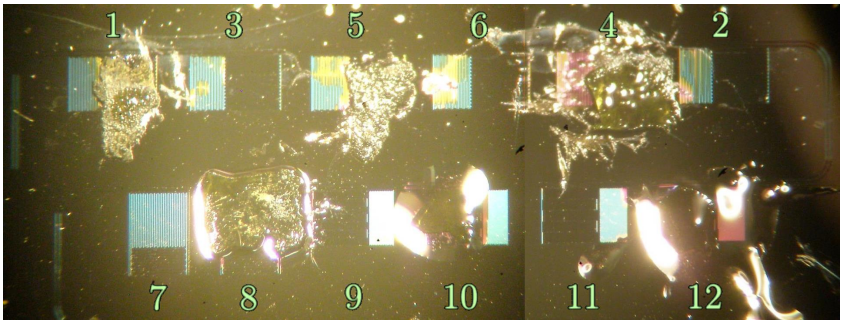

Figure 5.29: Locations of DPPH samples in the first run of experiments with chip *Test 2*. Samples where placed on LERs 1, 4, 5, 8, 10 and 12.

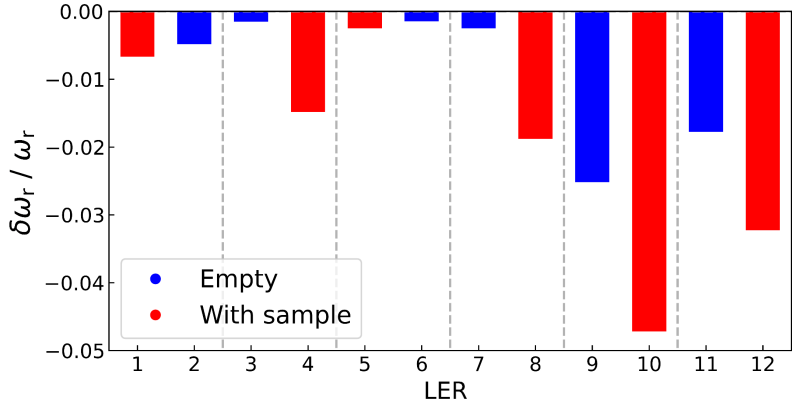

Figure 5.30: Relative shift of the resonance frequency of each LER in chip *Test 2* after the deposition of DPPH samples on LERs 1, 4, 5, 8, 10 and 12 (in red). Shift for the six empty resonators (LERs 2, 3, 6, 7, 9 and 11) in blue.

A frequency shift is observed too in the empty resonators, although smaller than in the resonator of each pair that is coupled to a magnetic sample. Part of the resonator capacitance comes from the parasitic capacitance between the whole lumped-element circuit and the ground plane, which can be partially filled by oil from the samples in neighbouring resonators. The shifts of LERs 9 and 11, which sit next to the two resonators with the largest shifts (LERs 10 and 12), are examples of this effect.

5.4.3 Spin-photon coupling in chip *Test 2*: coupling to remote resonators and dependence on ω_r

Chip *Test 2* has pairs of resonators with very close frequencies (a few MHz between their resonance frequencies): LERs 1 and 2, LERs 3 and 4, and so on. DPPH samples were deposited only in one resonator of each pair. This was

done as an attempt to detect the coupling of the spin ensemble to the 'empty' resonator through its coupling to the other resonator of the pair. This remote coupling would be mediated by the transmission line. The transmission of *Test 2* was measured near the resonances of LERs 1, 4, 5, 8, 10 and 12, which were coupled to DPPH samples, and also near the resonances of two of the other six 'empty' resonators (LERs 2 and 3), for magnetic fields around their respective resonance fields B_{res}. The experimental results and their fits are shown in Figs. 5.31, 5.32 and 5.33. The fitting parameters are listed in table A.5 in Appendix A and table 5.7. The remote coupling effect could not be detected, as no coupling was observed for LERs 2 and 3 (see Fig. 5.31). This means that the line-mediated coupling between resonators in this setup is too small. Current research on this topic is focused on improving resonator-resonator coupling by reducing the distance between the capacitors of the LERs in each pair.

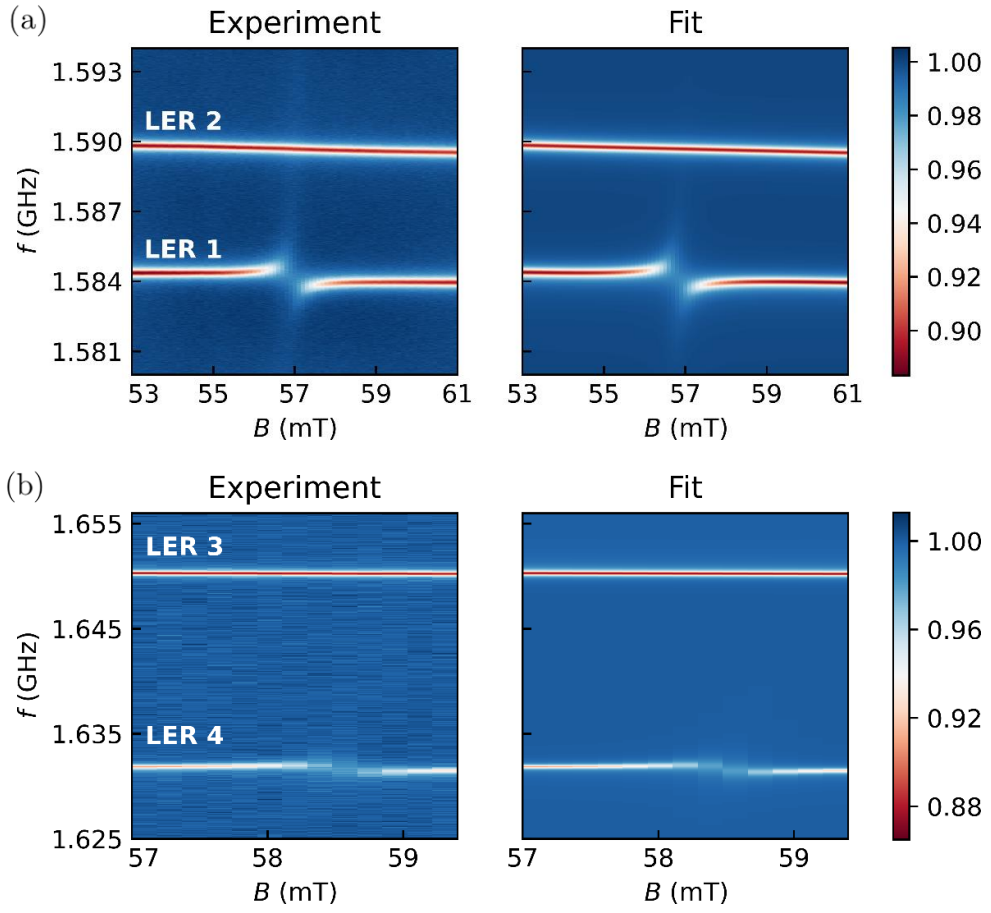

Figure 5.31: (a) Transmission of LERs 1 and 2 of chip *Test 2*, with a DPPH sample on LER 1. (b) Transmission of LERs 3 and 4 of chip *Test 2*, with a DPPH sample on LER 4. See table A.5 in Appendix A and table 5.7 for the fit parameters.

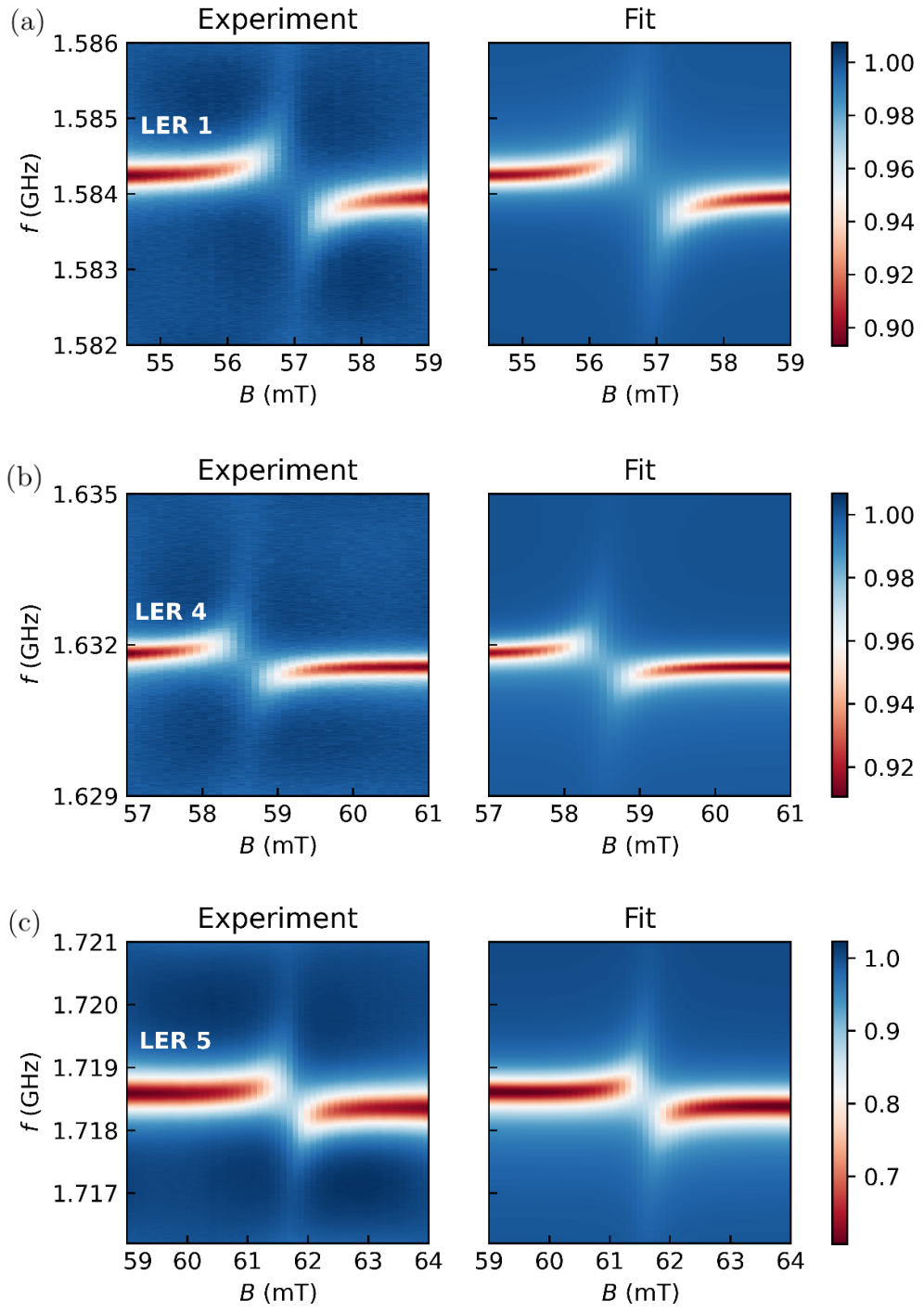

Figure 5.32: (a) Transmission of LER 1 of chip *Test 2* coupled to a DPPH sample. Below, transmission of LER 4 (b) and LER 5 (c) of the same chip, each coupled to a DPPH sample. See table A.5 in Appendix A and table 5.7 for the fit parameters.

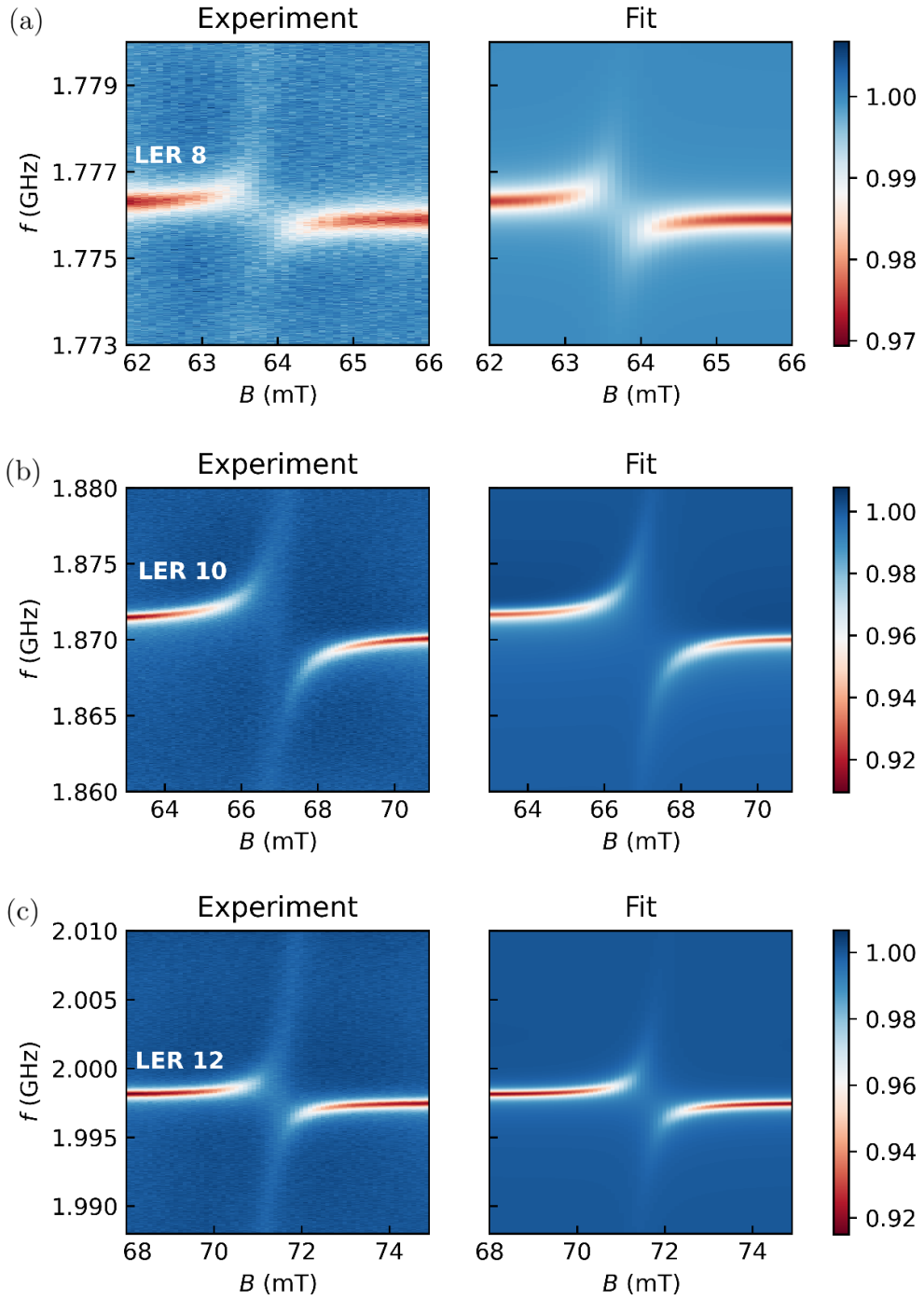

Figure 5.33: Transmission of LER 8 (a), LER 10 (b) and LER 12 (c) of chip *Test 2*, each coupled to a DPPH sample. See table A.5 in Appendix A and table 5.7 for the fit parameters.

LER	g_S	$G_N/2\pi$ (MHz)	$G_N/\gamma_\perp$	C
1	$1.98818 \pm 3 \cdot 10^{-5}$	2.530 ± 0.002	0.35 ± 0.02	6.2 ± 0.3
4	$1.9928 \pm 1 \cdot 10^{-4}$	2.10 ± 0.01	0.29 ± 0.01	4.5 ± 0.2
5	$1.98965 \pm 3 \cdot 10^{-5}$	1.819 ± 0.002	0.25 ± 0.01	2.0 ± 0.1
8	$1.98878 \pm 4 \cdot 10^{-5}$	2.555 ± 0.004	0.35 ± 0.02	4.8 ± 0.2
10	$1.99324 \pm 2 \cdot 10^{-5}$	7.395 ± 0.002	1.0 ± 0.1	29.9 ± 1.5
12	$1.99829 \pm 2 \cdot 10^{-5}$	4.670 ± 0.002	0.64 ± 0.03	13.7 ± 0.7

Table 5.7: Parameters from the fit of the transmission of the lumped-element resonators in chip *Test 2* at 4 K.

All experiments were fitted with the same ensemble decoherence rate $\gamma_\perp = 7.30 \pm 0.03$ MHz. The collective spin-photon coupling is largest for LERs 10 and 12. The former lies just in the limit of strong coupling ($G_N = \gamma_\perp$). For these two resonators, the spin-photon coupling is enhanced by their larger resonance frequency (see section 5.3.2) and lower inductance. This can be seen with a simple description of the conversion of the energy in the resonator in resonance into the amplitude of its oscillating magnetic field. The energy of the vacuum fluctations of the resonator is $E_0 = \hbar\omega_r/2$, with half of this energy is stored in the inductor in resonance. Then the RMS (root mean square) current in the inductor is $I_{RMS} = \sqrt{\hbar\omega_r/2L}$. The oscillating field, and therefore the spin-photon coupling, is proportional to this current. It increases with increasing ω_r and decreases with increasing L.

The ensemble-line coupling was not included in the fit of these experiments, although in some of the resonators with larger ensemble-resonators coupling (LERs 10 and 12, see Fig. 5.33) it seems that it could be present. The coupling should be present in all measurements, but a consistent value of $G_N^{(line)}$ for all of them was not found.

5.4.4 Effect of the magnetic field inhomogeneity: coupling to small spin ensembles

For the the second run of experiments with chip *Test 2*, the DPPH samples were moved to the previously empty resonators (more details in Fig. 5.34): LERs 2, 3, 6, 7, 9 and 11. Only the transmission of the pairs of LERs 1 and 2, 7 and 8, and 11 and 12, was measured. Results are shown in Fig. 5.35. The fit parameters are listed in table A.6 in Appendix A and table 5.8. Both resonators in each pair are coupled to an ensemble, one of them with higher coupling (presumably the one with the DPPH sample on top).

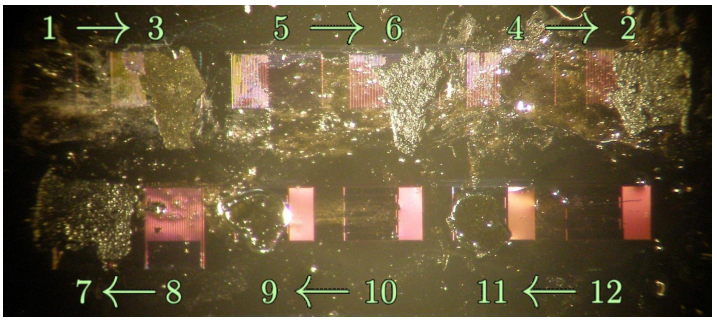

Figure 5.34: Deposition of DPPH samples in the second run of experiments with chip *Test 2*. Samples on LERs 2, 3, 6, 7, 9 and 11. Each sample was moved from its position in Fig. 5.29 to the closest empty resonator. Small pieces of DPPH powder remain in the resonators where the samples were previously placed, most noticeably in LER 8. However, samples that were originally deposited with more oil could be moved more easily and left almost no powder behind (see LERs 10 and 12).

LER	g_S	$G_N/2\pi$ (MHz)	$G_N/\gamma_\perp$	C
1	$2.04501 \pm 4 \cdot 10^{-5}$	1.166 ± 0.001	0.16 ± 0.01	1.9 ± 0.1
2	$2.04407 \pm 3 \cdot 10^{-5}$	3.343 ± 0.002	0.46 ± 0.02	10.8 ± 0.5
7	$2.04529 \pm 6 \cdot 10^{-5}$	5.437 ± 0.004	0.75 ± 0.04	20.06 ± 0.99
8	$2.04209 \pm 8 \cdot 10^{-5}$	2.020 ± 0.004	0.28 ± 0.01	3.7 ± 0.2
11	$2.03565 \pm 2 \cdot 10^{-5}$	4.812 ± 0.001	0.66 ± 0.03	19.0 ± 0.9
12	$2.0336 \pm 1 \cdot 10^{-4}$	0.515 ± 0.003	0.071 ± 0.004	0.24 ± 0.01

Table 5.8: Parameters from the fit of the transmission of the lumped-element resonators in chip *Test 2* at 4 K. All experiments were fitted with the same ensemble decoherence rate $\gamma_\perp/2\pi = 7.30 \pm 0.03$ MHz.

Let us focus first in the ensemble-resonator coupling of resonators hosting a large DPPH sample. These are LERs 2, 7 and 11. The coupling observed for samples on LERs 2 and 7 is higher than in the previous run for the same samples on LERs 4 and 8. This increase in the coupling is due to the smaller gap between the chip and sample surface as some oil is lost during sample transfer, the same effect already discussed in section 5.3.2. In the case of the sample on LER 11, the coupling remains similar to the one measured for LER 12 in the previous section. This sample was deposited with more oil, so the relative change in the gap as the sample is moved is smaller. Also, the increase in the coupling is probably compensated by the slight shift in the sample location with respect to the inductor, which leaves half a turn of the inductor without sample on top (check the upper part of LER 11 in Fig. 5.34). This highlights the importance of the filling factor, that is, how much of the resonator mode volume is covered by the sample.

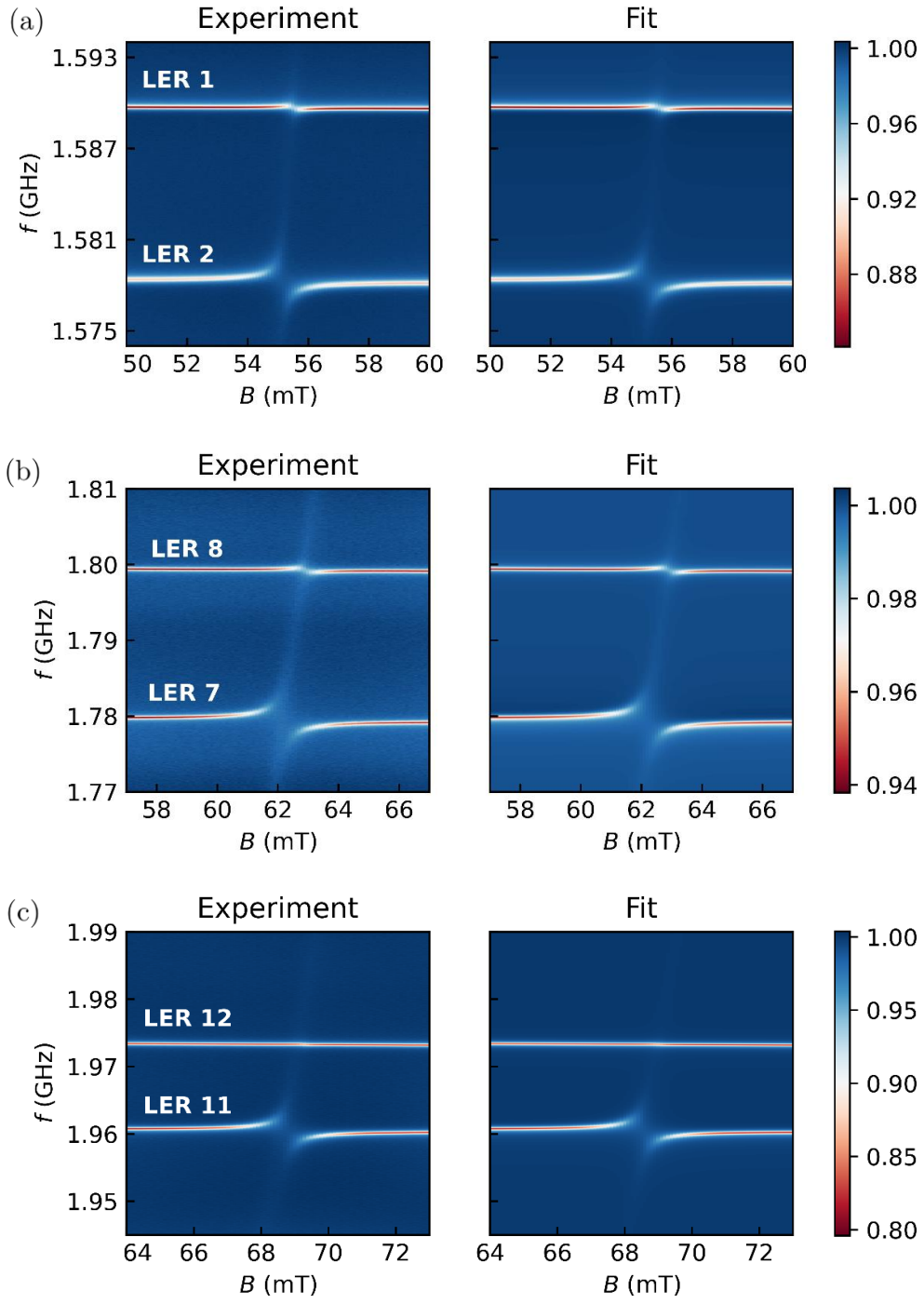

Figure 5.35: Transmission of LERs 1 and 2 (a), LERs 7 and 8 (b), and LERs 11 and 12 (c) of chip *Test 2*, with DPPH samples on top of LERs 2, 7 and 11. See table A.6 in Appendix A and table 5.8 for the fit parameters.

In the case of the seemingly empty resonators (LERs 1, 8 and 12), it is possible that the small observed coupling is due to their coupling to samples on other resonators through a resonator-resonator coupling. However, this effect is ruled out by the measurements in the previous section, where it was not present. The resonator-resonator coupling in this chip is too low. If it is smaller than the resonator bandwidth, then the effect its hardly detectable. A closer inspection of Fig. 5.34 shows that small pieces of DPPH powder have remained stuck on the oil layer when the samples were moved, which make for the coupling that is observed in the otherwise empty resonators (see Fig. 5.36a).

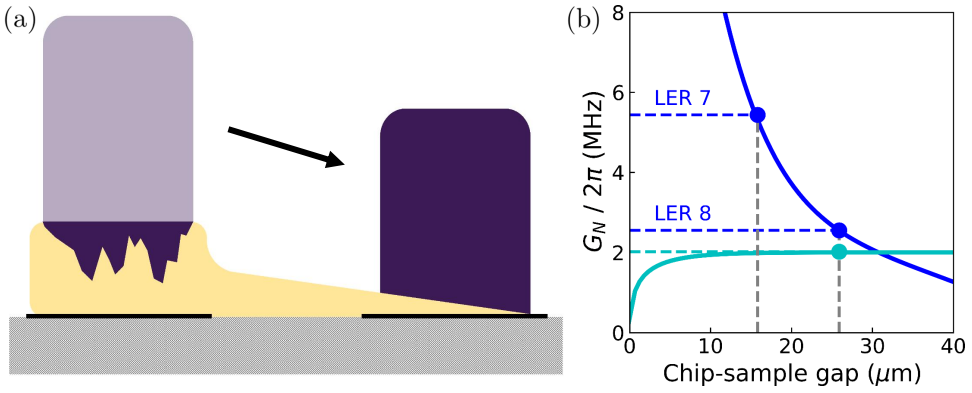

Figure 5.36: (a) Scheme of the DPPH sample transfer (not to scale). A layer of oil remains in the first resonator with small pieces of DPPH embedded in it. The bulk of the sample is transferred to the second resonator, taking part of the oil layer with it. (b) Collective spin-resonator coupling computed from the simulation of the distribution of fields generated by the inductor of LERs 7 and 8 of chip *Test 2* (blue solid lines) as a function of the gap (the height of the oil layer) between the chip surface and the surface of the bulk of the DPPH sample. Cyan solid line is the simulation of the coupling for small sample pieces covering a 5% of the gap volume in LER 8. The gap in each resonator can be estimated from the measured couplings (dashed lines).

The coupling to the pieces is smaller than for whole samples, yet of the same order of magnitude. Let us focus on LER 8, where there are clearly DPPH pieces on top of the resonator after sample transfer (see Fig. 5.34). Comparing the area of its inductor covered by these pieces with that of the original sample (100 % of the inductor), an upper bound $N/10$ to the number N' of remaining DPPH spins is estimated. The measured coupling $G_{N'}/2\pi = 2.020 \pm 0.004$ MHz is about 80 % of that obtained with the whole sample, $G_N/2\pi = 2.555 \pm 0.004$ MHz. This is more than two times larger than what one would expect by simply scaling the spin-photon coupling using the upper bound to N' ($G_{N'} = G_N\sqrt{N'/N} < G_N/\sqrt{10}$, which gives $G_{N'}/2\pi < 0.8$ MHz). This suggests that, due to the inhomogeneity of the resonator field,

a small sample volume close to the resonator surface contributes more to the collective coupling than large volumes farther from it. Figure 5.36b shows the result of the simulation of the collective spin-photon coupling in LERs 7 and 8 for a bulk sample of DPPH, together with the simulation for small pieces of DPPH embedded in the oil layer on top of LER 8, covering a 5% of the gap volume. The results are consistent with a gap of 26 μm in LER 8 that closes to 16 μm in LER 7 after sample transfer.

5.5 Conclusions

The coupling of free-radical molecular spin ensembles to the photon modes of lumped-element superconducting resonators has been explored. The collective coupling G_N of relatively large samples ($N \sim 10^{17}$) was found to be at least of the same order of the spin decoherence rate $\gamma_\perp$, reaching the high cooperativity regime for all resonators. In one case, the signatures that characterize the strong, or coherent, coupling regime ($G_N > \gamma_\perp$) between the spins and the photons, and the existence of hybrid polaritonic excitations were also observed. The results show also that the spin-photon coupling can be tuned, in situ, by modifying the orientation of the magnetic field that polarizes the molecular spins. In this way, we have been able to detect the direct coupling of the spins to the transmission line. Taken together, these results show that these circuits provide a suitable basis for combining a broadband control of the spin states with the possibility of dispersively reading out the results; i.e. they provide the basic ingredients for performing the basic operations of a hybrid molecular spin quantum processor [31].

Before depositing the samples, the resonators were tested with different temperatures and magnetic fields. It was found, as expected for these superconducting circuits, that at higher temperatures and magnetic fields both the resonance frequency ω_r and the internal quality factor $Q_\mathrm{i} = \omega_\mathrm{r}/2\kappa_\mathrm{i}$ of the resonators decrease. Different orientations of the resonators with respect to the transmission line were tested. The dominant mechanism of the line-resonator coupling is inductive coupling. Upon the deposition of the DPPH samples, the capacitance of the resonators increases due to the oil layer used to stick the samples to the chip surface. This further decreases the resonance frequency of the LERs.

I tested how changing the experimental setup or the properties of the resonator affects the coupling. By changing the orientation of the static magnetic field, different components of the oscillating field generated by the resonator contribute to the coupling. Also, the coupling is enhanced by using resonators with higher resonance frequency and lower geometric inductance. However,

the dominant effect on the coupling is the location of the spins above the resonator. Due to the inherently inhomogenous distribution of the microwave magnetic field that the LERs generate, the attainable coupling is, to a large extent, determined by how closely the sample can be placed above the surface of the chip. The need of fixing, and thermalizing, the samples with the help of some intermediate agent, in this case paratone oil, limits the maximum coupling that can be achieved in practice. The results in this chapter provide also some practical tricks to minimize this effect when dealing with macroscopic molecular samples. Still, it is clear that fully exploiting the possibilities offered by lumped element resonators to maximize their coupling to molecular spins, e.g. by reducing their impedance and/or their mode volume [32–35], must go hand in hand with methods that allow optimizing the chip-molecules interface. The results show that this second aspect can contribute very significantly to enhance the coupling to very small spin ensembles.

The fact that many molecular nanomagnets are stable in solution provides an alternative to the use of bulk samples. The combination of this method and of soft nanolithography techniques with a high spatial resolution, like Dip Pen Nanolithography, has enabled reaching very high single spin-photon couplings with coplanar superconducting resonators [36]. However, this idea is only applicable whenever the molecular orientation does not play a major role, e.g. when one deals with isotropic spins such as those in DPPH. The case of anisotropic molecular spins, which are very interesting to encode spin qudits, requires a different approach. Interesting possibilities are based on the application of molecular self-organization techniques, which can be assisted by previously deposited mono-layers of non-magnetic molecules acting as grafting centers [37], or by employing chemical tools that allow transferring a preformed molecular lattice onto the device [38]. In these cases, the strong inhomogeneity of the microwave magnetic field can be advantageously exploited to address certain molecular spins from the lattice, via a proper circuit design, thus helping to circumvent the need of positioning the molecules one by one. Even though still challenging, the results suggest that lumped element resonators are very promising for the control and readout of molecular spin qubits.

References

[1] B. Aja, M. C. de Ory, L. de la Fuente, E. Artal, J. P. Pascual, M. T. Magaz, D. Granados, and A. Gomez, IEEE Transactions on Microwave Theory and Techniques **69**, 578 (2021).

[2] I. Gimeno Alonso, Ph.D. thesis, Universidad de Zaragoza (2023).

[3] A. Ghirri, C. Bonizzoni, F. Troiani, N. Buccheri, L. Beverina, A. Cassinese, and M. Affronte, Physical Review A **93**, 063855 (2016).

[4] M. Mergenthaler, J. Liu, J. J. Le Roy, N. Ares, A. L. Thompson, L. Bogani, F. Luis, S. J. Blundell, T. Lancaster, A. Ardavan, et al., Physical Review Letters **119**, 147701 (2017).

[5] C. Bonizzoni, A. Ghirri, M. Atzori, L. Sorace, R. Sessoli, and M. Affronte, Scientific Reports **7**, 13096 (2017).

[6] S. Weichselbaumer, M. Zens, C. W. Zollitsch, M. S. Brandt, S. Rotter, R. Gross, and H. Huebl, Physical Review Letters **125**, 137701 (2020).

[7] M. Rubín-Osanz, M. C. de Ory, I. Gimeno, D. Granados, D. Zueco, A. Gomez, and F. Luis, Fizyka Nyzkykh Temperatur/Low Temperature Physics **50**, 520 (2024).

[8] M. M. Khapaev, M. Yu Kupriyanov, E. Goldobin, and M. Siegel, Superconductor Science and Technology **16**, 24 (2003).

[9] D. R. Lide, ed., *A Century of Excellence in Measurements Standards and Technology* (U.S. Government Printing Office, 2001), chap. Effects of Configuration Interaction on Intensities and Phase Shifts.

[10] S. Fan, Applied Physics Letters **80**, 908 (2002).

[11] U. Fano, Physical Review **124**, 1866 (1961).

[12] A. İmamŏglu, Physical Review A **50**, 3650 (1994).

[13] M. S. Khalil, M. J. A. Stoutimore, F. C. Wellstood, and K. D. Osborn, Journal of Applied Physics **111**, 054510 (2012).

[14] S. Doyle, Ph.D. thesis, Cardiff University (2008).

[15] N. D. Yordanov, Applied Magnetic Resonance **10**, 339 (1996).

[16] D. Z. Žilić, D. Pajić, M. Jurić, K. Molčanov, B. Rakvin, P. Planinić, and K. Zadro, Journal of Magnetic Resonance **207**, 34 (2010).

[17] *PubChem Compound Summary for CID 74358, 1,1-Diphenyl-2-picrylhydrazine.*, https://pubchem.ncbi.nlm.nih.gov/compound/1_1-Diphenyl-2-picrylhydrazine. Accessed Aug. 31, 2023.

[18] D. E. Williams, Journal of the American Chemical Society **88**, 5665 (1966).

[19] D. E. Williams, Journal of the American Chemical Society **89**, 4280 (1967).

[20] H. Ohya-Nishiguchi, Bulletin of the Chemical Society of Japan **52**, 3480 (1979).

[21] T. Fujito, Bulletin of the Chemical Society of Japan **54**, 3110 (1981).

[22] J. H. Van Vleck, Physical Review **74**, 1168 (1948).

[23] P. W. Anderson and P. R. Weiss, Reviews of Modern Physics **25**, 269 (1953).

[24] R. Bachmann, J. DiSalvo, F. J., T. H. Geballe, R. L. Greene, R. E. Howard, C. N. King, H. C. Kirsch, K. N. Lee, R. E. Schwall, H. Thomas, et al., Review of Scientific Instruments **43**, 205 (1972).

[25] H. W. J. Blöte, Physica B+C **79**, 427 (1975).

[26] C. T. Kiers, J. L. de Boer, R. Olthof, and A. L. Spek, Acta Crystallographica **B32**, 2297 (1976).

[27] M. D. Jenkins Sánchez, Ph.D. thesis, Universidad de Zaragoza (2015).

[28] M. Jenkins, T. Hümmer, M. J. Martínez-Pérez, J. García-Ripoll, D. Zueco, and F. Luis, New Journal of Physics **15**, 095007 (2013).

[29] V. Rollano, M. C. de Ory, C. D. Buch, M. Rubín-Osanz, D. Zueco, C. Sánchez-Azqueta, A. Chiesa, D. Granados, S. Carretta, A. Gomez, et al., Communications Physics **5**, 246 (2022).

[30] N. G. Ebensperger, M. Thiemann, M. Dressel, and M. Scheffler, Superconductor Science and Technology **29**, 115004 (2016).

[31] A. Chiesa, S. Roca, S. Chicco, M. C. de Ory, A. Gómez-León, A. Gomez, D. Zueco, F. Luis, and S. Carretta, Physical Review Applied **19**, 064060 (2023).

[32] A. Bienfait, J. J. Pla, Y. Kubo, M. Stern, X. Zhou, C. C. Lo, C. D. Weis, T. Schenkel, M. L. W. Thewalt, D. Vion, et al., Nature Nanotechnology **11**, 253 (2016).

[33] S. Probst, A. Bienfait, P. Campagne-Ibarcq, J. J. Pla, B. Albanese, J. F. Da Silva Barbosa, T. Schenkel, D. Vion, D. Esteve, K. Mølmer, et al., Applied Physics Letters **111**, 202604 (2017).

[34] C. Eichler, A. J. Sigillito, S. A. Lyon, and J. R. Petta, Physical Review Letters **118**, 037701 (2017).

[35] B. Sarabi, P. Huang, and N. M. Zimmerman, Physical Review Applied **11**, 014001 (2019).

[36] I. Gimeno, W. Kersten, M. C. Pallarés, P. Hermosilla, M. J. Martínez-Pérez, M. D. Jenkins, A. Angerer, C. Sánchez-Azqueta, D. Zueco, J. Majer, et al., ACS Nano **14**, 8707 (2020).

[37] L. Tesi, F. Stemmler, M. Winkler, S. S. Y. Liu, S. Das, X. Sun, M. Zharnikov, S. Ludwigs, and J. van Slageren, Advanced Materials **35**, 2208998 (2023).

[38] A. Urtizberea, E. Natividad, P. J. Alonso, L. Pérez-Martínez, M. A. Andrés, I. Gascón, I. Gimeno, F. Luis, and O. Roubeau, Material Horizons **7**, 885 (2020).

Chapter 6

Dispersive qubit readout: pump-probe experiments on PTM organic free radicals

The experimental results from the previous chapter demonstrate that the high cooperativity and strong coupling regimes can be attained with molecular spin qubits coupled to lumped-element resonators (LERs). The experiments described in it measure the response of the hybrid spin-LER system to low microwave power excitations and for long times. These conditions keep the system in equilibrium or stationary conditions. The goal in a quantum processor like that shown in chapter 1 is however very different from this: the qubits are firstly set out of equilibrium (or away from the initialized ground state in a single qubit) with microwave pulses that represent the quantum gates, then their final state is measured.

This chapter is dedicated to the first experiments towards qubit manipulation with microwave pulses combined with quantum non-demolition (QND) measurements performed by coupling the molecular spin qubits to LERs. For this, the hybrid spin-LER system must be set in the dispersive regime (see section 3.4 in chapter 3 for a proper definition), where the spin transition frequency ω_{q} — the qubit frequency — and the resonator frequency ω_{r} are sufficiently detuned so that no real exchange of excitations occurs between both systems. This condition is met for a qubit-resonator detuning $\Delta = \omega_{\mathrm{q}} - \omega_{\mathrm{r}}$ much larger than the collective spin-photon coupling G_N (in absolute value, that is, $|\Delta| \gg G_N$). The interest of the dispersive regime lies in that, even if the resonator and spin states are effectively decoupled, their frequencies ω_{q} and ω_{r} are still modulated — or 'dressed' — by the coupling. In particular, ω_{r} is shifted to lower or higher frequencies depending on the state of the spins,

and the spin state can be inferred from the response of the resonator. This 'dispersive readout' of the qubit state is a well established technique in superconducting qubits [1, 2], nowadays extended to other qubit realizations in circuit-QED platforms [3].

6.1 Experimental setup for pulse experiments

6.1.1 Chip design

Two superconducting chips were designed for pulse experiments, labeled *Test 3* and *Test 4*. *Test 3* hosts 10 superconducting LERs coupled to a single transmission line, with resonance frequencies between 1.7 and 2.9 GHz. *Test 4* is an evolution of *Test 3* with an additional transmission line, and hosts 10 lumped-element resonators with resonance frequencies between 1.4 and 2.8 GHz. In both chips, LERs are labeled from highest resonance frequency to lowest (that is, in increasing order of resonator area). The designs of both chips are shown in Fig. 6.1.

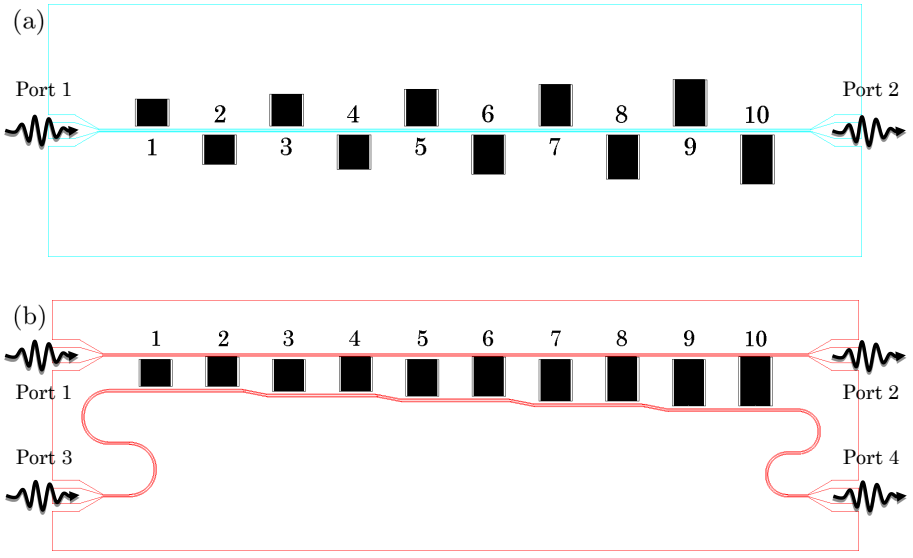

Figure 6.1: Vector file design of *Test 3* (a) and *Test 4* (b). LERs (black) are side-coupled to either a single transmission line (*Test 3*, blue) or two transmission lines (*Test 4*, red), and labeled in order of decreasing resonance frequency ω_r.

The first tests of the microwave setup for pulse experiments were performed with *Test 3*. This chip was originally intended for achieving the highest possible single spin-photon coupling strength [4, Ch.5], which calls for the highest possible current at the inductor in resonance, thus the smallest possible in-

ductance L. Thus, the design of these resonators is radically different from those in the previous chapter: most of the LER area is now taken by the inter-digital capacitor, with the inductor being just a short superconducting strip connecting the two ends of the capacitor (see Fig. 6.2). In addition, a nano-constriction was fabricated in the inductor by FIB lithography in order to locally increase the microwave magnetic field, thus further enhancing the spin-photon coupling for molecules sitting just above the constriction.

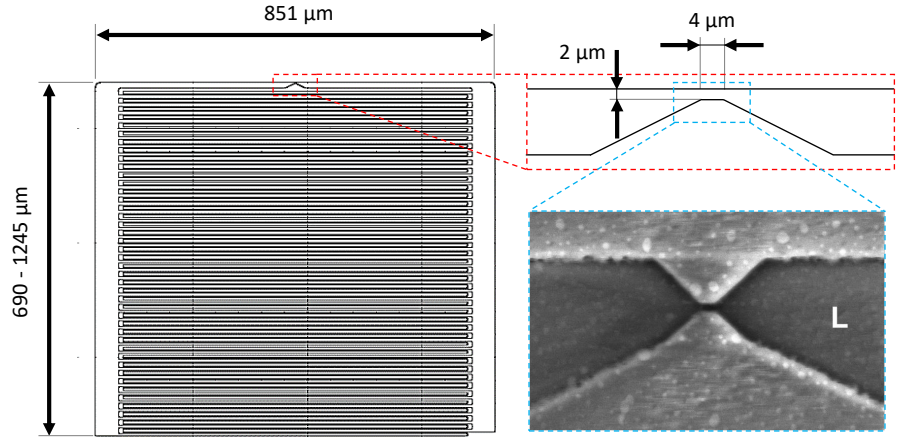

Figure 6.2: Design of a low inductance (low-L) LER with a nano-constriction, adapted from [4, Ch.5]. The inductor is the strip at the top of the figure. The frequency of the resonator is tuned by changing the size of the capacitor, thus the different lengths in the dimension perpendicular to the inductor (ranging from 690 to 1245 μm). The inductor has a 2 μm wide constriction that is further narrowed to tens of nm by FIB lithography.

Test 4 introduces an additional transmission line, which allows sending excitation and readout signals separately via different lines. LERs are coupled to both lines. The excitation line goes from port 1 to port 2 in Fig. 6.1b. This line is coupled to the inductor of the LERs. The readout line connects ports 3 and 4 in Fig. 6.1b, and it is capacitively coupled to the opposite side of the resonators. The weak capacitive coupling between this line and the resonator does not pose a limitation to the visibility of the resonances if the measurements are carried out in the millikelvin regime. None of the resonators in this chip has a nano-constriction in the inductor.

6.1.2 Molecular spin samples

Free radicals provide the simplest systems to test the pump-probe microwave setup. Hosting a spin 1/2, each radical molecule has a single spin transition that is easily tunable with magnetic field ($\omega_q \propto B$). For clarity, the Hamilto-

nian of a free radical is reproduced here:

$$H = \mu_{\mathrm{B}} g_{\mathrm{S}} B \hat{S}_z = \frac{\mu_{\mathrm{B}} g_{\mathrm{S}} B}{2} \hat{\sigma}_z, \tag{6.1}$$

which contains just the Zeeman term of the interaction of the $S = 1/2$ spin with the magnetic field. The spin transition frequency is $\omega_{\mathrm{q}} = \mu_{\mathrm{B}} g_{\mathrm{S}} B/\hbar$.

If g_{S} is isotropic and the radicals can be considered as non-interacting spin systems, all of them are identical from a magnetic point of view. This makes DPPH an unsuitable candidate for pulse experiments, as it exhibits antiferromagnetic interactions at very low temperatures. This will be discussed further in chapter 8.

A different free radical molecule, the PTM radical or $\mathrm{PTM_r}$, was chosen as the molecular spin qubit for the first tests with pulsed experiments. $\mathrm{PTM_r}$ is composed of three fully chlorinated phenyl groups bridged by a central carbon atom with an unpaired electron (see Fig. 6.3) [5, 6]. The spin 1/2 of this electron is the spin of the molecule.

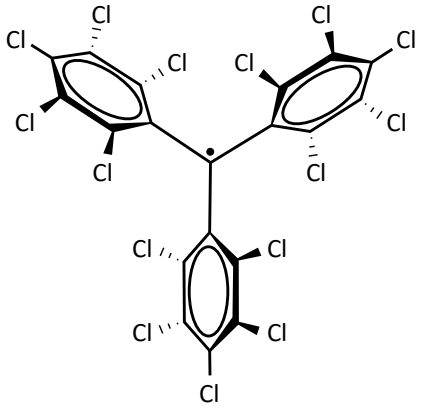

Figure 6.3: Chemical structure of the PTM radical, adapted from [6]. The unpaired electron (pictured as a black dot) that gives the effective spin 1/2 of the molecule is localized in the carbon atom that bridges the three fully chlorinated phenyl groups.

A sample of $\mathrm{PTM_r}$ and polystyrene (PS) in chlorobenzene (CB), with a mass ratio of 0.1% between $\mathrm{PTM_r}$ and PS, was measured with conventional EPR by the group of Joris van Slageren (University of Stuttgart). The spectrum showed a broadening of its resonance at low temperatures [4, Ch.5]. Their tentative explanation is that this spectrum is a convolution of unresolved hyperfine splittings due to the interaction of this spin 1/2 with the nuclear spin $I = 3/2$ of the chlorine atoms. Despite these interactions, they measured a memory time $T_{\mathrm{m}} = 4$ μs at 15 K. The relaxation time T_1, which limits the repetition time of the experiments, is quite long (tens of milliseconds at 15

K). These times are expected to become even longer in the millikelvin regime. More recent measurements by the same group yielded spin coherence values as high as $T_m = 123$ μs for PTM_r in CS_2 at 7 K [7].

The samples for the experiments in these chapter were drops of PTM_r/PS in 0.1 μl of CB, with different PTM_r/PS mass ratios. PTM radical molecules were synthesized by Imma Ratera, Nuria Crivillers and Nerea González from the Nanomol-Bio group at ICMAB-CSIC (Barcelona). Drops were deposited on top of the surface of the lumped-element resonators by Anabel Gracia Lostao and Mari Carmen Pallarés from INMA (Instituto de Nanociencia y Materiales de Aragón) and LMA (Laboratorio de Microscopía Avanzada), Zaragoza. After chlorobenzene evaporates, a solid $\sim$7 μm thick film of PTM_r/PS remains, covering an area similar to that of a resonator ($\sim$ 1 mm^2).

Figure 6.4 shows an example of these deposits on *Test 3*. The deposition process ensures that PTM_r molecules are homogeneously distributed and placed very close to the chip surface, thus avoiding the effect of the sample-resonator gap observed in chapter 5 (see the SEM image in Fig. 6.2).

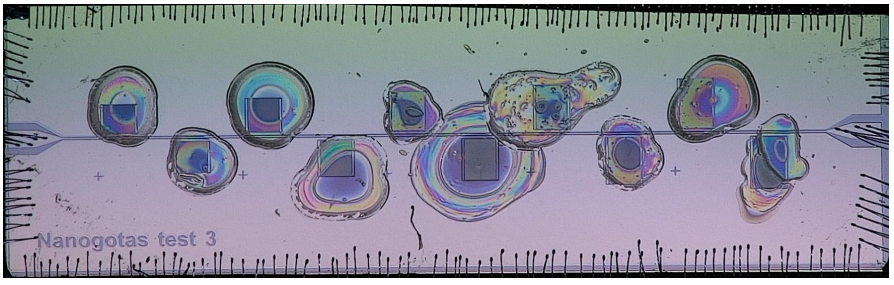

Figure 6.4: Optical close-up of the PTM_r/PS films deposited on top of *Test 3* LERs.

6.1.3 Microwave setup for pulse experiments

The microwave setup for pulse experiments can be divided into three main stages: the generation stage, the cryogenic stage, and the detection stage (see Fig. 6.5). The cryogenic stage includes the superconducting chip (*Test 3* or *Test 4*) with the PTM_r deposits on the LERs, which has been already discussed. The chip is placed in the center of a superconducting magnet inside a cryostat (see section 2.2 in chapter 2 for more details), which generates the magnetic field that tunes the qubit frequency ω_q. The input lines of the cryostat incorporate either 0 dB or 10 dB attenuators at each constant temperature plate (see Fig. 6.5). Therefore, different net attenuations can be chosen for the excitation and readout lines. (the same in the case of *Test 3*, different for *Test 4*). The output readout line is amplified at $T = 4$ K with a Low Noise Factory (LNF) cryogenic amplifier with a gain of $\sim$30 dB.

The generation and detection stages depend on each specific experiment. The output of the generation stage is a sequence of excitation pulses with frequencies close to ω_q that goes to the excitation line of *Test 4* or the single line of *Test 3*. An optional reference signal can be set to the readout stage for synchronization. This stage is composed of a Keysight M9180A single-channel Arbitrary Waveform Generator (AWG), see section 2.3.2, plus all the necessary microwave elements (attenuators, amplifiers, switches, splitters/combiners) to have the desired power for each of the pulses. For *Test 4*, each signal (excitation/readout) generated by the AWG must be routed to its corresponding line in the chip.

The detection stage is either a Keysight MSOS404A oscilloscope or a ZVB14 VNA from R&S (see sections 2.3.1 and 2.3.3). The oscilloscope reads the in-phase (I) and quadrature components (Q) of the transmission of the resonator generated by an IQ mixer with a reference LO (local oscillator) signal from the generation stage. Alternatively, the VNA can be used to detect the output signal in those cases in which it also generates the readout pulses. For *Test 3*, excitation and readout signals must be separated with microwave switches in order to protect the readout stage from too high power inputs.

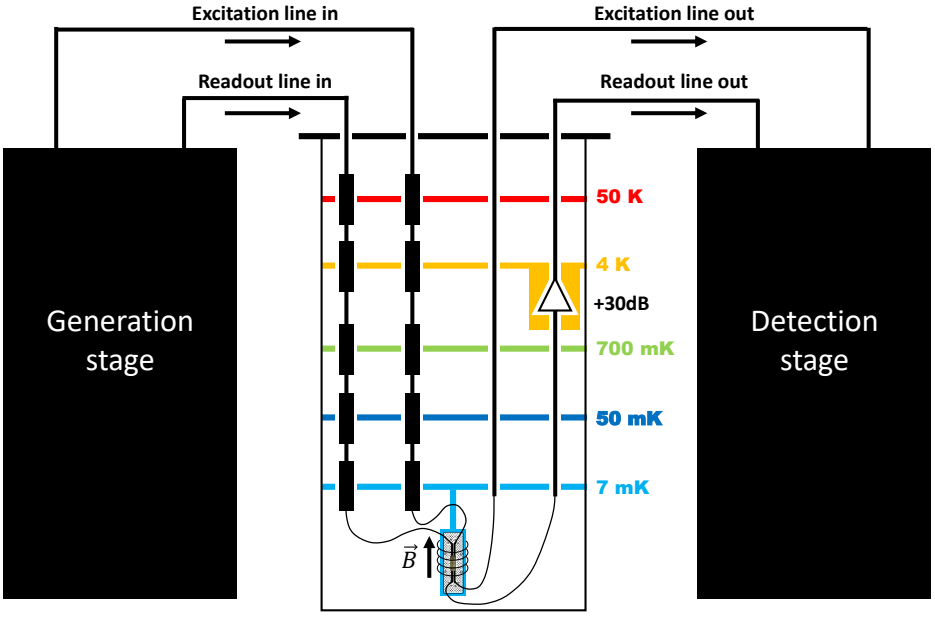

Figure 6.5: Schematic microwave setup for pulse experiments. Input excitation and readout lines have 10 dB attenuators in each plate of the cryostat, for a total of 50 dB of attenuation. The power of the excitation pulses that reach the superconducting chip can be increased by replacing some attenuators from the excitation line with 0 dB DC blocks. The readout line is amplified 30 dB at 4 K. The schemes of the generation and detection stages will be detailed below for each particular experiment.

6.2 Characterization of the collective spin-resonator coupling

This section explores the effect of using different PTM_r/PS samples on the collective spin-photon coupling G_N. The effect of changing the PTM_r/PS ratio between 0.01% ($N = 10^{11}$ spins) and 0.5% ($N = 5 \cdot 10^{12}$ spins) has been already determined. The results, reported in [4, Ch.5], show that G_N scales with $\sqrt{N_{\text{eff}}}$, where $N_{\text{eff}} \sim N/100$ is the effective number of spins that actually couple significantly to the microwave magnetic field generated by the resonator inductor (with or without constriction).

Here, I take the sample with the highest PTM_r/PS ratio (0.5%) and explore the effect of increasing the spin concentration even further by reducing the amount of PS in the solution in CB. The idea is to have more PTM radical molecules closer to the inductor by removing part of the PS matrix. The details of the samples are listed in table 6.1. Figures 6.6 and 6.7 show the resonances of the 10 *Test 3* LERs measured with these deposits at 10 mK and as a function of magnetic field. S_{21} is measured for different regular input frequencies $f = \omega_d/2\pi$ and magnetic fields B (tuning the qubit frequency $\omega_q = \mu_B g_S B/\hbar$). The input power was chosen in order to feed less than -70 dBm into the chip. For higher input powers, the collective spin-photon coupling was observed to decrease in some of the resonators.

LERs	1 and 2	3 and 4	5 and 6	7 and 8	9 and 10
PS concentration (g/l)	0	6.3	6.3	12.6	12.6
PTM_r/PS mass ratio (%)	–	1	0.5	1	0.5
N (10^{12} spins)	5	5	2.5	10	5

Table 6.1: Properties of the 0.1 μl PTM_r/PS solutions in CB that were deposited on each of the 10 *Test 3* LERs. I list the PS concentration in the 0.1 μl solution before the evaporation of CB, as well as the PTM_r/PS mass ratio and the estimated number N of spins in the sample.

The characterization of the resonances follows a similar procedure to that described in the previous chapter for the case of DPPH samples. The chip transmission is measured with input frequencies around the resonance frequency ω_r of each resonator, for different fields around the resonance condition $\omega_r = \omega_q$. The experimental data are fitted with Eq. (4.103) from chapter 4:

$$S_{21}(\omega_d) = 1 - \frac{\kappa_c}{i(\omega_r - \omega_d) + \kappa + \dfrac{G_N^2 \Delta P}{i(\omega_q - \omega_d) + \gamma_\perp}} \,. \tag{6.2}$$

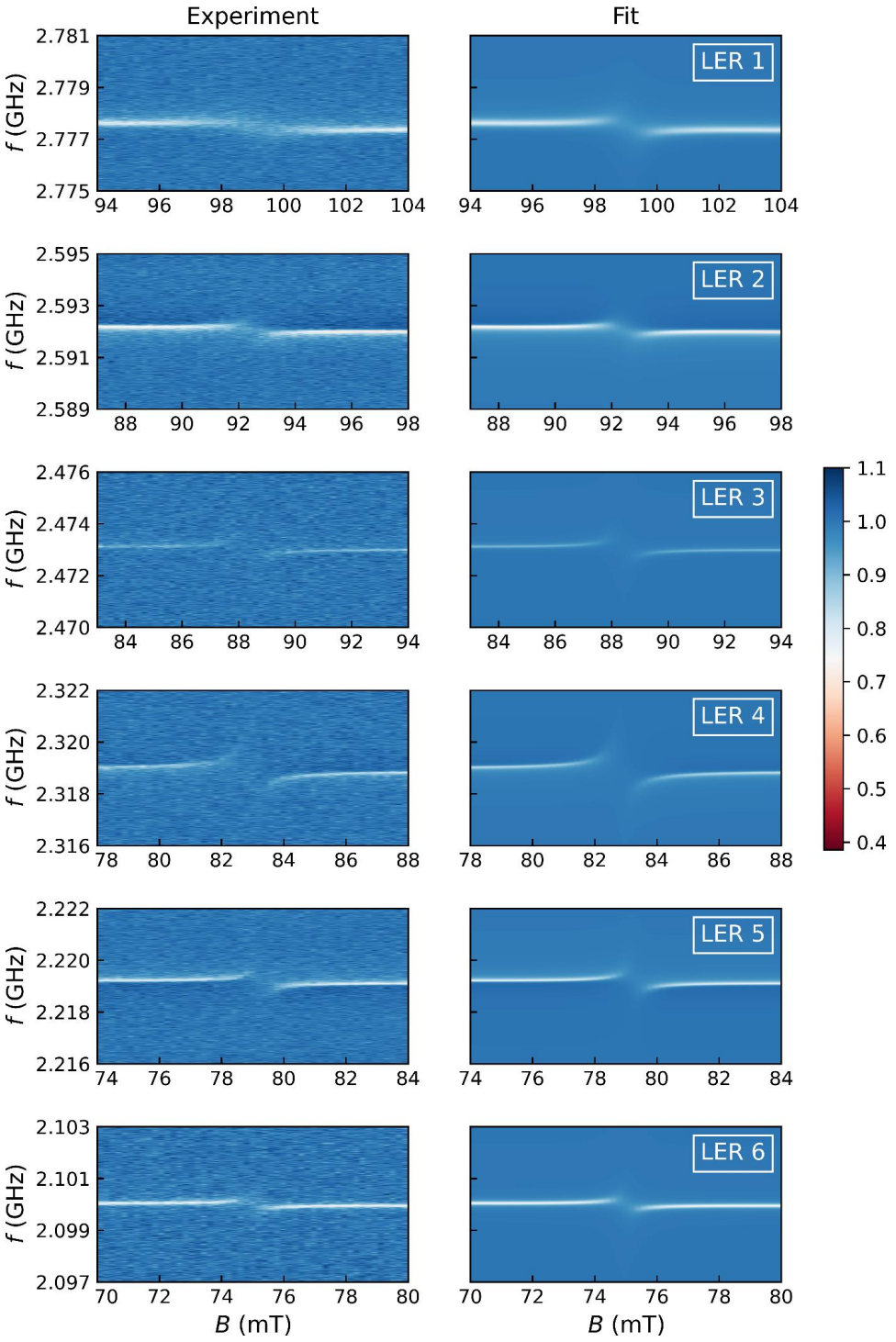

Figure 6.6: Transmission of LERs 1 to 6 of chip *Test 3* coupled to PTM samples. *Left:* Experimental results. *Right:* Theoretical simulations based on Eq. (6.2) with the parameters given in tables 6.2 and 6.3.

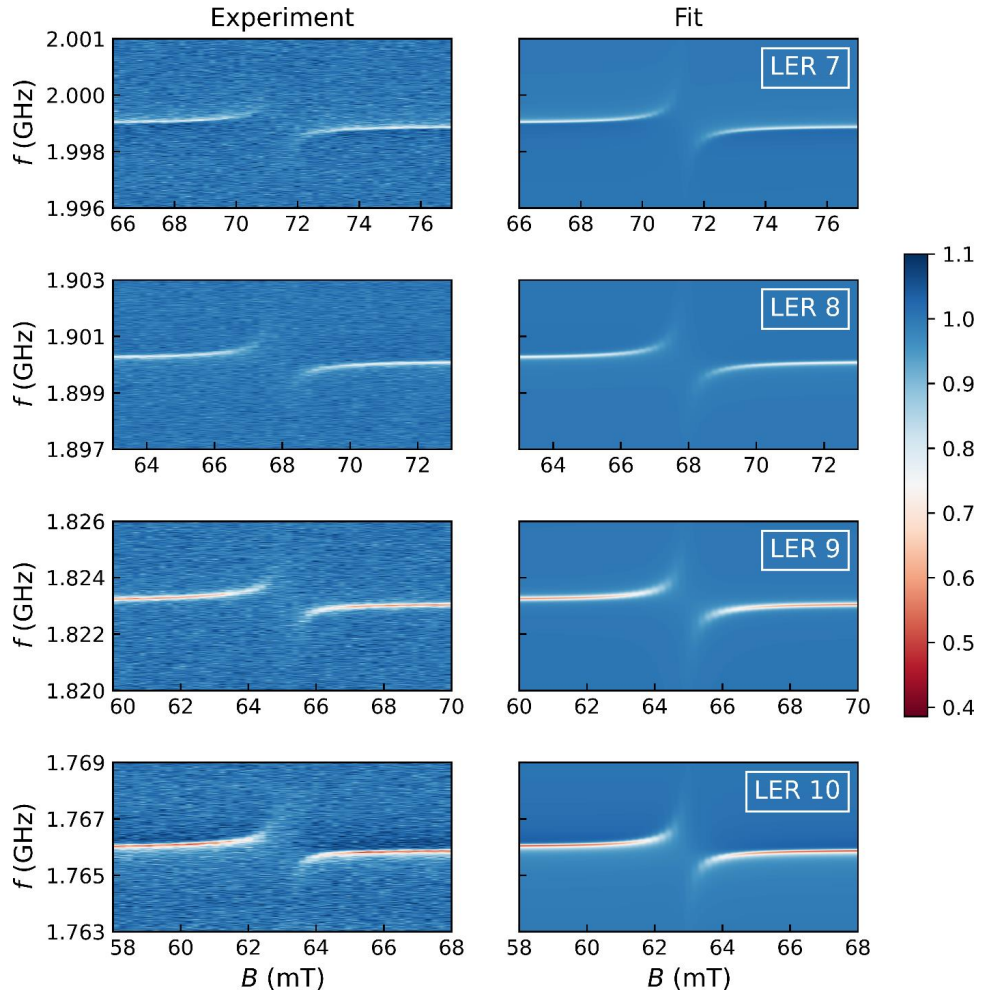

Figure 6.7: Transmission of LERs 7 to 10 of chip *Test 3* coupled to PTM_r samples. *Left:* Experimental results. *Right:* Theoretical simulations based on Eq. (6.2) with the parameters given in tables 6.2 and 6.3.

The resonance frequency ω_r, the photon mode decay rate κ, and line-coupling rate κ_c of each LER are listed in table 6.2. The resonators show remarkably high quality factors $Q = \omega_r/2\kappa \leqq 10^5$, i.e. small widths, which makes them well suited to perform dispersive readout experiments. Table 6.3 reports the parameters related to the sample: the g-factor g_S, the decoherence rate of the spin ensemble, $\gamma_\perp$, and the temperature dependent collective spin-photon $G_N(T) \propto \sqrt{\Delta P}$. The population difference ΔP between the spin down and spin up states at a temperature $T \sim 10$ mK and $\omega_q \simeq \omega_r \sim 1$–3 GHz can be safely assumed to be nearly 1.

Collective spin-photon couplings up to 3.42 MHz are reached, almost as high as in the previous chapter with DPPH, but with the number N of spins

being 5 orders of magnitude smaller. The fact that such a large G_N can be attained with much smaller spin ensembles is due to the low-inductance design of these LERs, and to the reduction of the sample-chip gap. That is, there are less spins, but they are closer to an inductor that generates a much stronger magnetic field that scales with $L^{-1/2}$. G_N is also enhanced as temperature is decreased from 4 K in the last chapter to 10 mK in these measurements. However, this would only account for an increase in the coupling by a factor $\sqrt{(\Delta P)_{T=10\,\mathrm{mK}}/(\Delta P)_{T=4\,\mathrm{K}}} < 3$. In comparison, reducing the number of spins from $N_{\mathrm{DPHH}} \sim 10^{17}$ to $N_{\mathrm{PTM}} \sim 10^{12}$ in the same experimental conditions decreases G_N by a factor $\sqrt{N_{\mathrm{DPHH}}/N_{\mathrm{PTM}}} > 300$.

LER	$\omega_\mathrm{r}/2\pi$ (GHz)	$\kappa/2\pi$ (kHz)	$\lvert\kappa_\mathrm{c}\rvert/2\pi$ (kHz)	ϕ_c (°)
1	$2.777535 \pm 2 \cdot 10^{-6}$	85.8 ± 1.6	23.4 ± 0.9	-10.1 ± 0.3
2	$2.5921684 \pm 9 \cdot 10^{-7}$	56.9 ± 0.5	20.1 ± 0.3	27.4 ± 0.3
3	$2.473073 \pm 3 \cdot 10^{-6}$	48.4 ± 1.8	5.1 ± 0.3	-9.5 ± 1.2
4	$2.318961 \pm 2 \cdot 10^{-6}$	50.3 ± 1.1	9.7 ± 0.4	28.3 ± 0.7
5	$2.2191717 \pm 9 \cdot 10^{-7}$	46.9 ± 0.6	12.2 ± 0.3	-29.4 ± 0.4
6	$2.100022 \pm 1 \cdot 10^{-6}$	53.7 ± 0.8	15.0 ± 0.4	-2.5 ± 0.5
7	$1.998962 \pm 1 \cdot 10^{-6}$	39.8 ± 0.8	10.7 ± 0.4	-29.8 ± 0.6
8	$1.900192 \pm 1 \cdot 10^{-6}$	46.1 ± 0.7	12.8 ± 0.3	14.8 ± 0.4
9	$1.823173 \pm 1 \cdot 10^{-6}$	58.5 ± 0.6	26.6 ± 0.5	-1.2 ± 0.3
10	$1.7659920 \pm 9 \cdot 10^{-7}$	55.5 ± 0.6	30.2 ± 0.6	24.9 ± 0.3

Table 6.2: Parameters of the resonances of the 10 *Test 3* LERs, obtained by fitting the transmission through the device at 10 mK.

LER	g_S	G_N / 2π (MHz)	$\gamma_\perp$ / 2π (MHz)
1	$2.0030 \pm 4 \cdot 10^{-4}$	3.16 ± 0.04	34.4 ± 1.0
2	$2.0029 \pm 3 \cdot 10^{-4}$	2.21 ± 0.01	15.7 ± 0.4
3	$1.999 \pm 1 \cdot 10^{-3}$	2.37 ± 0.03	8.3 ± 0.9
4	$1.9994 \pm 3 \cdot 10^{-4}$	3.31 ± 0.02	7.1 ± 0.4
5	$1.9996 \pm 2 \cdot 10^{-4}$	2.08 ± 0.01	7.1 ± 0.3
6	$1.9998 \pm 4 \cdot 10^{-4}$	1.72 ± 0.01	8.9 ± 0.5
7	$2.0010 \pm 3 \cdot 10^{-4}$	3.27 ± 0.01	5.9 ± 0.3
8	$1.9997 \pm 2 \cdot 10^{-4}$	3.42 ± 0.01	6.1 ± 0.2
9	$2.0052 \pm 2 \cdot 10^{-4}$	3.36 ± 0.01	6.6 ± 0.2
10	$2.0046 \pm 2 \cdot 10^{-4}$	3.08 ± 0.01	5.8 ± 0.2

Table 6.3: Parameters from the fit of the magnetic field dependent resonances of LERs 1, 3 and 5 in chip *Test 3* at $T = 10$ mK shown in Figs. 6.6 and 6.7.

The collective spin-LER coupling G_N scales with the square root of the

number N of spins (see Fig. 6.8a). This coupling does not seem to get enhanced by reducing the PS concentration. In fact, the main consequence of removing the PS matrix is a broadening of the spin spectrum, as shown in Fig. 6.8b. First, there is an increase from $\gamma_\perp/2\pi$ = 5.8-6.6 MHz (LERs 7 to 10) to $\gamma_\perp/2\pi$ = 7.1-8.9 MHz (LERs 3 to 6) as the original PS concentration of 12.6 g/l is halved. Then, a sharp increase to $\gamma_\perp/2\pi$ = 34.4 and 15.7 MHz is observed in LERs 1 and 2, where PTM_r was deposited without PS. The broadening can be attributed to the onset of spin-spin interactions that were previously suppressed by the dilution of PTM_r in the diamagnetic PS matrix. From this results I decided to keep the parameters of the deposits on LERs 9 and 10 for the pulsed experiments, as the broadening overcomes any gain achieved in G_N by removing part of the PS matrix. Figure 6.8c shows the $G_N/\gamma_\perp$ ratio and the cooperativity $C = G_N^2/\gamma_\perp\kappa$ for each LER. None of the hybrid spins-LER systems is in the strong coupling regime ($G_N/\gamma_\perp > 1$), but the high cooperativity regime ($C > 1$) is achieved for all of them.

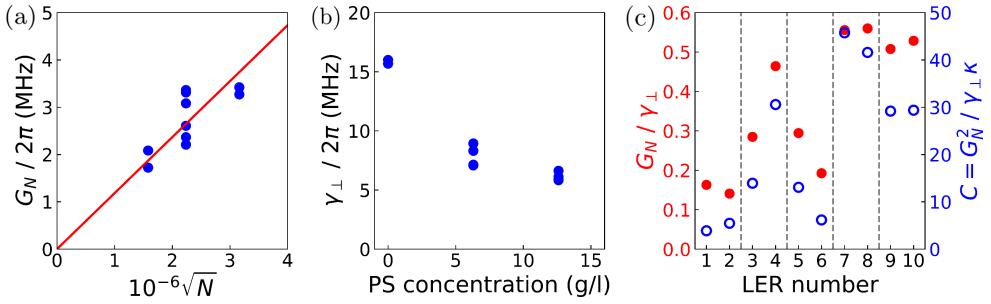

Figure 6.8: (a) Collective spin-photon coupling G_N as a function of the square root of the number of spins in the sample. (b) $\Gamma_\perp$ as a function of the PS concentration in the PTM_r/PS solution in CB. (c) The ratios $G_N/\gamma_\perp$ (red closed dots) and $C = G_N^2/\gamma_\perp\kappa$ (blue open dots) for each resonator. These quantities define the strong coupling ($G_N/\gamma_\perp > 1$) and the high cooperativity ($C > 1$) regimes. Only the latter is attained with this experimental setup.

6.3 Testing pulse generation and the resonator dynamics

The pulse generation system was tested by measuring the response of a LER to 20 μs long pulses with driving frequencies ω_d close to its resonance frequency ω_r. Figure 6.9a shows the output signal transmitted by the bare resonator. The transmitted signal was fitted with the theory that describes the dynamics of a LER, the details of which can be seen in section 4.4.2 from chapter 4. The resonator evolution under a coherent drive $b_{in}(t) = \alpha_{in}e^{-i\omega_d t}$ is given by Eq.

(4.64), reproduced here for clarity:

$$\langle \hat{a} \rangle(t) = \langle \hat{a} \rangle(0) e^{-(i\omega_{\mathrm{r}}+\kappa)t} - i\sqrt{\kappa_{\mathrm{c}}} \frac{1 - e^{-(i(\omega_{\mathrm{r}}-\omega_{\mathrm{d}})+\kappa)t}}{i(\omega_{\mathrm{r}} - \omega_{\mathrm{d}}) + \kappa} \alpha_{\mathrm{in}} e^{-i\omega_{\mathrm{d}}t}. \tag{6.3}$$

From input-output theory, the transmitted signal is:

$$b_{\mathrm{out}}(t) = b_{\mathrm{in}}(t) - i\sqrt{\kappa_{\mathrm{c}}} \langle \hat{a} \rangle(t). \tag{6.4}$$

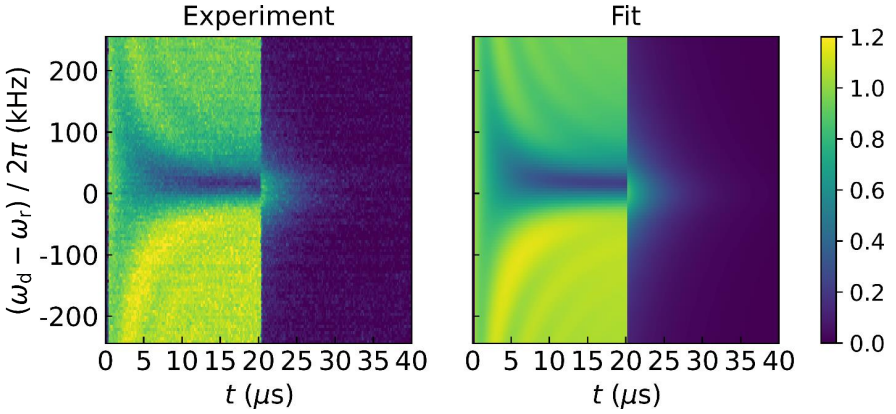

Figure 6.9: Comparison between the maps of the experimental and theoretical amplitude of the transmission of 20 μs long pulses microwave pulses with driving frequencies ω_{d} close to the resonance frequency ω_{r} of a LER, measured at zero field. At this field, the resonator is completely decoupled from the spins. Both maps show the absolute value of the output signal normalized by the amplitude of the input pulse, α_{in}.

The LER response can be analyzed in two stages. The first comprises the duration of the pulse, described by the equations above with $\langle \hat{a} \rangle(0) = 0$. That is, the resonator is assumed to be initially discharged. It then follows that:

$$\langle \hat{a} \rangle(t) = -i\sqrt{\kappa_{\mathrm{c}}} \frac{1 - e^{-(i(\omega_{\mathrm{r}}-\omega_{\mathrm{d}})+\kappa)t}}{i(\omega_{\mathrm{r}} - \omega_{\mathrm{d}}) + \kappa} \alpha_{\mathrm{in}} e^{-i\omega_{\mathrm{d}}t} \quad \text{for } t < t_{\mathrm{pulse}}\,, \tag{6.5}$$

which yields:

$$b_{\mathrm{out}}(t) = \left(1 - \kappa_{\mathrm{c}} \frac{1 - e^{-(i(\omega_{\mathrm{r}}-\omega_{\mathrm{d}})+\kappa)t}}{i(\omega_{\mathrm{r}} - \omega_{\mathrm{d}}) + \kappa}\right) \alpha_{\mathrm{in}} e^{-i\omega_{\mathrm{d}}t} \quad \text{for } t < t_{\mathrm{pulse}}\,, \tag{6.6}$$

with $t_{\mathrm{pulse}} = 20$ μs. After the pulse, the driving amplitude α_{in} becomes zero, and the time reference is shifted to $T = 20$ μs: $t \to t' = t - t_{\mathrm{pulse}}$. For this second part, $\langle \hat{a} \rangle(t' = 0)$ equals $\langle \hat{a} \rangle(t = t_{\mathrm{pulse}})$ computed with Eq. (6.5):

$$b_{\mathrm{out}}(t) = -i\sqrt{\kappa_{\mathrm{c}}} \langle \hat{a} \rangle(t = t_{\mathrm{pulse}}) e^{-(i\omega_{\mathrm{r}}+\kappa)(t-t_{\mathrm{pulse}})} \quad \text{for } t > t_{\mathrm{pulse}}\,. \tag{6.7}$$

The experiment was repeated with the qubit frequency ω_q tuned with the magnetic field to lie at $\Delta/2\pi = (\omega_q - \omega_r)/2\pi = 30$ MHz from ω_r. With this detuning, the ensemble-LER system is in the dispersive regime ($\Delta \sim 10\,G_N \gg G_N$). Figure 6.10b shows the transmission of 20 μs pulses with driving frequencies ω_d close to ω_r in this new experimental condition.

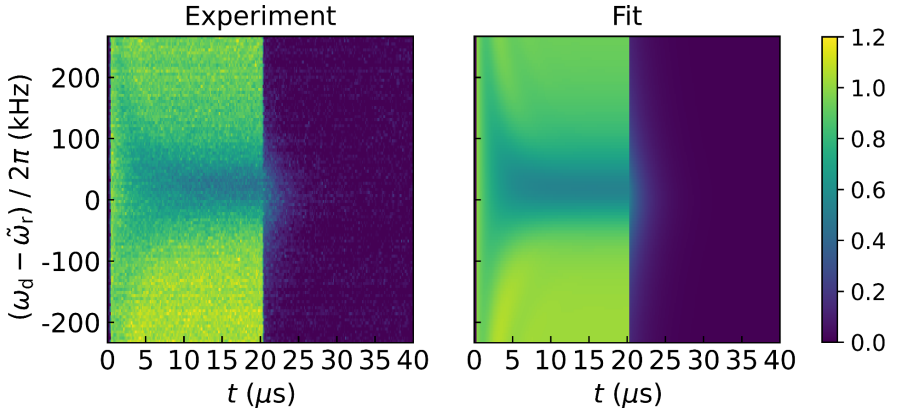

Figure 6.10: Comparison between the maps of the experimental and theoretical amplitude of the transmission of 20 μs long pulses microwave pulses sent with drive frequencies ω_d close to the LER resonance frequency $\tilde{\omega}_r$. The qubit frequency ω_q was tuned with the static magnetic field to set a detuning $(\omega_q - \omega_r)/2\pi = 30$ MHz between ω_q and the resonator frequency ω_r. $\tilde{\omega}_r$ is the resonance frequency for this detuning (see Eq. (6.8) in chapter 4). Both maps show the absolute value of the output signal normalized by the amplitude of the input pulse, α_{in}.

In this case, the output signal should be computed using the input-output theory for the dynamics of the hybrid spin ensemble-resonator system, which is described in section 4.6.3 from chapter 4. However, the characterization of the collective spin-LER coupling in the previous sections sets the hybrid system in the weak coupling. In this regime, the coupled resonator can be described as a bare resonator with effective resonance frequency $\tilde{\omega}_r$ and effective decay rate $\tilde{\kappa}$ modified by the spin-photon coupling (see section 4.6.4):

$$\begin{aligned} \tilde{\omega}_r &:= \omega_r + \left[\frac{G_N^2(\Delta P)_e}{(\omega_q - \omega_r)^2 + \gamma_\perp^2}\right](\omega_r - \omega_q), \\ \tilde{\kappa} &:= \kappa + \left[\frac{G_N^2(\Delta P)_e}{(\omega_q - \omega_r)^2 + \gamma_\perp^2}\right]\gamma_\perp, \end{aligned} \tag{6.8}$$

which depend on the (uncoupled) LER resonance frequency ω_r, its photon decay rate κ, the magnetic field dependent qubit frequency ω_q, the spin decoherence rate $\gamma_\perp$, the collective spin-photon coupling G_N, and the spin population difference in equilibrium $(\Delta P)_e$.

Tables 6.4 and 6.5 list the fit parameters of the resonance for the bare and coupled resonators respectively. The coupling of the LER photons to the PTM_r/PS sample broadens the resonance, with κ increasing from 35.4 to 67.6 MHz. That is, the photon lifetime ($1/\kappa$) in the resonator is reduced, even in the dispersive regime, as can be seen by comparing Figs. 6.9 and 6.10. The line-resonator coupling, κ_c, does not depend on the presence of the sample and its absolute value remains in the 30–33 MHz range. Assuming $(\Delta P)_e \simeq 1$ and $\gamma_\perp/2\pi \sim 6$ MHz, a collective spin-photon coupling $G_N/2\pi \sim 2$ MHz can be estimated from the expression of $\tilde{\kappa}$ (see Eq. (6.8)).[1]

$\omega_r/2\pi$ (GHz)	$\kappa/2\pi$ (kHz)	$\lvert\kappa_c\rvert/2\pi$ (kHz)	ϕ_c (°)
$2.2515944 \pm 2 \cdot 10^{-7}$	35.4 ± 0.2	30.6 ± 0.2	-29.0 ± 0.2

Table 6.4: Fit parameters of the dynamics of the bare resonator with 20 μs long pulses.

$\tilde{\omega}_r/2\pi$ (GHz)	$\tilde{\kappa}/2\pi$ (kHz)	$\lvert\kappa_c\rvert/2\pi$ (kHz)	ϕ_c (°)
$2.2510931 \pm 5 \cdot 10^{-7}$	67.6 ± 0.5	33.3 ± 0.4	-23.0 ± 0.3

Table 6.5: Fit parameters from the fit of the dynamics of the resonator coupled to a PTM_r/PS sample with 20 μs long pulses and a detuning $(\omega_q - \omega_r)/2\pi = 30$ MHz between the qubit frequency ω_q and uncoupled LER resonance frequency ω_r.

Figure 6.11 highlights the fit of the dynamics of the resonator for a selection of detunings between the driving frequency of the input pulse, ω_d, and the LER resonance frequency (ω_r or $\tilde{\omega}_r$). It is remarkable that the model defined by Eq. (6.6) and (6.7) provides a good account of the dynamical response of the uncoupled or coupled LER for all detunings $\omega_d - \omega_r$ (or $\omega_d - \tilde{\omega}_r$) with a common set of parameters. Note that the asymmetry of the resonance lineshape, encoded in the argument of the complex-valued resonator-line coupling κ_c, leads also to an asymmetry in the dynamics.

These results show clearly the strong effect of collective spin-photon coupling in reducing the photon lifetimes that was mentioned before. The lifetime reduction is parametrized by the increase in $\tilde{\kappa}$ predicted by Eq. (6.8). The coupled resonator in the dispersive regime is already in its steady-state at the end of the pulse, while the uncoupled resonator is still charging. That is, there is a dead time before the steady-state can be probed that is reduced by decreasing the detuning between ω_q and ω_r (in absolute value). This shortening of the dead time will be relevant for the readout of the resonator state that is described in the following sections.

[1] See the reported $\gamma_\perp$ for LERs 9 and 10 in table 6.3. The PTM_r/PS sample in this experiment is the same 0.5% PTM_r/PS deposit.

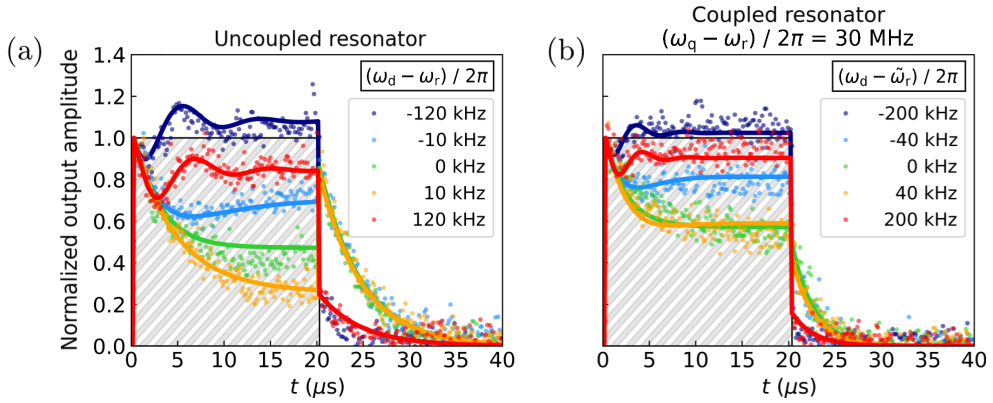

Figure 6.11: Comparison between the experimental (dots) and theoretical (solid lines) amplitudes of the chip output signal resulting from the application of 20 μs long microwave pulses with driving frequencies ω_d close to the LER resonance frequency ω_r. Two cases are illustrated: the uncoupled resonator at 0 mT (a) and the resonator coupled to a PTM_r/PS sample in the dispersive regime (b). The absolute value of the output signal is shown, normalized by the amplitude of the input pulse, α_{in}.

6.4 First pump-probe experiments on PTM radicals: measurement of the spin ensemble absorption spectrum and relaxation time T_1

The first pump-probe experiments on PTM radicals were performed with the *Test 3* chip, with only one transmission line coupled to the LERs. The PTM_r/PS samples were the 0.5% PTM_r/PS (in mass) deposits on LERs 9 and 10 (see section 6.2). Therefore, a collective spin-photon coupling $G_N/2\pi \sim 3.2$ MHz is expected, with an ensemble decoherence rate $\gamma_\perp/2\pi \sim 6$ MHz. There are $N \sim 5{\cdot}10^{12}$ spins on each PTM_r/PS sample. This gives a root mean square (RMS) single spin-photon coupling $G_{1,\mathrm{RMS}}/2\pi = G_N/2\pi\sqrt{N} \sim 1.4$ Hz. However, a better estimate considers only the effective number of coupled spins, $N_{\mathrm{eff}} \sim N/100$, giving $G_{1,\mathrm{RMS}}/2\pi \sim 10.4$ Hz.

6.4.1 Basics of dispersive readout with pump-probe experiments

The theory of the dispersive regime of an ensemble of spins 1/2 coupled to a resonator is described in section 3.4.2 from chapter 3. The resonance frequency ω_r of the uncoupled LER is shifted to higher or lower frequencies depending

on the state of the spins in the ensemble:

$$\omega_{\mathrm{r}} \quad \rightarrow \quad \omega_{\mathrm{r}} + \sum_{i=1}^{N} \chi_i \langle \hat{\sigma}_{z,\,i} \rangle, \tag{6.9}$$

which depends on the expectation value $\langle \hat{\sigma}_{z,\,i} \rangle$ for each spin. Each weight χ_i in the sum is the single spin *dispersive shift*, defined as:

$$\chi_i := \frac{|G_{1,i}|^2}{\Delta_i} = \frac{|G_{1,i}|^2}{\omega_{\mathrm{q},\,i} - \omega_{\mathrm{r}}}. \tag{6.10}$$

Here I do not use the modified detunings Δ_i' discussed in section 3.4.2. They can be replaced by $\Delta_i = \omega_{\mathrm{q},\,i} - \omega_{\mathrm{r}}$ in these experiments, as they are two order of magnitude smaller than ω_{r}. Having different qubit frequencies $\omega_{\mathrm{q},\,i}$ accounts for any inhomogeneous broadening of the spin resonance.

At 10 mK all molecular spin qubits are considered to be initialized in their ground state, with $\langle \hat{\sigma}_{z,\,i} \rangle \simeq -1$ for every spin. Then, the resonance frequency that is measured without exciting the spins is not ω_{r}, but the *reference frequency* ω_{ref}:

$$\omega_{\mathrm{ref}} := \omega_{\mathrm{r}} - \sum_{i=1}^{N} \chi_i = \omega_{\mathrm{r}} - \chi, \tag{6.11}$$

where χ is the ensemble dispersive shift.

After this initialization by temperature, a control sequence of *pump* pulses is sent to excite the spin system, with carrier frequencies ω_{d} close to the qubit frequency ω_{q}. These pulses induce changes in the expectation values $\langle \hat{\sigma}_{z,\,i} \rangle$. The resulting new resonance frequency $\omega_{\mathrm{shifted}}$ is measured by sending *probe* pulses with frequencies close to ω_{r}, and then compared to the reference frequency ω_{ref}:

$$\delta\omega_{\mathrm{r}} := \omega_{\mathrm{shifted}} - \omega_{\mathrm{ref}} = \sum_{i=1}^{N} \chi_i \left(1 + \langle \hat{\sigma}_{z,\,i} \rangle\right). \tag{6.12}$$

The shift $\delta\omega_{\mathrm{r}}$ contains the information of the changes in the expected values $\langle \hat{\sigma}_{z,\,i} \rangle$ of the spins generated by the excitation pulses. It also gives insight into the distribution in couplings $(G_{1,\,i})$ and in qubit frequencies $(\omega_{\mathrm{q},\,i})$ through the dispersive shifts χ_i. Figure 6.12 summarizes the basic ingredients of the dispersive readout.

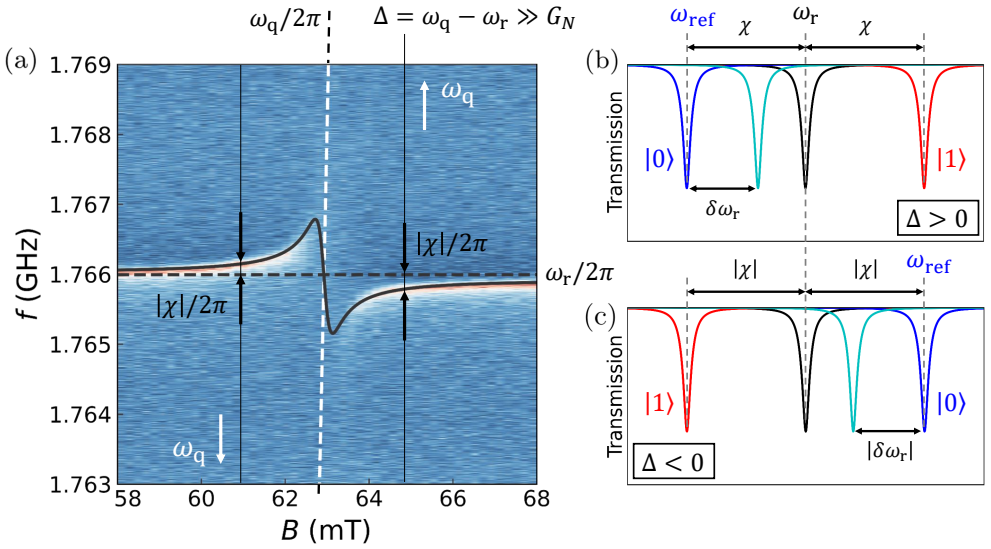

Figure 6.12: (a) Transmission of LER 10 of chip *Test 3* coupled to a PTM_r samples. The coupled LER resonance frequency $\tilde{\omega}_r$ (solid black line) is compared to the uncoupled LER resonance frequency ω_r (dashed black line). At 10 mK, with the spins initialized in the ground state, the solid black line also marks the position of the reference frequency ω_{ref} for magnetic fields in which the dispersive regime condition $|\Delta| = |\omega_q - \omega_r| \gg G_N$ is fulfilled. For $\Delta > 0$ (right hand side), the ensemble dispersive shift is positive ($\chi > 0$), and $\omega_{ref} = \omega - \chi$ is below ω_r. Conversely, for $\Delta < 0$ (left hand side), $\chi < 0$ and ω_{ref} is above ω_r. (b) Dispersive shift of ω_r for Δ, $\chi > 0$. The reference frequency ω_{ref} (blue resonance) associated with the ground state of the spins is lower than ω_r (black resonance). If all spins were excited, ω_r would be shifted by the same amount to higher frequencies (red resonance). Changes in the spin state are tracked by measuring the positive shift $\delta\omega_r$ between the LER resonance (cyan resonance) and comparing it to ω_{ref}. (c) Dispersive shift of ω_r for Δ, $\chi < 0$. ω_{ref} is now above ω_r, and any excitation of the spins is measured as a negative shift $\delta\omega_r$ from ω_{ref}.

6.4.2 Microwave generation and detection setups

Two sets of signals are required to measure the shift $\delta\omega_r$. First, a sequence of high power pulses with frequencies ω_{pump} close to ω_q are sent to control the spin state. These pulses change the expectation value $\langle\hat{\sigma}_{z,i}\rangle$ of each spin in the ensemble. Then, low power pulses with frequencies ω_{probe} close to ω_r are sent to measure the resonance shift $\delta\omega_r$. The generation of these two sequences of pulses, the *pump* sequence and the *probe* sequence, their interaction with the spins and the resonator, and the readout of the transmission probe signal constitute together what is called here the *pump-probe* experiment sketched in Fig. 6.13.

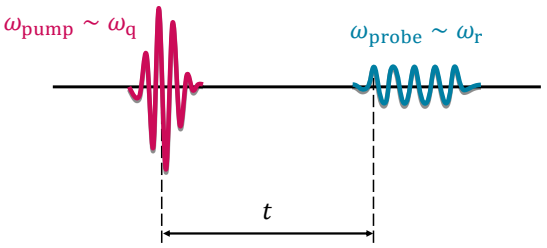

Figure 6.13: Scheme of a pump-probe experiment with a single high power pump pulse (magenta) with carrier frequency ω_{pump} close to ω_q followed after a time lapse t by a single low power probe pulse (cyan) with carrier frequency ω_{probe} close to ω_r.

The generation and detection stages for pump-probe experiments are shown in Figs. 6.14 and 6.15 respectively. The pump (magenta) and probe (cyan) signals are generated at a 0 dBm power level by the AWG through a single output line. A reference TTL signal (*REF*) generated also by the AWG triggers a switch that sends the pump signal to the excitation circuit and the probe signal to the readout circuit. In the former, the pump signal is amplified by 10 dB. The probe signal in the readout circuit is split into a local oscillator reference for the readout stage (*LO*) and the signal that goes through the cryogenic stage, the latter attenuated by 20 dB. The pump and probe signals are combined again into a single line (*IN*) and led through the same port of the cryostat, as *Test 3* has only one transmission line.

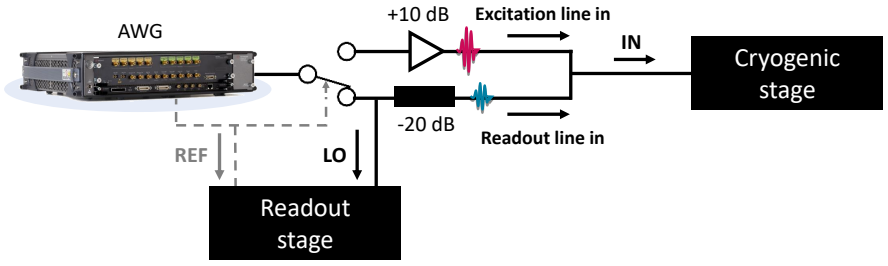

Figure 6.14: Generation stage for chip *Test 3* using an Arbitrary Waveform Generator (AWG), and its relation with the cryogenic and readout stages.

The output of the cryogenic stage (*OUT*) is the transmission of the pump and probe signals through *Test 3*. A second switch triggered by *REF* at the start of the detection stage sends the transmitted pump signal to the excitation line and the transmitted probe signal to the readout line. The transmitted pump signal is sent to a channel of the oscilloscope.[2] The transmitted probe signal (*RF*) is amplified by 40 dB. After this amplification, the power of *RF* is roughly 0 dBm. An IQ mixer fed with the *LO* and *RF* signals demodulates

[2]The pump pulse is not measured, it is only sent to the oscilloscope to check it.

the probe signal, extracting the in-phase (I, green) and quadrature (Q, yellow) components of RF. The detection stage ends with the acquisition of I and Q with the oscilloscope. The digitized I and Q signals are then sent to the computer for post-processing.

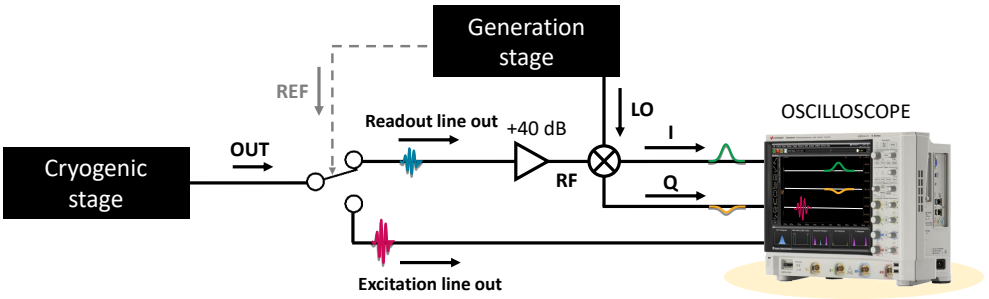

Figure 6.15: Detection stage for chip *Test 3* using an oscilloscope, and its relation with the cryogenic and generation stages.

6.4.3 Spin ensemble absorption spectrum and T_1 measurements

The qubit frequency was tuned to $\omega_q/2\pi \simeq 1.83$ GHz applying a magnetic field $B = 65$ mT. At this field, there is a detuning $\Delta \,/\, 2\pi = (\omega_q - \omega_r) \,/\, 2\pi \sim 44$ MHz between the qubit frequency and the resonance frequency $\omega_r \,/\, 2\pi = 1.7865$ GHz of *Test 3* LER 10. This detuning fulfills the dispersive regime condition $|\Delta| \gg G_N$. At 10 mK, the reference frequency is $\omega_{ref} = \omega_r - \chi$, which is below ω_r (positive dispersive shift χ). Any change in the spins from their ground state will induce a positive shift $\delta\omega_r$ from ω_{ref} (see Fig. 6.12b).

The pump sequence used here was a 50 μs pulse with a carrier frequency ω_{pump} close to ω_q. After the pulse, the induced shift $\delta\omega$ with respect to ω_{ref} immediately starts to decay to zero with a relaxation time T_1. In fact, there may be different times $T_{1,i}$ associated with the $\langle\hat{\sigma}_{z,i}\rangle$ of each spin. If some $T_{1,i}$ are very short, this imposes a limitation on the probe time for measuring $\delta\omega_r$. A simple solution is to calibrate the full resonance of the LER beforehand, then obtaining $\delta\omega_r$ from a single pulse at a fixed frequency close to ω_r just after the excitation pulses. The calibration curve translates the IQ data of the transmission of the probe pulse into a frequency ω_{cal}. This frequency, compared to the known input probe frequency ω_{probe}, gives $\delta\omega_r$. The procedure is illustrated in Fig. 6.16a. The difference $\omega_{cal} - \omega_{probe}$ has the opposite sign to $\delta\omega_r$:

$$\delta\omega_r := -\left(\omega_{cal} - \omega_{probe}\right). \tag{6.13}$$

The minus sign comes from the fact that it is not the input frequency that shifts to ω_{cal}, but the whole resonance in the opposite direction.

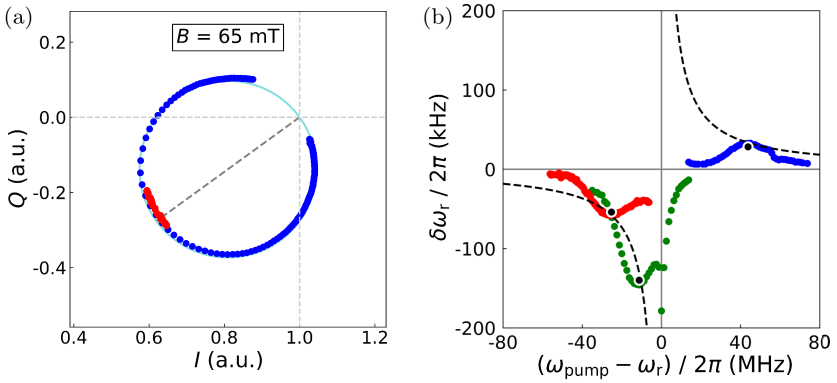

Figure 6.16: (a) Dispersive shift (red dots) of the point in the IQ plane (in-phase & quadrature) corresponding to a fixed readout frequency close to the resonance frequency ω_r of *Test 3* LER 10 as the drive frequency is swept around the qubit frequency ω_q, measured at 65 mT. In the absence of the pump pulse, the point would remain still in the plane. Blue dots are the calibration of the full resonance of LER 10 at 65 mT, which traces a circle in the IQ plane. The frequency associated to the shifted resonance (red dots) is extracted by inverting the parametrized calibration curve $(I(\omega), Q(\omega))$. (b) Measured shift $\delta\omega_r$ for pump frequencies ω_{pump} around the qubit frequency ω_q, measured at three fields: 62.3 mT (red dots), 63 mT (green dots) and 65 mT (blue dots). The maximum shift, in absolute value, measured at each field B is obtained for $\omega_{pump} = \omega_q = \mu_B g_S B/\hbar$. These maximum values (black dots) follow closely the predicted dependence with $1/\Delta$ (black dashed lines).

With this technique, the ensemble spin spectrum and the relaxation time T_1 of the PTM_r/PS samples were measured at 65, 63 and 62.3 mT. See [8] for an example of this kind of experiments on NV center spins in diamond, and [9, 10] for similar experiments on other free radical molecules. The latter two fields, 63 and 62.3 mT, correspond to detunings $\Delta\ /\ 2\pi \sim$ -12.3 and -27.3 MHz, respectively. That is, at these two fields the qubit frequency ω_q is smaller than the bare resonator ω_r. This implies a negative dispersive shift χ, with the reference frequency ω_{ref} above ω_r and a negative shift $\delta\omega_r$ from it if the spins are excited, in agreement with the experimental results. It was necessary to use relatively long pulses (50 μs) and remove two 10 dBm attenuators from the cryostat lines in order to see a significant shift $\delta\omega_r$. This pulse length is much longer than the expected ensemble decoherence time $T_2^* = 1/\gamma_\perp \sim 26.5$ ns, which means that the microwave field generated by the line in this setup is too low to do coherent operations on the spins.

At each field, the ensemble spin spectrum was obtained by scanning over the pump frequency ω_{pump} and detecting the ensuing $\delta\omega_r$. The lineshape of PTM_r is inhomogeneously broadened, with a distribution of qubit frequencies $\omega_{q,i}$. Each pulse excites only the part of the distribution within its bandwidth, that is, in a frequency window $\Delta\omega_{pump} \sim 1/(50\,\mu s) = 20$ kHz centered at ω_{pump}.

The sweep in ω_{pump} reconstructs the distribution of spins with different $\omega_{\mathrm{q},\,i}$. The spectra measured at 62.3 mT, 63 mT and 65 mT (detunings $\Delta \simeq$ -27.3, -12.3 and 44 MHz) are shown in Figs. 6.17a-c, respectively. Also, Fig. 6.16b shows how the peaks of the spectra, i.e. the maximum shifts measured at each field, follow closely the $1/\Delta$ dependence of the dispersive shift χ (and $\delta\omega_{\mathrm{r}}$) predicted by Eq. (6.10). The width of the spin resonance, in particular in relation to Δ, puts some spins with frequencies $\omega_{\mathrm{q},\,i}$ too close to ω_{r}, thus beyond the dispersive regime condition. This can be seen in the high-frequency end of the 62.3 mT spectrum not going back to $\delta\omega_{\mathrm{r}} = 0$ and, most notably, in the 63 mT spectrum with $\delta\omega_{\mathrm{r}}$ decreasing sharply as it crosses the LER frequency ω_{r}. The spectra are fitted to Gaussian profiles with $\sigma/2\pi = 10.01 \pm 0.24$ MHz. The half-width at half maximum (HWHM) of this distribution is $\sqrt{2\ln(2)}\sigma/2\pi = 11.79 \pm 0.28$ MHz. This is consistent with the decoherence rate $\gamma_\perp/2\pi = 5.8 \pm 0.2$ MHz estimated for the spin ensemble on LER 10 in section 6.2, where a Lorentzian profile $|1/(\gamma_\perp + i(\omega_{\mathrm{q}} - \omega_{\mathrm{d}}))|$ with HWHM $= \sqrt{3}\gamma_\perp/2\pi = 10.0 \pm 0.3$ MHz is assumed.

Figure 6.17 also shows the measurement of the relaxation time T_1 for the same three fields. The pump frequency ω_{pump} was fixed to the value that gives the maximum of the spectrum shift at each magnetic field, $\omega_{\mathrm{pump}} = \omega_{\mathrm{q}}$. The time t between the pump and the probe pulses was varied between a few milliseconds and several seconds. The shift $\delta\omega_{\mathrm{r}}$ decays back to ω_{ref} as the $\langle\hat{\sigma}_{z,\,i}\rangle$ expectation values relax to -1 with characteristic times $T_{1,\,i}$. The distribution of exponential decays can be fitted with a stretched exponential [10]:

$$\delta\omega_{\mathrm{r}}(t) := \delta\omega_{\mathrm{r}}(0)e^{-(t/T_1)^x}, \tag{6.14}$$

where x is the stretch parameter, which takes here values around ~ 0.5. T_1 stands as an average relaxation time of the sample, with values of a few seconds for the three measured fields: $T_1 = 4.9 \pm 0.2$ s at 62.3 mT, $T_1 = 6.9 \pm 0.2$ s at 63 mT, and $T_1 = 8.5 \pm 0.4$ s at 65 mT.

A simple model of the distribution of spin-photon couplings accounts for the observed distribution in relaxation times. An ensemble of uncoupled spins would decay to their ground state with a single relaxation time T_1. However, spins coupled to a resonator in the dispersive regime have a small hybridization (of the order of $|G_1/\Delta| \ll 1$) with the wavefunction of a photon in the resonator (see section 3.4). The relaxation rate of the coupled spins is then:

$$\Gamma_{\parallel} := \frac{1}{T_1} + \left(\frac{G_1}{\Delta}\right)^2 \frac{1}{T_\kappa}, \tag{6.15}$$

where $T_\kappa = 1/(2\kappa) \sim 1.4$ μs is the photon lifetime in LER 10. The hybridization with the resonator imparts the distribution of spin-photon couplings $G_{1,\,i}$ to the decay times.

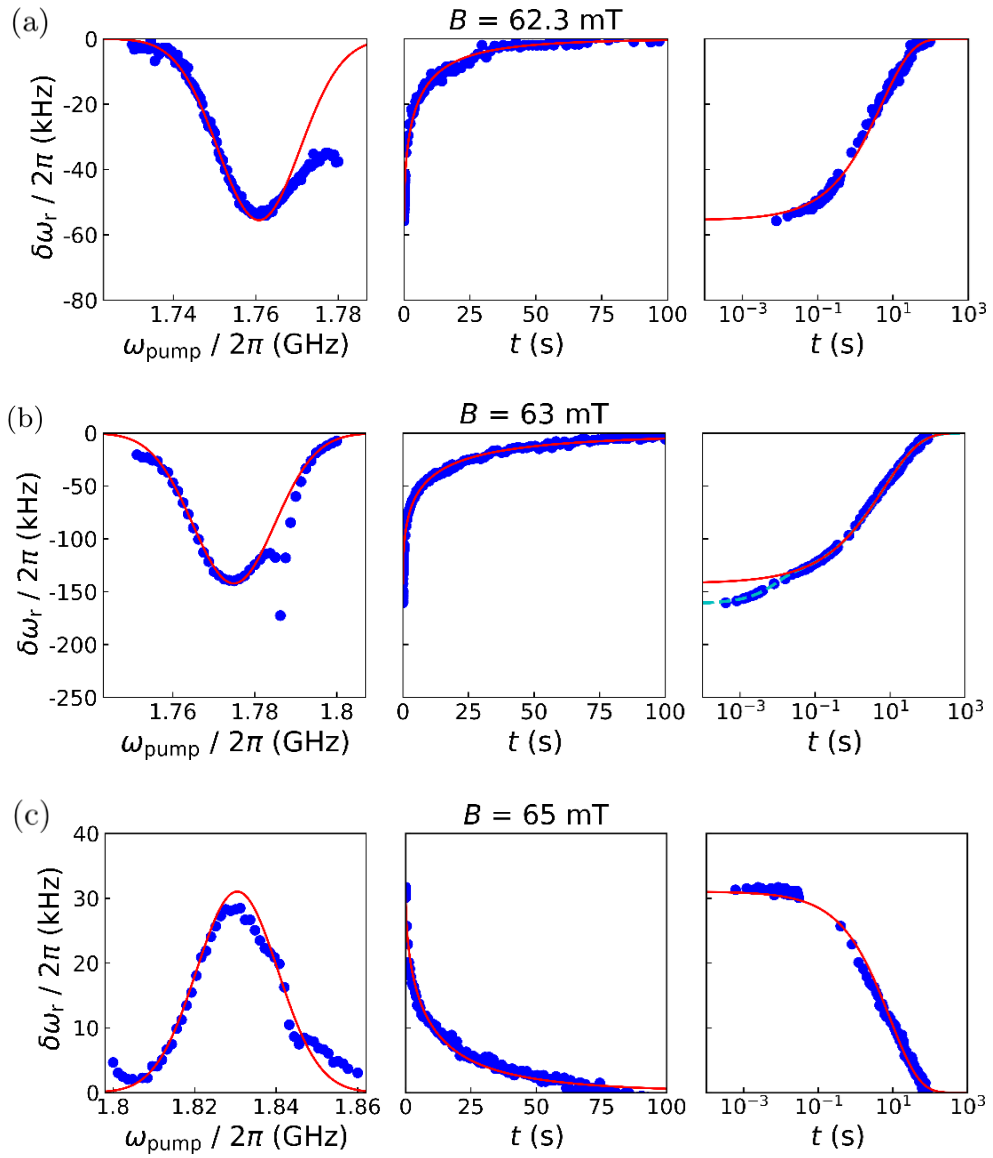

Figure 6.17: The shift $\delta\omega_r$ in the LER resonance frequency with respect to the reference frequency ω_{ref}, measured for different drive frequencies ω_{pump} of the pump pulse and different times t between the pump and probe pulses (blue dots). The sweep in t is shown in linear and logarithmic time scales. These measurements were performed at three magnetic fields: 62.3 mT (a), 63 mT (b) and 65 mT (c). The sweep in ω_{pump} gives the inhomogeneously broadened ensemble spin spectrum of PTM_r, which is fit to a Gaussian profile (red solid line). The sweep in t gives the decay of $\delta\omega_r$ as the spins relax to their ground state. This decay has been fitted to a stretched exponential (red solid line, see Eq. (6.14)) that is the result of having a distribution of exponential decays with different characteristic times $T_{1,i}$ up to seconds. At 63 mT, where ω_q is closer to ω_r, an additional decay with a fast $T_1 \sim 8.6$ ms is observed at very short times.

If a single wire is considered, these couplings, which are proportional to the magnetic field generate by the wire, can be assumed to scale with $1/r$, where r is the distance of the spin to the wire. Integrating in a cylinder or radius R around the wire, one obtains the following expression for $\delta\omega_r(t)$:

$$\delta\omega_r(t) \propto e^{-(t/T_1)} \int_{r=w}^{R} \frac{\mathrm{d}\, r}{r} e^{-t/T_G(r)} \propto e^{-(t/T_1)} \int_{T_G(w)}^{T_G(R)} \frac{\mathrm{d}\, T_G}{T_G} e^{-t/T_G}, \tag{6.16}$$

where $T_G(r)$ is the time that characterizes the spin relaxation time induced by its coupling to photons. It is defined as:

$$T_G(r) := \left(\frac{r}{w}\right)^2 T_G(w) = \left(\frac{r}{w}\right)^2 \left(\frac{\Delta}{G_1(w)}\right)^2 T_\kappa, \tag{6.17}$$

which scales quadratically with the detuning Δ [11].

Figure 6.18 compares the decay of $\delta\omega_r$ measured at 65 mT with the results of Eq. (6.16) for $T_1 \sim 60$ s, $T_G(w) = 0.2$ s and $T_G(R) = 250$ s. From these values, the single spin-photon couplings $G_1(w) \sim 116$ kHz and $G_1(R) \sim 3$ kHz are estimated. These values are of the same order of magnitude of single spin-photon couplings found in [4] for spins coupled to the inductor constriction. At 63 mT, where ω_q is closer to ω_r, the dispersive regime theory starts to fail and the effect of the coupling to the resonator is more prominent, generating an additional fast decay with a relaxation time of 8.6 ms (see Fig. 6.17b). This relaxation corresponds to a spin-photon coupling as high as ∼160 kHz.

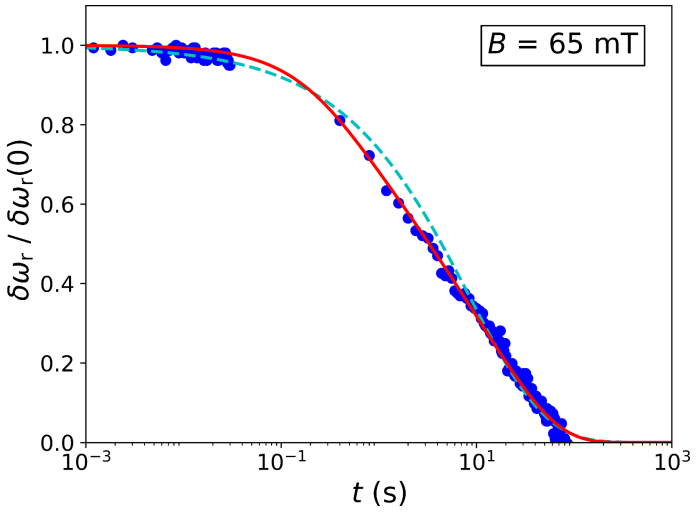

Figure 6.18: Decay of the shift ω_r in the LER resonance frequency with respect to the reference frequency ω_{ref} with the time t between the pump and probe pulses (blue dots), measured at 65 mT. The red solid line is the comparison with the model for the distribution of relaxation time from Eq. 6.16. The cyan dashed line is the fit with a stretched exponential decay.

Having very long spin relaxation times, even taking into account that they are shortened by the coupling to the resonator, places a limitation to the repetition time of the experiment. Before starting the next pump-probe experiment, the spins have to relax to their ground state. This means waiting $\sim 5T_1$, which in this case amounts to several minutes. However, a long T_1 also opens the possibility of measuring $\delta\omega_r$ by probing the whole LER resonance after the pump pulse. This is explored in the next sections.

6.4.4 Modulating T_1 with the magnetic field

An alternative, simple setup that allows measuring the LER resonance within a few milliseconds after the excitation of the spins is shown in Fig. 6.19. The probe sequence is now a train of pulses generated by a vector network analyzer (VNA). These pulses have carrier frequencies ω_{probe} spanning the whole resonance. The same VNA receives the transmitted signal and compares it to the sent pulses.

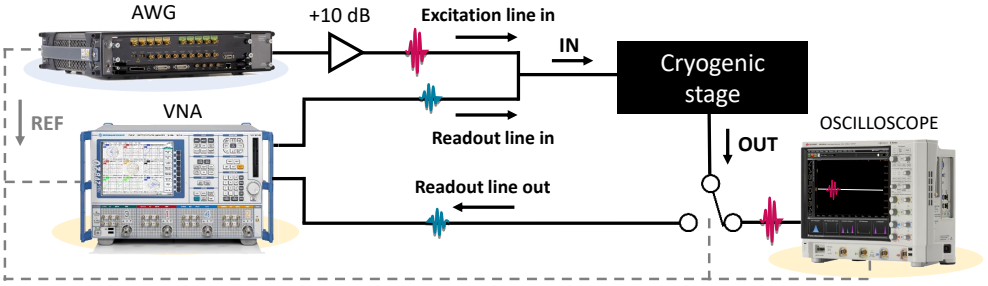

Figure 6.19: Generation and detection stages for chip *Test 3* using a vector network analyzer (VNA).

The shift $\delta\omega_r$ is obtained by comparing the resonance measured after a pump sequence ($\omega_{shifted}$) with a reference measurement without exciting the spins (ω_{ref}). Figure 6.20 compares the transmission of *Test 3* around the resonance frequency ω_r of LER 10 in these two situations, with the shift $\delta\omega_r$ clearly visible in the close-up of the measurement of the phase of the transmission parameter S_{21}. Even if this shift is small compared to the width of the resonance, it can be faithfully recovered by fitting both resonances with the theory for the transmission through the transmission line for frequencies close to the resonance frequency of a LER, given by Eq. (4.67). The formula for the transmission parameter S_{21} is reproduced below:

$$S_{21}(\omega_d) = 1 - \frac{\kappa_c}{i(\omega_r - \omega_d) + \kappa}, \tag{6.18}$$

where $\omega_d \equiv \omega_{probe}$ is the carrier frequency of each of the pulses in the probe sequence. The two resonances are fitted with the same resonator decay rate κ and line-resonator coupling κ_c, leaving ω_r as the only free parameter for each resonance.

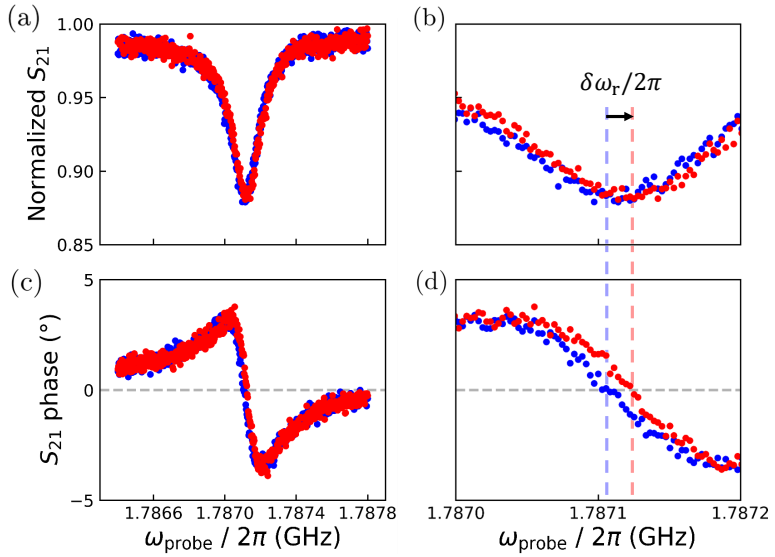

Figure 6.20: (a) Normalized module of the complex-valued transmission S_{21} of *Test 3* for probe frequencies close to the LER 10 resonance frequency ω_r, measured at $B =$ 65 mT. Two situations are compared: blue dots show the resonance without exciting the spins, red dots show the same resonance after a pump pulse at the qubit frequency $\omega_q = \mu_B g_S B/\hbar$ has been applied. (b) Close-up centered at ω_r, showing the shift $\delta\omega_r$ of the center frequency of the resonance. Figures (c, d) illustrate more clearly this shift with the measurement of the phase of S_{21}.

The spectrum of the PTM_r ensemble was measured with this technique at two fields with detuning $\Delta/2\pi = (\omega_q - \omega_r)/2\pi \simeq \pm$ 40 MHz. Figure 6.21 shows the change in $\delta\omega_r$ as the pump frequency is swept in the vicinity of the spin resonance frequency ω_q for each field. As in the previous section, the sign of the shift $\delta\omega_r$ follows the sign of Δ, which confirms that the effect is due to the coupling of the LER to the spin ensemble. Both spectra are fit to a Gaussian lineshape with $\sigma/2\pi = 10.01$ MHz. This confirms that the results of measuring the whole resonance are compatible with those obtained from measurements with a single probe pulse.

Similarly, the decay of the shift $\delta\omega_r$ with the delay time between the pump pulse and probe sequence was measured again, now for a wider range of magnetic fields. Figure 6.22 shows the results of these measurements, in which $\delta\omega_r$ decays faster as the field is brought closer to the spin-LER resonance field $B_{res} = \hbar\omega_r/\mu_B g_S$. This is the well-known *Purcell effect* [12–15], the enhance-

ment of the effective decay rate of the spins due to their coupling to a cavity (in this case, a superconducting resonator). $\delta\omega_r$ is normalized at each field by $|\delta\omega_r|$, which is the shift measured by triggering the VNA right after the pump pulse.

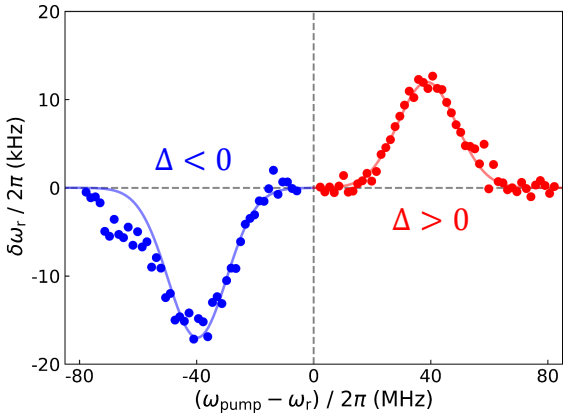

Figure 6.21: Shift $\delta\omega_r$ of the *Test 3* LER 10 resonance frequency for pump frequencies ω_{pump} around the qubit frequency ω_q, measured at two magnetic fields with detunings $\Delta/2\pi = (\omega_q - \omega_r)/2\pi \simeq \pm$ 40 MHz (blue dots for negative Δ, red dots for positive Δ). The sign of the shift $\delta\omega_r$ follows the sign of Δ. In both cases, the dependence of $\delta\omega_r$ with ω_{pump} traces the absorption spectrum of the spin ensemble, centered at $\omega_q = \mu_B g_S B/\hbar$, which is fit to a Gaussian lineshape with $\sigma/2\pi = 10.01$ MHz (solid lines).

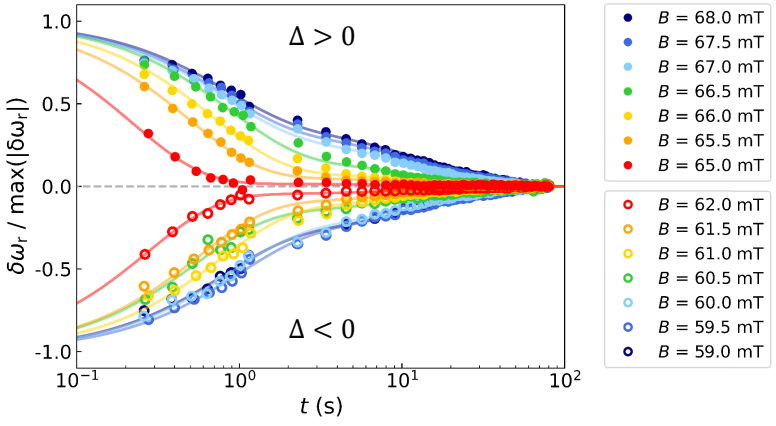

Figure 6.22: Shift $\delta\omega_r$ of the *Test 3* LER 10 resonance frequency for different delay times t between the pump pulse and the probe sequence, measured at several magnetic field between 59 and 68 mT. This magnetic field includes both positive and negative detunings $\Delta/2\pi = (\omega_q - \omega_r)/2\pi$. The decay of $\delta\omega_r$ is faster for fields associated to smaller Δ (in absolute value). Solid ($\Delta > 0$) and open ($\Delta < 0$) are experimental data, solid line show their fit to a sum of two exponential decays with different characteristic times (see Eq. (6.19)).

Obtaining a precise delay time is not possible for measurements with $t < 0.1$ s, due to the relatively slow VNA measurement compared to the arbitrarily short pulses generated by the AWG as well as any additional delay introduced by the triggering of the VNA. Lacking this time range, here I use a simple model capturing the two timescales observed the experiment instead of explaining these results with the model of Eq. (6.16) [9]:

$$\delta\omega_{\mathrm{r}}(t) = \delta\omega_{\mathrm{r}}(0)\left[C_G e^{-t/T_{1,\,\mathrm{fast}}} + (1 - C_G)e^{-t/T_{1,\,\mathrm{slow}}}\right], \tag{6.19}$$

where C_G is the ratio of the contribution of spins with the shorter decay time $T_{1,\,\mathrm{fast}}$ — the faster relaxation induced by resonator — to that of spins with the longer decay time $T_{1,\,\mathrm{slow}}$. This ratio can be related to the collective spin-photon coupling of each set of spins:

$$C_G := \frac{(\delta\omega_{\mathrm{r}})_{\mathrm{fast}}}{(\delta\omega_{\mathrm{r}})_{\mathrm{slow}}} \simeq \frac{\chi_{\mathrm{fast}}}{\chi_{\mathrm{slow}}} \simeq \left(\frac{(G_N)_{\mathrm{fast}}}{(G_N)_{\mathrm{slow}}}\right)^2. \tag{6.20}$$

Here I assumed that the distribution in $\langle\sigma_{z,\,i}\rangle$ generated by the inhomogeneity of the microwave magnetic field generated by the line is not correlated to the distribution of single spin-photon couplings to the resonator, which depends on the inhomogeneity of the microwave field generated by the resonator inductor. The same detuning Δ has been assumed as well.

The C_G ratios and the shorter decay times $T_{1,\,\mathrm{fast}}$ that result from the fit of the decay of $\delta\omega_{\mathrm{r}}$ for each magnetic field with Eq. (6.19) are shown in Fig. 6.23. All fields were fitted with a longer decay time $T_{1,\,\mathrm{fast}} \sim 15$ s associated to spins in the ensemble that are more weakly coupled to the resonator.

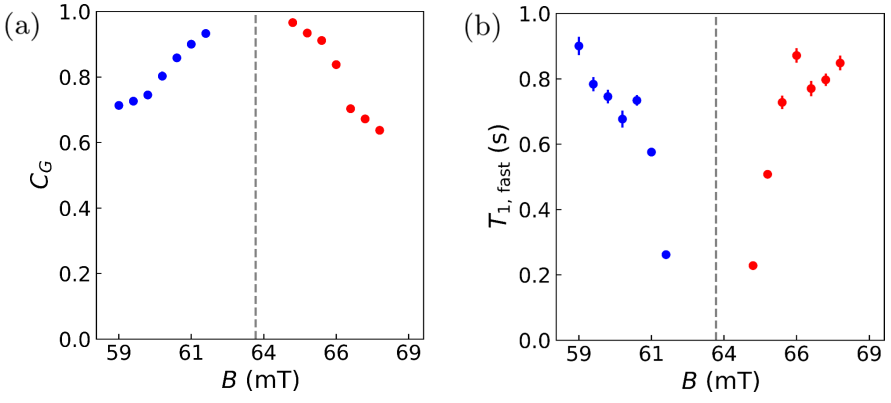

Figure 6.23: Magnetic field dependence of the C_G ratio (a) and the shorter decay time $T_{1,\,\mathrm{fast}}$ (b) that result form the fit of the decay of $\delta\omega_{\mathrm{r}}$ with Eq. (6.19). All fields were fitted with a longer decay rate $T_{1,\,\mathrm{fast}} \sim 15$ s. Blue dots used for magnetic fields with negative Δ, red dots for fields with positive Δ. The grey dashed line marks the spin-LER resonance field $B_{\mathrm{res}} = \hbar\omega_{\mathrm{r}}/\mu_{\mathrm{B}}g_{\mathrm{S}}$.

As the magnetic field is set closer to the spin-LER resonance field $B_{\mathrm{res}} = \hbar\omega_{\mathrm{r}}/\mu_{\mathrm{B}}g_{\mathrm{S}}$, the decay time $T_{1,\,\mathrm{fast}}$ decreases sharply due to the influence of the resonator. Also, the increase of C_G towards 1 means that the resonator-induced decay of the fast decaying spins provides the dominant contribution to $\delta\omega_{\mathrm{r}}$, over that of the weakly-coupled and slow decaying spins. That is, the relaxation rate of the isolated spins is so long that any hybridization with the resonator becomes the faster pathway for relaxation, unless Δ is made large enough and the spins become effectively decoupled from the photons. However, increasing the detuning has the drawback of having a lower shift $\delta\omega_{\mathrm{r}}$, which scales with $1/\Delta$. In the end, there is a trade-off between the optimization of magnitude of the shift by decreasing Δ and having a sufficiently long effective decay time by increasing Δ.

6.5 Towards a coherent manipulation of molecular spin qubits

6.5.1 Testing the setup for shorter pump pulses

The pump-probe experiments described in section 6.4 were carried out with 50 μs long pump pulses in order to see a change in $\delta\omega_{\mathrm{r}}$. These pulses are way too long to coherently manipulate the spins, as they should be shorter than the decoherence time $T_2^* = 1/\gamma_\perp \sim 26.5$ ns (see table 6.3). The duration of the pump pulse can be reduced by increasing the microwave power.

Test 4 was designed to overcome the power limitation of using a single transmission line for both pump and probe pulses. With its two lines (see Fig. 6.1b), the pump and probe pulses can be sent through two distinct coaxial lines in the cryostat. The input readout line keeps the 50 dB attenuation of the scheme shown in Fig. 6.5, while all the attenuators are removed from the input excitation line. The amplifier at 4 K is then mounted only at the output of the readout line.

The main risk of this setup is the possibility of a leaking of the input signal in the excitation line into the readout line through the resonator, damaging the cryogenic amplifier and the detection instruments. However, by working in the dispersive regime ($|\Delta| \gg G_N \sim 3$ MHz) and using high quality factor resonators ($Q \sim 16000$, $\kappa = 55.5$ kHz for LER 10), the high power pump signal is filtered by the resonator bandwidth as long as $\Delta \gg \kappa$. The same $\mathrm{PTM_r}$/PS samples used in *Test 3* were deposited on top of each LER in *Test 4* (see Fig. 6.24a). The interfacing of the chip with the excitation and readout lines in the cryostat is shown in Figs. 6.24b-d.

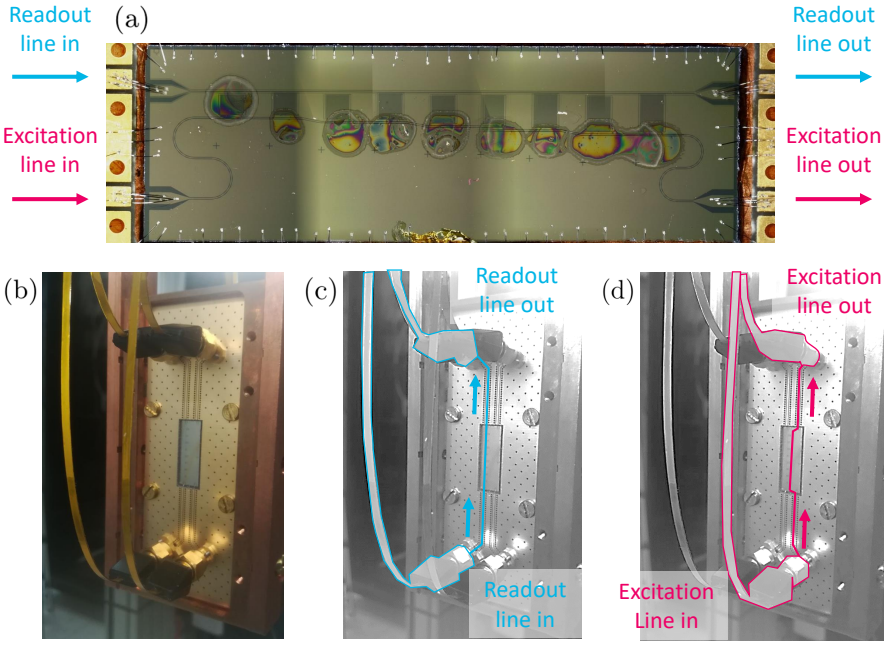

Figure 6.24: (a) PTM_r/PS deposits in *Test 4*. (b) Interfacing of *Test 4* with the excitation and readout lines in the cryostat with flexible cables. Readout and excitation lines are highlighted in (c, d).

The detection method of $\delta\omega_r$ in these new experiments with shorter pulses is a compromise between the techniques used in sections 6.4.3 and 6.4.4. The former requires a previous fine calibration of the resonance to indirectly obtain $\delta\omega_r$ with a single probe pulse, but the pulse can be easily triggered right after the pump pulse, thus minimizing the decay of $\delta\omega_r$. Conversely, the latter recovers the full shifted resonance, giving a nice visualization of $\delta\omega_r$ (see Fig. 6.20), but the slow VNA measurement tends to reduce the maximum $|\delta\omega_r|$. Here, the AWG was programmed to generate a train of probe pulses, each of a different frequency spanning the resonance, in the style of a VNA measurement. This way, the maximum $|\delta\omega_r|$ can be optimized by measuring the resonance much faster with shorter probe pulses, their length limited only by the time it takes for the resonator to reach its steady state ($t \gg 1/\tilde{\kappa}$). In addition, the AWG generates both the pump and probe pulses, which allows sending with precision the probe sequence right after the excitation of the spins.

Figure 6.25 summarizes the changes in the microwave setup for the pump-probe experiments in this section. A microwave switch triggered by the reference signal of the AWG is needed in the generation stage to send the pump and probe signals to their corresponding lines (the excitation and the readout lines). From there on, the design of *Test 4* with two transmission lines allows managing each signal independently.

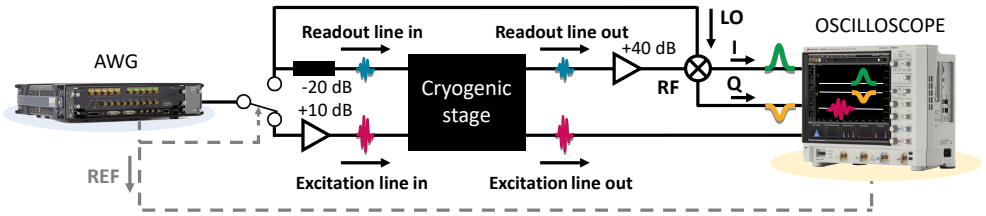

Figure 6.25: Generation and detection stages for chip *Test 4* using an Arbitrary Waveform Generator (AWG) and an oscilloscope. The setup is similar to that in Figs. 6.14 and 6.15, with some small changes. A microwave switch triggered by the reference signal of the AWG is needed in the generation stage to send the pump and probe signals to their corresponding lines (the excitation and the readout lines). From then on, the design of *Test 4* with two transmission lines allows managing each signal independently. The pump signal is amplified before the cryogenic stage to optimize the microwave power in the excitation line, and therefore the microwave magnetic field that drives the spins. At the output of the cryogenic stage, only the probe signal in the readout line is amplified.

The oscilloscope receives the in-phase (I) and quadrature (Q) components of the transmission of the probe pulses, acquiring the whole train of pulses in a single shot with a low sampling rate (see Fig. 6.26). The acquired data are processed by discarding the first $5/\tilde{\kappa} \sim 12$ μs of each pulse, when the resonator is charging, then averaging the I and Q levels in the steady state. The results are analysed as detailed in section 6.4.4: the LER resonance is fitted with (ω_{shifted}) and without (ω_{ref}) exciting the spins, obtaining the shift of the resonance as $\delta\omega_{\text{r}} = \omega_{\text{shifted}} - \omega_{\text{ref}}$. Figure 6.27 shows an example of the resonance shift obtained in one of these experiments.

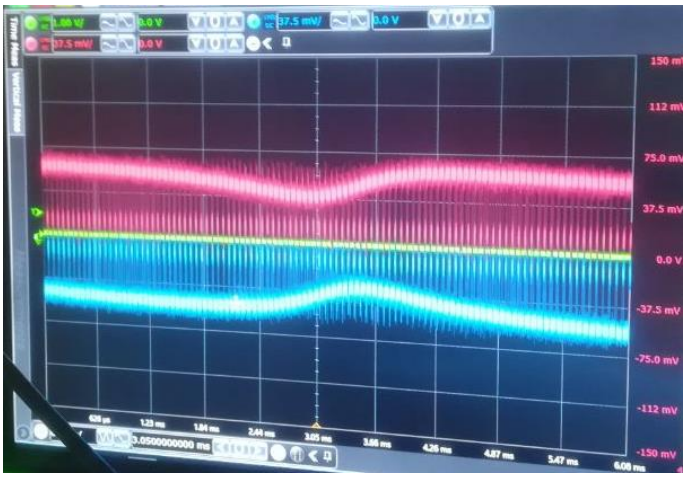

Figure 6.26: Photo of the oscilloscope screen acquiring I (magenta) and $-Q$ (cyan) signals for a train of probe pulses with carrier frequencies spanning the whole LER resonance.

Setting the magnetic field at 99.08 mT, the resonance of *Test 4* LER 1 was measured without the pump pulse (blue dots). The detuning at this field is $\Delta/2\pi = (\omega_q - \omega_r)/2\pi \simeq 40$ MHz. The same resonance was measured again after sending a 50 μs long pump pulse with carrier frequency $\omega_q/2\pi = \mu_B g_S B/h = 2.77424$ GHz, observing a shift $\delta\omega_r$ to higher frequencies (red dots). As a comparison, the resonance was also measured after pumping at a frequency $(\omega_r - \Delta)/2\pi = 2.69424$ GHz (cyan dots). This 'mirror' frequency is as close to ω_r as ω_q, but no shift $\delta\omega_r$ is observed. This rules out that the shift be associated to some non-linear effect of the resonator due to the microwave power of the pump pulse leaking into the resonator.

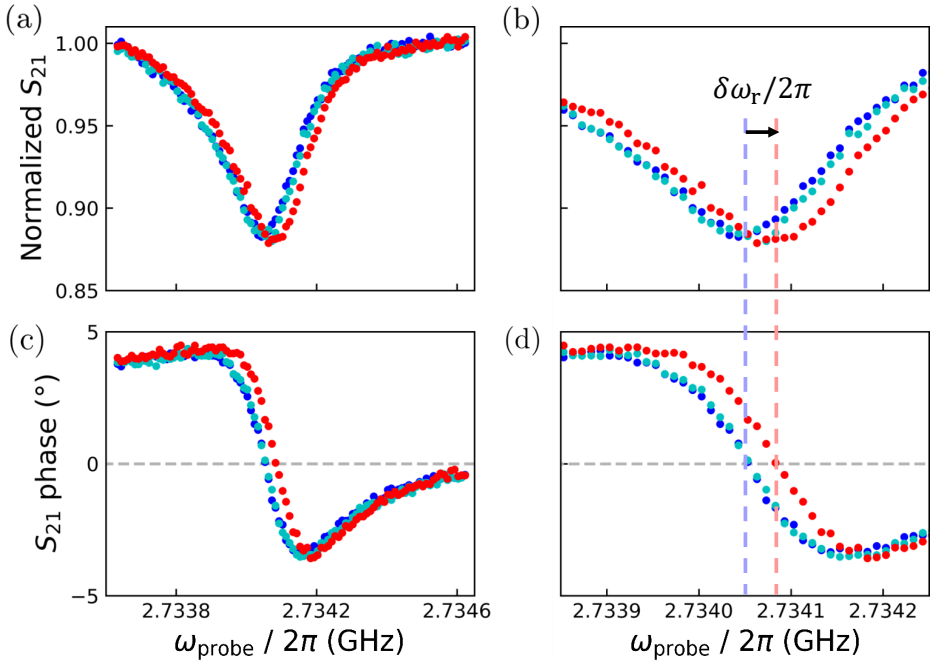

Figure 6.27: (a) Normalized module of the complex-valued transmission S_{21} of *Test 4* for probe frequencies close to the LER 1 resonance frequency ω_r, measured at $B = 99.08$ mT. Three situations are compared: blue dots show the resonance without exciting the spins, red dots show the same resonance measured after a pump pulse at the qubit frequency $\omega_q = \mu_B g_S B/\hbar$, and cyan dots are those measured after a pump pulse at the 'mirror' frequency $\omega_r - \Delta$. (b) Close-up picture of the resonance, centered at ω_r, showing its shift $\delta\omega_r$. Figures (c, d) illustrate more clearly this shift with the measurement of the phase of S_{21}.

6.5.2 Parallel pathways to generate the dispersive shift

I consider first experiments in which the excitation of the spins is introduced with a microwave square pulse. This method introduces two excitation paths

that generate different dispersive shifts. The results provide an interesting insight of the nature of the states of the hybrid spin-resonator system. The magnetic field was set at $B = 98.36$ mT, with ω_q above the resonance frequency ω_r of *Test 4*. This choice sets the qubit-resonator detuning at $\Delta/2\pi = (\omega_q - \omega_r)/2\pi \simeq 20$ MHz. The shift $\delta\omega_r$ of the resonance of LER 1 was measured for excitation pulses with carrier frequency $\omega_{pump} = \omega_q$ and pulse lengths between 10 and 500 ns. The results of this experiment are shown as red dots in Fig. 6.28a. As a comparison, blue dots show the result of a measurement performed with the same pump frequency at zero magnetic field, when the spins and the resonator are completely decoupled and the pump pulse has no effect on the resonator frequency.

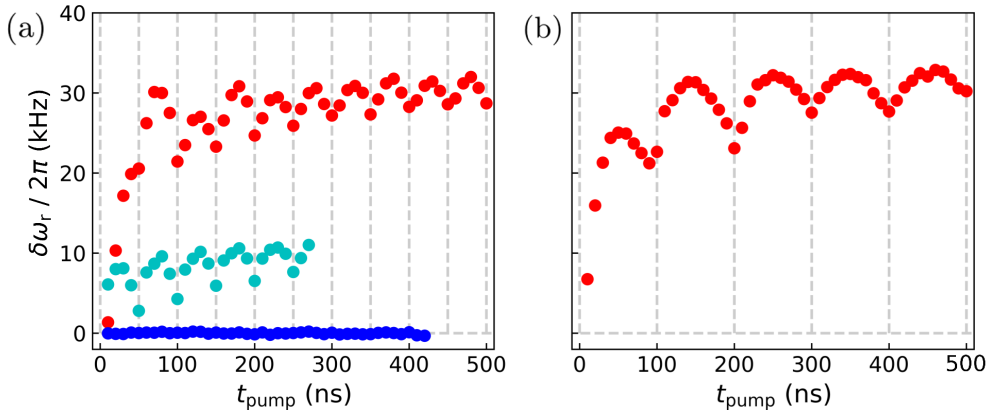

Figure 6.28: (a) Dependence of $\delta\omega_r$ on the length of the pump pulse, t_{pump}. Three experiments are shown. Red dots are the result of pumping at the qubit frequency ω_q at a magnetic field $B = 98.36$ mT, where the qubit-resonator detuning is $\Delta/2\pi \simeq 20$ MHz. Blue dots show the same experiment carried out at zero magnetic field, when the spins and the resonator are decoupled. Finally, cyan dots show the result of pumping at the 'mirror' frequency $\omega_r - \Delta$, again with at $B = 98.36$ mT. (b) Dependence of $\delta\omega_r$ on the length of the pump pulse, t_{pump}. The pump frequency is in the middle between ω_r and ω_q, $\omega_{pump} = (\omega_r + \omega_q)/2 = \omega_r + \Delta/2$, and the magnetic field was set at $B = 98.36$ mT.

An oscillation with a period T = 50 ns is observed in the data measured at $B = 98.36$ mT pumping with $\omega_{pump} = \omega_q$. A similar experiment pumping with the 'mirror' frequency $\omega_{pump} = \omega_r - \Delta$ yields oscillations with the same amplitude and period, but at over a lower $\delta\omega_r$ base level (cyan dots in Fig. 6.28b). This discards that these are Rabi oscillations. An additional experiment was carried out with $\omega_{pump} = (\omega_r + \omega_q)/2 = \omega_r + \Delta/2$. In this case, the period doubles to T = 100 ns. These results suggest that the period of the oscillation is related to the detuning between the pump frequency ω_{pump} and the resonator frequency ω_r. In Fig. 6.28a, the period matches $2\pi/|\omega_{pump} - \omega_r| = 2\pi/\Delta$. Sim-

ilarly, in Fig. 6.28b the period equals $2\pi/|\omega_{\text{pump}} - \omega_{\text{r}}| = 4\pi/\Delta$. I argue next that the relation between pump pulse duration and $\omega_{\text{pump}} - \omega_{\text{r}}$ is a consequence of using square pulses.

The Fourier transform of a square pulse of length t_{pump} is the cardinal sine function function $\text{sinc}(x) = \sin(x)/x$, with $x = (\omega - \omega_{\text{pump}})t_{\text{pump}}/2$. The zeros of this function are located at $x = m\pi$, that is, $(\omega - \omega_{\text{pump}})t_{\text{pump}}/2\pi = m$, with $m \neq 0$ an integer (see Fig. 6.29). This is precisely the condition that is met by the values of t_{pump} at which the oscillation minima are observed in $\delta\omega_{\text{r}}$, if we set $\omega = \omega_r$ (see vertical dashed lines in Fig. 6.28). The underlying physical origin of these oscillations is then that a small part of the microwave power of the pulse with frequency ω_r directly drives the resonator except when this condition is met. The fact that the excitation of the resonator by the sideband frequencies of the pump pulse leads to changes in $\delta\omega_{\text{r}}$ shows that it carries some spin changes with it. As a proof, the measurement performed at zero field shows no change in $\delta\omega_{\text{r}}$ (see Fig. 6.28a).

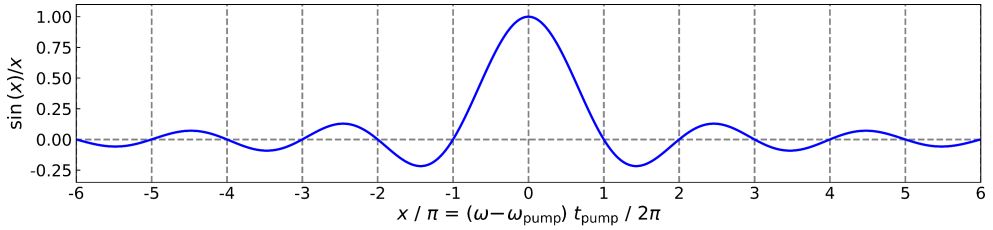

Figure 6.29: The cardinal sine function $\text{sinc}(x) = \sin(x)/x$, with $x = (\omega - \omega_{\text{pump}})t_{\text{pump}}/2$. The zeros of this function are located at $x = m\pi$, with $m \neq 0$ an integer.

The mechanism through which an excitation of the resonator changes $\delta\omega_{\text{r}}$ can be understood by recalling what do exciting the qubit or the resonator actually mean in the context of the dispersive regime. Assuming positive detuning ($\Delta > 0$), the hybrid qubit-resonator excited states can be approximated by (see section 3.4):

$$\begin{aligned} |\psi_{n,+}\rangle &\simeq \frac{G_1\sqrt{n}}{\Delta}\Big| \, |\psi_{n,\text{g}}\rangle + |\psi_{n-1,\text{e}}\rangle \\ |\psi_{n,-}\rangle &\simeq |\psi_{n,\text{g}}\rangle - \left|\frac{G_1\sqrt{n}}{\Delta}\right| |\psi_{n-1,\text{e}}\rangle \, . \end{aligned} \tag{6.21}$$

Figure 6.30 shows the energy levels of the spin-resonator system in the dispersive regime up to $n = 2$. From the ground state $|\psi_{0,\text{g}}\rangle$, the only transition with a frequency close to ω_{r} is the $|\psi_{0,\text{g}}\rangle \leftrightarrow |\psi_{1,-}\rangle$ transition, with frequency $\omega_{\text{ref}} = \omega_{\text{r}} - \chi$. This is the resonance that is observed in the absence of a pump

pulse. The pump pulse, with carrier frequency ω_q, generates the qubit excitation $|\psi_{0,e}\rangle$, which is not a stationary state of the system. Using Eq. (6.21), this state can be written as the superposition $|\psi_{0,e}\rangle \simeq |\psi_{1,+}\rangle - (G_1/\Delta)\,|\psi_{1,-}\rangle$. From $|\psi_{1,+}\rangle$, the only transition with a frequency close to ω_r is the $|\psi_{1,+}\rangle \leftrightarrow |\psi_{2,+}\rangle$ transition, with frequency $\omega_r + \chi = \omega_{ref} + 2\chi$. This is the standard procedure to measure the dispersive shift of ω_r.

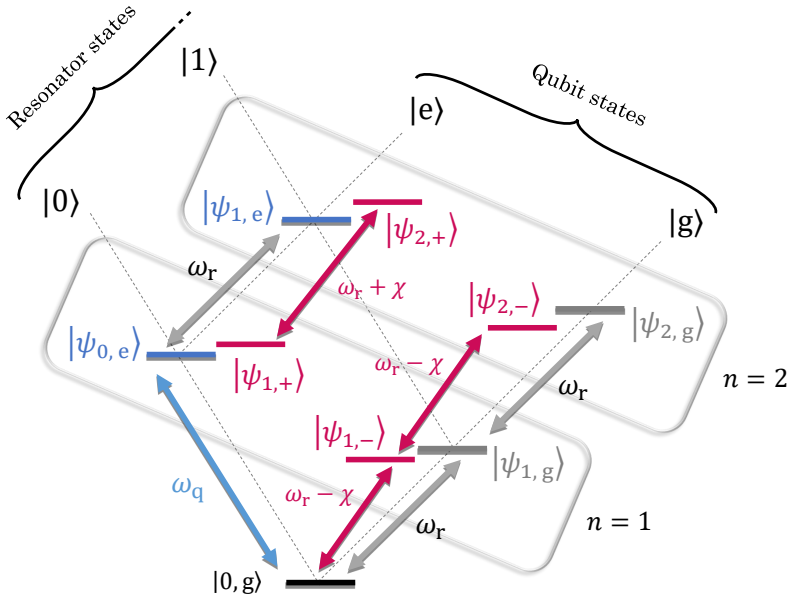

Figure 6.30: Energy levels of the spin-resonator system in the dispersive regime up to $n = 2$. Stationary states of the hybrid system are shown in magenta, with the independent excitations of the spin and the resonator in blue and grey for reference. Transitions between $|\psi_{n,-}\rangle$ states resonate at $\omega_{ref} = \omega_r - \chi$, while transitions between $|\psi_{n,+}\rangle$ states resonate at $\omega_r + \chi = \omega_{ref} + 2\chi$.

There is, however, another way of generating the state $|\psi_{1,+}\rangle$. Pumping at a frequency ω_r produces the resonator excitation $|\psi_{1,g}\rangle$. This is not a pure stationary state of the hybrid system. Inverting the relations in Eq. (6.21), this state can be written as the superposition $|\psi_{1,g}\rangle \simeq |\psi_{1,-}\rangle + (G_1/\Delta)\,|\psi_{1,+}\rangle$. That is, $|\psi_{1,+}\rangle$ can be generated by driving at the resonator frequency ω_r, although not efficiently: $|\psi_{1,+}\rangle$ is only a small part, of the order of $G_1/|\Delta| \ll 1$, of the resonator excitation. The resulting contribution to the dispersive shift is usually negligible, as the pump pulse is sent at ω_q, and the probe pulse at ω_r has a very low microwave power. However, the leaking of the square pump pulse with carrier frequency ω_q into the resonator whenever $(\omega_{pump} - \omega_r)t_{pump}/2\pi \neq 1$ has enough power to excite $|\psi_{1,+}\rangle$ significantly. The experiments provide a direct detection of the degree of 'mixture' between the spin and photon excitations at the given magnetic field (and detuning Δ).

6.5.3 Detection of damped oscillations

The results shown in Fig. 6.28a are the combination of pumping the spins at a frequency close to ω_q — the main peak of the sinc function — and the excitation of the resonator with the frequency sidebands of the square pulse. The latter can be removed by subtracting the measurement of $\delta\omega_r$ at the 'mirror' frequency $\omega_r - \Delta$, which displays the same fast oscillations due to the resonator excitation but involves no direct spin excitations. Figure 6.31 shows the hint of a damped Rabi oscillation that is recovered with this subtraction.

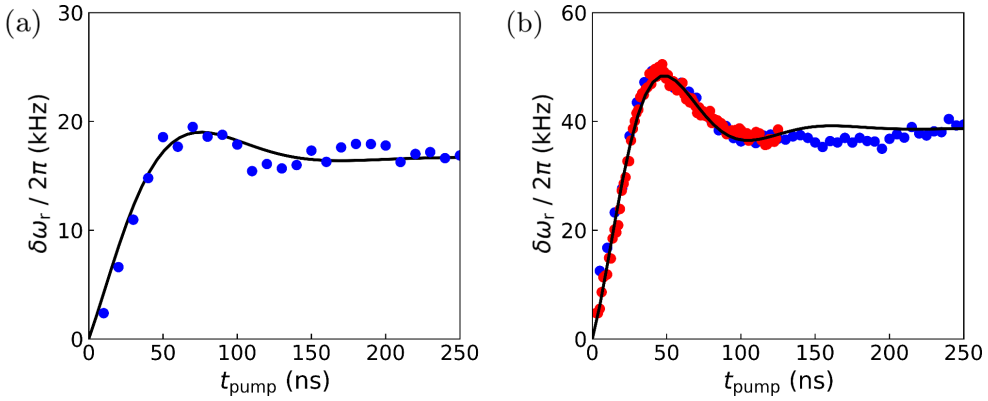

Figure 6.31: (a) Difference between the measurement of $\delta\omega_r$ sending a square pulse at the qubit frequency $\omega_q = \omega_r + \Delta$ (red dots in Fig. 6.28a) and at the 'mirror' frequency $\omega_r - \Delta$ (cyan dots in that same figure). The black solid line is the fit to a damped oscillation with with decay time $\tau = 43 \pm 4$ ns and a period $T = 94 \pm 6$ ns. The time it takes for the pump pulse to invert the population (π-pulse, maximum $\delta\omega_r$) is $t_\pi = T/2 = 47 \pm 3$ ns. (b) Dependence of $\delta\omega_r$ on the length of the pump pulse, $t_{pump} \equiv 2\sigma$, pumping at the qubit frequency ω_q with a Gaussian pulse. Two data sets are show. First, the $\delta\omega_r$ was measured with increasing t_{pump} up to 250 ns (blue dots). Then, the time range around the maximum of the oscillation was measured with a shorter step in the t_{pump} sweep (red dots). The black solid line is the fit to a damped oscillation with with decay time $\tau = 37.8 \pm 0.8$ ns and π-pulse length $t_\pi = 28.2 \pm 0.2$ ns.

The fit of $\delta\omega_r$ to a damped oscillation gives a period $T = 94 \pm 6$ ns and a decay time $\tau = 43 \pm 4$ ns. The time it takes for the pump pulse to invert the population is half the period, when $\delta\omega_r$ is maximum (without the damping). This time is the optimal length of the π-pulse, $t_\pi = T/2 = 47 \pm 3$ ns. Both t_π and τ are similar in the experiment. τ is of the same order of the ensemble decoherence time $T_2^* = 1/\gamma_\perp \simeq 26.5$ ns. The damping of the oscillation arises from the comparison between the bandwidth of the pulse and the width of the spin spectrum. As the length of the pulse increases beyond T_2^*, the bandwidth of the pulse becomes thinner than the width of the spectrum, thus not exciting

part of the spin ensemble.

A practical removal of the effect of the leakage of the pump pulse into the resonator is the use of Gaussian pulses. The Fourier transform of a Gaussian pulse is a Gaussian distribution of frequencies, without the sidebands of the sinc function that cause the leakage into the resonator. Figure 6.31b shows the result of repeating the measurement of $\delta\omega_{\mathrm{r}}$ using Gaussian pulses. The pulse length is defined in this case as $t_{\mathrm{pump}} = 2\sigma$. The oscillation with $1/\Delta$ that was present for square pulses is gone, leaving only the damped Rabi oscillations. The fit of $\delta\omega_{\mathrm{r}}$ to a damped oscillation yields a decay time $\tau = 37.8 \pm 0.8$ ns and π-pulse length $t_\pi = 28.2 \pm 0.2$ ns.

6.6 Conclusions

The dispersive readout of molecular spin qubits coupled to lumped-element resonators has been performed in this chapter. The absorption spectrum and the relaxation time T_1 of the spin ensemble can be obtained from the shift $\delta\omega_{\mathrm{r}}$ of the LER resonance in pump-probe experiments. In addition, these measurements give some insight on the role of the resonator on the relaxation of the spin ensemble. An estimation of the highest single spin-photon couplings (as high as ∼160 kHz) and their distribution can be obtained as well. With short pulses (10-500 ns), the first signs of coherent manipulation of the spin ensemble have been detected in a specific superconducting chip designed for that purpose (*Test 4*). π-pulse lengths t_π similar to the ensemble decoherence rate T_2^* are obtained.

A limitation of these experiments is the distribution of microwave magnetic fields in the sample. Each spin is driven by a different field b_{mw}, which reduces the precision of the experiment compared to the ideal case of all the spins being driven together. This can be improved in future experiments by designing an excitation line that generates a more homogeneous microwave field in the sample. A promising proposal consists on two-sided superconducting chips, one side with the LERs coupled to the readout line and the other with the excitation line. This would give freedom to design a excitation line with a loop at the position of the LER inductor with the sample (on the opposite side), generating a more homogeneous b_{mw} at the position of the sample. Another improvement is the use composite pulses like the BB1 sequence, which can mitigate the error generated by a small microwave field inhomogeneity [16].

References

[1] D. I. Schuster, A. Wallraff, A. Blais, L. Frunzio, R.-S. Huang, J. Majer, S. M. Girvin, and R. J. Schoelkopf, Physical Review Letters **94**, 123602 (2005).

[2] A. Wallraff, D. I. Schuster, A. Blais, L. Frunzio, J. Majer, M. H. Devoret, S. M. Girvin, and R. J. Schoelkopf, Physical Review Letters **95**, 060501 (2005).

[3] P. Scarlino, D. J. van Woerkom, A. Stockklauser, J. V. Koski, M. C. Collodo, S. Gasparinetti, C. Reichl, W. Wegscheider, T. Ihn, K. Ensslin, et al., Physical Review Letters **122**, 206802 (2019).

[4] I. Gimeno Alonso, Ph.D. thesis, Universidad de Zaragoza (2023).

[5] O. Armet, J. Veciana, C. Rovira, J. Riera, J. Castañer, E. Molins, J. Rius, C. Miravitlles, S. Olivella, and J. Brichfeus, Journal of Physical Chemistry **91**, 5608 (1987).

[6] J. Guasch, X. Fontrodona, I. Ratera, C. Rovira, and J. Veciana, Acta Crystallographica **C69**, 225 (2013).

[7] D. Schäfter, J. Wischnat, L. Tesi, J. A. De Sousa, E. Little, J. McGuire, M. Mas-Torrent, C. Rovira, J. Veciana, F. Tuna, et al., Advanced Materials **35**, 2302114 (2023).

[8] R. Amsüss, C. Koller, T. Nöbauer, S. Putz, S. Rotter, K. Sandner, S. Schneider, M. Schramböck, G. Steinhauser, H. Ritsch, et al., Physical Review Letters **107**, 060502 (2011).

[9] A. K. V. Keyser, J. J. Burnett, S. E. Kubatkin, A. V. Danilov, M. Oxborrow, S. E. de Graaf, and T. Lindström, Journal of Magnetic Resonance **321**, 106853 (2020).

[10] C. Bonizzoni, A. Ghirri, S. Nakazawa, S. Nishida, K. Sato, T. Takui, and M. Affronte, Advanced Quantum Technologies **4**, 2100039 (2021).

[11] V. Ranjan, S. Probst, B. Albanese, A. Doll, O. Jacquot, E. Flurin, R. Heeres, D. Vion, D. Esteve, J. J. L. Morton, et al., Journal of Magnetic Resonance **310**, 106662 (2020).

[12] E. M. Purcell, H. C. Torrey, and R. V. Pound, Physical Review **69**, 37 (1946).

[13] M. Boissonneault, J. M. Gambetta, and A. Blais, Physical Review A **79**, 013819 (2009).

[14] G. M. Reuther, D. Zueco, F. Deppe, E. Hoffmann, E. P. Menzel, T. Weißl, M. Mariantoni, S. Kohler, A. Marx, E. Solano, et al., Physical Review B **81**, 144510 (2010).

[15] A. Bienfait, J. J. Pla, Y. Kubo, X. Zhou, M. Stern, C. C. Lo, C. D. Weis, T. Schenkel, D. Vion, D. Esteve, et al., Nature **531**, 74 (2016).

[16] J. J. L. Morton, A. M. Tyryshkin, A. Ardavan, K. Porfyrakis, S. A. Lyon, and G. A. D. Briggs, Physical Review Letters **95**, 200501 (2005).

Chapter 7

Circuit QED with electro-nuclear spin qudits

The previous chapter described pulse experiments performed on ensembles of simple free radical molecules. With their spin 1/2, these molecules are model realizations of spin qubits. The next logical step is to extend these experiments to more complex systems, able to implement richer quantum functionalities. A promising alternative is to exploit the multiple spin states within a magnetic molecule hosting multiple magnetic centers. However, synthesizing magnetically diluted crystals made of these molecules, which is necessary to combine a good protection from the decoherence induced by intermolecular interactions with the ability to resonantly address each spin transition, has proven quite challenging [1, 2].

Nuclear spins are interesting candidates to encode qubits or d-dimensional qudits due to their isolation from magnetic noise and potentially long coherence times. However, their weak coupling to external stimuli makes them hard to integrate into superconducting circuits. Conversely, coupling to electronic spins is easier, but with the drawback of having shorter coherence times. A promising architecture is based on magnetic ions that combine an electronic spin 1/2 and a non-zero nuclear spin. The qubit/qudit is encoded in the nuclear spin, but the readout is performed in the electronic spin: the state of the nuclear spin is inferred from its coupling to the electronic spin.

The [Yb(trensal)] complex [3], a molecule with a Yb^{3+} ion with effective electronic spin 1/2, showcases this electronic spin-nuclear spin architecture. Two stable isotopes of Yb have non-zero nuclear spin, ^{171}Yb with $I = 1/2$ and ^{173}Yb with $I = 5/2$. The large hyperfine coupling in [Yb(trensal)] with ^{173}Yb ($\sim$ 900 MHz) ensures a non-negligible electro-nuclear mixing even for fields up to 100 mT. The hyperfine-enhanced coupling of ^{173}Yb nuclear tran-

sitions to LERs has been measured with transmission experiments and pulsed experiments [4]. Additionally, I describe the first results of dispersive readout experiments performed on a isotopically enriched crystal of [Yb(trensal)].

7.1 Experimental setup

7.1.1 [Yb(trensal)] samples

[Yb(trensal)] is a coordination complex with an effective electronic spin 1/2 localized in its Yb^{3+} ion. Here (trensal) is shorthand for the trianionic[1] form of the heptadentate[2] ligand H_3trensal [5–8]. Figure 7.1a shows the molecular structure of the complex. It has C_3 symmetry, with the symmetry axis — the C_3 axis — defined by the coordination bond between the Yb^{3+} ion and the tertiary amine of the triethylamine.

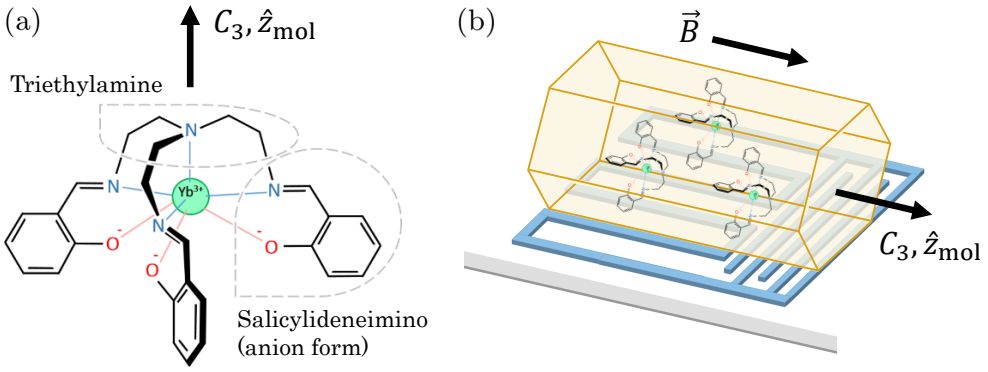

Figure 7.1: (a) Molecular structure of the Yb(trensal) complex, adapted from [6, 7]. The (trensal) trianionic ligand consists of a triethylamine bridging three salicylideneimino groups in anion form. The complex has axial symmetry, with the molecular z axis being the same as the C_3 symmetry axis defined by the coordination bond between the Yb^{3+} ion and the tertiary amine of the triethylamine. (b) Scheme of a [Yb(trensal)] crystal on a lumped-element resonator. The crystal is a hexagonal prism with the C_3 symmetry axis of all molecules perpendicular to the hexagonal faces. The static magnetic field is applied along the C_3 axis, parallel to the transmission line and the longer resonator inductor lines.

The [Yb(trensal)] samples used in this work are molecular crystals in the form of hexagonal prisms, see Fig. 7.1b, synthesized by the group of S. Piligkos

[1] With charge 3−, trensal forms neutral complexes with Ln^{3+} ions of the lanthanide series. The neutral H_3trensal has a hydrogen atom bonded to each oxygen atom of trensal.

[2] A heptadentate ligand has seven donor groups that can bind the magnetic ion. In this case, these donor groups are the tertiary amine of the triethylamine, the three imine groups, and the three oxygen atoms.

at the University of Copenhagen. The C_3 symmetry axis of all [Yb(trensal)] molecules is normal to the hexagonal faces of the crystal. In order to mitigate the spin-spin interactions between molecules, [Yb(trensal)] is doped into a matrix of the isostructural diamagnetic host [Lu(trensal)], preserving the orientation of all [Yb(trensal)] molecules with respect to the applied magnetic field $\boldsymbol{B}$ and the chip.

Yb^{3+} is a Kramers ion with a two-fold degeneracy of the ground energy state at zero magnetic field (see 3.1.2 in chapter 3). Magnetic anisotropy lifts the energy of other excited states so that at low temperatures this ground doublet can be considered as an effective two-state system, that is, an effective spin 1/2 system. The electronic Zeeman term of this spin 1/2 is affected by magnetic anisotropy: the g-tensor is diagonal but non-isotropic, with $g_x = g_y \equiv g_\perp = 2.935$ and $g_z \equiv g_\parallel = 4.225$ (axial symmetry). Here the molecular z axis is the C_3 symmetry axis. The resulting spin Hamiltonian is:

$$H = H_{\mathrm{el,Z}} = \mu_{\mathrm{B}} \left[g_\perp \left(B_x \hat{S}_x + B_y \hat{S}_y \right) + g_\parallel B_z \hat{S}_z \right]. \tag{7.1}$$

The hyperfine splitting of [Yb(trensal)] with a non-zero nuclear spin Yb isotope is well described by a diagonal, non-isotropic hyperfine tensor in the molecular axes defined by the anisotropy Zeeman interaction. In these experiments, I am interested in the ^{173}Yb isotope, with $I = 5/2$ and a natural abundance of 16%. Its nuclear spin adds a hyperfine interaction with axial symmetry, a nuclear Zeeman interaction with $g_I = -0.02592$, and a quadrupolar term with $P_\parallel = 66$ MHz to the effective spin Hamiltonian:

$$\begin{aligned} H = H_{\mathrm{el,Z}} + & A_\perp \left(\hat{S}_x \otimes \hat{I}_x + \hat{S}_y \otimes \hat{I}_y \right) + A_\parallel \hat{S}_z \otimes \hat{I}_z \\ & - \mu_N g_I \boldsymbol{B} \cdot \hat{\boldsymbol{I}} + P_\parallel \left(\hat{I}_z^2 - \tfrac{1}{3} I(I+1) \right). \end{aligned} \tag{7.2}$$

The hyperfine interaction is the dominant energy scale for the ^{173}Yb nuclear spin in [Yb(trensal)], [^{173}Yb(trensal)] in what follows, with $A_\perp/h = -615$ MHz and $A_\parallel/h = -897$ MHz. The magnetic field dependence of the energy spectrum derived from Eq. (7.2) with these parameters is shown in Fig. 7.2a. In this figure, the magnetic field is applied along the C_3 symmetry axis, that is, parallel to the molecular z axis.

At high magnetic fields, the twelve spin states in the spectrum are divided into two subsets: six low-energy states with $m_S = -1/2$, the ground electronic spin state, and six high-energy states with $m_S = +1/2$, the excited electronic spin state. For each subset, there are five nuclear spin transitions with frequencies in the range of hundreds of MHz between states with $|\Delta m_I| = 1$. In practice, only nuclear spin transitions between states in the low-energy subset are detected (see Fig. 7.2b), as the population difference between states in the

high-energy subset is negligible even at very low temperatures. There are also six electronic spin transitions ($|\Delta m_S| = 1$) between the two subsets, one for each value of m_I from $-5/2$ to $+5/2$. All six transitions, with frequencies in the range of a few GHz, can be easily detected at low temperatures (see Fig. 7.2c).

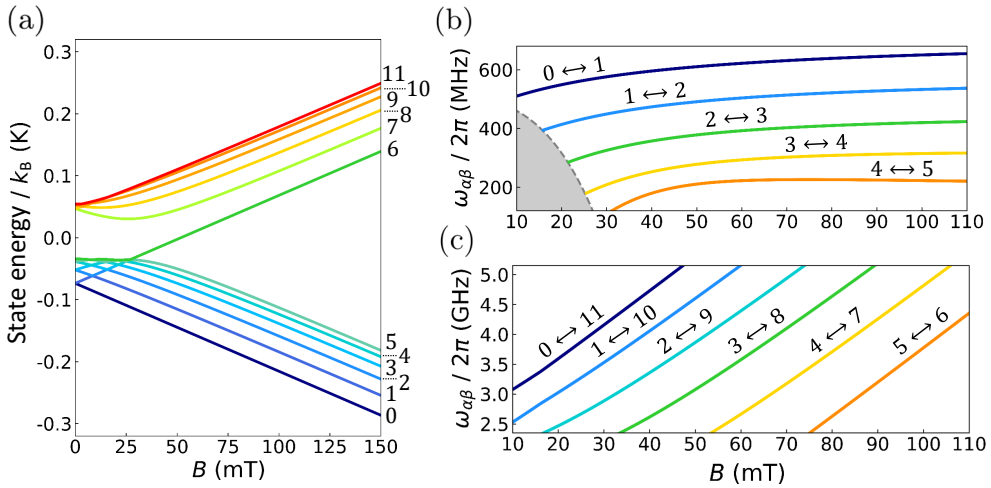

Figure 7.2: (a) Energy spectrum of [^{173}Yb(trensal)] ($I = 5/2$), with its twelve spin states split by magnetic field into a low-energy subset with $m_S = -1/2$ and a high-energy subset with $m_S = +1/2$. The magnetic field is applied along the C_3 symmetry axis of the molecules. (b) Magnetic field dependence of the resonance frequencies of the transitions between the six low-energy states of [^{173}Yb(trensal)]. From highest to lowest frequency, these transitions correspond approximately — save for the mixing introduced by the hyperfine interaction — to the nuclear transitions $m_I = -5/2 \leftrightarrow -3/2$ ($0 \leftrightarrow 1$), $m_I = -3/2 \leftrightarrow -1/2$ ($1 \leftrightarrow 2$), $m_I = -1/2 \leftrightarrow +1/2$ ($2 \leftrightarrow 3$), $m_I = +1/2 \leftrightarrow +3/2$ ($3 \leftrightarrow 4$) and $m_I = +3/2 \leftrightarrow +5/2$ ($4 \leftrightarrow 5$) with $m_S = -1/2$. At low fields (shaded region) these transitions start to mix due to the hyperfine interaction. (c) Magnetic field dependence of the six transitions between the two subsets. Left to right, these transitions correspond approximately to different nuclear spin states: $m_I = -5/2$ ($0 \leftrightarrow 11$), $m_I = -3/2$ ($1 \leftrightarrow 10$), $m_I = -1/2$ ($2 \leftrightarrow 9$), $m_I = +1/2$ ($3 \leftrightarrow 8$), $m_I = +3/2$ ($4 \leftrightarrow 7$), and $m_I = +5/2$ ($5 \leftrightarrow 6$).

The strong hyperfine interaction and the presence of a sizeable quadrupolar splitting in [^{173}Yb(trensal)] gives rise to the level of anharmonicity necessary for addressing its $(2S + 1) \times (2I + 1) = 12$ spin states and, therefore, to properly encode a $d = 12$ electronuclear spin qudit. Alternatively, this system can seen as a $d = 6$ nuclear spin qudit coupled to an electronic spin ancilla. This kind of architecture has been proposed to embed quantum error correction within a single molecule [3, 9].

Nuclear spins were one of the first platforms for quantum technologies that

were studied experimentally [10, 11]. These experiments focused on nuclear spins in organic molecules, which show long coherence times. However, nuclear spins are also difficult to address due to the weak interaction of nuclear magnetic moments with electromagnetic radiation fields. The hyperfine coupling of the nuclear and electronic spins in [^{173}Yb(trensal)] could in principle enhance the coupling of photons to nuclear spin transitions through the mixing of the electronic spin and nuclear spin wavefunctions [3].

7.1.2 Chip design

In order to obtain the best nuclear spin-photon coupling possible, it is interesting to study the nuclear spin qudits encoded in [Yb(trensal)] in the context of circuit quantum electrodynamics (c-QED), one of the most reliable platforms for solid-state quantum technologies [12]. Two superconducting chips were designed for coupling lumped-element resonators (LERs) to electronic spin and nuclear spin transitions in [^{173}Yb(trensal)], labeled *Yb-cw* and *Yb-pulsed*. Figure 7.3 shows both designs.

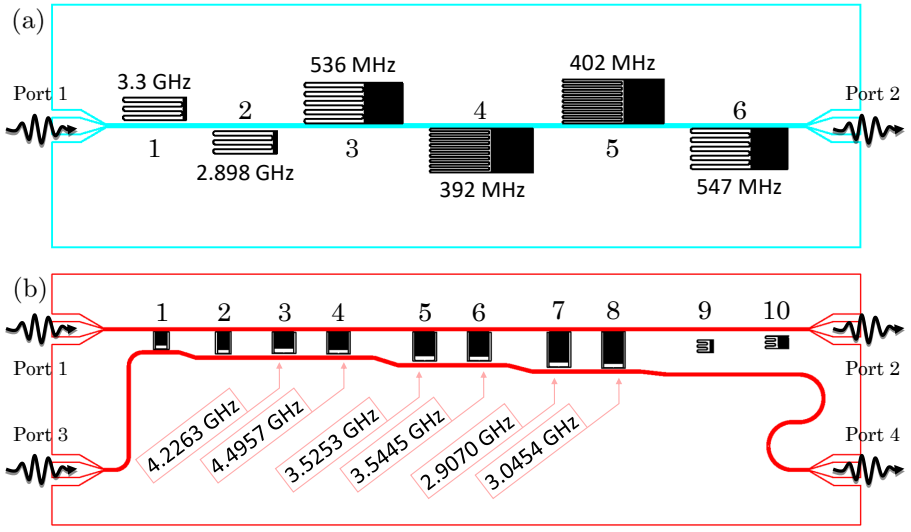

Figure 7.3: (a) Chip *Yb-cw*, with a single transmission line, designed to measure the collective spin-photon coupling of LERs to electronic spin and nuclear spin transitions in [^{173}Yb(trensal)]. LERs 1 and 2, with frequencies $\sim$ 3 GHz, are designed to couple to electronic spin transitions. LERs 3 to 6, with frequencies in the range between 400 and 550 MHz, are designed to couple to nuclear spin transitions. (b) Chip *Yb-pulsed*, with two transmission lines, designed for pulse experiments. LERs 3 and 4 (4.2-4.5 GHz) are tuned to the $0 \leftrightarrow 11$ transition ($m_I = -5/2$) with a magnetic field $B =$ 30 mT. At the same magnetic field, LERs 5 and 6 ($\sim$ 3.5 GHz) are tuned to the $1 \leftrightarrow 10$ transition ($m_I = -3/2$), and LERs 7 and 8 ($\sim$ 3 GHz) are tuned to the $2 \leftrightarrow 9$ transition ($m_I = -1/2$).

The design of *Yb-cw* is similar to the designs of *Test 1* and *Test 2* for free-radicals, with 6 LERs consisting of an inter-digital capacitor and a meandering inductor. All six resonators are side-coupled to the same transmission line with both inductive and capacitive couplings. The resonance frequencies of the *Yb-cw* LERs, shown in Fig. 7.3a, were tailored to match different electronic spin and nuclear spin transitions. LERs 1 and 2, with a smaller size, have frequencies in the range of ~ 3 GHz. These two LERs couple to the electronic spin transitions in [^{173}Yb(trensal)], see Fig. 7.2c. Conversely, larger resonators (LERs 3 to 6) couple to the nuclear spin transitions, with frequencies in the range between 400 and 550 MHz (see Fig. 7.2b).

Yb-pulsed hosts ten LERs, of which only LERs 3 to 8 (see Fig. 7.3b) were designed for pulsed experiments with [^{173}Yb(trensal)]. Therefore, I will focus only on these six resonators. They share a similar design with the low-inductance resonators used in the previous chapter for dispersive readout experiments with $\mathrm{PTM_r}$. Most of the resonator area is taken by a large inter-digital capacitor, with its ends connected by a single strip — the inductor — close to the transmission line. Each pair of LERs with similar frequencies is tuned to be close to the frequency of a specific electronic spin transition of [^{173}Yb(trensal)] when a magnetic field of 30 mT is applied. LERs 3 and 4 are tuned to the $0 \leftrightarrow 11$ transition ($m_I = -5/2$), LERs 5 and 6 are tuned to the $1 \leftrightarrow 10$ transition ($m_I = -3/2$) and LERs 7 and 8 are tuned to the $2 \leftrightarrow 9$ transition ($m_I = -1/2$).

7.2 High cooperativity coupling to nuclear spin transitions

A complete characterization of the collective spin-photon coupling of electronic spin and nuclear spin transitions of [^{173}Yb(trensal)] to the photon modes of LERs in *Yb-cw* was performed with single crystals of [Yb(trensal)] having natural abundances of all Yb isotopes. Each crystal had a different concentration of [Yb(trensal)] in the diamagnetic [Lu(trensal)] matrix (see Fig. 7.4). With the sample sizes shown in Fig. 7.4, 10^{15}–10^{16} [Yb(trensal)] molecules with ^{173}Yb are estimated per crystal.

Crystals were placed on top of the meandering inductor of each LER, with the C_3 symmetry axis of the molecules aligned with both the transmission line and the inductor lines. The deposition process is detailed in Fig. 7.4. The magnetic field was also oriented parallel to C_3. A previous characterization based on the coupling to the transmission line provided broadband access to the different spin transitions. The results can be found in [4].

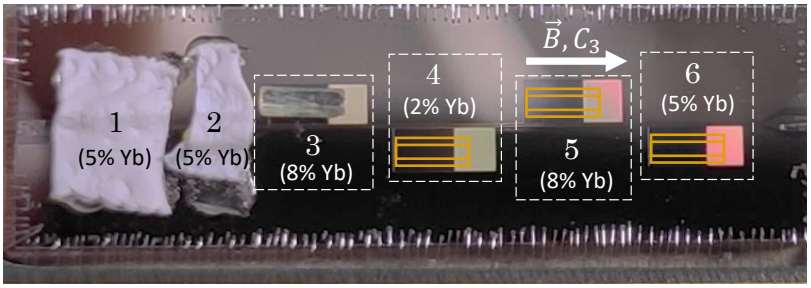

Figure 7.4: Superconducting chip with 6 LERs coupled to [Yb(trensal)] crystals. In the picture, only LERs 1, 2 and 3 have a crystal. Crystals were deposited later in the remaining resonators, here they are represented with pictures. After placing the crystals on top of the resonator inductor (see LER 3), crystals were covered with a Teflon strips stuck to the chip surface with vacuum grease (see LERs 1 and 2). Each crystal had a different concentration of [Yb(trensal)] in the diamagnetic [Lu(trensal)] matrix. The % of [Yb(trensal)] in each crystal is shown.

7.2.1 Electronic spin transitions

First, the electronic spin transitions of [Yb(trensal)] were addressed. Electronic spin transitions are in principle easier to measure than nuclear spin transitions, as the coupling of an isolated electronic spin to microwave magnetic fields is higher than that of isolated nuclear spins (the electronic Zeeman interaction is three orders of magnitude stronger than the nuclear Zeeman interaction). Moreover, the resonance frequency of an electronic spin transition can be easily tuned with the magnetic field in order to match the resonance frequency of LERs 1 and 2 (see Fig. 7.2c).

Figure 7.5 shows the transmission of *Yb-cw* for regular input frequencies $f \equiv \omega_{\rm d}/2\pi$ spanning the resonance of LER 2, measured in a range of magnetic fields for which the frequency of the $1 \leftrightarrow 10$ transition is close to the resonance frequency $\omega_{\rm r}$ of this LER. The $1 \leftrightarrow 10$ transition corresponds roughly to the electronic spin transition $m_S = -1/2 \leftrightarrow m_S = +1/2$ with $m_I = -3/2$. The transmission data are fitted with the theory for a resonator coupled the transition between states α and β of a qudit (see Eq. (4.137)), with frequency $\omega_{\alpha\beta}$:

$$S_{21}(\omega_{\rm d} \simeq \omega_{\alpha\beta}) = 1 - \frac{\kappa_{\rm c}}{i(\omega_{\rm r} - \omega_{\rm d}) + \kappa + \dfrac{(G_N)^2_{\alpha\beta}\Delta P_{\alpha\beta}}{i(\omega_{\alpha\beta} - \omega_{\rm d}) + \gamma_{\perp,\alpha\beta}}}\,. \tag{7.3}$$

The LER parameters are its resonance frequency $\omega_{\rm r}$ and decay rate κ, and the line-resonator coupling $\kappa_{\rm c}$. The $\alpha \leftrightarrow \beta$ transition has a decoherence rate $\gamma_{\perp,\alpha\beta}$

and a population difference $\Delta P_{\alpha\beta}$, and couples to the resonator with a rate $(G_N)_{\alpha\beta}$. In what follows, $\Delta P_{\alpha\beta}$ is included in the definition of the coupling: $(G_N)_{\alpha\beta} \propto \sqrt{\Delta P_{\alpha\beta}}$. The data in Fig. 7.5 corresponds to $\alpha = 1$ and $\beta = 10$. Table 7.1 shows the fit parameters of the resonance of LER 2 with Eq. (7.3).

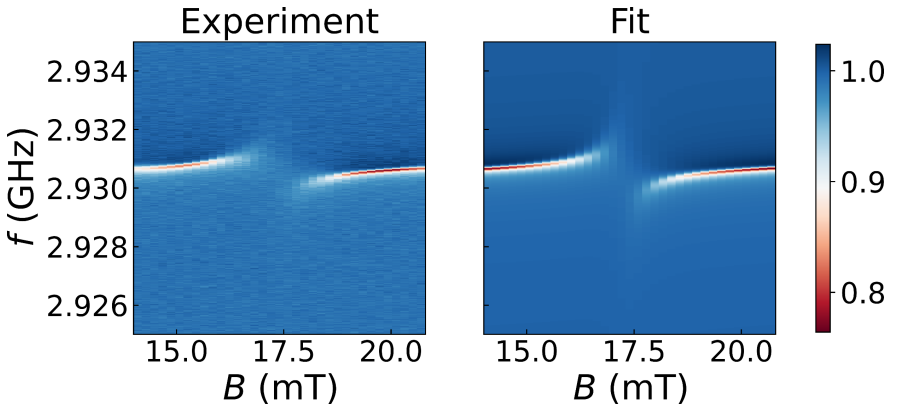

Figure 7.5: Transmission of *Yb-cw* for frequencies $f \equiv \omega_d/2\pi$ spanning the resonance of LER 2, measured for magnetic fields between 14 mT and 21 mT at $T = 10$ mK. In this field range, LER 2 couples to the $1 \leftrightarrow 10$ transition of [^{173}Yb(trensal)].

LER 2, 5% [Yb(trensal)]	
ω_r / 2π (GHz)	$2.9306714 \pm 4 \cdot 10^{-7}$
κ / 2π (kHz)	45.8 ± 0.3
$\lvert\kappa_c\rvert$ / 2π (kHz)	14.8 ± 0.2
ϕ_c (°)	33.1 ± 0.1
$(G_N)_{1\,10}$ / 2π (MHz)	4.67 ± 0.06
$\gamma_{\perp,1\,10}$ / 2π (MHz)	14.7 ± 0.1

Table 7.1: Fit parameters of the transmission of LER 2 coupled to the $1 \leftrightarrow 10$ transition of [^{173}Yb(trensal)] at 10 mK.

Since $(G_N)_{1\,10}/\gamma_{\perp,1\,10} \simeq 0.32 < 1$, the hybrid electronic spin-photon system is in the weak coupling regime. However, the high cooperativity regime is achieved, with $C_{1\,10} = (G_N)^2_{1\,10}/\gamma_{\perp,1\,10}\kappa \simeq 32.5 \gg 1$, thanks to the LER high quality factor $Q \simeq 3 \cdot 10^4$ ($\kappa = \omega_r/2Q = 45.8$ kHz). Note that only 5% of the molecules in the crystal on top of LER 2 are [Yb(trensal)], and of these only a 16% contain the ^{173}Yb isotope, that is, less than 1 out of 100 of all the molecules in the crystal have the $1 \leftrightarrow 10$ transition measured in Fig. 7.5. Still, a remarkably high coupling is attained. The full set of electronic transitions — 6 transitions, one for each value of m_I — was studied with [^{173}Yb(trensal)] isotopically purified samples. The results are described in section 7.4.

7.2.2 Nuclear spin transitions

The hyperfine interaction in [^{173}Yb(trensal)] dominates over the nuclear Zeeman interaction, making the frequencies of the nuclear spin transitions almost magnetic field independent for a wide range of fields (see Fig. 7.2b). This calls for a careful design of the LER frequencies in order to match the nuclear spin transition frequencies. *Yb-cw* LERs 4 and 5, with respective resonance frequencies $\omega_r = 392$ MHz and $\omega_r = 402$ MHz, were designed to match the frequency of the $1 \leftrightarrow 2$ transition at low fields ($B < 20$ mT) and the $2 \leftrightarrow 3$ transition at higher fields ($B > 60$ mT). These transitions correspond approximately to the $m_I = -3/2 \leftrightarrow -1/2$ and $m_I = -1/2 \leftrightarrow +1/2$ nuclear spin transitions with $m_S = -1/2$, respectively (see Fig. 7.6).

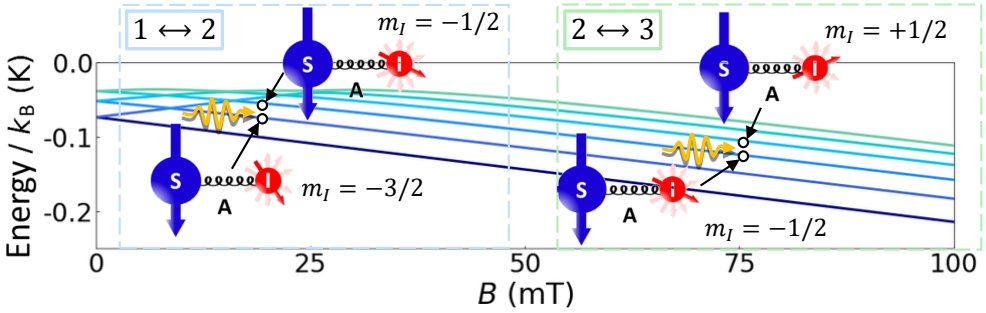

Figure 7.6: Picture of the transitions $1 \leftrightarrow 2$ and $2 \leftrightarrow 3$ in the energy scheme of Fig. 7.2a. These transitions correspond approximately to the $m_I = -3/2 \leftrightarrow -1/2$ and $m_I = -1/2 \leftrightarrow +1/2$ nuclear spin transitions with $m_S = -1/2$.

Figures 7.7a-b show the intersection of the transition frequencies ω_{12} and ω_{23} with the resonator frequencies as the magnetic field is swept between 0 and 75 mT in the case of LER 4, and between 0 and 100 mT for LER 5. The resonances were measured in these magnetic field ranges and at 10 mK (see Figs. 7.7c-d). In addition to the couplings associated to the $1 \leftrightarrow 2$ and $2 \leftrightarrow 3$ transitions, the couplings to transitions corresponding to other Yb isotopes are also observed.

Close-up plots of the transmission measured near the spin-photon resonant conditions for both LERs are shown in Figs. 7.8 (LER 4) and 7.9 (LER 5). The response of LERs 4 and 5 in the magnetic field ranges around the crossings of ω_{12} and ω_{23} with their resonance frequencies were fitted with the model of an effective, broadened resonator, valid in the weak spin-photon coupling regime (see section 4.6.4).

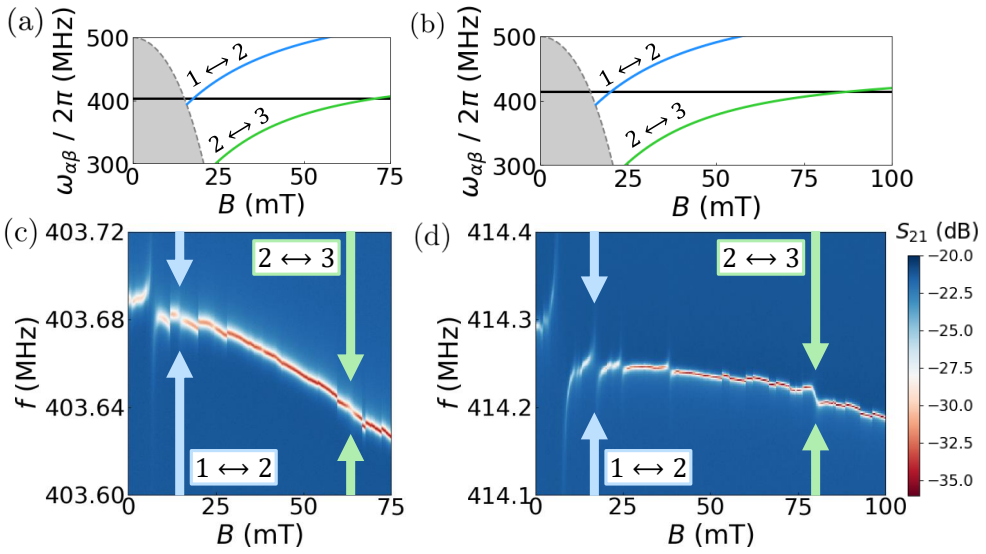

Figure 7.7: (a, b) Resonance frequencies of the nuclear spin transitions $1 \leftrightarrow 2$ and $2 \leftrightarrow 3$. Black horizontal lines are the resonance frequencies of LERs 4 (a) and 5 (b). (c, d) Transmission through the chip, measured for input frequencies $f = \omega_d/2\pi$ close to the resonance frequencies of LERs 4 (c) and 5 (d) and at $T = 10$ mK. Couplings to several transitions of [Yb(trensal)] with different Yb isotopes are observed. Here I focus on two nuclear transitions of [^{173}Yb(trensal)]: $1 \leftrightarrow 2$ and $2 \leftrightarrow 3$.

From weak coupling theory, the magnetic field dependence of $\tilde{\omega}_r$ and $\tilde{\kappa}$ is described by:

$$\begin{aligned} \tilde{\omega}_r &:= \omega_r + \left[\frac{(G_N)^2_{\alpha\beta}(\Delta P)_{e,\alpha\beta}}{(\omega_{\alpha\beta}-\omega_r)^2+\gamma^2_{\perp,\alpha\beta}}\right](\omega_r-\omega_{\alpha\beta}), \\ \tilde{\kappa} &:= \kappa + \left[\frac{(G_N)^2_{\alpha\beta}(\Delta P)_{e,\alpha\beta}}{(\omega_{\alpha\beta}-\omega_r)^2+\gamma^2_{\perp,\alpha\beta}}\right]\gamma_{\perp,\alpha\beta}, \end{aligned} \tag{7.4}$$

where $\omega_{\alpha\beta}$ is either ω_{21} (for the $1 \leftrightarrow 2$ transition) or ω_{32} (for $2 \leftrightarrow 3$). Each transition has a collective spin-photon coupling $(G_N)_{\alpha\beta}$ and a spin decoherence rate $\gamma_{\perp,\alpha\beta}$. $(\Delta P)_{e,\alpha\beta}$ is the population difference between states α and β in equilibrium. The fit of $\tilde{\omega}_r$ and $\tilde{\kappa}$ to Eq. (7.4) yields the collective $(G_N)_{\alpha\beta}$ and $\gamma_{\perp,\alpha\beta}$ for spin transition, which are reported in table 7.2. The comparison between $\tilde{\omega}_r$, $\tilde{\kappa}$ and the fit is shown later in section 7.3.2. A consistent simultaneous fit of $\tilde{\omega}_r$ and $\tilde{\kappa}$ with Eq. (7.4) for LER 5 coupled to the $2 \leftrightarrow 3$ transition at 10 mK turned out to be impossible. For that reason, the experiment was repeated at 50 mK (see Fig. 7.9c).

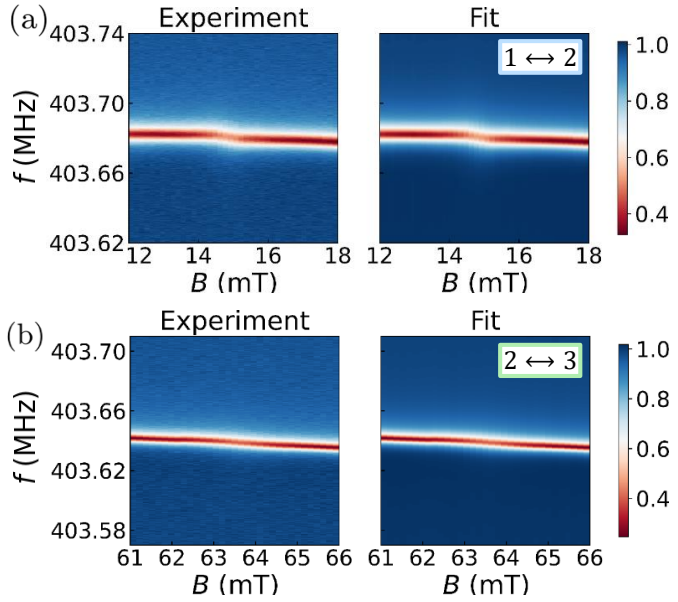

Figure 7.8: Transmission of *Yb-cw* for input frequencies close to the resonance frequency of LER 4, measured at 10 mK and for magnetic fields in which LER 4 is coupled to the $1 \leftrightarrow 2$ (a) and $2 \leftrightarrow 3$ (b) nuclear spin transitions of [^{173}Yb(trensal)]. The experimental data are compared to simulations for an effective resonance at each magnetic field, shifted in frequency and broadened by the interaction with the nuclear spins, which valid in the weak spin-photon coupling regime.

LER 4, 2% [Yb(trensal)]

Transition (temperature)	$1 \leftrightarrow 2$ (10 mK)	$2 \leftrightarrow 3$ (10 mK)
$(G_N)_{\alpha\beta}$ / 2π (kHz)	68 ± 3	29 ± 2
$\gamma_{\perp,\alpha\beta}$ / 2π (MHz)	2.6 ± 0.2	0.80 ± 0.10
$(G_N)_{\alpha\beta}$ / $\gamma_{\perp,\alpha\beta}$	0.026 ± 0.002	0.036 ± 0.005
$C_{\alpha\beta}$	0.51 ± 0.06	0.31 ± 0.06

LER 5, 8% [Yb(trensal)]

Transition (temperature)	$1 \leftrightarrow 2$ (10 mK)	$2 \leftrightarrow 3$ (50 mK)
$(G_N)_{\alpha\beta}$ / 2π (kHz)	262 ± 4	71 ± 5
$\gamma_{\perp,\alpha\beta}$ / 2π (MHz)	2.20 ± 0.06	0.39 ± 0.04
$(G_N)_{\alpha\beta}$ / $\gamma_{\perp,\alpha\beta}$	0.12 ± 0.04	0.18 ± 0.02
$C_{\alpha\beta}$	7.8 ± 0.6	3.6 ± 0.8

Table 7.2: Collective spin-photon coupling $(G_N)_{\alpha\beta}$ of LERs 4 and 5 to transitions $1 \leftrightarrow 2$ ($\alpha = 1$, $\beta = 2$) and $2 \leftrightarrow 3$ ($\alpha = 2$, $\beta = 3$), with spin decoherence rates $\gamma_{\perp,\alpha\beta}$. The population difference in equilibrium, $(\Delta P)_{\mathrm{e},\,\alpha\beta}$, is included here in $(G_N)_{\alpha\beta}$: $(G_N)_{\alpha\beta} \propto \sqrt{(\Delta P)_{\mathrm{e},\,\alpha\beta}}$. The ratios $(G_N)_{\alpha\beta}$ / $\gamma_{\perp,\alpha\beta}$ and the cooperativities $C_{\alpha\beta} = (G_N)^2_{\alpha\beta}$ / $\kappa\gamma_{\perp,\alpha\beta}$ are also listed.

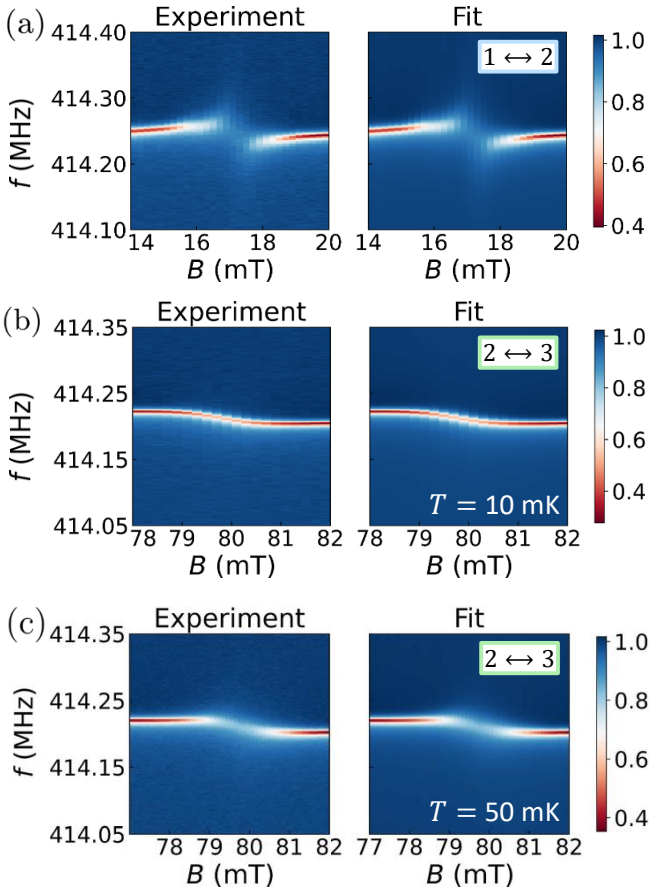

Figure 7.9: Transmission of *Yb-cw* for input frequencies close to the resonance frequency of LER 5, measured at 10 mK and for magnetic fields in which LER 5 is coupled to the $1 \leftrightarrow 2$ (a) and $2 \leftrightarrow 3$ (b) nuclear spin transitions of [^{173}Yb(trensal)]. The experimental data are compared to simulations for an effective resonance at each magnetic field, shifted in frequency and broadened by the interaction with the nuclear spins, which valid in the weak spin-photon coupling regime. The coupling of LER 5 to the $2 \leftrightarrow 3$ transition was also measured at 50 mK (c).

Couplings observed for LER 5 are clearly higher than in LER 4. This is just a consequence of the increase in the concentration of [Yb(trensal)] from the sample in LER 4 (2%) to the one in LER 5 (8%). The cooperativity is also enhanced. *High-cooperativity to nuclear spin transitions is achieved* for LER 5 with 8% of [Yb(trensal)] i.e. $C_{21}, C_{32} \gg 1$. Both the couplings ($(G_N)_{21}$, $(G_N)_{32}$), and cooperativities (C_{21}, C_{32}) reported here are about ten times smaller than what is achieved for the electronic spin transitions in the same molecular system (compare them to the values reported in section 7.2.1). They are nevertheless remarkably high. If the nuclear and electronic spins were uncoupled, the spin-photon coupling mediated by the nuclear Zeeman

interaction would lead to a ratio of about 10^{-4} — of the order of μ_B/μ_N — between the coupling rates of nuclear spin and electronic spin transitions. The fact that much higher couplings are observed for nuclear spin transitions means that the presence of the electronic spin ancilla acts as an effective mediator between the nuclear spin qudit and the resonator photons.

In each resonator, the coupling to the $1 \leftrightarrow 2$ transition is higher than the coupling to the $2 \leftrightarrow 3$ transition. The dominant parameter here is temperature. For LER 4, the difference in population $(\Delta P)_{\mathrm{e},\,\alpha\beta}$ in transition $1 \leftrightarrow 2$ at $B \simeq 15$ mT is 15 times higher than in $2 \leftrightarrow 3$ at $B \simeq 63$ mT. Similarly, for LER 5 $(\Delta P)_{\mathrm{e},\,\alpha\beta}$ is 20 times higher in $1 \leftrightarrow 2$ at $B \simeq 17$ mT than in $2 \leftrightarrow 3$ at $B \sim 80$ mT. A lower decoherence rate is observed for the $2 \leftrightarrow 3$ transition. I argue that this is due to the flatness of the nuclear spin transitions at higher fields, as shown in Figs. 7.7a-b, which makes them more insensitive to magnetic field fluctuations. Conversely, the $1 \leftrightarrow 2$ transition couples to LERs 4 and 5 at lower fields, where the slope of transition frequency ω_{12} with magnetic field is still high in comparison.

7.3 Pulse experiments on [Yb(trensal)] molecular spin qudits

The coupling of *Yb-cw* LERs to electronic spin and nuclear spin transitions was also characterized by measuring the transmission of pulses with driving frequencies ω_d close to the resonance frequency ω_r of each resonator at different fields, following the experimental protocols already described for LERs coupled to $\mathrm{PTM_r}$ samples (see section 6.3). Measuring the transmission of the pulses adds a new dimension — *time* — to each point of the maps in Figs. 7.5, 7.8 and 7.9, and allows tracking the dynamics of the system before reaching the steady state.

7.3.1 Electronic spin transitions

The transmission of 100 μs long pulses with driving frequencies $\omega_\mathrm{d} = 2\pi f$ spanning the resonance of LER 2 was measured at 10 mK for magnetic fields in the range of Fig. 7.5. Figure 7.10 shows the results for two fields, one at which the resonator is uncoupled from the transition (a) and one at which it is coupled (b). The results show that, as observed in stationary state measurements, the spin-photon coupling leads to a shift and broadening of the LER resonance. Besides, it has a consequence on the photon dynamics. The change and discharge of the resonator become significantly faster when photons are close to resonance with an electronic spin transition.

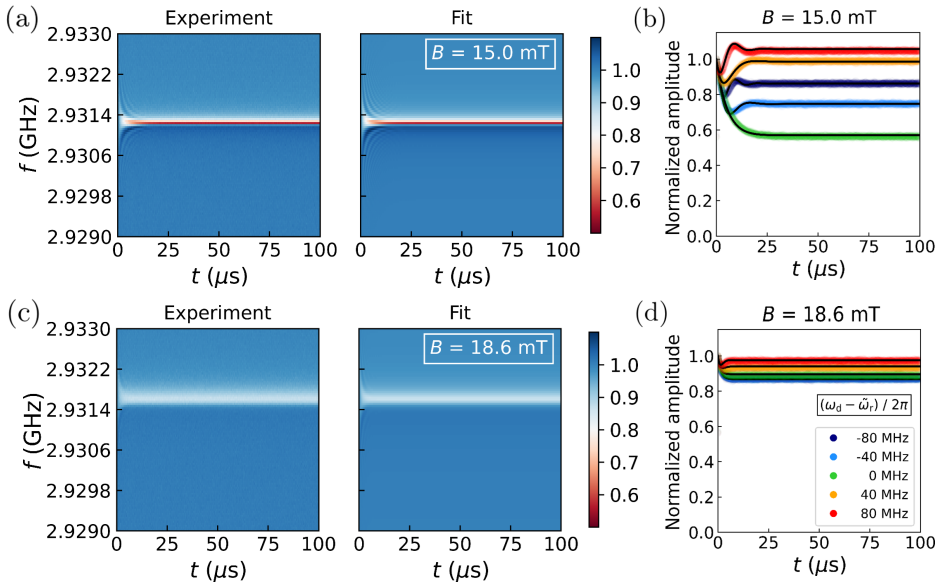

Figure 7.10: (a, c) Dynamics of LER 2 for two magnetic fields: 15 mT (a), showing the bare resonator, and 18.6 mT (c), where it is coupled to the $1 \leftrightarrow 10$ transition. (b, d) show cuts of Figs. (a, c) at various detunings between the driving frequency ω_d and the effective resonance frequency $\tilde{\omega}_\mathrm{r}$.

The coupling between LER 2 and the $1 \leftrightarrow 10$ electronic spin transition is in the weak coupling regime, thus the pulse transmission experiments can be fitted with the dynamical model of a broadened resonator described in section 6.3. The expression for the dynamics of the broadened resonator during the pulse is reproduced here for clarity:

$$b_\mathrm{out}(t) = \left(1 - \kappa_\mathrm{c} \frac{1 - e^{-(i(\omega_\mathrm{r}-\omega_\mathrm{d})+\kappa)t}}{i(\omega_\mathrm{r}-\omega_\mathrm{d})+\kappa}\right) \alpha_\mathrm{in} e^{-i\omega_\mathrm{d} t} \quad \text{for } t < t_\mathrm{pulse}\,, \tag{7.5}$$

with ω_r and κ replaced by the effective effective resonance frequency $\tilde{\omega}_\mathrm{r}$ and decay rate $\tilde{\kappa}$. Figure 7.11 shows the of $\tilde{\omega}_\mathrm{r}$ and $\tilde{\kappa}$ values obtained from the fit with Eq. (7.5) of the pulse transmission measurements on LER 2 at difference magnetic fields. These results are compared with the values predicted by the weak coupling formulas in Eq. (7.4) using the parameters from continuous wave experiments (see table 7.1), showing a reasonable good agreement between the two experimental methods. The effective parameters derived from pulse transmission experiments are fitted with Eq. (7.4), obtaining the collective spin-photon coupling $(G_N)_{1\,10}$ and decoherence rate $\gamma_{\perp,1\,10}$ associated to transition $1 \leftrightarrow 10$ coupled to LER 2. They are listed in table 7.3. The underestimation of $\tilde{\omega}_\mathrm{r}$ and $\tilde{\kappa}$ in pulse transmission measurements can be due to the fact that the precision of the model of an effective, broadened resonator works better for $(G_N)_{1\,10} \,/\, \gamma_{\perp,1\,10} \ll 1$ (here I find $0.1 < (G_N)_{1\,10} \,/\, \gamma_{\perp,1\,10} < 1$).

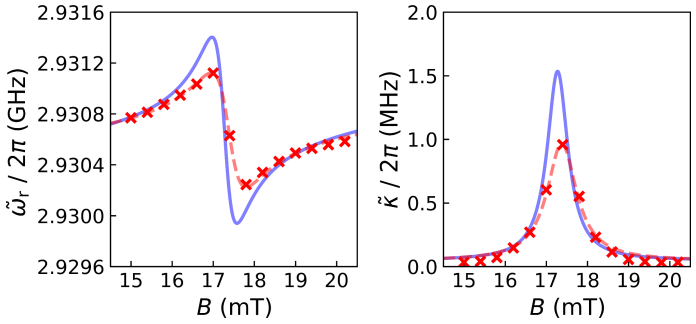

Figure 7.11: Effective resonance frequency $\tilde{\omega}_r$ and effective decay rate $\tilde{\kappa}$ of LER 2 coupled to the electronic spin transition $1 \leftrightarrow 10$, extracted from the pulse transmission experiments at 10 mK (red crosses). The red dashed lines are the fit of these effective parameters with Eq. (7.4). As a comparison, the blue solid line uses the parameters from the continuous wave experiment with this same equation.

LER 2, 5% [Yb(trensal)], pulse transmission	
ω_r / 2π (GHz)	$2.930673 \pm 8 \cdot 10^{-6}$
κ / 2π (kHz)	44 ± 12
$\lvert\kappa_c\rvert$ / 2π (kHz)	17 ± 3
ϕ_c (°)	35 ± 7
$(G_N)_{1\,10}$ / 2π (MHz)	4.3 ± 0.1
$\gamma_{\perp,1\,10}$ / 2π (MHz)	20.7 ± 1.0
$(G_N)_{1\,10}$ / $\gamma_{\perp,1\,10}$	0.211 ± 0.011
$C_{1\,10}$	21 ± 6

Table 7.3: Parameters of the fit of the effective resonance frequency $\tilde{\omega}_r$ and decay rate $\tilde{\kappa}$ of LER 2 coupled to the $1 \leftrightarrow 10$ transition with Eq. (7.4), obtained from pulse transmission experiments. The ratio $(G_N)_{1\,10}$ / $\gamma_{\perp,1\,10}$ and the cooperativity $C_{1\,10} = (G_N)^2_{1\,10}$ / $\kappa\gamma_{\perp,1\,10}$ are also shown.

7.3.2 Nuclear spin transitions

The transmission of 400 μs long pulses with driving frequencies $\omega_d = 2\pi f$ spanning the resonances of LERs 4 and 5 were measured at 10 mK for magnetic fields in the range of Figs. 7.8 and 7.9. Figure 7.12 shows the results for LER 4 coupled to the nuclear spin transition $1 \leftrightarrow 2$ at two magnetic fields, one at which the resonator is uncoupled from the transition (a) and one at which it is coupled (b). Similar pulse transmission experiments were carried out for LER 4 coupled to the $2 \leftrightarrow 3$ transition (Fig. 7.13), LER 5 coupled to $1 \leftrightarrow 2$ (Fig. 7.14), and LER 5 to the $2 \leftrightarrow 3$ (Fig. 7.15). As in electronic spin transitions, the nuclear spin-photon coupling influences both the frequency and width of the resonance and the decay times of the resonator.

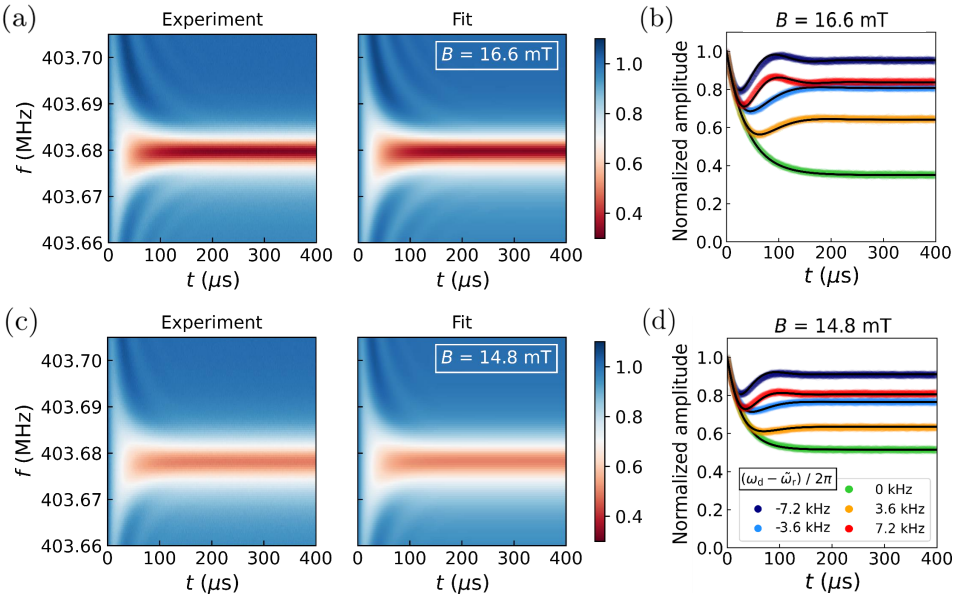

Figure 7.12: (a, c) Dynamics of LER 4 for two magnetic fields: 16.6 mT (a), showing the bare resonator, and 14.8 mT (c), where it is coupled to the $1 \leftrightarrow 2$ transition. (b, d) show cuts of Figs. (a, c) at various detunings between the driving frequency ω_d and the effective resonance frequency $\tilde{\omega}_\mathrm{r}$.

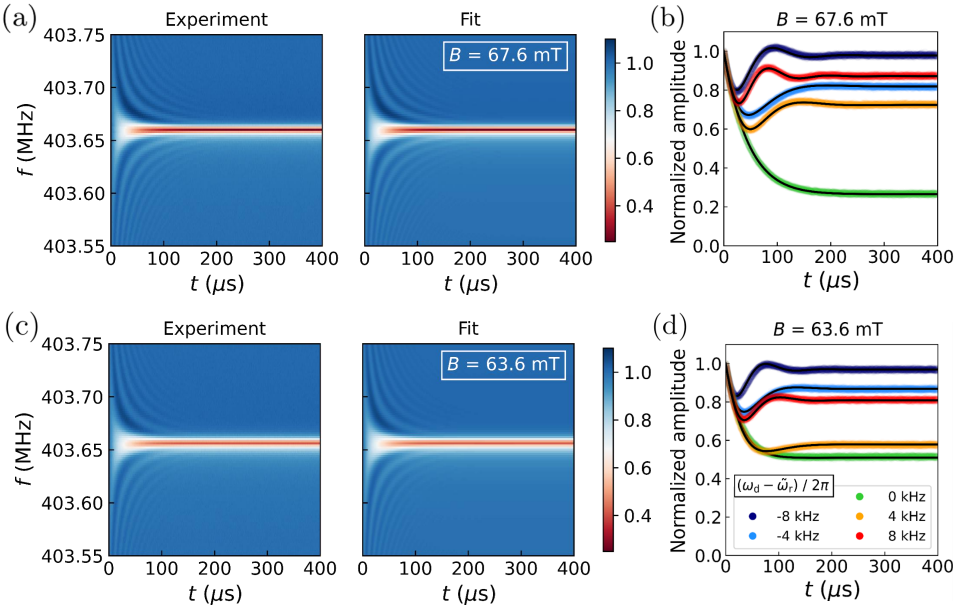

Figure 7.13: (a, c) Dynamics of LER 4 for two magnetic fields: 67.6 mT (a), showing the bare resonator, and 63.6 mT (c), where it is coupled to the $2 \leftrightarrow 3$ transition. (b, d) show cuts of Figs. (a, c) at various detunings between the driving frequency ω_d and the effective resonance frequency $\tilde{\omega}_\mathrm{r}$.

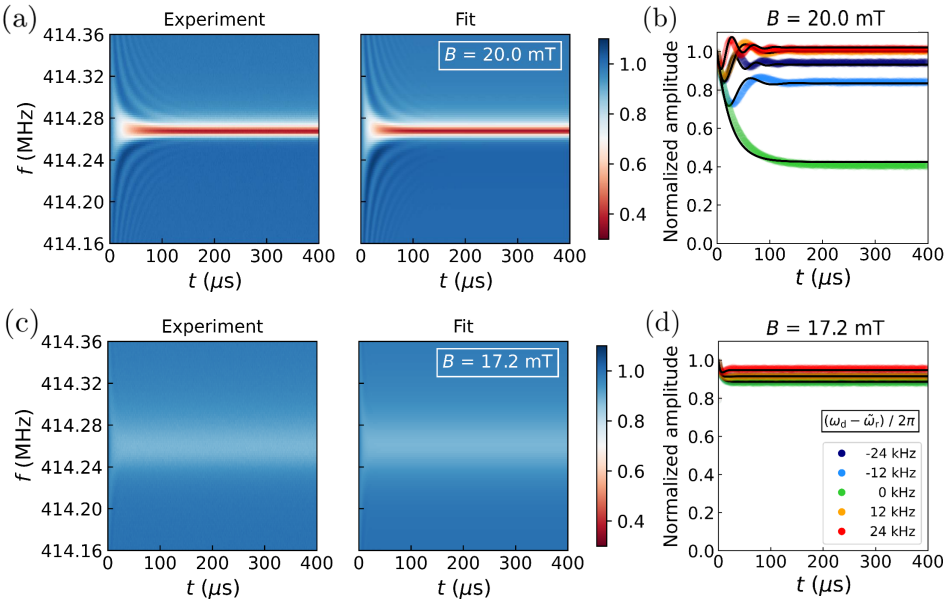

Figure 7.14: (a, c) Dynamics of LER 5 for two magnetic fields: 20.0 mT (a), showing the bare resonator, and 17.2 mT (c), where it is coupled to the $1 \leftrightarrow 2$ transition. (b, d) show cuts of Figs. (a, c) at various detunings between the driving frequency ω_d and the effective resonance frequency $\tilde{\omega}_\mathrm{r}$.

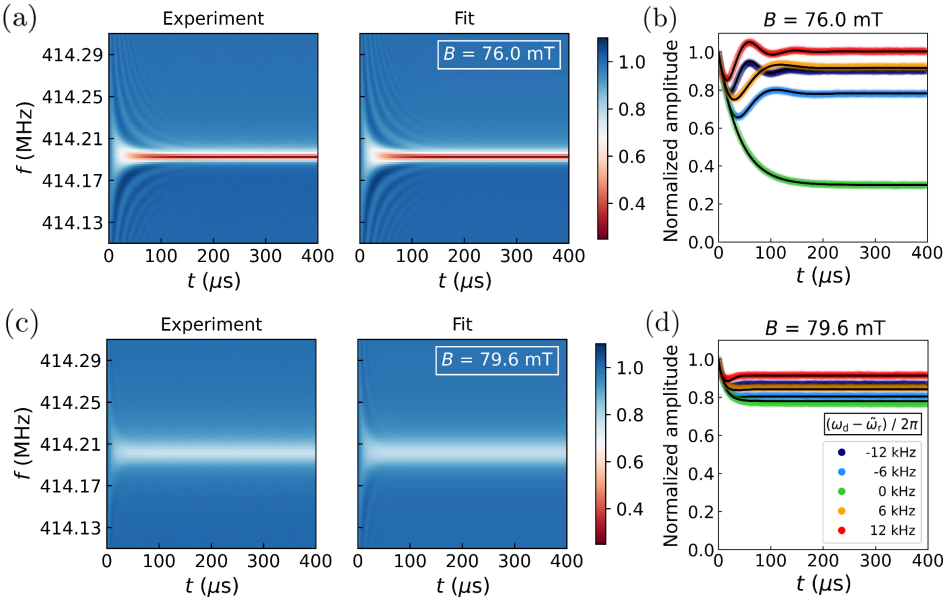

Figure 7.15: (a, c) Dynamics of LER 5 for two magnetic fields: 76.0 mT (a), showing the bare resonator, and 79.6 mT (c), where it is coupled to the $2 \leftrightarrow 3$ transition. (b, d) show cuts of Figs. (a, c) at various detunings between the driving frequency ω_d and the effective resonance frequency $\tilde{\omega}_\mathrm{r}$.

The nuclear spin-photon coupling is also in the weak regime, and the experiments can be fitted with the model of a broadened resonator shown above in Eq. (7.5). The resulting $\tilde{\omega}_\mathrm{r}$ and $\tilde{\kappa}$ are shown in Fig. 7.16, along with their fit with Eq. (7.4). Table 7.4 reports the collective spin-photon coupling $(G_N)_{\alpha\beta}$ and spin decoherence rate $\gamma_{\perp,\alpha\beta}$ of transitions $1 \leftrightarrow 2$ ($\alpha = 1$, $\beta = 2$) and $2 \leftrightarrow 3$ ($\alpha = 2$, $\beta = 3$) for LERs 4 and 5. Figure 7.16 also compares these values with those obtained from continuous wave experiments (see section 7.2.2).

LER 4, 2% [Yb(trensal)], pulse transmission

Transition (temperature)	$1 \leftrightarrow 2$ (10 mK)	$2 \leftrightarrow 3$ (10 mK)
$(G_N)_{\alpha\beta}$ / 2π (kHz)	67 ± 6	29 ± 9
$\gamma_{\perp,\alpha\beta}$ / 2π (MHz)	3.0 ± 0.4	0.8 ± 0.4
$(G_N)_{\alpha\beta}$ / $\gamma_{\perp,\alpha\beta}$	0.022 ± 0.004	0.035 ± 0.022
$C_{\alpha\beta}$	0.39 ± 0.09	0.30 ± 0.24

LER 5, 8% [Yb(trensal)], pulse transmission

Transition (temperature)	$1 \leftrightarrow 2$ (10 mK)	$2 \leftrightarrow 3$ (10 mK)
$(G_N)_{\alpha\beta}$ / 2π (kHz)	244 ± 17	62 ± 9
$\gamma_{\perp,\alpha\beta}$ / 2π (MHz)	2.5 ± 0.3	0.4 ± 0.1
$(G_N)_{\alpha\beta}$ / $\gamma_{\perp,\alpha\beta}$	0.097 ± 0.015	0.16 ± 0.05
$C_{\alpha\beta}$	4.4 ± 1.1	2.7 ± 1.3

Table 7.4: Collective spin-photon coupling $(G_N)_{\alpha\beta}$ of LERs 4 and 5 to transitions $1 \leftrightarrow 2$ ($\alpha = 1$, $\beta = 2$) and $2 \leftrightarrow 3$ ($\alpha = 2$, $\beta = 3$), with spin decoherence rates $\gamma_{\perp,\alpha\beta}$, obtained from pulse transmission experiments. The difference in population in equilibrium, $(\Delta P)_{\mathrm{e},\,\alpha\beta}$, is included here in $(G_N)_{\alpha\beta}$: $(G_N)_{\alpha\beta} \propto \sqrt{(\Delta P)_{\mathrm{e},\,\alpha\beta}}$. These are the fit parameters for the values of $\tilde{\omega}_\mathrm{r}$ and $\tilde{\kappa}$ in Fig. 7.16 (solid and dashed lines).

Overall, there is a good agreement between the collective couplings and decoherence rates obtained with continuous wave and pulse transmission experiments, confirming the high cooperativity regime of LERs coupled to nuclear transitions in [^{173}Yb(trensal)]. The main difference between the two techniques is that the resonator frequency ω_r in pulse experiments is a few kHz above that observed in continuous measurements. There is also a jump in $\tilde{\omega}_\mathrm{r}$ in Fig. 7.16a, which I attribute to a sudden change in ω_r due to the formation of vortices in the superconducting material as the magnetic field is swept [13]. These jumps are also visible in the field sweeps of Figs. 7.7c and 7.7d (in addition to the coupling to other transitions in [Yb(trensal)]).

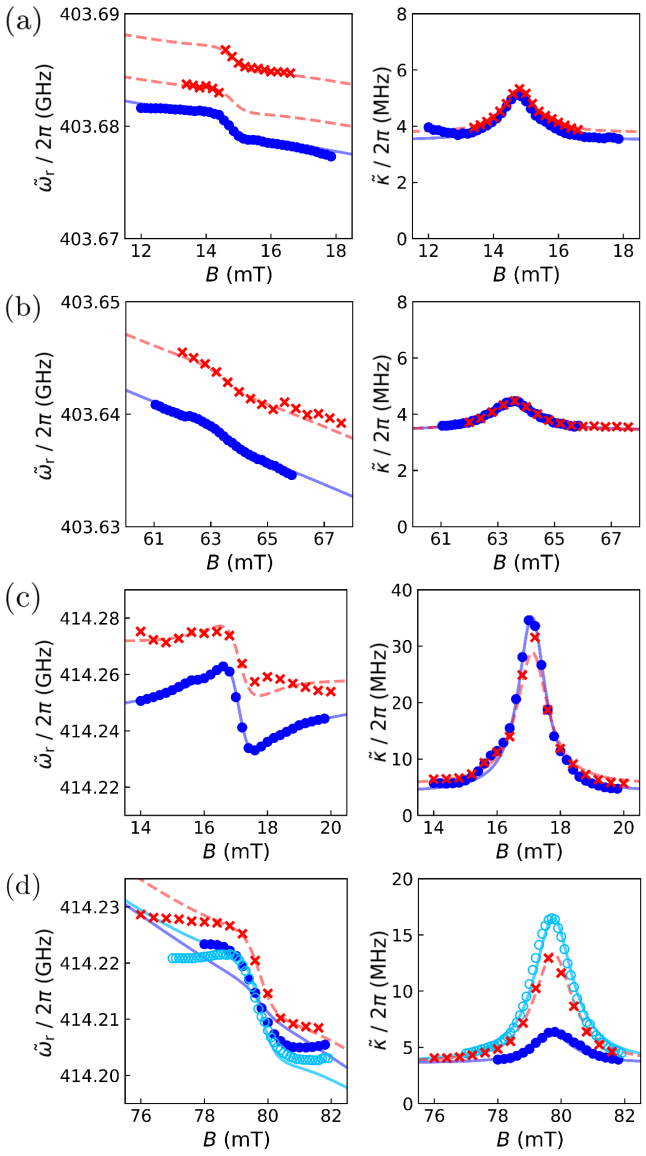

Figure 7.16: Effective resonance frequency $\tilde{\omega}_r$ and effective decay rate $\tilde{\kappa}$ of LER 4 coupled to nuclear spin transitions $1 \leftrightarrow 2$ (a) and $2 \leftrightarrow 3$ (b), and of LER 5 coupled to these same transitions (c, d). Blue dots are the fit parameters from continuous wave experiments at 10 mK, while red crosses are the fit parameters from pulse transmission experiments at this same temperature. The solid blue lines and red dashed lines are fits of these parameters based on Eq. (7.4). The continuous wave measurement of LER 5 coupled to the $2 \leftrightarrow 3$ transition was repeated at 50 mK. The fit parameters of this measurement are the cyan dots in (d), with the cyan solid line being their fit to Eq. (7.4).

These results show that the decay rate of the resonator is maximum when-

ever the photons are hybridized with the nuclear spins states. Besides, the characteristic ensemble coherence time $(T_2^*)_{\alpha\beta} = 1/\gamma_{\perp,\alpha\beta}$ obtained near resonance is about ten times higher for nuclear spin transitions than for electronic ones, and agrees well with the value derived from continuous wave measurements. This enhanced coherence compensates for the lower spin-photon coupling of nuclear spin transitions: $(G_N)_{\alpha\beta}(T_2^*)_{\alpha\beta} = (G_N)_{\alpha\beta}/\gamma_{\perp,\alpha\beta} \sim 0.1$–$0.2$ is achieved for both electronic and nuclear spin transitions.

7.4 Pump-probe experiments with isotopically purified samples

In pump-probe experiments, the coupling of photons in both the transmission line and the resonator to transitions in [^{173}Yb(trensal)] must be as large as possible, as they limit how fast the qudit state can be operated and read out. For this, the experimental setup in the previous section may be not enough. A large gap of ~ 50 μm between the chip surface and the [Yb(trensal)] crystals is reported [4]. This means that the spins do not couple to the mode volume just above the inductor or the transmission line, where the microwave magnetic field is strongest. Furthermore, the number of [Yb(trensal)] molecules is reduced by diluting them in a diamagnetic matrix, and of these only a 16% has ^{173}Yb in a crystal with natural isotopical abundances.

Several improvements were carried out for the next experiments. A new chip, *Yb-pulsed* (Fig. 7.3b), was used instead of *Yb-cw*. The low-inductance design of LERs in *Yb-pulses* enhances the microwave magnetic field close to the inductor, which now is just a narrow superconducting strip close to the transmission line. The mode volume of the LER is much smaller than before. Microscopic ($V \sim 10^{-13}$ m^3) [Yb(trensal)] crystals were placed by David Rodríguez (CAB, Madrid) on top of the inductor of LERs in *Yb-pulses* using a micro-manipulator. The crystal size matches the mode volume (see Fig. 7.17). Besides, these crystals were synthesized with isotopically purified ^{173}Yb, optimizing the number of [^{173}Yb(trensal)] molecules close to the inductor. The crystals have a 5% of [^{173}Yb(trensal)] molecules in a diamagnetic [Lu(trensal)] matrix. This section describes the experiments aimed at measuring the spin-photon couplings to the different electronic spin transitions in these crystals, and at performing the first attempts to dispersively read out the spin states.

7.4.1 Characterization of electronic spin transitions

The resonators in *Yb-pulsed* are designed to couple to the six allowed electronic transitions of [^{173}Yb(trensal)] (see Fig. 7.2c). In order to characterize the col-

lective spin-photon coupling of the six transitions, the transmission of the chip for driving frequencies close to the resonance frequency of LER 6 was measured for magnetic fields between 0 an 105 mT and at six different temperatures: 11, 25, 50, 100, 150 and 250 mK.

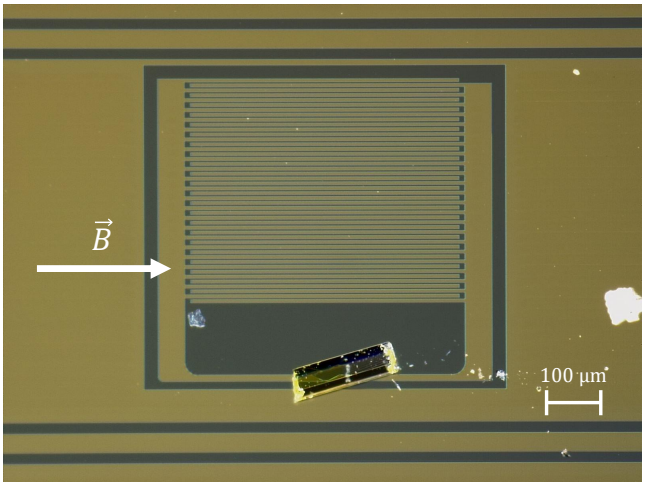

Figure 7.17: [Yb(trensal)] crystal on top of the inductor of LER 3 of *Yb-pulsed*. The crystal size matches the inductor size. The magnetic field $\boldsymbol{B}$ was applied parallel to the the inductor and transmission lines.

Figure 7.18 shows the results of these experiments. Six clear features in the resonance of LER 6 are observed, corresponding to the coupling of the resonator to the six electronic spin transitions (one for each nuclear spin projection $m_S = -5/2$, $-3/2$, $-1/2$, $+1/2$, $+3/2$ and $+5/2$). These couplings happen approximately at $B_{\text{res}} = 23.4$, 35.0, 48.7, 64.4, 82.0 and 101.0 mT. As temperature increases, the effect of the couplings on the resonance of LER 6 is less prominent, as it is expected from the decrease in the population difference between the low energy ($m_S = -1/2$) and high energy ($m_S = +1/2$) subsets of spin states. The highest measured temperature, 250 mK, is of the same order as the energy difference (in temperature units) between the subsets up to ∼100 mT, see Fig. 7.2a)).

Close-ups of the measurement at 11 mK around these fields are shown in Fig. 7.19. The maximum collective spin-photon coupling at 11 mK, $G_N/2\pi \simeq 12.3$ MHz, is obtained for $m_I = -5/2$. This corresponds to the $0 \leftrightarrow 11$ transition between the ground state and the highest excited state, that is, the transition with the largest population difference in thermal equilibrium. For higher m_I, the electronic spin transitions are between excited states. The fact that a change in the coupling is observed means that the temperature of the system is low enough to generate significant population differences between

the nuclear states in each of the two subsets with $m_S = \pm 1/2$. This condition holds for temperatures below 100 mK (see Fig. 7.2a).

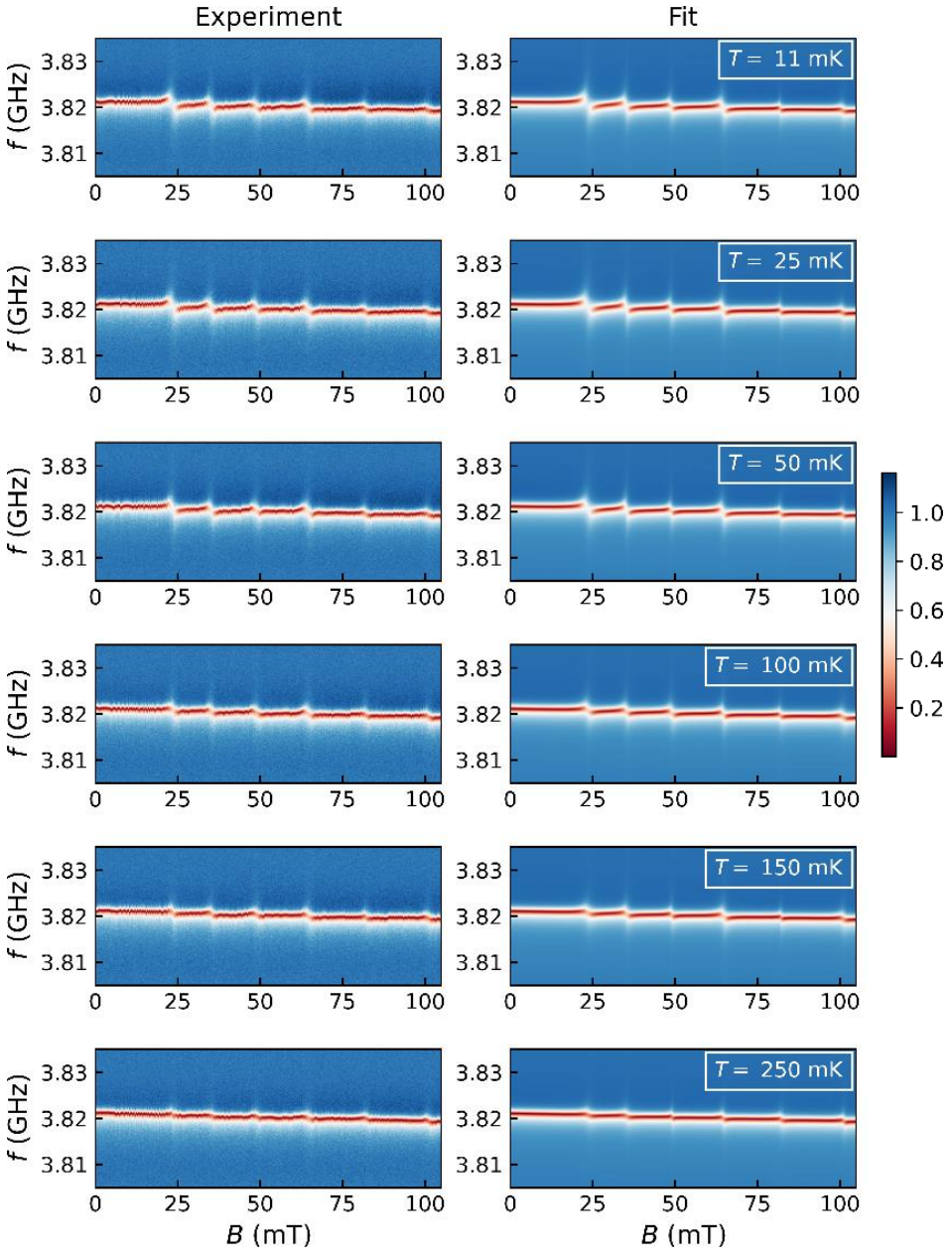

Figure 7.18: Normalized transmission of *Yb-pulsed* for driving frequencies close to the resonance frequency of LER 6, measured for magnetic fields between 0 an 105 mT at six different temperatures: 11 mK, 25 mK, 50 mK, 100 mK, 150 mK and 250 mK. Experimental data is compared to the fit of the coupling of LER 6 to the six electronic spin transitions of [^{173}Yb(trensal)] with Eq. (7.3).

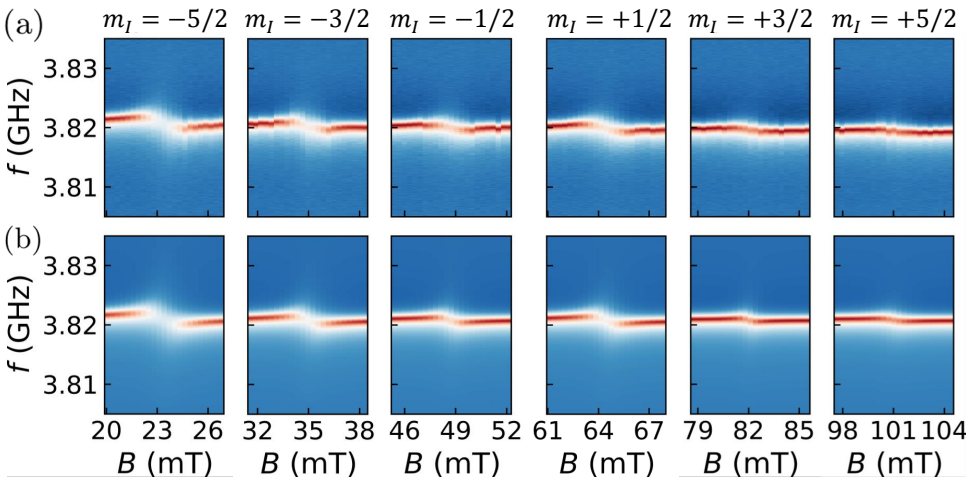

Figure 7.19: Close up of the experimental (a) and simulated (b) transmission of *Yb-pulsed* around each field where LER 6 resonates with an electronic spin transition (B_{res} = 23.4, 35.0, 48.7, 64.4, 82.0 and 101.0 mT) associated to a different nuclear spin projection m_I, measured at T = 11 mK.

The experimental maps in Figs. 7.18 and 7.19 were fitted with the transmission of the resonator coupled to each of the electronic spin transitions, given by Eq. (7.3). The same LER parameters were used to fit the coupling to all transitions: $\omega_{\mathrm{r}} = 3.821314 \pm 1.6 \cdot 10^{-5}$ GHz, $|\kappa_{\mathrm{c}}| \simeq \kappa = 1.04 \pm 0.03$ MHz, $\phi_{\mathrm{c}} = 15.9° \pm 0.7°$, with a small drift of ω_{r} with magnetic field (-15.6 ± 0.3 MHz / T).

Figures 7.20a-b show the temperature dependence of the collective spin-photon coupling $(G_N)_{\alpha\beta}$ and the decoherence rate $\gamma_{\perp,\alpha\beta}$ associated to each electronic spin transition. The collective spin-photon coupling is not much higher that the one obtained for transition $1 \leftrightarrow 10$ ($m_I = -3/2$) in sections 7.2.1 and 7.3.1. Note, however, that the isotopically purified crystals are much smaller ($V \sim 10^{-13}$ m^3, , 10^{13}–10^{14} [^{173}Yb(trensal)] molecules) than those with natural abundances ($V \sim 10^{-10}$ m^3, 10^{15}–10^{16} [^{173}Yb(trensal)] molecules): Fig. 7.17 shows how the former fit in the resonator inductor line. Therefore, a similar collective spin-photon coupling is achieved with a smaller number of spins thanks to having the microwave field generated by the resonator localized in a volume around the inductor matching the crystal size.

The inhomogeneous broadenings $\gamma_{\perp,\alpha\beta}$ derived from these experiments are significantly higher than in crystals with natural abundances [4]. In the latter, [^{173}Yb(trensal)] molecules were both diamagnetically diluted in a [Lu(trensal)] matrix and isotopically diluted by their natural abundance. Most Yb nuclei have zero nuclear spin ($I = 0$), which leads to a distinct different energy spectrum from that of [^{173}Yb(trensal)], where the large hyperfine coupling plays

an import role. This can hinder the exchange of spin excitations between [^{173}Yb(trensal)] and other [Yb(trensal)] molecules with $I = 0$. In the isotopically purified crystals, however, the density of [^{173}Yb(trensal)] molecules is higher, which have identical spin excitations. This might lead to the observed broadening.

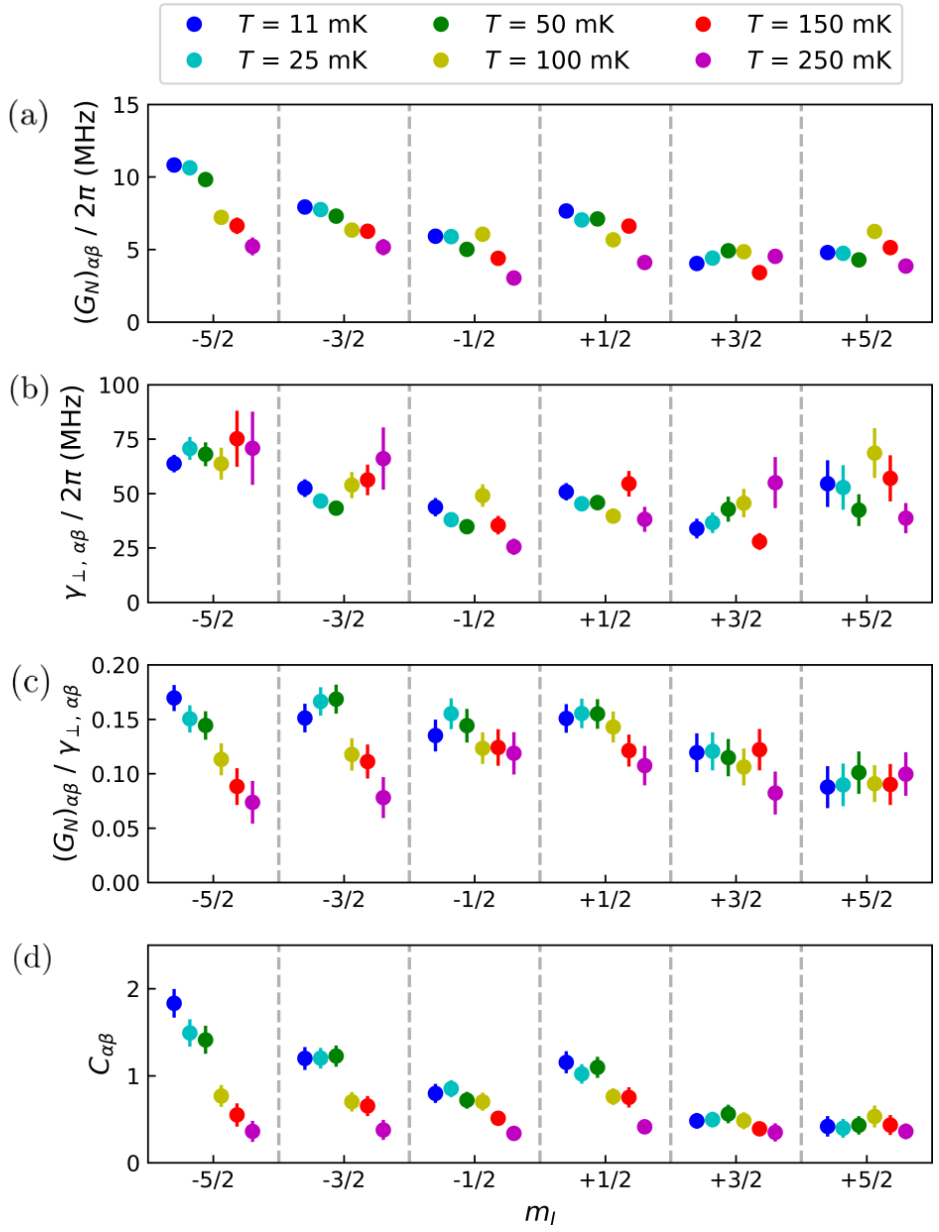

Figure 7.20: Collective spin photon coupling $(G_N)_{\alpha\beta}$ (a), decoherence rate $\gamma_{\perp,\alpha\beta}$ (b), $(G_N)_{\alpha\beta}/\gamma_{\perp,\alpha\beta}$ ratio (c) and cooperativity $C_{\alpha\beta} = (G_N)^2_{\alpha\beta}/\kappa\gamma_{\perp,\alpha\beta}$ for each electronic spin transition in [^{173}Yb(trensal)] at 11, 25, 50, 100, 150 and 250 mK.

The couplings of all six electronic spin transitions to LER 6 are in the weak coupling regime, while high cooperativity is achieved for the $0 \leftrightarrow 11$ ($m_I = -5/2$) and $1 \leftrightarrow 10$ ($m_I = -3/2$) transitions below 100 mK (see Figs. 7.20c-d). Again, these values have been obtained with a number of spins much smaller than in previous sections and in spite of the larger $\gamma_{\perp,\alpha\beta}$ values.

7.4.2 Dispersive readout in an electro-nuclear qudit

The theory of a hybrid qudit-resonator system in the dispersive regime is detailed in section 3.4.3. In the case of the electro-nuclear qudit encoded in [^{173}Yb(trensal)], with $d = 12$ states, the shift in the resonator frequency is:

$$\omega_{\mathrm{r}} \rightarrow \omega_{\mathrm{r}} + \sum_{\alpha=0}^{11} \chi'_{\alpha} \langle \hat{X}^{\alpha,\alpha} \rangle, \tag{7.6}$$

where $\langle \hat{X}^{\alpha,\alpha} \rangle$ is the expectation value of the Hubbard operator $\hat{X}^{\alpha,\alpha}$ associated to each state $|\alpha\rangle$, with a dispersive shift:

$$\chi'_{\alpha} := \sum_{\beta \neq \alpha} \frac{|\Lambda_{\alpha\beta}|^2}{\Delta'_{\alpha\beta}}. \tag{7.7}$$

Here $\Delta'_{\alpha\beta}$ is a modified detuning, related to the actual detuning $\Delta_{\alpha\beta} = \omega_{\alpha\beta} - \omega_{\mathrm{r}}$ between the frequency of transition $\alpha \leftrightarrow \beta$ and the resonator frequency ω_{r} by:

$$\Delta'_{\alpha\beta} := \frac{1 + \dfrac{\Delta_{\alpha\beta}}{2\omega_{\mathrm{r}}}}{1 + \dfrac{\Delta_{\alpha\beta}}{\omega_{\mathrm{r}}}}. \tag{7.8}$$

The resonators in *Yb-pulsed* are tuned to the electronic spin transitions. This means that the detuning between ω_{r} and the electronic spin transitions is much smaller than that between ω_{r} and the nuclear spin transitions. In addition, sections 7.2 and 7.3 showed how the collective coupling of nuclear spin transitions to the resonator is at least one order of magnitude smaller than with electronic spin transitions. This means that the dominant contribution to the dispersive shift is the one associated to electronic spin transitions, and Eq. (7.6) can be approximated by:

$$\omega_{\mathrm{r}} \rightarrow \omega_{\mathrm{r}} + |\Lambda_{\mathrm{el}}|^2 \sum_{\alpha=0}^{5} \left(\frac{\langle \hat{X}^{\alpha,\alpha} \rangle}{\Delta'_{\alpha,11-\alpha}} + \frac{\langle \hat{X}^{11-\alpha,11-\alpha} \rangle}{\Delta'_{11-\alpha,\alpha}} \right), \tag{7.9}$$

where Λ_{el} is the coupling of the resonator to the electronic spin transitions.

In an ensemble of [^{173}Yb(trensal)] molecules at very low temperatures, the populations of the states in the high energy subset ($\langle \hat{X}^{11-\alpha,\alpha} \rangle_{\rm e}$) in thermal equilibrium can be neglected. Then, the reference frequency $\omega_{\rm ref}$ for pump-probe experiments is:

$$\omega_{\rm ref} := \omega_{\rm r} + |\Lambda_{\rm el}|^2 \sum_{\alpha=0}^{5} \frac{\langle \hat{X}^{\alpha,\alpha} \rangle_{\rm e}}{\Delta'_{\alpha,11-\alpha}}. \tag{7.10}$$

There are two types of pump-probe experiments that can be performed in this setup, depending on whether the electronic spin transitions or the nuclear spin transitions are driven (see Fig. 7.21). The simplest experiment consists on pumping at the frequency of one of the electronic spin transitions, say $\beta \leftrightarrow 11-\beta$, as if it were the transition between the two states of a qubit, then measuring the resonator coupled to that same transition. The shift $\delta\omega_{\rm r}$ from $\omega_{\rm ref}$ after pumping at the frequency $\omega_{\beta,11-\beta}$ of the $\beta \leftrightarrow 11-\beta$ transition is:

$$\begin{aligned} \delta\omega_{\rm r} =& |\Lambda_{\rm el}|^2 \left(\frac{\langle \hat{X}^{\beta,\beta} \rangle - \langle \hat{X}^{\beta,\beta} \rangle_{\rm e}}{\Delta'_{\beta,11-\beta}} + \frac{\langle \hat{X}^{11-\beta,11-\beta} \rangle}{\Delta'_{11-\beta,\beta}} \right) \\ \simeq& \frac{|\Lambda_{\rm el}|^2}{\Delta_{11-\beta,\beta}} \left[\langle \hat{X}^{\beta,\beta} \rangle_{\rm e} + \left(\langle \hat{X}^{11-\beta,11-\beta} \rangle - \langle \hat{X}^{\beta,\beta} \rangle \right) \right]. \end{aligned} \tag{7.11}$$

In the last step, the modified detuning $\Delta'_{11-\beta,\beta}$ was approximated to $\Delta_{11-\beta,\beta}$, and $\Delta'_{\beta,11-\beta}$ to $-\Delta_{11-\beta,\beta}$. This is valid if the transition frequency $\omega_{\beta,11-\beta}$ of the $\beta \leftrightarrow 11-\beta$ transition is set close enough to $\omega_{\rm r}$ ($|\Delta_{11-\beta,\beta}| \ll \omega_{\rm r}$), while still being in the dispersive regime ($|\Delta_{11-\beta,\beta}| \gg |\Lambda_{\rm el}|$).

This experiment, sketched in Fig. 7.21b, is similar to the experiments that were carried out in the previous chapter with molecular spin qubits. The difference $\langle \hat{X}^{11-\beta,11-\beta} \rangle - \langle \hat{X}^{\beta,\beta} \rangle$ plays the role of $\langle \hat{\sigma}_z \rangle \equiv \langle \hat{X}^{1,1} \rangle - \langle \hat{X}^{0,0} \rangle$ in a qubit. The constant $\langle \hat{X}^{\beta,\beta} \rangle_{\rm e}$ includes the effect of an incomplete initialization to the ground state if the different nuclear spin states in the subset with $m_S = -1/2$ are slightly populated by temperature.

The other type of pump-probe experiments involves controlling the nuclear state by driving the nuclear spin transitions, with the magnetic field set at a value where the LER resonance frequency $\omega_{\rm r}$ sits in between the electronic spin transitions associated to the different m_I states (see Fig. 7.21c). This is the method that is proposed to read the nuclear spin qudit state coupled to an electronic spin ancilla [14].

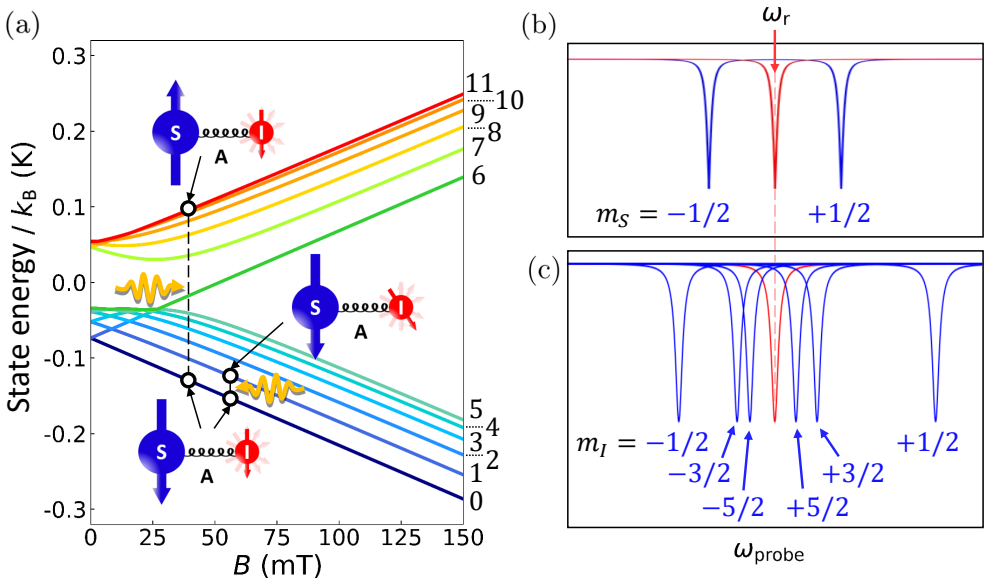

Figure 7.21: (a) The two types of pump-probe measurement are associated to whether electronic spin or nuclear spin transitions are driven with the pump pulse. (b) If an electronic spin transition is set close to ω_r with magnetic field while keeping the spin-LER system in the dispersive regime, the dispersive shift of ω_r depends on the state of the electronic spin (blue solid lines). The electronic spin state can be changed by driving the electronic spin transition. In this case, a transition frequency above ω_r is assumed (positive detuning). As reference, the red solid line is the resonance of the uncoupled resonator. (c) Another type of pump-probe experiment involves the control of the nuclear spin states. The resonance of the uncoupled resonator (red solid line) is shifted differently depending on the nuclear spin state (blue solid lines). The magnetic field is chosen to have the electronic spin transitions associated to a negative m_I above ω_r and those associated to a positive m_I below ω_r.

The shift $\delta\omega_r$ after pumping the nuclear transition $\beta \leftrightarrow \gamma$ is:

$$\delta\omega_r = |\Lambda_{el}|^2 \left(\frac{\langle \hat{X}^{\beta,\beta} \rangle - \langle \hat{X}^{\beta,\beta} \rangle_e}{\Delta'_{\beta,11-\beta}} + \frac{\langle \hat{X}^{\gamma,\gamma} \rangle - \langle \hat{X}^{\gamma,\gamma} \rangle_e}{\Delta'_{\gamma,11-\gamma}} \right), \tag{7.12}$$

which depends on the difference in population between nuclear states induced by pulses. Measuring this shift requires a good initialization of the system by lowering the temperature in order to see an appreciable change in $\delta\omega_r$. Here the modified detunings can not be approximated by $\Delta_{\beta,11-\beta}$ and $\Delta_{\gamma,11-\gamma}$, as in general it is not possible to simultaneously set both associated electronic spin transition frequencies $\omega_{\beta,11-\beta}$ and $\omega_{\gamma,11-\gamma}$ close to ω_r.

7.4.3 First pump-probe experiments

The first pump-probe experiments were carried out pumping the $0 \leftrightarrow 11$ electronic spin transition, which has the largest population difference in the system in thermal equilibrium. Thus, this transition provides the closest analogue of the pump-probe experiments with qubits. The magnetic field was set to 25.5 mT, which places the $0 \leftrightarrow 11$ transition frequency 123 MHz above the resonance frequency ω_r of LER 6 (see Fig. 7.22). This value was chosen to be ten times the coupling obtained for this transition at 11 mK, $(G_N)_{0,11} = 12.3$ MHz, so that the dispersive regime condition $|\Delta_{0,11}| \gg (G_N)_{0,11}$ is fulfilled.

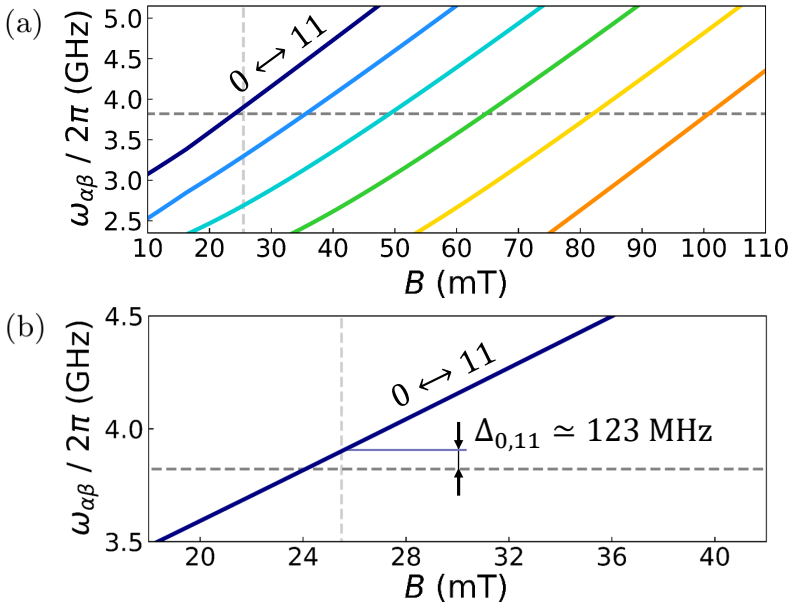

Figure 7.22: (a) Electronic spin transitions in [^{173}Yb(trensal)]. The horizontal dashed line marks the resonance frequency ω_r of LER 6, while the vertical line marks the magnetic field, $B = 25.5$ mT, at which pump-probe experiments were carried out. (b) Close-up of the range of magnetic fields for which the $0 \leftrightarrow 11$ transition frequency is close to ω_r. At $B = 25.5$ mT, the detuning between the transition frequency and ω_r is $\Delta_{0,11} = 123$ mT.

Pump pulses with lengths up to 500 μs were sent at the frequency of the $0 \leftrightarrow 11$ electronic spin transition at 25 mT. Figure 7.23 shows the resonance measured after the longest pump pulse was applied, compared to the reference. The shift $\delta\omega_r$ between the two is small compared to what was expected ($\delta\omega_r \sim (G_N)^2_{0,11}/\Delta_{0,11} \sim (G_N)_{0,11}/10 \sim 1$ MHz), and it is detected only for very long pulses. Note that this was obtained with a non-attenuated excitation line, so this is not due to input power limitation as in the first pump-pulse experiments with PTM$_r$.

The main difference between these experiments and those in the previous chapter is how the sample is interfaced with the superconducting chip. PTM_r/PS deposits were directly on top of the resonator, in particular its inductor. This produced high spin-photon couplings in a small set of PTM_r spins, which were responsible for most of the shift $\delta\omega_r$. Here, [^{173}Yb(trensal)] samples were crystals, which are susceptible to a small chip-sample gap due to any irregularities in the sample surface. The subsequent loss of the spins that would have the highest spin-photon couplings is probably the main limitation for producing a higher shift $\delta\omega_r$.

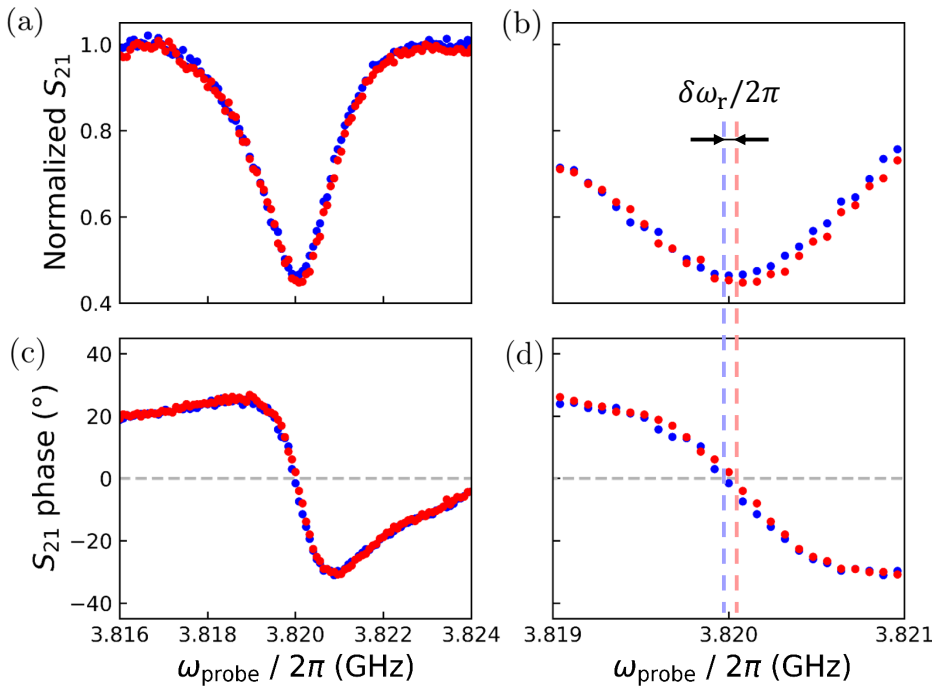

Figure 7.23: (a) Normalized module of the complex-valued transmission S_{21} of *Yb-pulsed* for probe frequencies close to the LER 6 resonance frequency ω_r, measured at $B = 25.5$ mT. Two situations are compared: red dots show the resonance after driving the $0 \leftrightarrow 11$ electronic spin transition, blue dots show the same resonance without any previous pump pulse. (b) Close-up centered at ω_r, showing the shift $\delta\omega_r$ of the center frequency of the resonance. Figures (c, d) illustrate more clearly this shift with the measurement of the phase of S_{21}.

7.5 Conclusions

High cooperativity has been observed in both electronic and nuclear transitions in [^{173}Yb(trensal)]. Reaching this regime the nuclear spin transitions was, a priori, much more demanding than with electronic ones due the very

small nuclear magnetic moment. Although the collective spin-photon couplings and cooperativities for nuclear spin transitions are indeed smaller than for electronic spin transitions in this same molecular system (about one order of magnitude), they are nevertheless remarkably high compared to the coupling of isolated nuclear spins to electromagnetic radiation, which would be three orders of magnitude lower ($\sim \mu_N/\mu_\mathrm{B}$) than for electronic spin transitions. The presence of the electronic spin, and its high hyperfine coupling to the nuclear spin, introduces an efficient path to couple nuclear spin transitions to the microwave magnetic field generated by the LER. Here the coupling is mediated by the *electronic* Zeeman interaction, which drives the nuclear transition due to the mixing of the electronic spin and nuclear spin wavefunctions through the hyperfine coupling. The lower coupling to nuclear spin transitions compared to electronic ones is compensated by their longer ensemble coherence times T_2^*. Thus, both nuclear and electronic spin transitions can be used in almost equal terms to define the states of a qudit. This opens prospects for QEC within a hybrid a circuit QED hybrid scheme.

The coupling of LERs to electronic spin and nuclear spin transitions was studied independently with continuous wave experiments and with pulse transmission, the latter unveiling the dynamics of the hybrid spin-LER system. The experimental results obtained with these two types of measurement are consistent with each other. This shows that the theory for the measurement of resonators coupled to molecular spins is not only valid in the driven steady state ($t \gg 1/\kappa, 1/\tilde{\kappa}$), but also for all the dynamics of the system.

Finally, additional experiments were carried out with isotopically purified [^{173}Yb(trensal)] crystals. The coupling of a resonator to the six electronic spin transitions was measured at different temperatures. The purification gives higher couplings to these transitions, but also increases their decoherence rate due to the higher concentration of ^{173}Yb nuclear spins ($I = 5/2$). The first pump-probe experiments with qudits were performed in these samples, giving a shift $\delta\omega_\mathrm{r}$ smaller than expected, which could be due to the presence of a sample-gap.

References

[1] E. Tancini, M. J. Rodriguez-Douton, L. Sorace, A.-L. Barra, R. Sessoli, and A. Cornia, Chemistry: A European Journal **16**, 10482 (2010).

[2] L. Vergnani, A.-L. Barra, P. Neugebauer, M. J. Rodriguez-Douton, R. Sessoli, L. Sorace, W. Wernsdorfer, and A. Cornia, Chemistry: A European Journal **18**, 3390 (2012).

[3] R. Hussain, G. Allodi, A. Chiesa, E. Garlatti, D. Mitcov, A. Konstantatos, K. S. Pedersen, R. D. Renzi, S. Piligkos, and S. Carretta, Journal of the American Chemical Society **140**, 9814 (2018).

[4] V. Rollano, M. C. de Ory, C. D. Buch, M. Rubín-Osanz, D. Zueco, C. Sánchez-Azqueta, A. Chiesa, D. Granados, S. Carretta, A. Gomez, et al., Communications Physics **5**, 246 (2022).

[5] M. Kanesato and T. Yokoyama, Chemistry Letters **28**, 137 (1999).

[6] P. V. Bernhardt, B. M. Flanagan, and M. J. Riley, Australian Journal of Chemistry **53**, 229 (2000).

[7] P. V. Bernhardt, B. M. Flanagan, and M. J. Riley, Australian Journal of Chemistry **54**, 229 (2001).

[8] B. M. Flanagan, P. V. Bernhardt, E. R. Krausz, S. R. Lüthi, and M. J. Riley, Inorganic Chemistry **41**, 5024 (2002).

[9] M. Chizzini, L. Crippa, L. Zaccardi, E. Macaluso, S. Carretta, A. Chiesa, and P. Santini, Physical Chemistry Chemical Physics **24**, 20030 (2022).

[10] J. A. Jones, V. Vedral, A. Ekert, and G. Castagnoli, Nature **403**, 869 (2000).

[11] L. M. K. Vandersypen, M. Steffen, G. Breyta, C. S. Yannoni, M. H. Sherwood, and I. L. Chuang, Nature **414**, 883 (2001).

[12] A. Blais, R.-S. Huang, A. Wallraff, S. M. Girvin, and R. J. Schoelkopf, Physical Review A **69**, 062320 (2004).

[13] D. Bothner, T. Gaber, M. Kemmler, D. Koelle, R. Kleiner, S. Wünsch, and M. Siegel, Physical Review B **86**, 014517 (2012).

[14] A. Gómez-León, F. Luis, and D. Zueco, Physical Review Applied **17**, 064030 (2022).

Chapter 8

Circuit QED beyond non-interacting magnetic molecules

The experiments in previous chapters were carried out with large ensembles of N magnetic molecules in order to enhance the ensemble-resonator coupling G_N, which scales with $\sqrt{N}$. Molecules were considered to be close to equivalent, and non-interacting, with the same effective spin Hamiltonian for each molecule. In this situation, the microwave magnetic field generated resonator couples to Dicke or Dicke-like states that are completely symmetric in the excitation of any of the N identical molecular spins.

As the temperature of the spin system is decreased, spin-spin interactions may play an important role on the physics of the ensemble. The question then arises of whether these intrinsic collective states affect the coupling to the circuit and, then, if this allows detecting the onset of magnetic correlations. Besides, the spin-photon coupling can be also seen as a source of correlations that eventually lead to a phase transition known as photon condensation [1]. It is therefore interesting to study the competition between these two interactions.

This chapter studies the effect of spin-spin interactions on transmission experiments performed with spin 1/2 and spin 1 ensembles. The step up from spin 1/2 to spin 1 is quite relevant. The two-fold energy degeneracy at zero magnetic field in a spin 1/2 can not be split by magnetic anisotropy (see section 3.1.2 from chapter 3), while in the spin 1 case its three spin states are non-degenerate in energy if there is some magnetic anisotropy in the ion. An additional competition is then expected between spin-spin interactions and magnetic anisotropy, which is not present in a spin 1/2.

8.1 Competition between spin-photon and spin-spin interactions in DPPH organic free radicals coupled to a superconducting transmission line

The collective character of the coupling of an ensemble of qubits to photons in a waveguide reflects itself in an enhanced superradiant emission of light and in the broadening of the absorption lines [2, 3]. The underlying mechanism is the light-mediated interaction among emitters, leading to the formation of collective spin states known as Dicke states [4, 5]. So far, the focus in waveguide QED (w-QED) has been mainly on non-interacting emitters, where all interactions occur through photons. Exploring the competition of this photon-mediated interactions and intrinsic spin-spin interactions in the material remains rather unexplored.

A sample of organic free radicals (DPPH) was chosen for this purpose. DPPH is a free radical with spin 1/2 and a g-factor $g_S = 2.004$ close to that of a free electron [6]. At low temperatures, it forms antiferromagnetic (AF) dimers and one-dimensional AF spin-chains. Figure 8.1a shows the increase of the spin-spin correlations (in absolute value) generated by the antiferromagnetic exchange interactions, as estimated from the magnetic susceptibility data in chapter 5.

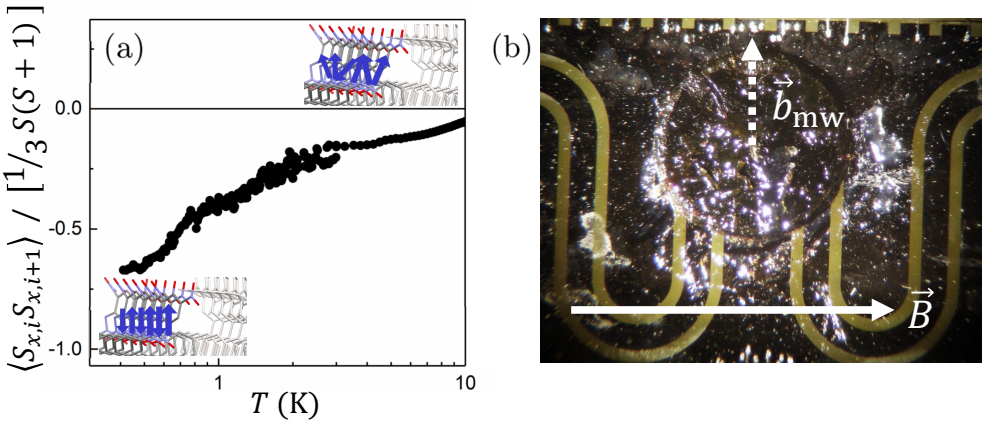

Figure 8.1: (a) Steady increase (in absolute value) in the spin-spin correlation $\langle S_{x,\,i}S_{x,\,i+1}\rangle$ between nearest neighbour type-B DPPH sites as temperature is lowered. The negative correlations reflect the formation of antiferromagnetic spin chains. They are computed from the dc-magnetic susceptibility of type-B DPPH molecules in Fig. 5.11, following the relation $\chi T/C \simeq 1 - |\langle S_{x,\,i}S_{x,\,i+1}\rangle/(1/3)\,[S(S+1)]\,|$ given in [7]. Here, C is the Curie constant of the type-B sublattice. (b) DPPH sample on top of a meandering transmission line. The static magnetic field $\boldsymbol{B}$ is applied horizontally. Only the top part of the sample, where the microwave magnetic field $\boldsymbol{b}_{\mathbf{mw}}$ generated by the line is perpendicular to $\boldsymbol{B}$, couples to the line.

A powder sample of DPPH was deposited on top of a superconducting coplanar waveguide (CPW) to measure how these correlations influence the interaction to photons travelling via the CPW (see Fig. 8.1b). The CPW was fabricated by optical lithography on a 100 nm thin film of Nb deposited on a crystalline sapphire wafer. The central line of the CPW had a width of 400 μm in order to match the sample size. The sample was glued to the CPW with apiezon grease, ensuring proper thermalization. The powder DPPH pellets used here for broadband transmission experiments are similar to the ones measured in chapter 5, where the full characterization of DPPH samples is detailed. The broadband nature of waveguides provides a distinct advantage over resonators, allowing the exploration of the transmission of DPPH in a wide range of frequencies [8–11] and the different phases of DPPH (paramagnetic / AF chains) within a single experiment. However, this advantage comes with the trade-off of a reduced sensitivity compared to that of a resonator ($(G_N)_{\text{line}} \ll G_N$).

8.1.1 Paramagnetic phase: spin-photon coupling enhancement

The broadband transmission of the CPW coupled to a DPPH powder sample was measured below 4.25 K. The device was thermally coupled to the mixing chamber of a 'wet' ^{3}He-^{4}He dilution refrigerator giving access to the temperature region between 130 mK and 4.2 K. Additional experiments were carried out with the dilution refrigerator described in section 2.2, which gives access to lower temperatures. Well above $T = 0.65$ K, half of the DPPH molecules are forming dimers with $S = 0$ (type-A DPPH, see section 5.2.2 in chapter 5), while the other half remain in the paramagnetic phase (type-B DPPH). Only the latter couple to the microwave magnetic field generated by the CPW.

Normalized transmission data, measured at 2 K from 10 MHz up to 14 GHz and for fields up to 500 mT are shown in Fig. 8.2a. A field-dependent resonant absorption of photons by the paramagnetic ensemble is observed, matching the transition frequency $\omega_{\text{q}} = \mu_{\text{B}} g_{\text{S}} B/\hbar$ of a spin $S = 1/2$ with $g_{\text{S}} = 2.004$. The transmission shows close to Lorentzian absorption minima. A nearly constant $\gamma_\perp \ / \ 2\pi \simeq 20$ MHz is measured at 2 K. The collective spin-photon coupling $G_N^{(\text{line})}$ increases with magnetic field B, and therefore also with frequency. This leads to a coupling visibility that also increases with B, as shown in Fig. 8.2b. These measurements were fitted using the theory for an ensemble of non-interacting spins 1/2 coupled to a transmission line (see section 4.5.3 in chapter 4):

$$S_{21}(\omega_{\text{d}}) = 1 - \frac{G_N^{(\text{line})}(\Delta P)_{\text{e}}}{i(\omega_{\text{q}} - \omega_{\text{d}}) + \gamma_\perp + G_N^{(\text{line})}(\Delta P)_{\text{e}}}, \tag{8.1}$$

where $G_N^{(\mathrm{line})}$ is the collective coupling of the spins to photons travelling via the line and $\gamma_\perp$ is the decoherence rate of the spin ensemble. In what follows, the population difference in thermal equilibrium, $(\Delta P)_\mathrm{e}$, between the down ($m_S = -1/2$) and up ($m_S = +1/2$) spin states is included in $G_N^{(\mathrm{line})}$: $G_N^{(\mathrm{line})} \propto (\Delta P)_\mathrm{e}$. This population difference alone encodes the temperature dependence of the intensity of the absorption signal in the paramagnetic phase:

$$(\Delta P)_\mathrm{e} := \tanh\left(\frac{\hbar\omega_\mathrm{q}}{2k_\mathrm{B}T}\right) = \tanh\left(\frac{\mu_\mathrm{B} g_\mathrm{S} B}{2k_\mathrm{B}T}\right). \tag{8.2}$$

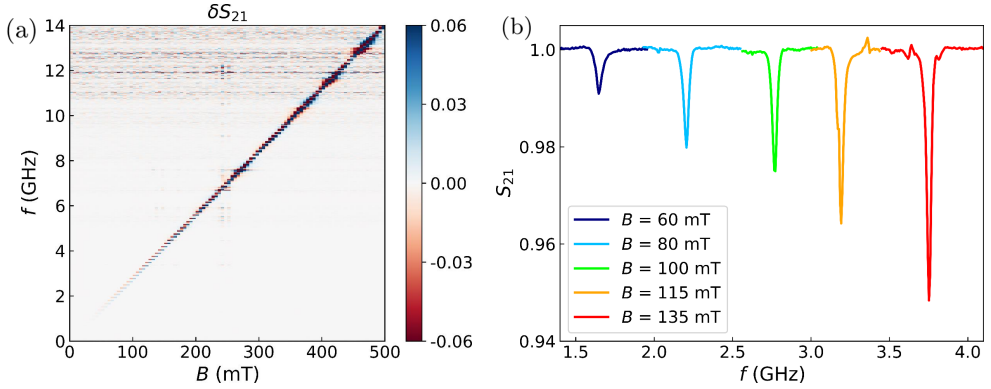

Figure 8.2: (a) Normalized transmission difference (δS_{21}) of a DPPH sample coupled to a transmission line at $T = 2$ K. This difference is computed at each field B as $\delta S_{21}(B) = [S_{21,\,\mathrm{exp}}(B) - S_{21,\,\mathrm{exp}}(B + \delta B)]\,/S_{21,\,\mathrm{exp}}(B + \delta B)$, effectively removing the baseline of the transmission signal. δB is a small field, but large enough so that the spin resonance signals at B and $B + \delta B$ do not overlap in frequency. A large increase in visibility is observed at some specific frequencies due to the coupling of spins to resonant modes in the transmission line. (b) Normalized transmission $S_{21} = 1 + \delta S_{21}$ at four selected fields, avoiding the coupling with resonant modes in the transmission line. The visibility of the resonance increases with frequency, as expected for the spin-photon coupling with a one-dimensional waveguide.

Figure 8.3 shows the field and temperature dependence of $G_N^{(\mathrm{line})}$ and $\gamma_\perp$. $G_N^{(\mathrm{line})}$ is proportional to the spectral density $J(\omega_\mathrm{d})$, which in turn is proportional to the input frequency $\omega_\mathrm{d} = 2\pi f$ in a one-dimensional waveguide (Ohmic bath). Close to the spin resonance ($\omega_\mathrm{d} \simeq \omega_\mathrm{q}$), and $G_N^{(\mathrm{line})}$ can be written as:

$$G_N^{(\mathrm{line})} := \alpha\omega_\mathrm{q}(\Delta P)_\mathrm{e} = \alpha\frac{\mu_\mathrm{B} g_\mathrm{S} B}{\hbar}\tanh\left(\frac{\mu_\mathrm{B} g_\mathrm{S} B}{2k_\mathrm{B}T}\right), \tag{8.3}$$

where α is a temperature-independent and field-independent dimensionless scaling factor. $\alpha = 0.00441 \pm 6 \cdot 10^{-5}$ is the only free parameter in the fit of $G_N^{(\mathrm{line})}$ in Fig. 8.3.

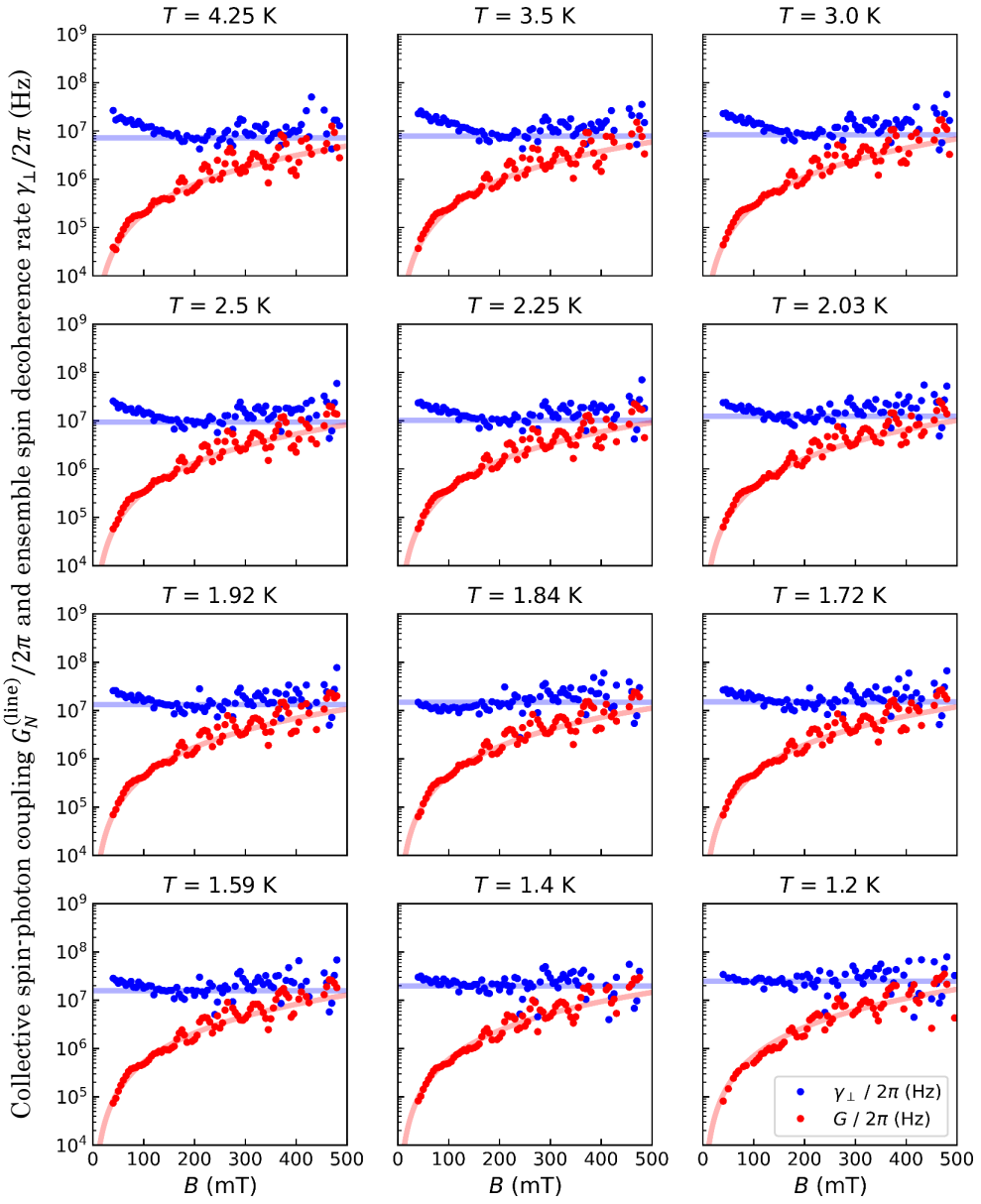

Figure 8.3: Magnetic field dependence of $G_N^{(\mathrm{line})}$ and $\gamma_\perp$ for several temperatures in the paramagnetic phase. Experimental values are shown as dots. The solid blue line is the average $\gamma_\perp$ at intermediate fields. The solid red line is the fit of $G_N^{(\mathrm{line})}$ to Eq. (8.3), with only α as a free parameter to fit all temperatures. Oscillations with magnetic field (and therefore frequency) in the the experimental $G_N^{(\mathrm{line})}$ values are associated to modes in the waveguide.

The coupling enhancement by $N_{\mathrm{eff}} = N(\Delta P)_{\mathrm{e}}$, where N is the number of spins in the DPPH sample coupled to the microwave magnetic field generated

by the waveguide, signifies the increase in the radiative rate decay in superradiant collective states. In the single-photon limit and at zero temperature, this serves as a signature of the formation of Dicke states. Here, at finite temperature, the system forms thermal collective states that also emit in a superradiant manner.

The decoherence rate $\gamma_\perp$ is found to be fairly temperature- and field-independent, except for the slight increase at lower temperatures as the model of the paramagnetic phase starts to fail. I associate it to a homogeneous broadening $\gamma_\perp = T_2^{-1}$. The observed $\gamma_\perp/2\pi \cong 8$ MHz at $T = 4.2$ K is compatible with the value measured for DPPH samples coupled to coplanar resonators ([12, Ch.7] and [13]) and to lumped-element resonators (see chapter 5). Remarkably, $G_N^{(\mathrm{line})}$ becomes of the same order of $\gamma_\perp$ for magnetic fields $B > 400$ mT. This yields a signal visibility:

$$\eta := \max(|\delta \mathrm{S}_{21}|) = \frac{\mathrm{G}_\mathrm{N}^{(\mathrm{line})}}{\mathrm{G}_\mathrm{N}^{(\mathrm{line})} + \gamma_\perp} \tag{8.4}$$

close to unity. Therefore, the spin ensemble and the waveguide are in a regime that resembles the strong coupling limit ($G_N \geq \gamma_\perp$) that is often reached with resonators, but in this case with a transmission line ($G_N^{(\mathrm{line})} \geq \gamma_\perp$).

8.1.2 Breakdown of superradiance by magnetic correlations

Below $T_\mathrm{N} = -\theta = 0.65$ K, B-type DPPH molecules tend to form AF chains (see section 5.2.2). Temperature controls the extension of spin correlations along the chains in a continuous and monotonic manner (see Fig. 8.1a). In order to explore how these correlations modify the transmission of the CPW, the CPW plus DPPH device was thermally coupled to the mixing chamber of a different ^{3}He-^{4}He dilution refrigerator giving access to the temperature region down to 10 mK.

Figure 8.4a shows the transmission data measured at a fixed magnetic field $B = 125$ mT as function frequency and (decreasing) temperature. At this field, the transmission of the waveguide is relatively 'clean', in the sense that the oscillations in $G_N^{(\mathrm{line})}$ (see Fig. 8.3) are not present. The spin resonance first gets enhanced on cooling below 2 K, as a result of the higher spin polarization (higher $(\Delta P)_\mathrm{e}$), but then it broadens out by an order of magnitude upon cooling from 2 K to 100 mK. This broadening is significantly larger than the broadening associated with the weak anisotropy, less than 1 in 1000, between the principal g-factors of DPPH [6]. Concurrently, the average resonance frequency ω_q increases by about 7% and the visibility decreases. Below 100 mK, the resonance becomes temperature independent.

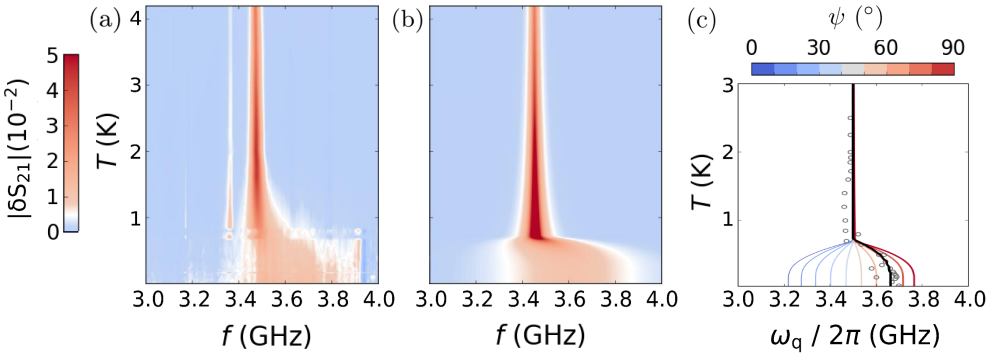

Figure 8.4: (a) Temperature dependence of the visibility of the resonance, given by δS_{21} at a magnetic field $B = 125$ mT. A large broadening of the resonance signal is observed below 1 K, marking the breakdown of superradiance due to the onset of antiferromagnetic correlations between type-B DPPH molecules. (b) Simulation of the experimental visibility with an antiferromagnetic mean-field model for type-B DPPH molecules with an imposed temperature independent visibility below T_N due to the formation of spin waves (see main text). (c) Dependence of the antiferromagnetic resonance frequency, ω_{res}, of each chain with the angle ψ between the anisotropy axis $\boldsymbol{\epsilon}$ of the chain and the applied magnetic field $\boldsymbol{B}$. The solid angle distribution favours the presence of larger angles (thicker solid lines) and therefore, larger frequencies, which is reflected in the transmission. The central frequency of the resonance in (b), ω_q, is represented by the solid black line. It fits quite well the experimental data, represented with grey open dots.

These features can not be explained anymore as just the transmission of a CPW coupled to an ensemble non-interacting spins. They are the consequence of the growing 1D spin correlations between DPPH spins from the sublattice B shown in Fig. 8.1a. A theory for the transmission of a waveguide coupled to 1D antiferromagnetic chains was developed by collaborators Sebastián Roca and David Zueco from the Q-MAD group at INMA. Using short chains does not suffice to describe the transmission, as longer chains have larger contributions. Unfortunately, a description of the coupling of arbitrarily long chains is computationally unaffordable. Therefore, a mean field (MF) theory was developed as a first approximation to describe the antiferromagnetism of the sample.

In antiferromagnetic MF theory, N spins are split into two sublattices with magnetization $\boldsymbol{M_1} = -(N/2)\mu_B g_S \boldsymbol{S_1}$ and $\boldsymbol{M_2} = -(N/2)\mu_B g_S \boldsymbol{S_2}$:

$$H = \mu_B g_S \boldsymbol{B} \cdot (\boldsymbol{S_1} + \boldsymbol{S_2}) + \boldsymbol{S_1} \cdot \boldsymbol{J} \cdot \boldsymbol{S_2}, \tag{8.5}$$

where $\boldsymbol{J}$ is a tensor encoding the anisotropy of the spin-spin exchange interactions. This anisotropy is defined by an axis $\boldsymbol{\epsilon}$ that depends on the orientation of the chains, introducing small corrections on the antiferromagnetic exchange constant J fixed via the Curie-Weiss law measured between 1 and 10 K and

shown in section 5.2.2: $J/k_{\mathrm{B}} = 4T_{\mathrm{N}}$, with $T_{\mathrm{N}} = -\theta = 0.65$ K. The module of $\boldsymbol{\epsilon}$ is the anisotropy exchange energy ϵ. With this model, the $k = 0$ spin wave frequency or *antiferromagnetic resonance* frequency ω_{res} is computed by solving the Landau-Lifshitz-Gilbert (LLG) equation with Eq. (8.5) in the linear regime [14]. This is the frequency at which each chain resonates with microwave light, provided that the photon wavelength λ is much longer than the size of the spin chains. Here this is a valid assumption, as the sample size is smaller than the smallest photon wavelengths ($\lambda = 4.4$ mm) for which the spin-photon coupling was measured ($\omega_{\mathrm{d}} \leq 14$ GHz).

The presence of a weak anisotropy in the spin-spin interactions along the chain is key to explain the observed shift in the resonance frequency ω_{q}. Each DPPH crystallite acquires a different resonance frequency depending on the angle ψ between the anisotropy axis $\boldsymbol{\epsilon}$ and the magnetic field. In a powder, the anisotropy introduces a distribution of resonance frequencies ω_{res} with a larger contribution for angles $\psi \sim \pi/2$ (see Fig. 8.4c). The ensuing inhomogeneous broadening makes different DPPH molecules 'distinguisable' and breaks down the Dicke state. The resonance frequency ω_{q} is computed as the central frequency of this broadened signal.

This simple model is therefore able to account for the change in the 'average resonance frequency' $\bar{\omega}_{\mathrm{q}}$ (Fig. 8.4c) and the resonance broadening (Fig. 8.5b) that are observed experimentally. $\bar{\omega}_{\mathrm{q}}$ is computed as the centre frequency of the average of the resonances for all solid angles. The only fit parameter is the magnitude ϵ of the anisotropy in $\boldsymbol{J}$:

$$\epsilon := \frac{J_{\parallel} - J_{\perp}}{J_{\perp}}, \tag{8.6}$$

where $J_{\parallel} \equiv (1+\epsilon)J$ and $J_{\perp} \equiv J$ are the components of $\boldsymbol{J}$ parallel and perpendicular to the anisotropy axis $\boldsymbol{\epsilon}$, respectively. Therefore, a reasonably good fit of $\bar{\omega}_{\mathrm{q}}$ gives a measure of the exchange coupling anisotropy, yielding $\epsilon \simeq -1/10$.

There is, however, an important limitation inherent to MF models: they overestimate the sharpness of the transition and predict a phase transition towards an ordered phase, which does not occur in 1D (see the dashed line in Fig. 8.5a). Besides, and MF model does not properly account for the elementary excitations of the AF chains, i.e. the spin waves. The temperature insensitivity of $\max(|\delta \mathrm{S}_{21}|)$ in Fig. 8.5a is indeed obtained by imposing the appearance of the spin-wave dynamics below T_{N}, which gives the solid line. This insensitivity provides direct evidence for a change in the commutation relations governing the elementary excitations of the spin system interacting with the microwave photons.

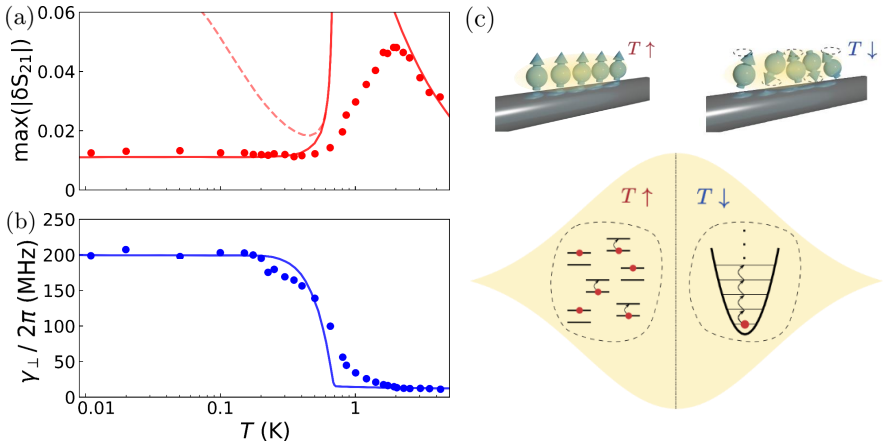

Figure 8.5: (a) Temperature dependence of the maximum visibility, $\max(|\delta S_{21}|)$, extracted from Figs. 8.4a (red dots) and 8.4b (solid red line). As a comparison, the red dashed line shows the expected visibility in the absence of spin waves below T_N. (b) Temperature dependence of $\gamma_\perp$. Blue dots represent the experimental values extracted from Fig. 8.4a. The blue solid line is the prediction from mean field theory, scaled to include the 'inhomogeneous' broadening that arises from exchange anisotropy in a powder sample. (c) Picture of the competition between spin-photon and spin-spin interactions. At high temperatures, type-B spins are in the paramagnetic phase and superradiant emission is observed. When the temperature is low enough, spins form chains, and spin waves appear. This is a change in the fundamental commutation relations of the spin system.

8.2 On-chip magnetic spectroscopy across a magnetic phase transition

8.2.1 Qubits based on spin clock states

The main source of decoherence in molecular spin qubits is the interaction of the spin with magnetic noise in the environment. Typical sources of these magnetic fields are other neighbouring spins, as in the previous section, or even nuclear spins from atoms in the same molecule. A straightforward strategy to achieve long coherence times T_2 is, therefore, to use molecules with effective spin 1/2 and nuclear spin-free ligands in dilution. The best coherence times are obtained with solvents which are also nuclear spin-free, like CS_2 (see Fig. 8.6 for some milestones).

A radically different strategy is inspired by the so-called 'clock transitions' that are used in atomic clocks, which appear in the anti-crossings between quantum states. In a magnetic molecule, these avoided crossings appear between superposition spin states with opposite symmetry — symmet-

ric/antisymmetric — that form at certain magnetic fields. These 'spin clock transitions' have a remarkable stability against magnetic field fluctuations, as dipolar decoherence vanishes at first order [15].

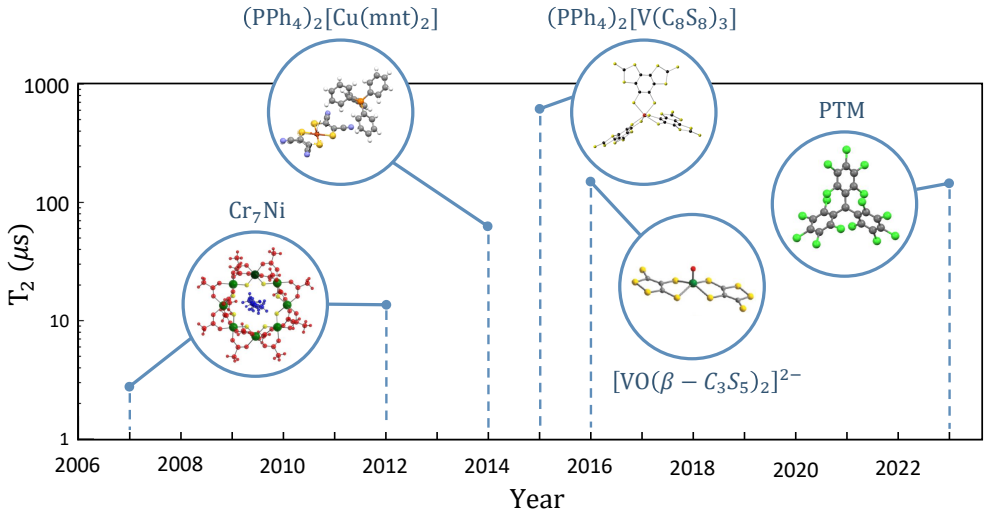

Figure 8.6: Beating decoherence in molecular spin qubits. These systems have and effective spin 1/2, with nuclear spin-free ligands and in solution with nuclear spin-free solvents. References: Cr_7Ni [16, 17], $(PPh_4)_2\,[Cu(mnt)_2]$ [18], $(PPh_4)_2\,[V(C_8S_8)_3]$ [19], $[VO(\beta - C_3S_5)_2]^{2-}$ [20], PTM [21].

Examples of these transitions have been found among molecular materials. A paradigmatic example is provided by the HoW_{10} complex. EPR experiments performed on diamagnetically diluted $Ho_xY_{1-x}W_{10}$ crystals show that spin coherence times increase sharply near each clock transition [22] as the spin-photon coupling becomes maximum [11]. However, the presence of sizeable hyperfine interactions turns them into non-ideal qubit candidates. First, getting to the clock transition requires the application of an external magnetic field. Second, and probably more important, the two levels involved in the clock transition might not include the actual ground spin state, thus hindering a simple qubit initialization by cooling.

The ideal situation is a clock transition between the ground and the first excited spin states. The simplest system that can achieve this is a spin 1 with tetragonal and orthorhombic distortions (only if $D < 0$), which is described by the following Hamiltonian:

$$H = D\hat{S}_z^2 + E\left(\hat{S}_x^2 - \hat{S}_y^2\right) + \mu_B g\left(B_x\hat{S}_x + B_y\hat{S}_y + B_z\hat{S}_z\right), \qquad (8.7)$$

where a constant term in the magnetic anisotropy has been dropped.

8.2.2 Molecular design of the simplest system with spin-clock states: the case of [Ni(2-Imdipa)]

The metallorganic compounds [Ni(Me_6tren)] and [Ni(2-imdipa)(NCS)]-(NCS) provide a physical realization of the system described by Hamiltonian (8.7) [23]. Here I focus on [Ni(2-imdipa)(NCS)]-(NCS), shortened as [Ni(2-Imdipa)] in what follows. It has a clock transition frequency of roughly 6 GHz, suitable for the frequency range of on-chip broadband experiments and for coupling to superconducting resonators. [Ni(2-Imdipa)] is composed of an organic ligand (2-imdipa) hosting a Ni^{2+} ion with spin 1 (see Fig. 8.7).

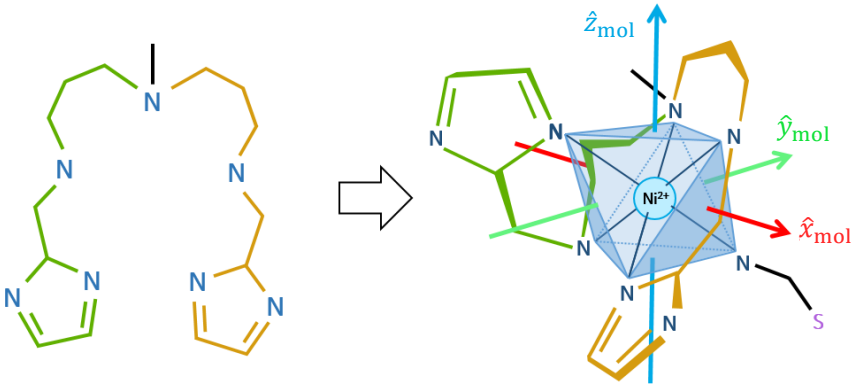

Figure 8.7: 2-imdipa pentadentate ligand (left) and its encasing of the Ni^{2+} ion in the Ni(2-Imdipa)(NCS) complex. Together with the NCS group, 2-imdipa forms an octahedral coordination site for Ni^{2+}. Only the magnetic anisotropy axis $\boldsymbol{y}_{\mathbf{mol}}$ was completely determined in previous experiments, with two possible solutions for the remaining axes $\boldsymbol{x}_{\mathbf{mol}}$ and $\boldsymbol{z}_{\mathbf{mol}}$. A guess, based on the symmetry of the coordination site, is shown here: the $\boldsymbol{z}_{\mathbf{mol}}$ is perpendicular to a face of the octahedron (although not exactly in practice, as it is a distorted octahedron).

The energy spectrum of [Ni(2-imdipa)] was calculated from the experimental results of heat capacity experiments [23]. Figure 8.8a shows the temperature dependence of the specific heat of a [Ni(2-imdipa)] crystal for fields in the range between 0 and 3 T applied along the longer dimension of the crystal. The specific heat measured at zero field has two peaks related to D and E, giving $D/k_B = -3.9$ K and $E/k_B = 0.15$ K. The Zeeman term is considered to be isotropic with $g_S = 2.34$, as the effect of magnetic anisotropy in the g-factor is negligible compared to the large D and E parameters. The evolution of the energy gap between the ground and first excited states with magnetic field is tracked by following the position of the low temperature peak in the specific heat (see figure 8.8b). The non-linear increase of the gap with the magnetic field is a signature of a clock transition. The results are consistent with the magnetic field being applied at 52.6° from the molecular z axis, $\boldsymbol{z}_{\mathbf{mol}}$.

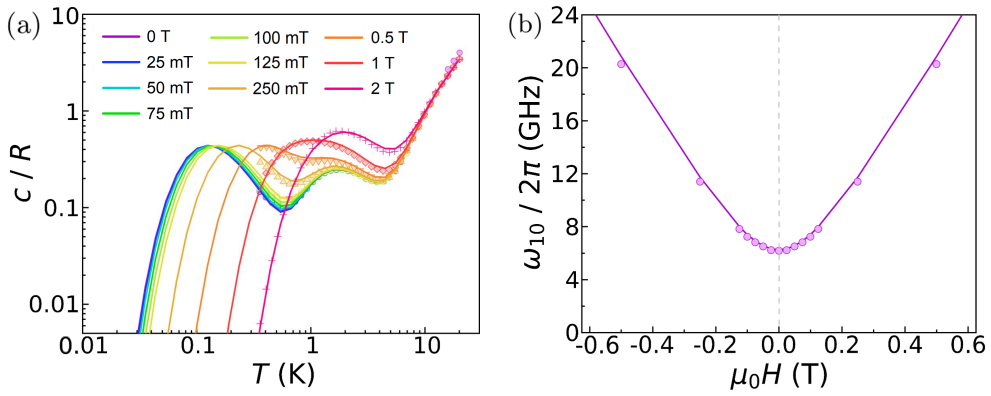

Figure 8.8: (a) Temperature dependence of the specific heat of a [Ni(2-imdipa)] crystal for magnetic fields in the range between 0 and 3 T applied along the longer dimension of the crystal. Solid lines show the simulated specific heat of a [Ni(2-imdipa)] molecule with its molecular z axis at 52.6° from the magnetic field. (b) Magnetic field dependence of the energy gap between the lowest lying energy spin states of this Ni complex, extracted form the position of the low temperature contribution to the specific heat at each measured field. The solid line is the expected evolution of the gap for this relative orientation of the magnetic field and the molecular z axis.

Figure 8.9 shows the energy spectrum of [Ni(2-imdipa)] as a function of magnetic field, with the parameters reported above and assuming the same relative orientation of the magnetic field to the $\boldsymbol{z}_{\mathbf{mol}}$. The orthorhombic term $D\hat{S}_z^2$ splits the $m_S = 0$ state from the $m_S = \pm 1$ doublet by $|D|$, while the orthorhombic term $E\left(\hat{S}_x^2 - \hat{S}_y^2\right)$ opens a gap $2E$ between the two levels associated with symmetric and antisymmetric superpositions of the $m_S = \pm 1$ states. For $D < 0$, $E \ll |D|$ and $|\mu_B g B_j| \ll |D|$ $(j = x, y, z)$, perturbation theory gives a simple formula for the energy gap Δ as a function of the static magnetic field:

$$\Delta \simeq 2\sqrt{E^2 + (\mu_B g B_z)^2} + \frac{(\mu_B g B_y)^2 - (\mu_B g B_x)^2}{|D|}. \tag{8.8}$$

The two lowest lying energy spin states of this Ni complex can encode a qubit with frequency of operation $\omega_q := \omega_{10} = \Delta/\hbar$. However, the fact that it has an integer total spin introduces significant differences with respect to a simple $S = 1/2$ system. The orthorhombic distortion gives ω_q stability against fluctuations in B_z ($\mu_B g B_z$ against E), while the longitudinal distortion gives it stability against fluctuations in B_x and B_y ($\mu_B g B_x$ and $\mu_B g B_y$ against $|D|$)). The large $|D|$ of [Ni(2-imdipa)] makes ω_q almost insensitive to B_x and B_y. All these features make the transition between the ground and first excited states of [Ni(2-imdipa)] at zero-field a textbook example of a spin clock transition. The transition frequency is protected against small magnetic field fluctuations,

as it is evident from Eq. (8.8): the leading order in a perturbation of the gap Δ at zero-field is of second order, while the first order contribution vanishes.

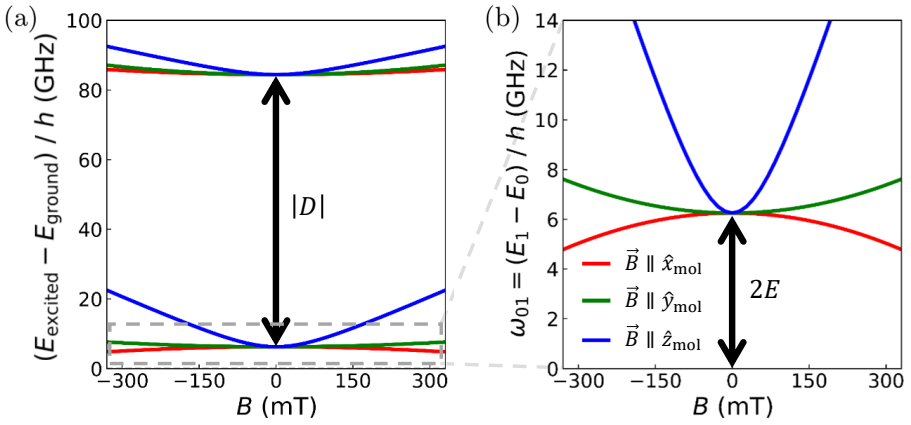

Figure 8.9: Magnetic field dependence of the transition frequencies between the ground and the excited spin states in [Ni(2-imdipa)] (a). A close up of the $0 \leftrightarrow 1$ transition between the ground and first excited states is shown in (b). $|D|$ is large enough to consider these two states as an isolated pair. The gap is easily tuned with the magnetic field parallel to the molecular z-axis $\hat{z}_{\text{mol}}$, while is more less insensitive to small fields parallel to $\hat{x}_{\text{mol}}$ and $\hat{y}_{\text{mol}}$.

At the clock transition ($B = 0$), two superposition spin states with opposite symmetry appear:

$$|\pm\rangle = \frac{1}{\sqrt{2}} \left(|m_S = +1\rangle \pm |m_S = -1\rangle \right). \tag{8.9}$$

The nature of these states determines the coupling of the qubit to photons. The transition between $|-\rangle$ and $|+\rangle$ is only addressable with the S_z spin operator, that is, with microwave magnetic fields $\boldsymbol{b}_{\mathbf{mw}}$ parallel to $\boldsymbol{z}_{\mathbf{mol}}$. This is shown in Fig. 8.10. If the static magnetic field is increased in the direction of $\boldsymbol{z}_{\mathbf{mol}}$, the coupling to $\boldsymbol{b}_{\mathbf{mw}}$ decreases. This is due to the increase in the magnetic field transforming the $|\pm\rangle$ superposition states into the $|m_S = \pm 1\rangle$ states, with the transition between the latter being forbidden. Conversely, the effect of magnetic fields of the same magnitude oriented perpendicular to $\boldsymbol{z}_{\mathbf{mol}}$ on $|\pm\rangle$ is negligible, yielding a coupling to $\boldsymbol{b}_{\mathbf{mw}}$ that remains close to its maximum value at zero field.

In view of this strong dependence of the coupling on the orientation of the molecules with respect to the static magnetic field $\boldsymbol{B}$ and the microwave field $\boldsymbol{b}_{\mathbf{mw}}$, it is important how [Ni(2-imdipa)] crystals are placed onto the chips. Figure 8.11a shows a [Ni(2-imdipa)] crystal in the form of a hexagonal prism. The axis going through the two hexagonal faces is the unit cell $\hat{c}$ axis. The $\hat{a}$ and $\hat{b}$ axes lie parallel to the hexagonal faces.

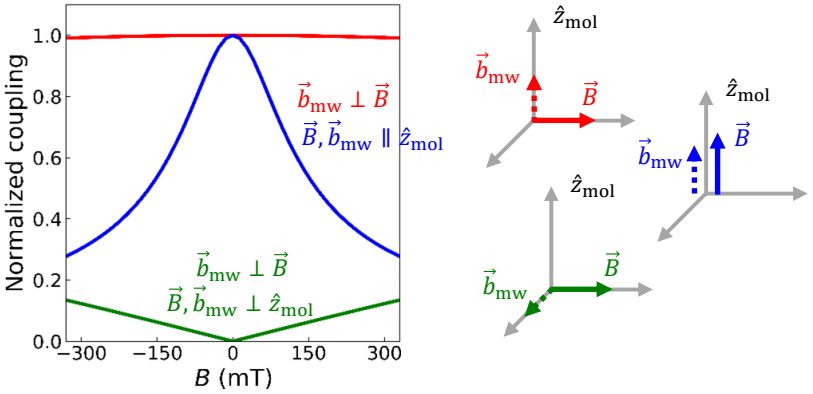

Figure 8.10: Single-spin photon coupling in [Ni(imdipa)], normalized by the maximum coupling. This maximum is located at the clock transition. Three cases are shown. In red, the microwave magnetic field $\boldsymbol{b}_{\mathbf{mw}}$ parallel to $\boldsymbol{z}_{\mathbf{mol}}$ ($\boldsymbol{b}_{\mathbf{mw}} \parallel \boldsymbol{z}_{\mathbf{mol}}$) and the static magnetic field $\boldsymbol{B}$ perpendicular to both ($\vec{B} \perp \boldsymbol{z}_{\mathbf{mol}}$). In green, $\boldsymbol{b}_{\mathbf{mw}}$, $\boldsymbol{B} \perp \boldsymbol{z}_{\mathbf{mol}}$ and $\boldsymbol{b}_{\mathbf{mw}} \perp \vec{B}$. In blue, $\boldsymbol{b}_{\mathbf{mw}}$, $\boldsymbol{B} \parallel \boldsymbol{z}_{\mathbf{mol}}$.

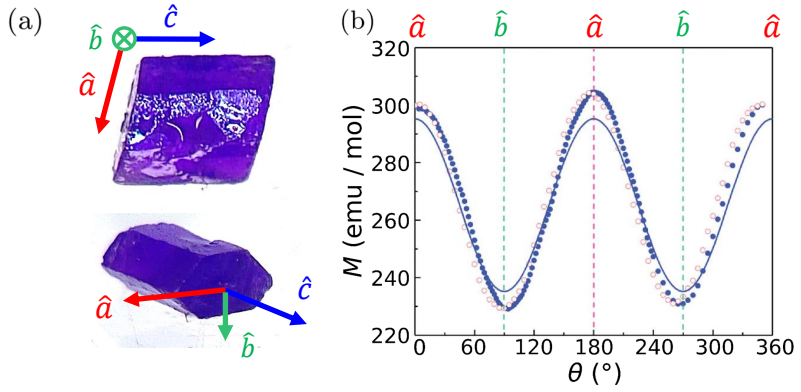

Figure 8.11: (a) A [Ni(2-imdipa)] crystal, showing the relation between the hexagonal prism and the unit cell axes. (b) Magnetization of the crystal at $B = 0.1$ T and $T = 5$ K as a function of rotation angle θ around an axis perpendicular to the $\hat{a}$-$\hat{b}$ unit cell plane. The difference between data measured while increasing (blue solid dots) and decreasing (red open symbols) angles is due to a mechanical hysteresis of the rotation system and provides a measure of the angular uncertainties. The crystal was placed so that the magnetic field aligned with the $\hat{b}$ cell axis at $\theta = 90, 270°$. The solid line shows the simulation of the magnetization with the parameters from heat capacity experiments and assuming that the molecular z axis lies in the $\hat{a}$-$\hat{c}$ plane.

The specific heat measurements in Fig. 8.8a were performed with the magnetic field applied along the longer dimension of the crystal, that is, parallel to the $\hat{c}$ axis. These measurements, combined with the measurement of the magnetization of the crystal for magnetic fields applied at different orientations in the $\hat{a}$-$\hat{b}$ plane, shown in Fig. 8.11b, are consistent with $\boldsymbol{z}_{\mathbf{mol}}$ being in the

$\hat{a}$-$\hat{c}$ plane at 52.6° from the $\hat{c}$ axis.

Each unit cell contains eight [Ni(2-imdipa)] molecules (see Fig. 8.12a), giving a spin density of $1.76 \cdot 10^{27}$ spins/m^3 in the crystal. These eight molecules are related by an inversion centre, a 2-fold screw axis along $\hat{b}$, and a glide plane spanned by $\hat{a}$ and $\hat{c}$. This means that the $\boldsymbol{z}_{\mathbf{mol}}$ axes of all 8 molecules are aligned. The tentative solution shown in Fig. 8.7 is compared with the cell axes in Fig. 8.12b.

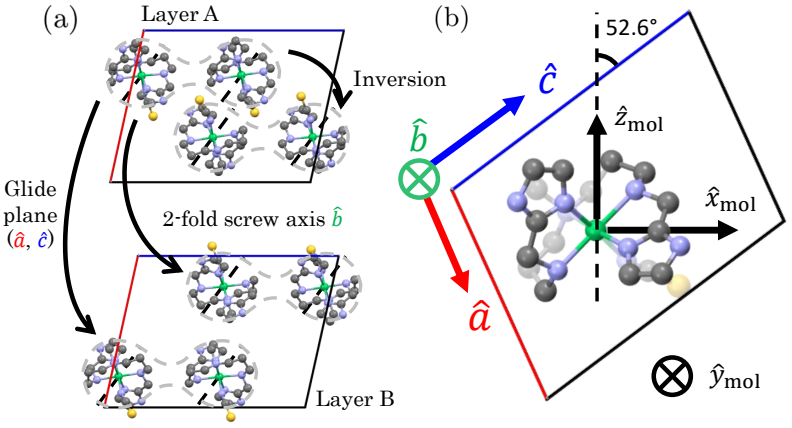

Figure 8.12: (a) The 8 [Ni(2-imdipa)] molecules in the unit cell, with their symmetry relations. They are distributed in two layers, labeled A and B. (c) Relation between the tentative solution for the molecular axes given in Fig. 8.7 and the unit cell axes.

8.2.3 Determination the molecular axes of [Ni(2-imdipa)] with transmission experiments

Measuring a molecular spin qubit encoded in the states of a spin clock transition coupled to a resonator is not as simple as with a qubit encoded in a spin 1/2. First, the latter can be easily tuned with the applied field ($\omega_{\mathrm{q}} = \mu_{\mathrm{B}} g B/\hbar$) to the match frequency of a resonator, ω_{r}. On the other hand, the anti-crossing of the spin clock transition makes the frequency of operation of the qubit more insensitive to the magnetic field, that is, more difficult to tune. For that reason, the first experiments of [Ni(2-imdipa)] samples coupled to superconducting circuits were carried out with a CPW, where a wide frequency range between 10 MHz and 14 GHz can be explored.

A [Ni(2-imdipa)] crystal was deposited on top of the waveguide, with the cell $\hat{c}$ axis parallel to the CPW (see Fig. 8.12), inside a dilution refrigerator mounting a superconducting vector magnet. This ensures that the microwave magnetic field generated by the line, which here is perpendicular to $\hat{c}$, has a component along the molecular z axis, $\boldsymbol{z}_{\mathbf{mol}}$. The transmission of the CPW

was measured at 128 mK and magnetic fields between -300 and +300 mT for two magnetic field orientations, one for each of the two possible orientations of $\boldsymbol{z}_{\mathbf{mol}}$, both lying at 52.6° from $\hat{c}$ in the $\hat{a}$-$\hat{c}$ plane. The temperature of the sample could not be lowered further in these experiments due to a thermalization problem. Figure 8.13 shows the transmission of the CPW for the two orientations.

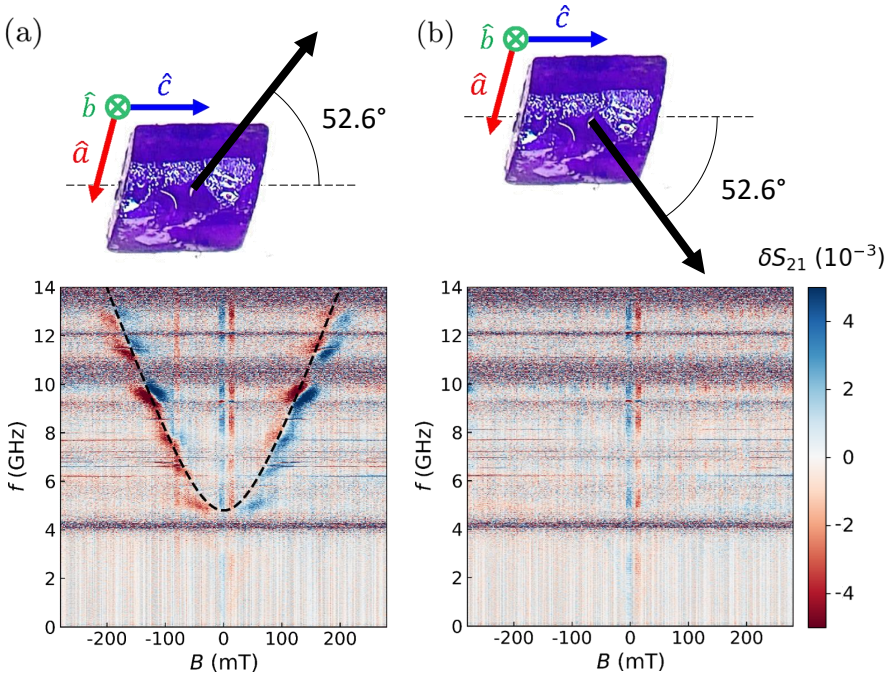

Figure 8.13: (a,b) Normalized transmission difference (δS_{21}) of a CPW coupled to a [Ni(2-imdipa)] crystal, for two magnetic field orientations that lie at 52.6° from $\hat{c}$ in the $\hat{a}$-$\hat{c}$ plane. This difference is computed at each field B as $\delta S_{21}(B) = [S_{21,\,\mathrm{exp}}(B) - S_{21,\,\mathrm{exp}}(B+\delta B)]\,/S_{21,\,\mathrm{exp}}(B+\delta B)$, effectively removing the baseline of the transmission signal. Here, δS_{21} is calculated with $\delta B = 10$ mT. The transmission measured for the orientation in (a) is consistent with the magnetic field applied along the molecular z axis, $\boldsymbol{z}_{\mathbf{mol}}$.

The absorption signal in Fig. 8.13a shows the non-linear dependence with magnetic field that is associated to clock transitions. The minimum resonance frequency, found at zero magnetic field, corresponds to a magnetic anisotropy gap $\Delta/h = 2E/h = 5$ GHz. This value is lower than the gap of ~ 6 GHz that was expected from heat capacity experiments. The observed magnetic field dependence of the signal is consistent with the magnetic field applied along $\boldsymbol{z}_{\mathbf{mol}}$ (compare with Fig. 8.9b). This confirms the choice of $\boldsymbol{z}_{\mathbf{mol}}$ in previous sections. The orientation of the magnetic field in Fig. 8.13b corresponds then to the magnetic field along $\boldsymbol{x}_{\mathbf{mol}}$. In this case, no absorption signal is

observed. The transition frequency between the ground and first excited states in [Ni(2-imdipa)] is more insensitive to magnetic fields applied along $\boldsymbol{x}_{\mathbf{mol}}$ than to magnetic fields applied along $\boldsymbol{z}_{\mathbf{mol}}$ (see Fig. 8.9b). The normalized transmission difference δS_{21} defined in Fig. 8.13 tends to lower the visibility of transitions that vary slowly with magnetic field, as is the case here for the magnetic field along $\boldsymbol{x}_{\mathbf{mol}}$. These results highlight how the relative orientation of the applied field and the magnetic anisotropy axes plays a crucial role in the coupling of the spin clock transitions to microwave photons.

8.2.4 Coupling spin-clock states to superconducting transmission lines

The experiment in the previous section was repeated in order to have access to the temperature range below 128 mK. This time, a DPPH powder sample was also placed on top of the CPW. The low temperature results of DPPH coupled to a CPW discussed in section 8.1.2 come from this experiment. Figure 8.14 shows how this setup allows a direct comparison between the standard electronic Zeeman transition in a $S = 1/2$ system, DPPH, and the clock transition in a $S = 1$ system, [Ni-(2-imdipa)]. The transmission of the CPW was measured in the temperature range between 10 mK and 800 mK, for magnetic fields between -300 mT and +300 mT applied parallel to the waveguide. The results are shown in Fig. 8.15.

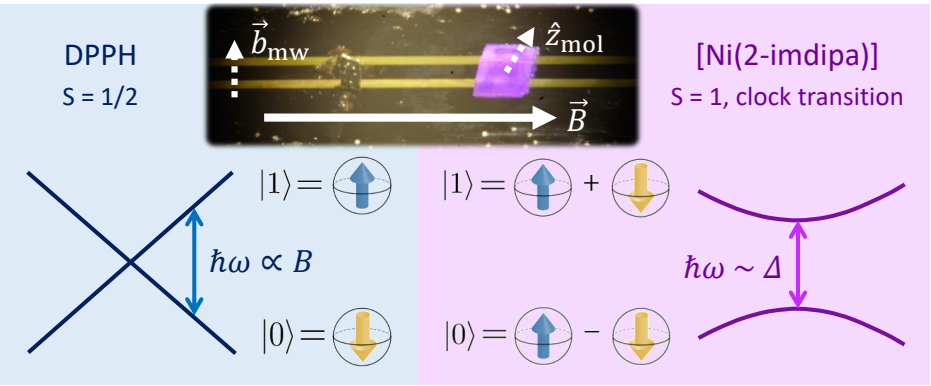

Figure 8.14: Comparison between the expected transmission for two samples deposited on the same CPW: DPPH (black powder pellet, $S = 1/2$) and [Ni-(2-imdipa)] (indigo-purple crystal, $S = 1$ with a clock transition). In DPPH, the transition frequency is proportional to the magnetic field, and therefore easy to tune. Conversely, the superposition states that arise at the clock transition of [Ni(2-imdipa)] make the transition frequency more insensitive to the magnetic field. This property makes clock transitions difficult to tune, but also more robust against magnetic field fluctuations.

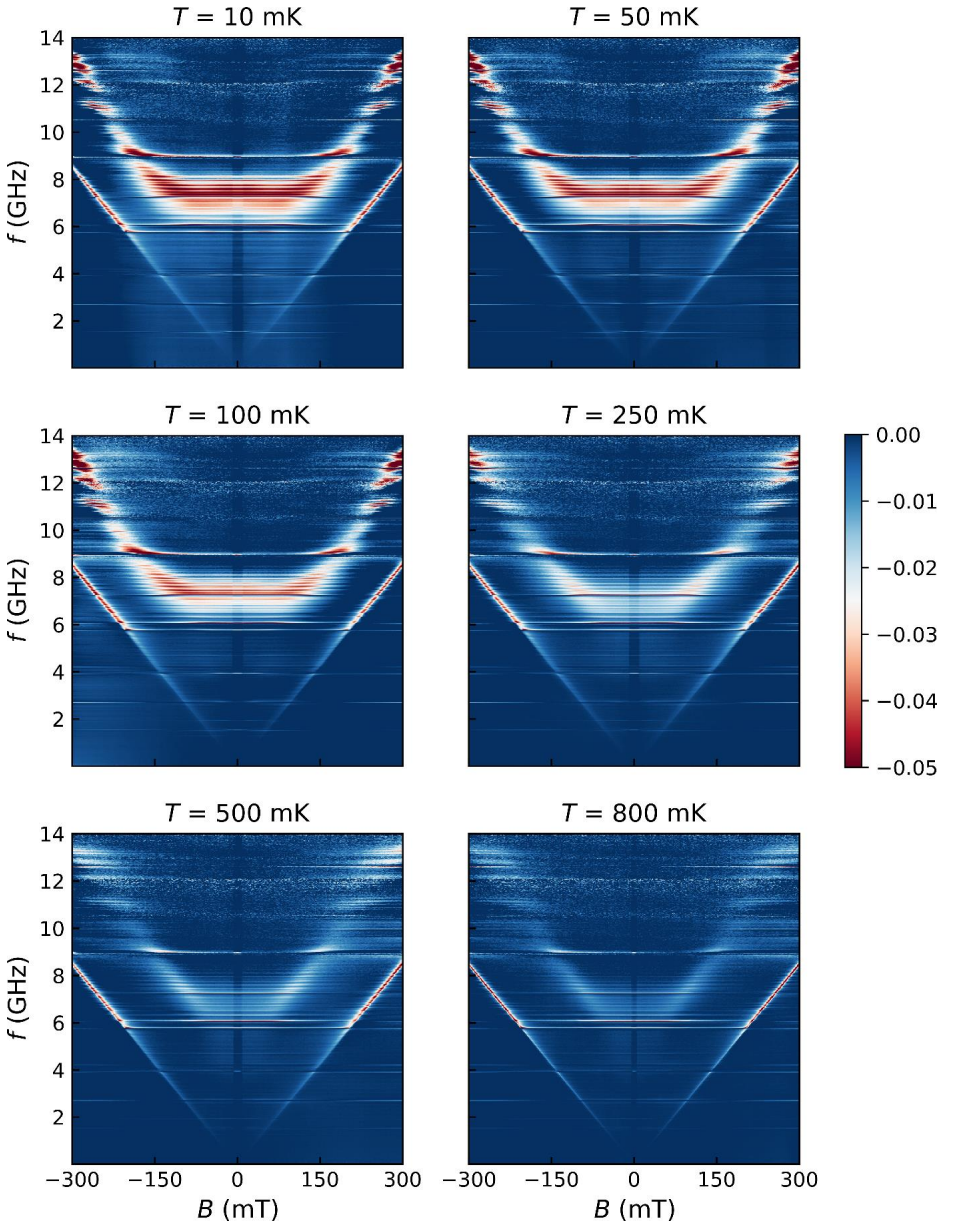

Figure 8.15: Normalized transmission of a CPW coupled to a a [Ni(2-imdipa)] crystal and a DPPH powder sample as a function of magnetic field and input microwave frequency, for six selected temperatures in the range between 10 and 800 mK. The complete set of measurements includes also the transmission at 20, 150, 175, 200, 225, 300, 350 and 400 mK.

Two absorption signals are observed, one with a linear dependence with field (DPPH, $S = 1/2$), and the non-linear dependence of the clock transition of [Ni(2-imdipa)] ($S = 1$). The transmission data was normalized by the

transmission of the uncoupled CPW, which was estimated by taking the values of the transmission S_{21} at those fields and frequencies that were sufficiently far from any of the absorption signals. The minimum resonance frequency of the [Ni(2-imdipa)], as in the previous section, appears at zero field, and is associated with a magnetic anisotropy gap $\Delta/h = 2E/h > 6$ GHz. At each field and temperature, the absorption resonance of [Ni(2-imdipa)] is fitted with Eq. (4.135):

$$S_{21}(\omega_{\mathrm{d}} \simeq \omega_{10}) = \frac{\gamma_{\perp,10} + i\,(\omega_{10} - \omega_{\mathrm{d}})}{\gamma_{\perp,10} + (G_N^{(\mathrm{line})})_{01}(\Delta P_{10})_{\mathrm{e}} + i\,(\omega_{10} - \omega_{\mathrm{d}})}. \tag{8.10}$$

Here, ω_{10} is the frequency of the transition $0 \leftrightarrow 1$ between the ground and first excited states, with collective spin-photon coupling $(G_N^{(\mathrm{line})})_{01}$ and decoherence rate $\gamma_{\perp,10}$.

The population difference $(\Delta P_{10})_{\mathrm{e}}$ between the two states of the clock transition is given by:

$$(\Delta P_{10})_{\mathrm{e}} = \frac{1 - e^{-\hbar\omega_{10}/k_{\mathrm{B}}T}}{Z} \simeq \tanh\left(\frac{\hbar\omega_{10}}{2k_{\mathrm{B}}T}\right), \tag{8.11}$$

as in a two-level system. The thermal population of the second excited state has been neglected in the approximation of the partition function Z, as $|D|$ is large enough to make this population less than 1% in the measured temperature range. In what follows, the collective spin-photon coupling $(G_N^{(\mathrm{line})})_{01}$ is redefined to include the population difference:

$$(G_N^{(\mathrm{line})})_{01} := \alpha\omega_{10}(\Delta P_{10})_{\mathrm{e}} \simeq \alpha\omega_{10}\tanh\left(\frac{\hbar\omega_{10}}{2k_{\mathrm{B}}T}\right), \tag{8.12}$$

where the linear dependence of the coupling in a 1D waveguide has been included and α is a dimensionless proportionality constant.

Figure 8.16a shows the fitted magnetic field-dependent transition frequency ω_{10} for all the measured temperatures. In the higher end of the measured temperatures (500-800 mK), the magnetic field dependence of the [Ni(2-imdipa)] signal is compatible with the behaviour expected for a a paramagnetic two-level system described by Eq. (8.8) with the magnetic field $\boldsymbol{B}$ applied at in the $(\boldsymbol{x_{\mathrm{mol}}}, \boldsymbol{z_{\mathrm{mol}}})$ plane at $\sim$52.6° from $\boldsymbol{z_{\mathrm{mol}}}$.

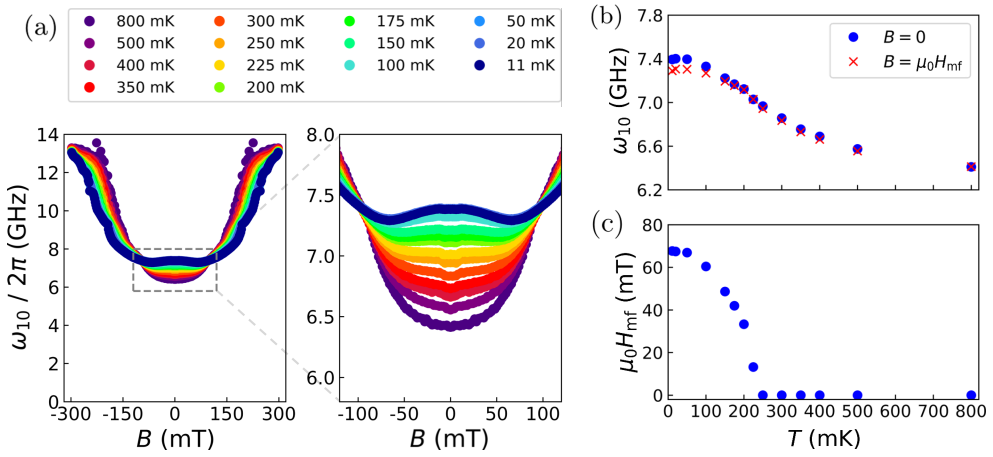

Figure 8.16: (a) Magnetic field dependence of the transition frequency ω_{10} for temperatures between 10 and 800 mK. A close-up of the area inside the dashed line is also shown. The gap at zero-field increases as temperature is lowered, while two minima appear at $B = \pm\mu_0 H_{\mathrm{mf}}$. (b) Temperature dependence of the zero-field gap (ω_{10} at $B = 0$, blue dots) and the minimum ω_{10} (ω_{10} at $B = \mu_0 H_{\mathrm{mf}}$, red crosses). ω_{10} increases steadily from ∼6.4 GHz at 800 mK to ∼7.4 GHz at 10 mK as temperature is lowered. (c) Temperature dependence of $\mu_0 H_{\mathrm{mf}}$, the magnetic field with minimum ω_{10}. Below 250 mK, two symmetric minima appear at $\pm\mu_0 H_{\mathrm{mf}} \neq 0$, with $\mu_0 H_{\mathrm{mf}}$ increasing sharply until it settles to ∼70 mT at the lowest measured temperatures.

However, as T decreases, the dependence of ω_{10} on B undergoes significant changes and deviates from this simple picture. First, below ∼ 350 mK the zero-field gap of the clock transition increases. Besides, the magnetic dependence near $B = 0$ flattens. This modulation of the gap, represented in Fig. 8.16b, suggests that there is a phase transition to a magnetically ordered state due to spin-spin interactions. The net interaction magnetic field stabilizes the ground state, lowering its energy with respect to the excited states. That is, the energies associated to the elemental excitations of the ground state are higher, thereby increasing ω_{10} at zero field. The steady increase of ω_{10} also suggests the presence of short range magnetic order at the higher measured temperatures. The extent of this order then grows as the temperature is lowered.

In addition to its increase at zero field, ω_{10} develops two minima at two magnetic fields with the same magnitude $\mu_0 H_{\mathrm{mf}}$ but opposite signs below 250 mK (see Fig. 8.16c). $\mu_0 H_{\mathrm{mf}}$ appears sharply at this temperature, indicating the onset of long range interactions. This can be seen as the different magnetization orientations of small parts of the sample with short range order aligning to generate a 'mean field' $\mu_0 H_{\mathrm{mf}}$.

In order to illustrate how spin-spin interactions modify the main features of the transmission spectrum, I used a simple toy model of a dimer of [Ni(2-

imdipa)] molecules with a $\hat{S}_{z,i} \otimes \hat{S}_{z,j}$ exchange interaction:

$$\begin{aligned} H = &\left[D\hat{S}_{z,1}^2 + E\left(\hat{S}_{x,1}^2 - \hat{S}_{y,1}^2\right) + \mu_\mathrm{B} g_\mathrm{S} \boldsymbol{B} \cdot \hat{\boldsymbol{S}}_1\right] \otimes \mathbb{I}_2 \\ &+ \mathbb{I}_1 \otimes \left[D\hat{S}_{z,2}^2 + E\left(\hat{S}_{x,2}^2 - \hat{S}_{y,2}^2\right) + \mu_\mathrm{B} g_\mathrm{S} \boldsymbol{B} \cdot \hat{\boldsymbol{S}}_2\right] \\ &+ J\hat{S}_{z,1} \otimes \hat{S}_{z,2}. \end{aligned} \tag{8.13}$$

Keeping only the $\hat{S}_{z,1}\hat{S}_{z,2}$ term to describe the interaction between the spins is justified by the insensibility of the energy gap to magnetic fields perpendicular to the molecular z axis. The spin-spin interaction can be seen as the interaction of a spin with a 'mean field' generated by the surrounding spins, then the z-axis Zeeman term of this field dominates against the other two axes.

At very low temperatures ($T \ll 2E/k_B$) and for small $|J|$, only one allowed transition of the dimer has non-negligible thermal population difference. Figure 8.17 compares the experimental ω_{10} at 10 mK with the frequency of this transition. The fit with the dimer model gives a zero-field gap $\Delta/h = 5.921 \pm 0.003$ GHz and an antiferromagnetic exchange constant $J/k_\mathrm{B} = 63.6 \pm 0.2$ mK. The two symmetric minima in the experimental ω_{10} are only possible with an antiferromagnetic coupling. The angle between the magnetic field and molecular z axis was slightly reduced to 47.7° for the fit.

Figure 8.18a shows the magnetic field and temperature dependence of the other two fit parameters of the resonance, the decoherence rate $\gamma_{\perp,10}$ and the collective spin-photon coupling $(G_N^{(\mathrm{line})})_{01}$. Both $\gamma_{\perp,10}$ and $(G_N^{(\mathrm{line})})_{01}$ decrease with increasing (absolute) magnetic field. On top, a small dip shows in $\gamma_{\perp,10}$ around the clock transition (close to zero magnetic field). The magnetic field dependence of $(G_N^{(\mathrm{line})})_{01}$ is a combination of the prediction in Fig. 8.10, with the maximum coupling at the clock transition, and the decrease in $(\Delta P_{10})_\mathrm{e}$ due to the increase of the transition frequency ω_{10} with magnetic field.

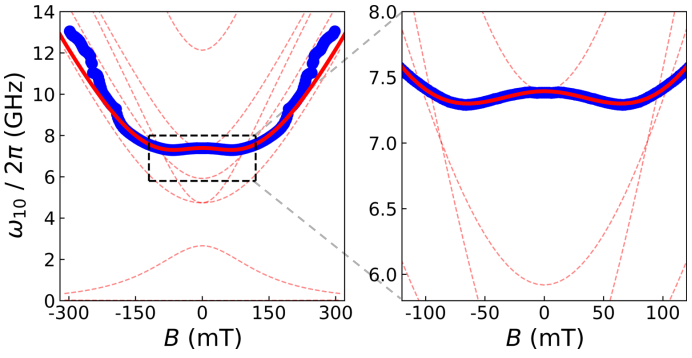

Figure 8.17: Comparison of ω_{10} measured at 10 mK (blue dots) with the only relevant transition of the dimer at 10 mK (red solid line). Red dashed lines are forbidden transition or with negligible population difference at 10 mK.

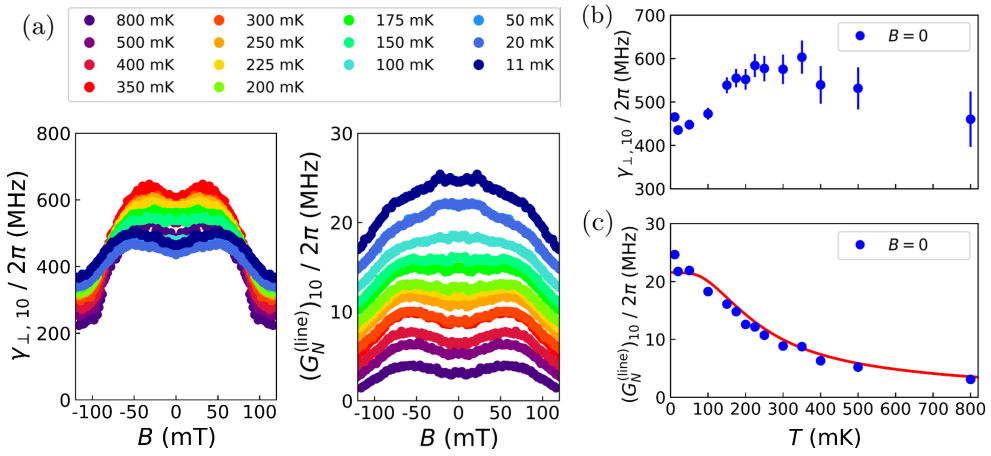

Figure 8.18: (a) Magnetic field dependence of the decoherence rate $\gamma_{\perp,10}$ and the collective spin-photon coupling $(G_N^{(\text{line})})_{01}$ for temperatures between 10 and 800 mK and fields between -100 and +100 mT. (b) Temperature dependence of $\gamma_{\perp,10}$ at zero magnetic field. A maximum in $\gamma_{\perp,10}$ is observed as the transition temperature is crossed ($\sim$ 200–300 mK). (c) Temperature dependence of $(G_N^{(\text{line})})_{01}$. Blue dots are the values from the fit of the experimental resonance, while the red solid line is the fit to Eq. (8.12).

The temperature dependence of $\gamma_{\perp,10}$ and $(G_N^{(\text{line})})_{01}$ at the clock transition — zero magnetic field — is shown in Figs. 8.18b and 8.18c respectively. As the transition temperature is crossed, a maximum in $\gamma_{\perp,10}$ is observed. Conversely, $(G_N^{(\text{line})})_{01}$ is fitted to Eq. (8.12), which assumes non-interacting spins, with a proportionality constant $\alpha \sim 0.0029$.

8.2.5 Coupling spin-clock states to lumped-element resonators

The coupling of spin-clock states in [Ni(2-imdipa)] to photons travelling through a waveguide has been characterized in the previous sections. The next step is then to enhance the spin-photon coupling by coupling [Ni(2-imdipa)] crystals to superconducting lumped-element resonators (LERs). A chip, labeled *Ni-cw*, was designed with ten LERs with frequencies slightly above the zero-field gap $2E/h \sim 6$ GHz of [Ni(2-imdipa)]. The chip design is shown in Fig. 8.19a. [Ni(2-imdipa)] crystals of different sizes were placed on top of each resonator with different orientations in order to see the effect of the number of spins and magnetic anisotropy on the coupling (see Fig. 8.19b). Unfortunately, most of the crystals in this experiment fell or broke into pieces during cooldown, as it can be seen in Fig. 8.19c. I decided then to focus the experiments on the sample on LER 9, which is the crystal that matches the size of the resonators (see Fig. 8.20).

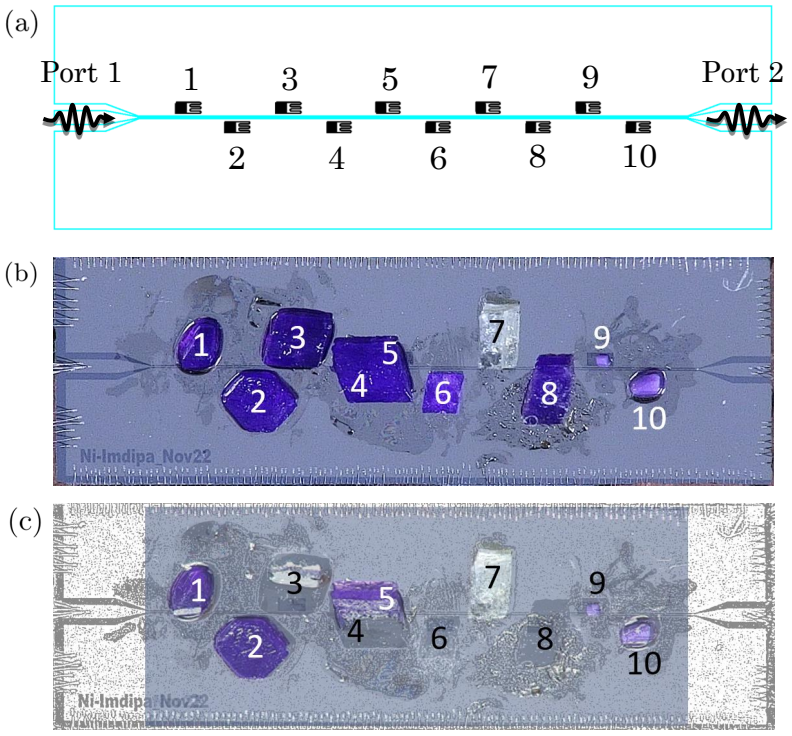

Figure 8.19: (a) Chip *Ni-cw*, hosting ten LERs (black) coupled to a single transmission line (cyan). (b) Superconducting chip with [Ni(2-imdipa)] crystals (indigo crystals) on top of *Ni-cw* LERs. One of the crystals is on top of two resonators, and also on top of the transmission line. White crystal is a sample of spin defects on ZnO, measurements with this sample are out of the scope of this work. (c) Remaining crystals after the experiments (color) superimposed over (b) in greyscale. Note that some of them fell from the chip at some point (crystals on top of LERs 3, 6 and 8) or even broke into pieces (half of a crystal on top LER 4).

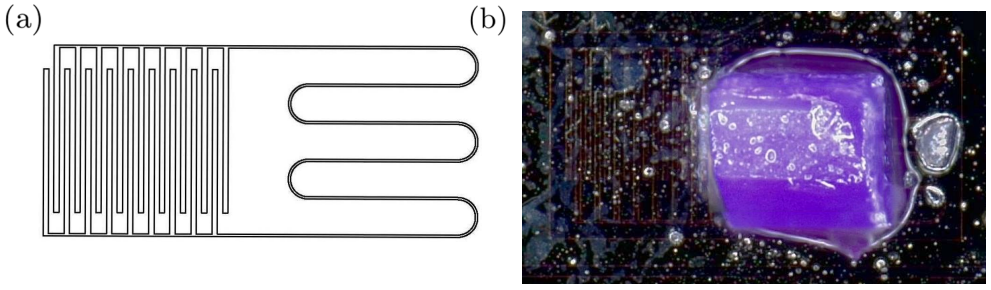

Figure 8.20: (a) Design of LER 1. The size of the resonator is smaller than in other chips, as they are aiming for a higher resonance frequency ω_r: smaller size $\rightarrow$ lower capacitance C and inductance L $\rightarrow$ higher $\omega_r = 1/\sqrt{LC}$. (b) [Ni(2-imdipa)] crystal on top of LER 9, matching the inductor size.

The transmission of *Ni-cw* with driving frequencies $\omega_d = 2\pi f$ close to the resonance frequency of LER 9 was measured for magnetic fields between -300 and +300 mT applied along the transmission line. The experiment was carried out at two temperatures: $T = 440$ mK (Fig. 8.21a) and $T = 128$ mK (Fig. 8.21b). A very large collective spin-photon coupling is observed, with the LER resonance almost vanishing completely for fields $|B| < 200$ mT. Note that an effect on the resonator is observed at zero field even if the resonance frequency $\omega_r/2\pi \simeq 8.2$ GHz of LER 9 is far from the zero field gap of [Ni(2-imdipa)] ($\Delta/h = 6$–7 GHz). This proves difficult for finding the LER resonances. The resonance of LER 9 was found by comparing the transmission data for $B = 0$ and $B = 300$ mT.

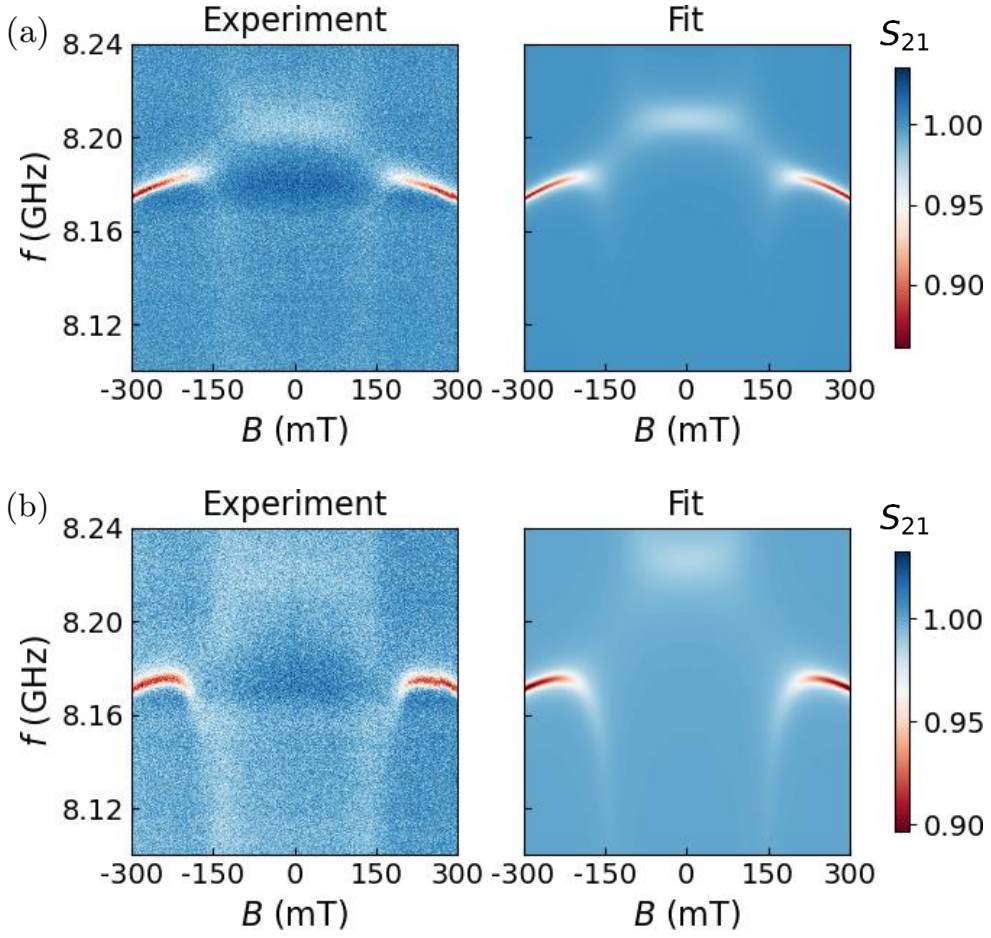

Figure 8.21: Normalized transmission of *Ni-cw* for driving frequencies ω_d close to the resonance frequency of LER 9, measured for magnetic fields between -300 mT and +300 mT along the transmission line and at two temperatures: 440 mK (a) and 128 mK (b). The resonator couples to the clock transition of [Ni(2-imdipa)].

The experimental data are fitted with the model for the resonance of a LER with frequency ω_r coupled to a qubit of frequency ω_q. The second excited state of [Ni(2-imdipa)] is neglected, as it lies ∼80 GHz above the measured range. The expression for the transmission parameter S_{21} is reproduced here:

$$S_{21}(\omega_\mathrm{d} \simeq \omega_{10}) = 1 - \frac{\kappa_\mathrm{c}}{i(\omega_\mathrm{r} - \omega_\mathrm{d}) + \kappa + \dfrac{(G_N)_{10}^2 \Delta P_{10}}{i(\omega_{10} - \omega_\mathrm{d}) + \gamma_{\perp,10}}}. \tag{8.14}$$

Here the qubit frequency $\omega_\mathrm{q} := \omega_{10} = \Delta/\hbar$ is defined by the evolution of the energy gap Δ between the ground and first excited states of [Ni(2-imdipa)], which is given in Eq. (8.8). The collective spin-photon coupling $(G_N)_{10}$ is also field dependent (see Fig. 8.10). In what follows, $(G_N)_{10}$ refers to the spin-photon coupling at zero field, which is scaled at other fields following the expected evolution of the coupling for a magnetic field at 52.6° from the molecular z axis. The fit parameters are listed in table 8.1 for both measured temperatures.

	$T = 440$ mK	$T = 128$ mK
$\omega_\mathrm{r} \,/\, 2\pi$ (GHz)	$8.196611 \pm 9 \cdot 10^{-6}$	$8.194578 \pm 1.7 \cdot 10^{-5}$
$\kappa \,/\, 2\pi$ (MHz)	1.135 ± 0.008	1.261 ± 0.011
$\kappa_\mathrm{c} \,/\, \kappa$	0.1487 ± 0.0009	0.1346 ± 0.0011
$(G_N)_{10} \,/\, 2\pi$ (MHz)	192.8 ± 0.2	279.1 ± 0.3
$\gamma_{\perp,10} \,/\, 2\pi$ (MHz)	831 ± 4	460 ± 3
$(G_N)_{10} \,/\, \gamma_{\perp,10}$	0.232 ± 0.001	0.606 ± 0.003
C_{10}	39.3 ± 0.3	134.1 ± 1.5
$\omega_{10}(B = 0)$ (GHz)	6.442 ± 0.004	6.801 ± 0.003

Table 8.1: Parameters of the fit of the transmission maps in Fig. 8.21 with Eq. 8.14.

The transition frequency at zero field, $\omega_{10}(B = 0)$ and the decoherence rate $\gamma_{\perp,10}$ obtained for both temperatures are of the same order of the values reported in the previous section for [Ni(2-imdipa)] coupled to a CPW. However, here it is assumed the same $\gamma_{\perp,10}$ for all fields, while Fig. 8.18a showed a magnetic field dependent $\gamma_{\perp,10}$. The change in both $\omega_{10}(B = 0)$ and $\gamma_{\perp,10}$ with temperature is consistent with previous results: $\omega_{10}(B = 0)$ increases with decreasing temperature, while $\gamma_{\perp,10}$ is higher at 440 mK (which is close to the temperature with maximum $\gamma_{\perp,10}$ in Fig. 8.18b).

The collective spin-resonator coupling is enhanced compared to the couplings to the CPW in Fig. 8.18a. A large coupling $(G_N)_{10}/2\pi = 192.8$ MHz is observed at $T = 440$ mK, and an even higher $(G_N)_{10}/2\pi = 279.1$ MHz at 128 mK. These couplings are not in the strong coupling regime $(G_N)_{10}/\gamma_{\perp,10} > 1$, but they are not far from it, with $(G_N)_{10}/\gamma_{\perp,10} > 0.6$ at 128 mK. In fact,

the increase of $(G_N)_{10}$ between 440 mK and 128 mK, combined with the decrease in $\gamma_{\perp,10}$, suggests that the strong coupling regime might be reached at base temperature ($T \sim 10$ mK). Unfortunately, the temperature region below 128 mK could not be explored in these experiments due to a thermalization problem in the cryostat. Similarly, it can be argued that the strong coupling regime could be achieved using a LER with resonance frequency $\omega_{\rm r}$ closer to $\omega_{10}(B = 0)$.

The high cooperativity regime $C_{10} = (G_N)^2_{10}/\kappa\gamma_{\perp,10} \gg 1$ is reached at both $T = 440$ mK and $T = 128$ mK, with a remarkably large $C_{10} = 134.1$ at the lowest temperature. This is more than four times the cooperativity of electronic spin transitions in [Yb(trensal)] at $T = 10$ mK, e.g. $C_{1\,10} = 32.5$ for the electronic spin transition $1 \leftrightarrow 10$ with $m_I = -3/2$ (see chapter 7). Note, however, that the [Yb(trensal)] crystals were diamagnetically diluted, while here the [Ni(2-imdipa)] crystal is fully concentrated. That is, the protection of the clock transition against decoherence is enough to obtain high cooperativity even without improving its coherence time by diamagnetically diluting the [Ni(2-imdipa)] molecules in a diamagnetic matrix. In comparison, the increase of the concentration of [^{173}Yb(trensal)] molecules in isotopically purified [Yb(trensal)] samples decreased significantly the cooperativity.

8.3 Conclusions

Powder samples of DPPH deposited on top of a CPW, an organic free radical molecule with spin 1/2, provide a platform to study the competition between spin-spin and spin-photon interactions. Above $T_{\rm N} = -\theta = 0.65$ K, the DPPH ensemble is in the paramagnetic regime, and the superradiant emission of thermal collective spin states is observed. Below $T_{\rm N}$, type-B DPPH molecules form antiferromagnetic (AF) chains. The insensitivity of the absorption signal in this temperature range is a signature of a change in the commutation relations of the elementary excitations of the spin system due to the formation of spin-waves. The coupling of the AF chains in a powder sample to a CPW allows estimating the weak anisotropy in the antiferromagnetic exchange interactions in the chains.

[Ni(2-imdipa)], a metallorganic compound with a Ni^{2+} ion with spin 1, adds a third element, spin clock transitions, to the competition between spin-spin and spin-photon interactions. The superposition spin states that form in this transitions are more robust against spin-spin interactions, and have also distinct geometrical properties concerning their interaction with microwave magnetic fields. The effect of spin-spin interaction on the properties of the coupling of the spin clock transition of [Ni(2-imdipa)] to photons in a CPW has been

studied with transmission measurements down to 10 mK, which suggest the presence of antiferromagnetic interactions below 200-300 mK. [Ni(2-imdipa)] crystals have been also coupled to lumped-element resonators, achieving a remarkably high cooperativity regime ($C > 100 \gg 1$).

References

[1] J. Román-Roche, F. Luis, and D. Zueco, Physical Review Letters **127**, 167201 (2021).

[2] M. O. Scully and A. A. Svidzinsky, Science **325**, 1510 (2009).

[3] M. O. Scully, Physical Review Letters **102**, 143601 (2009).

[4] R. H. Dicke, Physical Review **93**, 99 (1954).

[5] R. G. DeVoe and R. G. Brewer, Physical Review Letters **76**, 2049 (1996).

[6] D. Z. Žilić, D. Pajić, M. Jurić, K. Molčanov, B. Rakvin, P. Planinić, and K. Zadro, Journal of Magnetic Resonance **207**, 34 (2010).

[7] L. J. de Jongh and A. R. Miedema, Advances in Physics **23**, 1 (1974).

[8] C. Clauss, D. Bothner, D. Koelle, R. Kleiner, L. Bogani, M. Scheffler, and M. Dressel, Applied Physics Letters **102**, 162601 (2013).

[9] Y. Wiemann, J. Simmendinger, C. Clauss, L. Bogani, D. Bothner, D. Koelle, R. Kleiner, M. Dressel, and M. Scheffler, Applied Physics Letters **106**, 193505 (2015).

[10] I. Gimeno, A. Urtizberea, J. Romáan-Roche, D. Zueco, A. Camón, P. J. Alonso, O. Roubeau, and F. Luis, Chemical Science **12**, 5621 (2021).

[11] I. Gimeno, V. Rollano, D. Zueco, Y. Duan, M. C. de Ory, A. Gomez, A. Gaita-Ariño, C. Sánchez-Azqueta, T. Astner, D. Granados, et al., Physical Review Applied **20**, 044070 (2023).

[12] M. D. Jenkins Sánchez, Ph.D. thesis, Universidad de Zaragoza (2015).

[13] I. Gimeno, W. Kersten, M. C. Pallarés, P. Hermosilla, M. J. Martínez-Pérez, M. D. Jenkins, A. Angerer, C. Sánchez-Azqueta, D. Zueco, J. Majer, et al., ACS Nano **14**, 8707 (2020).

[14] F. Keffer and C. Kittel, Physical Review **85**, 329 (1952).

[15] G. Wolfowicz, A. M. Tyryshkin, R. E. George, H. Riemann, N. V. Abrosimov, P. Becker, H.-J. Pohl, M. L. W. Thewalt, S. A. Lyon, and J. J. L. Morton, Nature Nanotechnology **8**, 561 (2013).

[16] A. Ardavan, O. Rival, J. J. L. Morton, S. J. Blundell, A. M. Tyryshkin, G. A. Timco, and R. E. P. Winpenny, Physical Review Letters **98**, 057201 (2007).

[17] C. J. Wedge, G. A. Timco, E. T. Spielberg, R. E. George, F. Tuna, S. Rigby, E. J. L. McInnes, R. E. P. Winpenny, S. J. Blundell, and A. Ardavan, Physical Review Letters **108**, 107204 (2012).

[18] K. Bader, D. Dengler, S. Lenz, B. Endeward, S.-D. Jiang, P. Neugebauer, and J. van Slageren, Nature Communications **5**, 5304 (2014).

[19] J. M. Zadrozny, J. Niklas, O. G. Poluektov, and D. E. Freedman, ACS Central Science **1**, 488 (2015).

[20] C.-J. Yu, M. J. Graham, J. M. Zadrozny, J. Niklas, M. D. Krzyaniak, M. R. Wasielewski, O. G. Poluektov, and D. E. Freedman, Journal of the American Chemical Society **138**, 14678 (2016).

[21] D. Schäfter, J. Wischnat, L. Tesi, J. A. De Sousa, E. Little, J. McGuire, M. Mas-Torrent, C. Rovira, J. Veciana, F. Tuna, et al., Advanced Materials **35**, 2302114 (2023).

[22] M. Shiddiq, D. Komijani, Y. Duan, A. Gaita-Ariño, E. Coronado, and S. Hill, Nature **531**, 348 (2016).

[23] M. Rubín-Osanz, F. Lambert, F. Shao, E. Rivière, R. Guillot, N. Suaud, N. Guihéry, D. Zueco, A.-L. Barra, T. Mallah, et al., Chemical Science **12**, 5123 (2021).

Chapter 9

Conclusions

- Superconducting lumped-element resonators (LERs) have been studied as an alternative to coplanar resonators. They are interesting due to their property of frequency multiplexing and the possibility to fabricate low-impedance resonators. This allows having LERs with very small inductance, which enhances the spin-photon coupling in a small volume around it. The experiments with DPPH powder samples coupled to LERs confirm that the strong coupling regime, defined by a collective spin-photon coupling G_N greater than the decoherence rate $\gamma_\perp$, can be achieved with LERs. The results also highlight the importance of minimizing the gap between the sample and the surface of the superconducting surface in order to have the largest collective spin-photon coupling.

- A low-inductance LER design was used to perform the control and dispersive readout of molecular spin qubits based on PTM_r organic radicals. The absorption spectrum and the relaxation time T_1 of the spin ensemble were measured. These measurements also showcased the effect of the resonator on spin relaxation, obtaining an estimation of the highest single spin-photon couplings and their distribution through their role in the dynamics of the spin ensemble. In addition, experiments with short pulses (10–500 ns) showed the first signs of coherent manipulation of a ensemble of molecular spin qubits in this platform.

- The step of going from qubits to qudits is explored in the [^{173}Yb(trensal)] complex, a magnetic molecule encoding an electro-nuclear qudit with $d = 12$ states coming from its electronic spin $S = 1/2$ and the nuclear spin $I = 5/2$ of the ^{173}Yb isotope. High cooperativity has been observed in both electronic and nuclear transitions in [^{173}Yb(trensal)], which puts electronic and nuclear states almost on equal footing in this system. The presence of the electronic spin, and its high hyperfine coupling to the

nuclear spin, introduces an efficient path to couple nuclear transitions to the microwave magnetic field generated by the LER.

- The effect of spin-spin interactions in molecular ensembles on their coupling to superconducting has been studied with molecular systems with spin 1/2 and spin 1. These interactions are unavoidable until the limit of measuring a single molecular spin qubit is achieved. DPPH powder samples coupled to superconducting coplanar waveguides (CPW) provide a platform to study the competition between spin-spin and spin-photon interactions in spin 1/2 ensembles. As the temperature is lowered, the characteristics of the coupling of the sample to the waveguide change, marking the formation of spin waves in antiferromagnetic DPPH chains. [Ni(2-imdipa)], a metallorganic compound with a Ni^{2+} ion with spin 1, adds a third ingredient, spin clock transitions. The effect of spin-spin interactions on the spin clock transition in [Ni(2-imdipa)] can be detected via the changes in the spin-photon interaction of the clock transition spin superposition states with photons propagating through the waveguide. [Ni(2-imdipa)] crystals have been also coupled to LERs, achieving a remarkably high cooperativity regime ($C > 100 \gg 1$)

Conclusiones

- Los resonadores de parámetros concentrados (LERs) son una alternativa interesante a los resonadores coplanares para integrar qubits de espín molecular en circuitos superconductores. A diferencia de los resonadores coplanares, varios LERs de distintas frecuencias pueden fabricarse en un chip y medir su resonancia con una única línea de transmisión. Además, estos resonadores pueden diseñarse con una inductancia muy baja, generando campos magnéticos de microondas muy intensos en volúmenes pequeños. Una propiedad importante que quedaba por comprobar era si los LERs pueden alcanzar el régimen de acoplo fuerte a muestras de qubits de espín molecular. Este régimen está definido por un acoplo espín-fotón colectivo mayor que la tasa de decoherencia del conjunto de espines en la muestra. Este régimen se ya se había alcanzado previamente con resonadores coplanares. Los experimentos de transmisión de microondas de LERs acoplados a muestras en polvo de DPPH, un radical libre con espín $1/2$, confirman que también es posible alcanzar el régimen de acoplo fuerte en estos resonadores. Los resultados de los experimentos también destacan la importancia que el espacio que queda entre la muestra y la superficie del resonador tiene en el acoplo obtenido.

- Se ha construido un montaje experimental de generación y detección de pulsos de microondas para realizar experimentos de control y lectura de estados de qubits de espín molécular acoplados a LERs de baja inductancia. Con esta técnica se ha medido el espectro de absorción de una muestra de $\mathrm{PTM_r}$, otro radical libre con espín $1/2$, así como su tiempo de relajación T_1. Los resultados de estos últimos experimentos muestran el efecto que tiene el resonador en la dinámica de los espines. Experimentos con pulsos más cortos (10–500 ns) muestran los primeros indicios de una manipulación coherente de estados de qubits de espín molecular basada en una plataforma basada en circuitos superconductores.

- Se ha estudiado el complejo molecular [^{173}Yb(trensal)] como un ejem-

plo qudit de espín molecular, con d estados cuánticos. La molécula de [^{173}Yb(trensal)] es un qudit electronuclear con $d = 12$ estados provinientes de su espín electrónico $1/2$ y el espín nuclear $5/2$ del isótopo ^{173}Yb. Se ha conseguido alta cooperatividad en este sistema tanto para transiciones de espín electrónico como para transiciones de espín nuclear, lo que permite utilizar los estados de espín nuclear de manera similar a los estados de espín electrónicos. La alta cooperatividad de las transiciones nucleares se debe al alto acoplo hiperfino del espín nuclear del ^{173}Yb al espín electrónico en esta molécula. Esto permite acoplar de manera eficiente el estado nuclear a campos magnéticos de microondas a través del espín electrónico.

- Se ha medido el efecto de las interacciones entre espines en el acoplo de muestras de qubits moleculares a fotones propagándose por una línea de transmisión. Las muestras en polvo de DPPH, con espín $1/2$, acopladas a líneas de transmisión ofrecen una plataforma para estudiar la competición que existe entre las interacciones espín-espín y las interacciones espín-fotón. Al bajar la temperatura, las propiedades del acoplo de la muestra a la línea de transmisión cambian, señalando la aparición de ondas de espín en cadenas antiferromagnéticas de DPPH. El complejo [Ni(2-imdipa)], con un ion Ni^{2+} ion con espín 1, introduce un nuevo ingrediente: una transición de reloj de espín entre su estado fundemental y su primer estado excitado. Estos dos estados son superposiciones de estados de espín que forman un qubit de espín molecular protegido frente a ruido magnético. El efecto de las interacciones entre espines en la transición de reloj a muy baja temperatura se ha detectado midiendo el acoplo de ésta a fotones propagándose por una línea de transmisión. También se han acoplado cristales de [Ni(2-imdipa)] a LERs, consiguiendo una cooperatividad muy alta ($C > 100 \gg 1$).

List of publications

- E. Macaluso, M. Rubín, D. Aguilà, A. Chiesa, L. A. Barrios, J. I. Martínez, P. J. Alonso, O. Roubeau, F. Luis, G. Aromí and S. Carretta, Chemical Science **11**, 10337-10343 (2020)
- M. Rubín-Osanz, F. Lambert, F. Shao, Eric Rivière, R. Guillot, N. Suaud, N. Guihéry, D. Zueco, A. Barra, T. Mallah and F. Luis, Chemical Science **12**, 5123-5133 (2021)
- V. Rollano, M. C. de Ory, C. D. Buch, M. Rubín-Osanz, D. Zueco, C. Sánchez-Azqueta, A. Chiesa, D. Granados, S. Carretta, A. Gomez, S. Piligkos and F. Luis, Communications Physics **5**, 246 (2022)
- M. Rubín-Osanz, M. C. de Ory, I. Gimeno, D. Granados, D. Zueco, A. Gomez and F. Luis, Fizyka Nyzkykh Temperatur/Low Temperature Physics **50**, 520 (2024)
- S. Roca-Jerat, M. Rubín-Osanz, M. D. Jenkins, A. Camón, P. J. Alonso, D. Zueco, and F. Luis, arXiv:2404.03727 (submitted)

Appendix A - Tables

LER	$\omega_r/2\pi$ (GHz)	$\kappa/2\pi$ (kHz)	$\kappa_c/2\pi$ (kHz)
1	1.8246150	48.4	47.4
2	1.8264478	49.3	48.3
3	1.8559130	26.4	25.3
4	1.8572975	26.5	25.4
5	2.2679124	18.8	17.4
6	2.2714567	19.2	17.8
7	2.4125265	3.5	1.7
9	3.7892397	13.2	9.8
10	–	–	–
11	4.1887260	19.5	15.7
12	4.1955763	19.5	15.7

Table A.1: Parameters from the simulation with Sonnet of the lumped-element resonators in chip *Test 1*.

LER	$\omega_r/2\pi$ (GHz)	$\kappa/2\pi$ (kHz)	$\lvert\kappa_c\rvert/2\pi$ (kHz)	ϕ_c (°)
1	$1.6696529 \pm 3 \cdot 10^{-7}$	254.7 ± 0.2	76.1 ± 0.1	0.19 ± 0.03
3	$1.7144528 \pm 4 \cdot 10^{-7}$	206.1 ± 0.2	26.64 ± 0.04	2.1 ± 0.1
5	$2.116451 \pm 1 \cdot 10^{-6}$	415.5 ± 0.8	30.4 ± 0.1	23.2 ± 0.1

Table A.2: Parameters from the fit of the resonances of LERs 1, 3 and 5 in chip *Test 1* measured at $T = 4.2$ K and $B \simeq B_{res}$, as defined in table 5.1. We placed the same DPPH sample on top of each of the three resonators (see Fig. 5.17).

LER	$\omega_r/2\pi$ (GHz)	$\kappa/2\pi$ (kHz)	$\lvert\kappa_c\rvert/2\pi$ (kHz)	ϕ_c (°)
1	$1.595572 \pm 1 \cdot 10^{-6}$	138.6 ± 1.3	13.4 ± 0.2	-10.6 ± 0.4
2	$1.598124 \pm 2 \cdot 10^{-6}$	199.0 ± 1.6	18.6 ± 0.2	-17.5 ± 0.3
3	$1.6537159 \pm 9 \cdot 10^{-7}$	167.1 ± 0.9	23.0 ± 0.2	-11.2 ± 0.2
4	$1.657256 \pm 1 \cdot 10^{-6}$	150.4 ± 1.1	16.3 ± 0.2	-14.7 ± 0.3
5	$1.723823 \pm 2 \cdot 10^{-6}$	219.4 ± 1.9	114.8 ± 1.2	-6.7 ± 0.4
6	$1.725325 \pm 2 \cdot 10^{-6}$	196.61 ± 1.99	94.7 ± 1.1	-13.5 ± 0.4
7	$1.806576 \pm 2 \cdot 10^{-6}$	206.1 ± 2.3	8.4 ± 0.1	10.8 ± 0.5
8	$1.811397 \pm 3 \cdot 10^{-6}$	212.1 ± 2.9	7.0 ± 0.1	-3.9 ± 0.6
9	$1.9589596 \pm 9 \cdot 10^{-7}$	149.0 ± 0.9	28.3 ± 0.2	6.4 ± 0.3
10	$1.964212 \pm 1 \cdot 10^{-6}$	179.7 ± 1.3	27.7 ± 0.2	-4.9 ± 0.3
11	$2.063403 \pm 1 \cdot 10^{-6}$	181.9 ± 1.4	32.5 ± 0.3	10.9 ± 0.3
12	$2.065999 \pm 2 \cdot 10^{-6}$	172.8 ± 1.5	27.2 ± 0.3	-6.1 ± 0.4

Table A.3: Parameters from the fit of the transmission of the lumped-element resonators in chip *Test 2* at 4 K and zero field, as defined in table 5.1.

LER	$\omega_r/2\pi$ (GHz)	$\kappa/2\pi$ (kHz)	$\lvert\kappa_c\rvert/2\pi$ (kHz)	ϕ_c (°)
1	$1.5848946 \pm 9 \cdot 10^{-7}$	98.3 ± 0.9	17.0 ± 0.2	-0.5 ± 0.4
2	$1.5904145 \pm 8 \cdot 10^{-7}$	95.0 ± 0.8	15.6 ± 0.2	-1.4 ± 0.3
3	$1.6511598 \pm 6 \cdot 10^{-7}$	110.9 ± 0.6	22.5 ± 0.2	-1.4 ± 0.2
4	$1.6326271 \pm 6 \cdot 10^{-7}$	101.0 ± 0.6	16.0 ± 0.1	7.4 ± 0.3
5	$1.719468 \pm 2 \cdot 10^{-6}$	210.1 ± 1.8	115.7 ± 1.2	-0.5 ± 0.3
6	$1.722812 \pm 2 \cdot 10^{-6}$	154.3 ± 2.1	61.94 ± 1.01	0.0 ± 0.6
7	$1.802034 \pm 3 \cdot 10^{-6}$	121.9 ± 2.9	6.2 ± 0.2	-0.08 ± 0.98
8	$1.777309 \pm 2 \cdot 10^{-6}$	107.9 ± 1.8	6.1 ± 0.1	-3.3 ± 0.7
9	$1.9096160 \pm 7 \cdot 10^{-7}$	126.3 ± 0.7	24.5 ± 0.2	13.0 ± 0.2
10	$1.8715570 \pm 7 \cdot 10^{-7}$	122.5 ± 0.7	22.0 ± 0.2	12.9 ± 0.2
11	$2.0267752 \pm 9 \cdot 10^{-7}$	131.4 ± 0.9	29.8 ± 0.2	13.3 ± 0.3
12	$1.9992826 \pm 8 \cdot 10^{-7}$	121.4 ± 0.8	21.9 ± 0.2	6.3 ± 0.3

Table A.4: Parameters from the fit of the transmission of the lumped-element resonators in chip *Test 2* at 4 K and zero field, as defined in table 5.1, with DPPH samples on top of LERs 1, 4, 5, 8, 10 and 12.

LER	$\omega_r/2\pi$ (GHz)	$\kappa/2\pi$ (kHz)	$\lvert\kappa_c\rvert/2\pi$ (kHz)	ϕ_c (°)
1	$1.5843312 \pm 2 \cdot 10^{-7}$	141.3 ± 0.1	16.07 ± 0.02	2.49 ± 0.03
2	$1.5898394 \pm 2 \cdot 10^{-7}$	140.2 ± 0.1	14.84 ± 0.02	-0.86 ± 0.03
3	$1.6502776 \pm 9 \cdot 10^{-7}$	181.1 ± 0.6	23.5 ± 0.1	-5.4 ± 0.1
4	$1.631767 \pm 2 \cdot 10^{-6}$	134.5 ± 1.6	13.6 ± 0.2	4.3 ± 0.2
5	$1.7185818 \pm 4 \cdot 10^{-7}$	232.0 ± 0.3	94.7 ± 0.1	6.18 ± 0.04
8	$1.7761841 \pm 9 \cdot 10^{-7}$	187.5 ± 0.5	5.19 ± 0.02	0.0 ± 0.1
10	$1.8712407 \pm 8 \cdot 10^{-7}$	252.5 ± 0.4	20.89 ± 0.05	20.27 ± 0.05
12	$1.9979448 \pm 5 \cdot 10^{-7}$	219.4 ± 0.3	19.39 ± 0.03	6.28 ± 0.04

Table A.5: Parameters from the fit of the transmission of the lumped-element resonators in chip *Test 2* at 4 K. The values of ω_r here are those of the resonators at their corresponding resonance fields B_{res} (between 56 and 72 mT, depending on the resonator). They are slightly shifted to lower frequencies compared to the values reported in table A.4 due to the effect of the static field on the resonators (see section 5.4.1).

LER	$\omega_r/2\pi$ (GHz)	$\kappa/2\pi$ (kHz)	$\lvert\kappa_c\rvert/2\pi$ (kHz)	ϕ_c (°)
1	$1.5897023 \pm 1 \cdot 10^{-7}$	99.3 ± 0.1	15.78 ± 0.01	-13.83 ± 0.03
2	$1.5782930 \pm 3 \cdot 10^{-7}$	142.5 ± 0.2	14.92 ± 0.02	-3.51 ± 0.04
7	$1.7796599 \pm 9 \cdot 10^{-7}$	203.2 ± 0.5	11.70 ± 0.04	19.7 ± 0.1
8	$1.7994068 \pm 5 \cdot 10^{-7}$	153.4 ± 0.3	9.09 ± 0.02	-1.3 ± 0.1
11	$1.9605984 \pm 3 \cdot 10^{-7}$	167.8 ± 0.2	35.02 ± 0.05	6.65 ± 0.03
12	$1.9733963 \pm 2 \cdot 10^{-7}$	155.1 ± 0.1	27.83 ± 0.03	1.43 ± 0.03

Table A.6: Parameters from the fit of the transmission of the lumped-element resonators in chip *Test 2* at 4 K.

LER	$\omega_r/2\pi$ (GHz)	$\kappa/2\pi$ (kHz)	$\kappa_c/2\pi$ (kHz)
1	2.8308	14.0 ± 1	2.0 ± 1
2	2.6597	11.0 ± 1	3.0 ± 1
3	2.5194	13.0 ± 1	4.0 ± 1
4	2.3896	17.0 ± 1	4.0 ± 1
5	2.2800	13.0 ± 1	4.0 ± 1
6	2.1756	23.0 ± 1	4.0 ± 1
7	2.0870	13.0 ± 1	5.0 ± 1
8	2.0059	10.0 ± 1	10.0 ± 1
9	1.9331	10.0 ± 1	5.0 ± 1
10	1.8585	11.0 ± 1	8.0 ± 1

Table A.7: Parameters from the characterization, just after fabrication at CAB, of the lumped-element resonators in chip *Test 3* at 12 mK.